The Application Of Positron Emission Particle Tracking To Study Non-metallic Inclusions In Metal Castings

By

Youssef Beshay

A Thesis Submitted To The University Of Birmingham
For The Degree Of
Doctor Of Philosophy

Metallurgy and Materials
School of Engineering
The University of Birmingham

July 2010

Acknowledgements

There are a number of people whose support and generosity were crucial to the completion of this project and therefore deserve acknowledgement and a great deal of gratitude:

First, I would like to thank my supervisor Dr. W. D. Griffiths for all his encouragement, support and invaluable guidance. Under his supervision I have learnt from his vast wealth of knowledge and experience, without which I would not have been able to complete this thesis. He has not only been my supervisor, but also a friend who has always offered his help and advice through very difficult times during this project and for that I could not thank him enough. I feel privileged to have been one of his students who was given the opportunity to explore, make mistakes and learn from them.

Furthermore, I would like to extend my gratitude to the foundry technicians, Adrian Caden and Peter Cramer. Adrian Caden's technical help and support made many of the very difficult practical requirements of the experiments carried out in this project possible. He has been a good friend who's continuous encouragement was one of the reasons of the success of this research.

I am also indebted to Dr. J.C. Gebelin who is currently the technical director of the Partnership for Research in the Simulation of Manufacturing and Materials, in the University of Birmingham. He has been very generous with his time, in which he enlightened me how to resolve many of the problems I encountered while using the mathematical modelling

packages to simulate various casings. Without his help I could not have attempted to undertake some of the work contained in this thesis.

Fourthly, I would like to express my thanks to Prof. D.J. Parker, the Director of Nuclear Physics group at the University of Birmingham. Prof. Parker and his research group have been developing the PEPT technique for various applications in the food and chemical industries and their help and cooperation was key to the success of this project.

I must also extend my gratitude for the provisions of funds from Beshay Steel, Egypt, without which I could not have attempted to undertake this degree.

The last mention has to go my family: Kamal, Sanaa, Jim, Penny, Sarah and Samy who have always been very kind, generous, supportive and encouraging.

Youssef Beshay

July 2010

Abstract

Non-metallic inclusions are detrimental to the mechanical and corrosion properties of metals, owing to their stress raising potential and being preferred locations for crack initiation and propagation. Currently the number of inclusions in metals can be minimised by using good casting practices due to the lack of information about their movement within the liquid metal. Several casting modelling packages have particle tracking features intended to predict the path of inclusions in castings, but these models could not be verified.

In this work Positron Emission Particle Tracking (PEPT) was adopted and developed to design an experimental technique that can track inclusions in castings for the first time. This experimental technique was developed in four stages. The initial stage of the technique was based on the radioactive labelling of an oxide particle (size 355-425 μm) by the partial conversion of some of the oxygen atoms into the radioactive isotope ^{18}F. These radioactive particles were then placed at a known initial position in a sand or investment mould and after the casting was carried out, the final particle location of the inclusion was determined with a reported uncertainty of ± 1-8mm. The second stage was aimed at radioactively labelling smaller alumina particles, of size 63-100 μm, using the ion exchange technique which involved the attachment of the ^{18}F in directly irradiated water molecules to the surface of the particles by ion exchange. These particles were cast with a low melting point alloy *in situ* between the γ-ray detector camera and hence a full particle path was obtained, with a reported uncertainty of ± 1-4mm.

The effects of changing the particle type (density), size and the use of ceramic foam filters on the particle final location was investigated. Although limited information could be obtained about the effects of changing the particle type, the new PEPT technique provided information about the different filtration mechanisms of 10, 20 and 30ppi filters, which could not have been obtained previously. The PEPT results have also been used to assess the reproducibility of the castings and demonstrated the importance of controlling inlet conditions to improve reproducibility. The PEPT results were also compared to MAGMAsoft™ and Flow-3D™ models of the castings carried out experimentally, where it became clear that particle tracking models have not predicted the particle behaviour correctly.

The ability of PEPT to track multiple particles was explored using experiments where 2 and 4 particles (size 90-150 μm) were tracked in 2 Al plate castings, using the modular camera which is a portable version of the γ-ray detector camera used in previous experiments. The results obtained showed that multiple particles could be tracked, although the accuracy of the results is a function of the radioactivity of each particle and the distance between them.

Three particles were successfully relocated after being deliberately introduced into 3 different castings at known initial positions. The particles were identified using an SEM / EDX and were found within ± 1.2-3.6mm from the final locations measured using the PEPT technique. This has demonstrated that the PEPT technique developed in this work is an essential tool to further our understanding of inclusion movement within castings and one which can now be reliably used to develop and validate the currently available particle tracking models.

Table of Contents

List of Figures

List of Tables

Chapter 1
INTRODUCTION

1.1 General Introduction

Inclusions in castings (such as Al_2O_3 and SiO_2 of size range 60-425μm) act as sources of fatigue cracks and reduce the quality of the cast product. This is true for both shape casting of metals, DC casting of light alloys, and continuous casting of iron and steel. These inclusions are usually exogenous, having their source outside the metal. Examples of these, for DC casting, include refractories undergoing wear and tool coatings. For shape casting, exogenous inclusions can consist of particles from the mould-making process trapped inside the mould, or particles released from the mould surface during filling, such as might occur in the case of sand casting. Indigenous inclusions refer to those inclusions that occur inside the liquid metal, perhaps due to *in situ* chemical reactions, such as alumina in Al-killed steel or MnS [1], or due to physical effects such as agglomerated TiB_2 particles in grain refined Al alloys.

It is desirable to know more about the behaviour of such inclusions, and their final locations in the cast product. In shape castings a range of inclusion-removal strategies are employed. These include running system designs intended to prevent liquid metal containing inclusions from entering the mould cavity, and ceramic foam filters intended to trap inclusions within their pores. Ceramic foam filters are also used in the DC casting of Al, being placed in the

launder before the mould but not in the continuous casting of steel. The study of the behaviour of inclusions in castings has been facilitated by models of particle movement within the computer simulation software now used widely in the castings industry. However, there is currently no known method available to validate these models experimentally.

Positron Emission Particle Tracking (PEPT) is a process where a radioactively labelled particle (an oxide particle of size range 500μm-4mm or a resin particle of size range 63-73μm) is tracked by detecting the pairs of back-to-back ɣ-rays arising from annihilation of positrons emitted during radioactive decay. This involves a positron camera, location algorithms for calculating the location of the radioactive tracer particle by triangulation, and suitable tracer labelling techniques. PEPT has been widely used in the food and chemical industries, where the tracking of a radioactively labelled tracer particle has provided detailed information of the particle velocity and location at any given time. Examples of applications of PEPT include the study of the motion and behaviour of granular materials in rotating kilns, mixers, chemical reactors, food processors and fluids in cracks in rock [2-9]. The information obtained by the PEPT technique can be used not only to optimise the design of a wide range of industrial process systems, but also to evaluate modelling work.

The aims of this work were to investigate the possibilities of developing Positron Emission Particle Tracking (PEPT) techniques for shape casting applications and hence create a novel experimental tool by which particle movement features of casting modelling packages can be validated or challenged.

1.2 Aims and Objectives

The objectives of this work were met through four main stages, which are listed as follows:

Stage 1: Determining the final location of an inclusion in a casting

- The application of PEPT to study alumina inclusions, of size 355-425 μm in diameter, in steel castings that were made using sand and investment moulds.
- A study of the effects of using ceramic foam filters on the final location of the particles as well as the effect of changing the particle size, type (density) and initial location in the casting.
- Determination of the sources of error affecting the accuracy of detecting the final particle location in steel castings.

Stage 2: Tracking an inclusion in a low melting point alloy

- The application of PEPT to study alumina inclusions, of size 63-100 μm in diameter (of similar size to inclusions found in shape castings) in low melting point alloys.
- Study of the effects of using ceramic foam filters on the path of the particles as well as the effects of changing the particle size, type (density) and initial location in the casting.
- Determination of the sources of error affecting the accuracy of detecting the particle location within low melting point alloy castings.

Stage 3: Possibilities and limitations of tracking multiple particles

- Investigation of the capabilities of the tracking algorithms to track multiple particles.

- Investigation of the possibilities of using a modular camera (portable positron camera) to track multiple inclusions in a casting in an industrial environment.

Stage 4: Validation of mathematical modelling packages

- Assessment of the capabilities of the particle tracking features of the currently available casting modelling packages.

Chapter 2
LITERATURE REVIEW

2.1 Non-metallic Inclusions in Steel

2.1.1 Types of Inclusions

2.1.1.1 Indigenous inclusions

Non metallic inclusions in steels can be split into 3 categories, indigenous, exogenous and a mixture of both [1, 10]. Indigenous inclusions tend to be smaller inclusions that form from reactions taking place in a molten or solidifying metal. Some of these reactions take place during alloy additions to the melt, or changes in solubility of elements during cooling or freezing. Indigenous inclusions in steels are usually small, such as oxides, nitrides or sulphides with sizes between 0.2-80 μm [1, 11, 12]. They are often uniformly distributed within the microstructure and can be particularly damaging to the mechanical properties.

Deoxidation of steels is one of the main sources of indigenous inclusions. Figure 1 shows the deoxidising power of elements such as Al, Si and Mn in steel at 1600^{o}C, common deoxidants used in steel making [1]. Al, for example is added to a steel melt and reacts with oxygen in solution by forming Al_2O_3. This Al_2O_3 can either float out to the slag layer or be retained in the melt as an indigenous inclusion [1].

Another type of indigenous inclusion in steel is MnS, which forms by additions of ferro-sillico-manganese or ferromanganese, made for more deoxidation, desulphurisation and to prevent hot shortness (see section 2.1.3.1). Figure 2 is a micrograph showing MnS inclusions of size, of approximately 5µm.

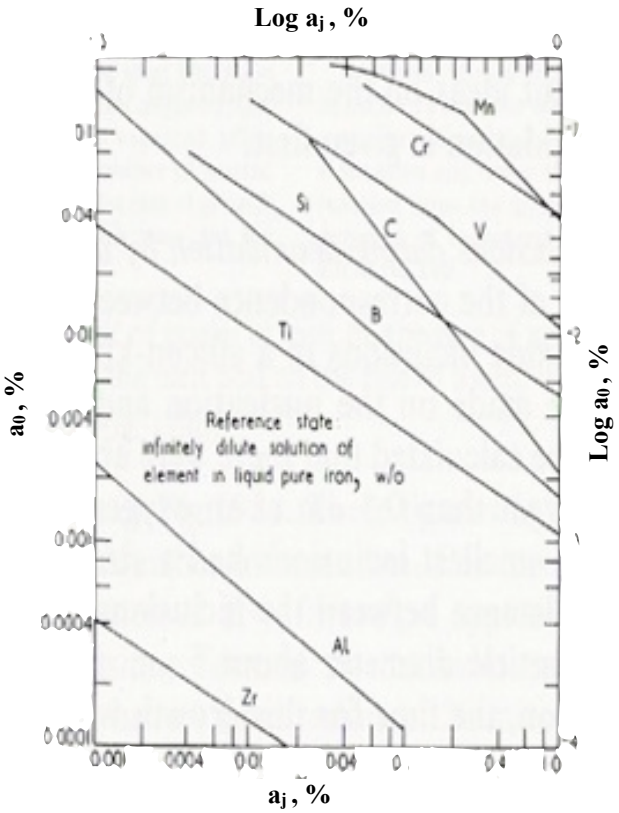

Figure 1. A graph showing the deoxidising power of Al, Si and Mn in steel at 1600°C [1]

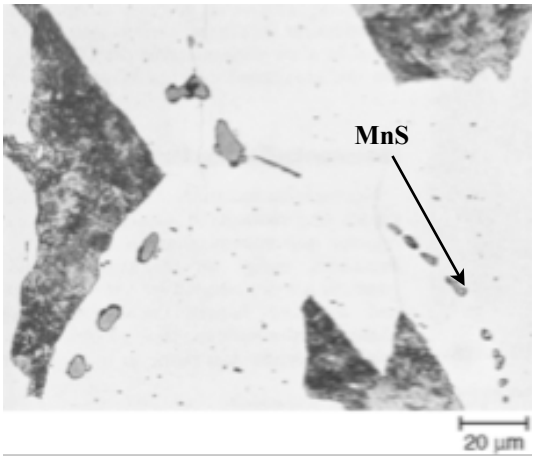

Figure 2. A micrograph showing manganese sulphide inclusions in steel. MnS inclusions (rounded grey particles) at grain boundaries of strand cast UNS G10170 steel that contains pearlite (mottled grey) in a matrix of ferrite (light). Etchant: picral. 500×. [13]

2.1.1.2 Exogenous Inclusions

Exogenous inclusions are entrained inclusions resulting from the mechanical incorporation of slags, refractories and other materials with which the molten steel comes in contact. Therefore there is a large variety of exogenous inclusions, mostly oxides which are the major slag and refractory materials for most liquid metal processes. These inclusions can be readily distinguished from indigenous inclusions because they are generally of a larger size, (e.g can be visible to the naked eye as shown in figure 3), and are characterised by irregular shapes and complex structures [13]. Figure 3 shows the surface appearance of a typical ductile iron crank shaft casting with a large number of exogenous inclusions. Moreover, exogenous inclusions have a sporadic occurrence [14] but an exact size range for these inclusions cannot be specified owing to the variable industrial environment in which the steel was produced. However some references used the size range of 100μm-2mm in diameter [1, 13, 15] .

CaO, MgO, Al_2O_3, Cr_2O_3 and SiO_2 are the main constituents of refractories used in steel making, as shown in Table 1 [1]. Mechanical and chemical erosion of these refractories results in the entrainment of these oxides as particles in the steel bath. Mechanical erosion can occur due to excessive stirring in the furnace and / or ladle which can result in excessive frictional forces between the liquid metal and the refractory walls. Chemical erosion can occur due to reactions between the melt and the refractory walls.

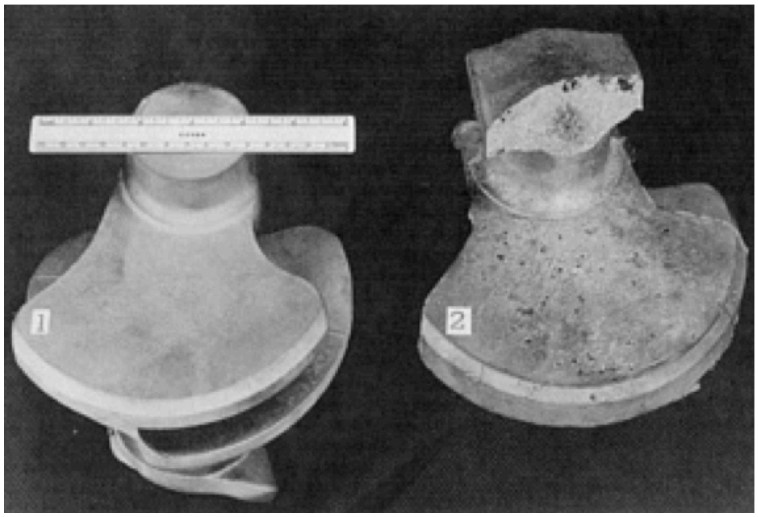

Figure 3. A ductile iron crankshaft segment essentially free of exogenous inclusions (1, left) and with numerous exogenous inclusions (2, right). Low pouring temperature and poor mould filling practice were the cause of the inclusions in part 2. [13]

Table 1. The typical compositions of refractories used in steel making [1].

	Refractory Type	**CaO**	**MgO**	**Al_2O_3**	**Cr_2O_3**	**SiO_2**	**Others (Fe_2O_3, TiO_2, ZrO_2, alk)**
Acid	Silicate brick	1.5-2.2	...	0.5-2	...	94-97	1-4
	Semi-silicate brick	1.5-2.2	...	7-28	...	70-90	1-4
	Chamotte brick	+	...	30-45	...	49-64	1-6
Neutral	Forsterite brick (olivine brick)	1	50-63	1-2	+	30-38	4-8
Basic	Magnesite brick	0.5-3	> 85	0.5-4	+	1-3	2-8
	Chrome-magnesite brick	0.5-2	35-50	10-16	25-30	3-5	8-14
	Magnesite-chromium brick	0.5-2	55-80	4-7	6-15	3-5	4-7
	Dolomite brick	50-60	36-40	0.5-3	...	0.5-5	0.5-3
	Acid mass	...	...	...	...	+	+
	Basic mass	...	+	...	...	...	+
	Aluminate cement	20-35	...	60-70	...	2-6	+

Inclusion origins are hard to trace because many non-metallic inclusions are continuously changing their structure and composition within the molten metal, and even after solidification, until diffusion rates are negligible [14]. This is demonstrated by indigenous inclusions precipitating on exogenous inclusions during the different stages of steel-making [14]. Therefore, a large multiphase inclusion with irregular shape and complex structure is not necessarily an exogenous piece of refractory; it may originate as the refractory material, but may also be associated with indigenous precipitation of different oxides and sulphides [16, 17]. Hence, a third type of non-metallic inclusions is a mixture of both indigenous and exogenous inclusions that combine due to heterogeneous nucleation, as shown in figure 4.

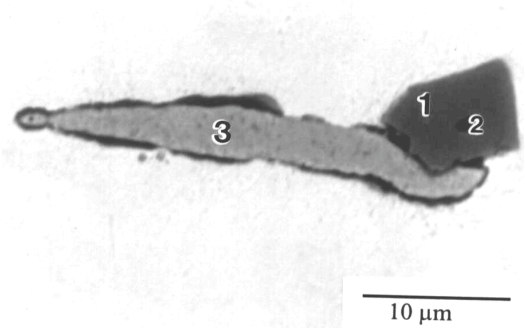

Figure 4. A complex inclusion of (1) (Ti,V)(C,N), (2) Al_2O_3 and (3) MnS [18]

2.1.2 Identification of Inclusion Origins in Steels

Inclusion origins can be roughly predicted using equilibrium phase diagrams and knowledge of the thermo chemical relationships and reaction rates taking place in the process. However the real industrial, non-equilibrium conditions and the materials used in those industrial processes have to be considered for an accurate representation of inclusion behaviour in practice [13].

2.1.2.1 Identification of Inclusions Origins in steel

Key elements in an inclusion's composition can suggest the possible processing stage or location from which an inclusion originated. Table 2 is a list of key elements that can be used to identify possible origins of inclusions in steel [1]. For example, according to table 2, inclusions containing Ca are more likely to have originated from furnace and ladle slags than refractories.The lime and dolomite mixture additions, made to control the slag foaming and slag basicity during melting in the furnace are the main source of Ca and can result in inclusions containing Ca, such as CaS, $CaO.Al_2O_3$ and CaO.

Table 3 shows the mean compositions of three inclusions in comparison to the typical compositions of known inclusion sources. The presence of MgO and CaO suggests an exogenous source, whereas inclusions with higher CaO (table 3, inclusion I) contents are more likely to be a result of slag entrainment and those with higher MgO contents, such as inclusions II and III, are most likely due to entrainment from refractories [1].

Table 2. The key elements that can be used to approximately identify inclusion origins in steels [1].

Possible Inclusion Sources in Steels		**Key Elements**
Furnace	Furnace slags	Ca
	Furnace refractories	Ca
	Ferroalloys	Cr, Al, Si
Tapping	Launder refractories	Mg, Ti, K
	Oxidation	FeO
Ladle	Deoxidation	-
	Ladle slag	Ca, Mg
	Ladle refractories	Mg, Ti, K

Possible Inclusion Sources in Steels		Key Elements
Teeming	Stopper and nozzle refractories	Mg, Ti, K
	Oxidation	FeO
	Deoxidation	-
Ingot Mould	Refractories	Mg, Ti, K
	Deoxidation	-
Heat Treatment and Rolling	Surface oxidation	FeO
	Surface sulphurisation	FeS
	Inner oxidation	SiO_2
	Hot-Shortness	FeS
Welding	Welding slags	Ca, Ti
	Electrode coatings	Ti, V
	Hot tearing	S

Table 3. Spectrochemical analyses of the composition of different possible exogenous inclusion sources as compared with inclusions *in situ.* The units used for the compositions are given in wt% while (+) indicates the presence of traces of the respective inclusion. [1]

Source /Inclusion	MnO	FeO	CaO	MgO	Al_2O_3	SiO_2	TiO_2
Furnace Slag	10	7	45	10	13.5	15	-
Ladle Slag:							
Before degassing	11	2.5	30	8	9.5	34	-
After degassing	10		27	6	14.5	37	-
Ladle refractories:							
Top Lining	-				75	22	
Main Lining	-	2			33	62	
Ingot mould refractories	-	2	-	20	38	40	-
Ingot scum	22	6		12.5	12.5	40	-
Inclusion I	13	-	23	7	20	41	-
Inclusion II	8	+	+	34	10	46	+
Inclusion III	31	-	4	14	8	43	+

2.1.2.2 Prediction of Indigenous inclusion formation

The formation of indigenous inclusions in steels can be predicted using thermodynamic relationships and phase diagrams. The formation of inclusions such as MnS and Al_2O_3 are described by equations 1 and 2:

$$Mn+S \rightarrow MnS \text{ ----------Equation 1}$$

$$2Al + 3O \rightleftharpoons Al_2O_3 \text{ ----------Equation 2}$$

These equations will only occur if the concentrations of Mn and S, for instance, exceed the solubility product for the formation of MnS, (K_{MnS}) [14]. To a reasonable approximation the solubility product is defined as:

$$K=[\%Mn][\%S] \text{ ----------Equation 3 [14]}$$

Where the concentrations of Mn and S are written as mass %. K however varies with temperature and therefore a more accurate representation would be as follows:

$$\text{Log } [\%Mn][\%S] = (-9020 / T) + 2.93 \text{ ----------Equation 4 [16]}$$

In a similar analogy, Al_2O_3 will form when the solubility product of formation $K_{alumina}$ exceeds the critical solubility product, $K'_{alumina}$, that is required for the reaction to occur.

$$\text{Log } [\%Al][\%O] = (-62680 / T) + 32.54 \text{ ----------Equation 5 [16]}$$

Therefore a knowledge of the temperatures involved in the different processing stages can provide some guidance as to which indigenous inclusions may be formed and hence an appropriate method to deal with them can be used.

The entrainment of exogenous inclusions cannot be predicted and their elimination relies heavily on experience and trial and error iterations where the sources of these inclusions are identified and minimised.

2.1.3 Control of Inclusions in Steels

Non metallic inclusions can be removed and/or their detrimental effects be minimised using chemical, mechanical or physical techniques during production [19]. These techniques include promoting the flotation of inclusions, optimising the fluid flow in a tundish or using ceramic filters, in the case of shape castings, to prevent the inclusions from reaching the final cast product.

2.1.3.1 Chemical Control

The addition of alloying elements and additives must be controlled to minimise the formation of indigenous inclusions. Processing operations must also be carefully controlled to minimise introduction of exogenous inclusions by erosion of refractories.

Work by Kiessling *et al*. showed that 83% of inclusions present in low carbon steels are due to re-oxidation, followed by 14% from mould erosion, 2% from slag entrainment, 1% from refractories and 1% from deoxidation products (see figure 5) [16]. Inclusions formed due to re-oxidation can be minimised by controlling the slag basicity by adding lime (CaO), which allows for a good slag foaming practice in the case of steel making. The target is to ensure that the slag remains foamy and is spread across the whole surface of the melt to minimise the risk of contact between the liquid steel with the atmosphere inside the furnace, which would consequently result in re-oxidation. Care should be taken during oxygen injection to avoid opening holes in the slag layer. The same care should be applied with Ar stirring in the melting or ladle furnace.

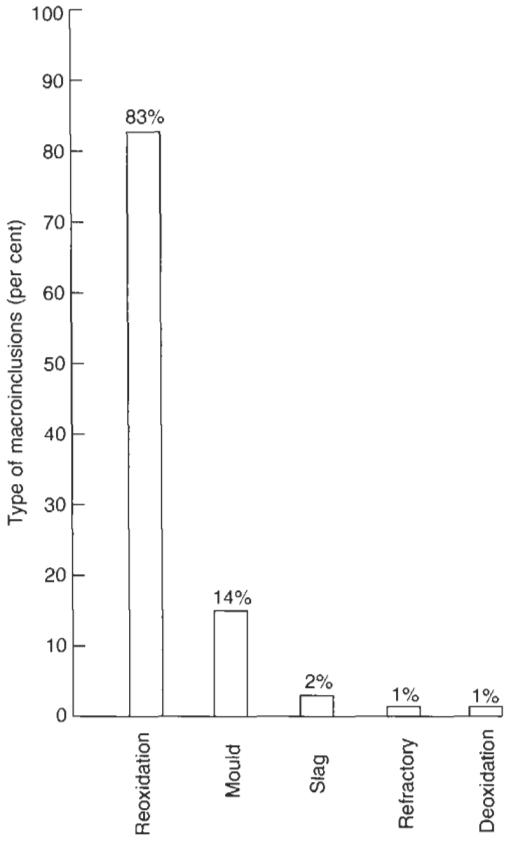

Figure 5. A graph showing the distribution of types of macro-inclusions in carbon and low alloy steel castings from a sample of 500 inclusions, in castings from 14 foundries [16].

Also controlling the slag basicity by CaO additions is critical to control reactions between the steel bath, slag and the surrounding refractories. These calcium rich additions are added to minimise the attack on the MgO-C brick lining of the furnace [16] which therefore decreases the chances of MgO particles being eroded into the melt and serving as nucleation points for various other indigenous inclusions in the steel bath. Increasing the slag basicity and decreasing the slag's FeO content has been reported to enhance the absorption of inclusions into the slag [20]. Slag basicity can be calculated using equations 6 and 7 for furnace and ladle slags respectively.

$$B = \frac{\%CaO + 1.4 \times \%MgO}{\%SiO_2 + 0.84 \times \%P_2O_5}$$ For furnace slags [9] ----------Equation 6

$$B_{LF} = \frac{\%CaO + 1.4 \times \%MgO}{\%SiO_2 + 0.6 \times \%Al_2O_3}$$ For ladle furnace slags [9] ----------Equation 7

Moreover, hot shortness (brittleness due to a high sulphur content) of certain grades of steels can occur between 900°C and 1000°C due to the presence of oxygen and/or sulphur and the formation of liquid oxysulphides during hot working (e.g rolling) [16]. This is controlled by maintaining an Mn:S ratio that is in accordance to equation 8, provided the steel has been killed (deoxidised).

$$(\%Mn) = 1.25(\%S) + 0.03$$ [1] ----------Equation 8

2.1.3.2 Mechanical Control

Argon stirring is a common practice in steel making and can be very beneficial in promoting agglomeration and inclusion flotation, provided it is carried out correctly. According to Stoke's Law (equation 9) inclusions will float out of the melt to the slag layer at different speeds, depending on the inclusions size, the difference in density between them and the molten metal, the viscosity of the molten metal and the time available for their flotation. Argon stirring allows these inclusions to collide more often and therefore increases their chances of combining and behaving as one particle with a larger diameter, and consequently becoming more buoyant. Figure 6 depicts the effect of mean inclusion diameter on the speed of flotation, calculated using Stoke's Law [18].

$$\text{Stoke's Law: } V_s = \frac{2(\rho_p - \rho_f)}{\mu} gR^2 \text{ ----------Equation 9}$$

V_S is the particle settling terminal velocity (m/s) (upwards if $\rho_f > \rho_p$), g is the gravitational acceleration (m/s ^{2}), ρ_p is the mass density of the particle (kg/m ^{3}), ρ_f is the mass density of the fluid (kg/m ^{3}) , and μ is the fluid's dynamic viscosity (Pa.s)

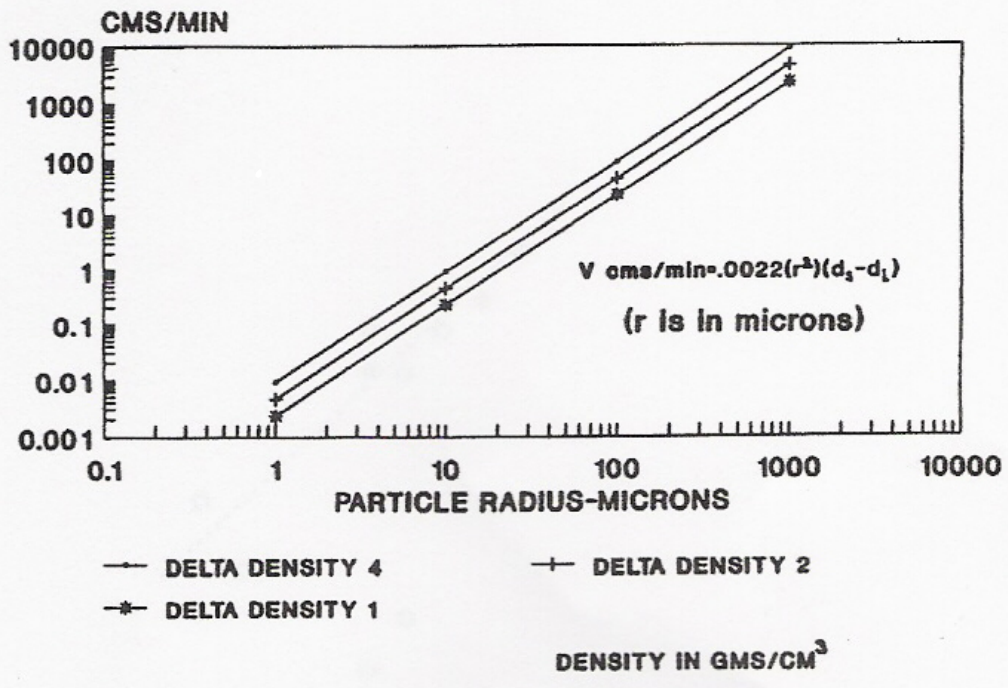

Figure 6. A graph showing the relationship between inclusion mean diameter and the terminal velocity of flotation, calculated using stoke's law [18].

Rigorous stirring however, can be detrimental to the slag foaming practice and could potentially result in opening holes in the slag layer and exposing the bath to re-oxidation.

Zhang Li-Feng reported that thousands of inclusions could be found attached to a bubble as shown in figure 7 [21], which showed alumina clusters, in a steel slab sample, that were arranged around the circumference of a former bubble.

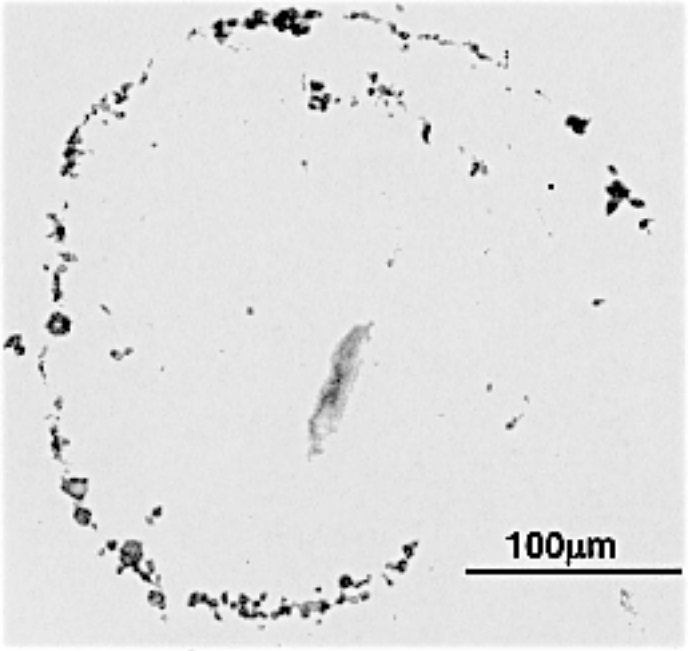

Figure 7. A micrograph showing a steel slab sample containing alumina clusters arranged around the circumference of a former bubble [21] .

Other mechanical techniques are used in steel making to enhance inclusion agglomeration and flotation such as using high pouring rates in the tundish, as well as using different tundish designs. The higher the pouring rate used to fill a tundish the more mixing can occur and the greater likelihood for inclusions to agglomerate and float upwards. Figure 8 is an example of a good tundish design where inclusions are encouraged to agglomerate by controlling the flow.

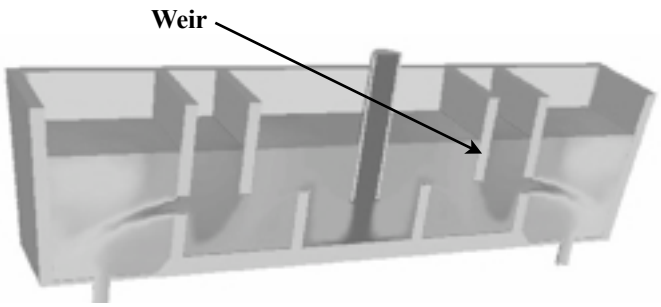

Figure 8. A schematic diagram showing the beneficial use of weirs in a tundish to promote a fluid flow behaviour that enhance agglomeration and flotation of inclusions.

Filtration using ceramic filters has also been used to minimise inclusions in shape castings. These filters are placed in strategic locations in the running system to trap inclusions and prevent them from entering the casting mould cavity. Ceramic monoliths (figure 9, a) and ceramic foams (figure 9, b) are the most commonly used types of filters and the mechanisms by which filtration takes place have been described as follows.

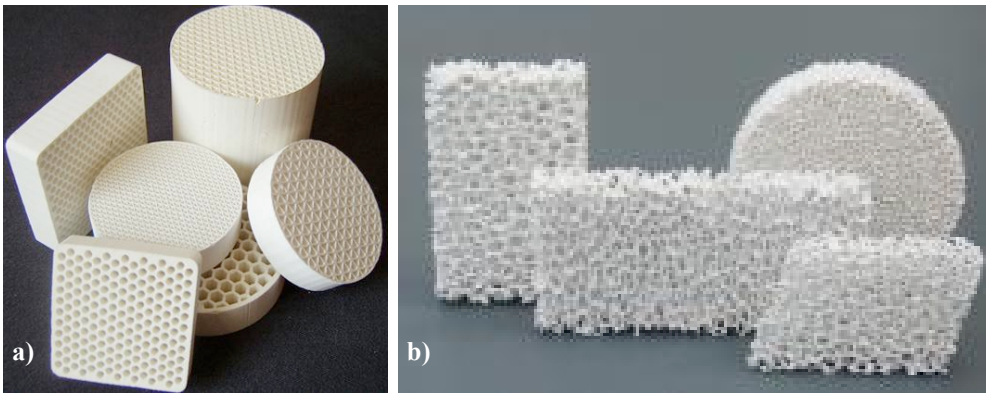

Figure 9. Photographs of a) Ceramic monoliths and, b) Ceramic foam filters

(i) Chemical sintering between the inclusion and the filter which applies to high melting point alloys such as steels,

(ii) Mechanical entrapment of the inclusions within the filter pores or against the filter front face.

(iii) Adhesion between the inclusions and the filter, which unlike sintering, can take place in low melting point alloys. Adhesion between an inclusion and the filter was reported to be promoted as the contact angle between the inclusion and the filter decreased and as the particle diameter increased [22].

(iv) Settling out of inclusions within the filter cell due to a reduction in liquid metal velocity owing to the tortuosity of the filter. [22, 23]

These theoretical filtration mechanisms have not been experimentally investigated, although previous work has focused at studying the filtration efficiency of different types of filters [22].

Taylor *et al*. used Neutron Activation Analysis (NAA) to determine the quantity of inclusion elements such as magnesium and oxygen that were retained in a ceramic foam filter by measuring the intensities of ɣ-rays produced from neutron activated ceramic foam filters before and after casting [24]. The filter block was exposed to a 14MeV beam of neutrons, and activated oxygen atoms present in the filter block decayed by emitting ɣ-rays of energy 613keV. Other activated elements within the filter block produced ɣ-rays of different energy and ɣ-ray detectors were used to quantify the amount of these ɣ-rays and hence quantify the amount of a certain element in the filter. This was carried out before and after casting and consequently the change in amount of oxygen and magnesium was determined as a measure of the inclusions trapped by the filter. These experiments were an advance in quantifying filtration efficiency when compared to qualitative techniques, but no information was obtained about the mechanisms by which the ceramic foam filters removed the inclusions. The obtained results, however, showed that ceramic foam filters contained 3 times the amount of sulphur containing inclusions, when compared to extruded cellular filters.

2.1.3.3 Physical Control

Physical control means relying on physical properties of the inclusions, liquid metal and slag (in case of steels) to promote their immersion into the metal/slag or metal/gas interface. It has been reported that a particle would adhere to a gas bubble, a furnace wall or a slag layer to lower its surface energy [22, 25]. The surface energy associated with the transfer of a particle from the metal to the slag phase is given by equation 10, where the subscripts M, I and S denote the metal, inclusion and slag respectively [22]. Thus when γ_{IS} is much smaller than γ_{MI} there will always be a driving force promoting the transfer of the particle from the metal to

the slag. This same driving force also promotes the spreading of liquid inclusions over ceramic filters or other solid inclusions.

$$\Delta G = 2(\gamma_{IS} - \gamma_{MI}) = -2\gamma_{MI}$$ ----------Equation 10

2.1.3.4 Engineering Inclusions

One example of the engineering of inclusions, is the CaSi treatment that is carried out in steel making, at the ladle refining stage. In this treatment CaSi additions are made to change the angular morphology of MnS or alumina inclusions to a spherical particle that is softer (due to the soft CaS-MnS ring formed around the particle) and has a significantly lower stress raising potential [26]. Figure 10 depicts the CaSi treatment for MnS and alumina.

Another example from steel making practices, is to allow inclusions such as SiO_2 to remain in the melt if the production process does not allow enough time for flotation because these inclusions would be liquid at subsequent rolling temperatures, and hence would not cause problems such as splitting or cracking in the rolled products. These liquid inclusions will continue to split into smaller droplets due to rolling unlike solid inclusions that would not behave in the same flexible manner [1, 27].

A further example of inclusion engineering is promoting the formation of specific oxide inclusions in steels, which have been proved to behave as ferrite nucleation sites in an austenitic matrix and therefore their benefit to the mechanical properties of the produced steel outweighs the detriment of the presence of such inclusions [28, 29].

Thermodynamic databases and phase diagram calculations have been shown to be useful tools that could be used to predict and minimise the effects of inclusions forming in steels. Work by Kang *et al*. demonstrated that the thermodynamic databases can be used to calculate ternary phase diagrams for oxide systems in a Si/Mn deoxidised steel, with the aim of predicting the composition of liquid oxide inclusions that would be present at the steel processing temperatures. Figure 11 shows the calculated phase diagram of the $MnO\text{-}SiO_2\text{-}Al_2O_3$ system which revealed that spessartite ($Mn_3Al_2Si_3O_{12}$) is a glassy phase that is liquid at 1100-1200^oC [28]. This means that if the chemical composition of inclusions was brought to this region it will be possible to have deformable inclusions during rolling, which are, like grain refinement, beneficial to the mechanical properties as they will hinder dislocation movement.

The same techniques were also successfully used to determine the optimum steel composition to promote MnS precipitation on oxide inclusions, as shown in figure 12 [30]. This was desirable to maximise the chances of acicular ferrite nucleation which has been reported to significantly enhance the toughness of steels [28, 30-32].

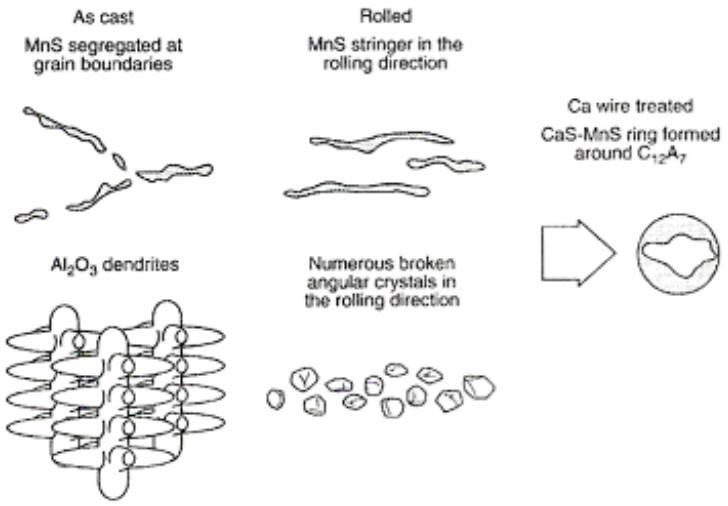

Figure 10. A schematic illustration showing the modification of inclusion morphology with calcium treatment of steel [26]

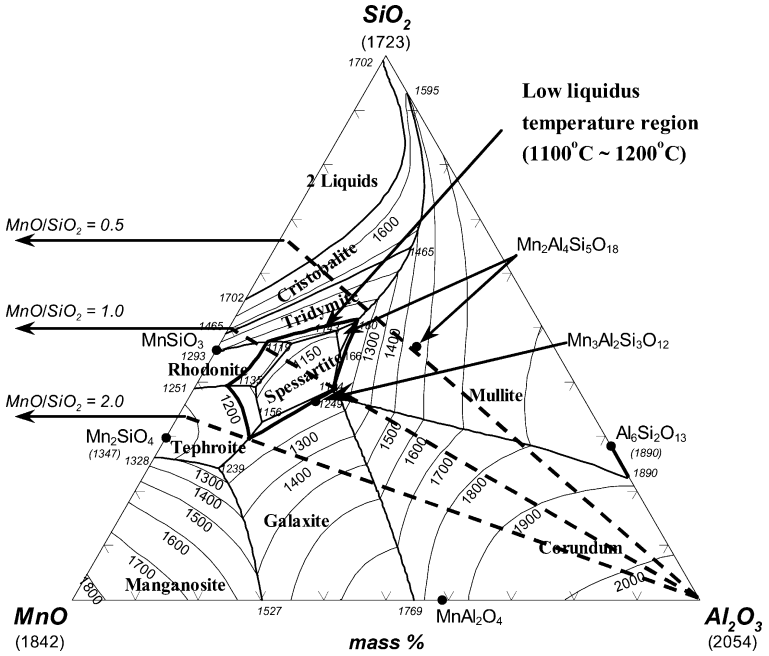

Figure 11. A calculated phase diagrams of the MnO-SiO_2-Al_2O_3 system [28].

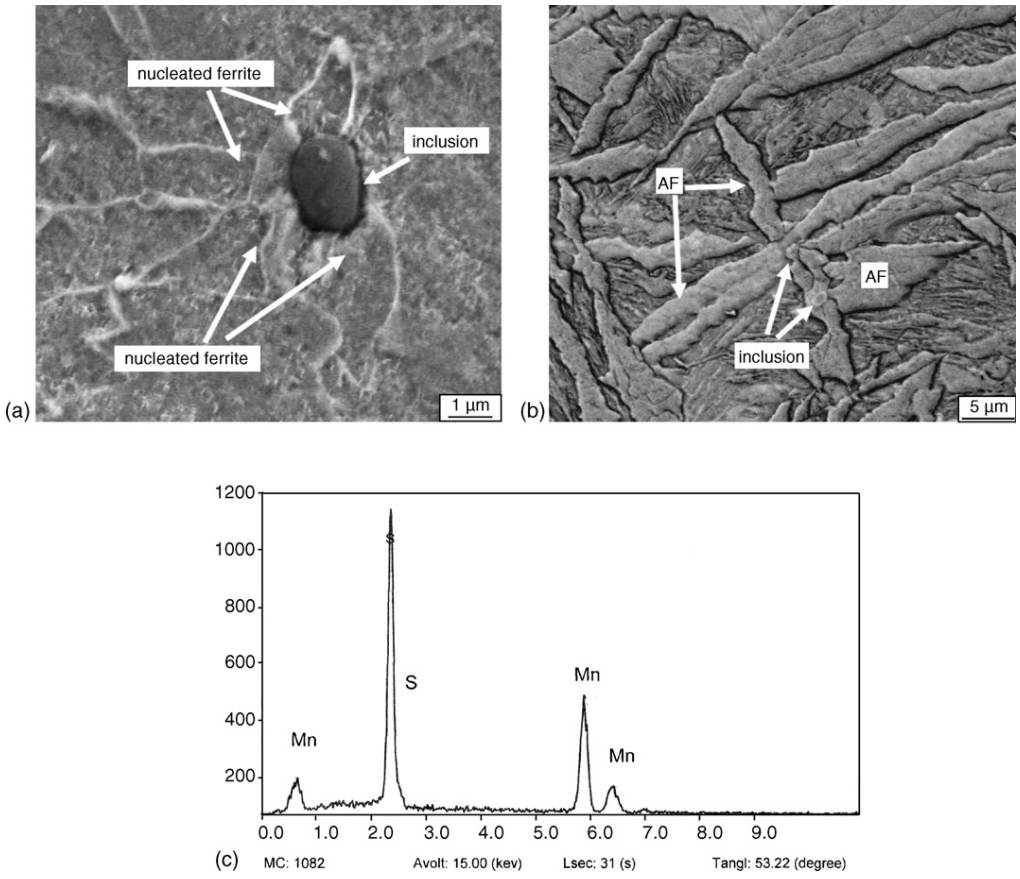

Figure 12. SEM observations of (a) the incipient period of IGF nucleation on MnS inclusions and (b) grown-up acicular ferrite on MnS inclusions (inverted image) (c) EDX analysis of inclusions indicated by arrows in (b) [30].

2.2 Inclusions in Aluminium Alloys

2.2.1 Types and Origins of inclusions in Aluminium Alloys

2.2.1.1 Non-metallic inclusions in aluminium alloys

The types of inclusions found in aluminium alloys are highly dependent on the processing route and the practice by which the alloy is produced and are better categorised into non-metallic and intermetallic inclusions. In cases where the primary aluminium is obtained by electrolysis, the inclusions present have been reported to be complex inclusions of alumina and carbides including, Fe, Si, Ti, Va, Ni and Zn [33]. These are non-metallic inclusions that occurred due to the oxidation of liquid aluminium and / or the reactions of residual impurities from the raw material with the electrodes. Work by Trokar *et al*. showed that these inclusions are usually between 10-100µm in size, with most Al and Si carbides being < 10µm in diameter while Ca containing carbides were of sizes 10-55µm [33]. Al_2O_3 inclusions were found to be of the size range 5-75µm [34]. Figure 13 shows typical oxide inclusions in a cast Al sample where the association of the alumina inclusions and an oxide film defect was demonstrated [35]. These oxide films formed in the case of pure aluminium were extensively studied [36, 37] and were found to be initially amorphous oxide films, that transform rapidly into crystalline α or γ alumina [35, 37]. In work by Zhang *et al*. it was reported that when using scrap aluminium, Al_2O_3 inclusions of size 30-75µm were found [34].

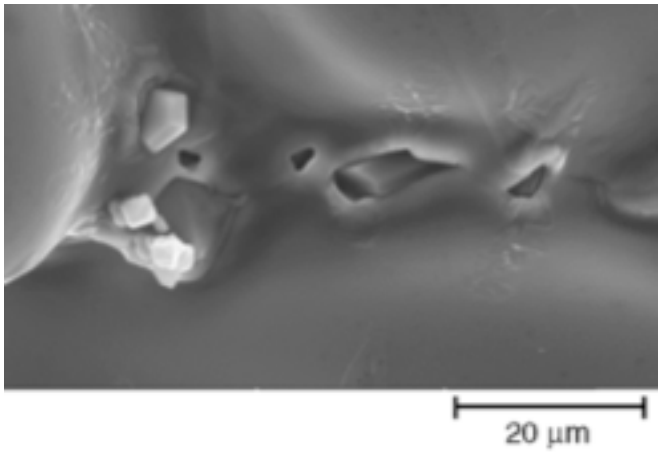

Figure 13. A scanning electron microscopy image of oxide inclusions in aluminium cast samples (fractured surface) [35]

2.2.1.2 Intermetallic inclusions in aluminium alloys

Other types of inclusions are intermetallic inclusions which are due to the presence of Fe, Cr and Mn in the aluminium scrap used during the melting of secondary aluminium alloys [38].The nucleation and growth temperatures of these needle-like intermetallic phases have been shown to decrease with the total content of Fe, Cr and Mn and hence can form at temperatures near the melting point of commercial aluminium alloys [38]. The typical size of such intermetallic inclusions is reported to be between 30-70µm [39] and the possible methods of reducing their detriment to mechanical properties will be described in the following sections [38, 40].

2.2.1.3 Other sources of inclusions

The main types of inclusions in aluminium alloys are entrained inclusions, whether inherited from the primary extraction of Al or due to the incorporation of refractories and slags. Table 4 shows the types of inclusions in Al alloys and their possible origins [38]. Al_4C_3 is usually

inherited from the primary metal (reactions with the electrodes during electrolysis) or formed due to reactions of the melt with the clay-graphite crucibles [33, 38]. Boro-carbides and TiB_2 are inclusions that arise due to the deliberate addition to the molten alloy to enhance grain refinement through heterogeneous nucleation [23, 38].

Different salt flux materials, with different chloride and fluoride contents, are used in shape casting of aluminium and aluminium alloys, to protect the surface from reoxidation, degassing and loss of Al in the dross layer. But these fluxes can also result in the entrainment of inclusions, due to the practical difficulty in removing the light or powdery slags produced completely from the melt surface [38]. Work by Majidi *et al*. showed that for salt fluxes to remove inclusions efficiently from an aluminium melt, the correct temperature (740^{o}C) and contact time with the liquid aluminium must be allowed by the process [41].

Table 4. The typical inclusions found in Al alloys [1].

Inclusion Type	Formula	Possible Origin
Carbides	Al_4C_3	Pot cells from Al smelters
Boro-carbides	Al_4B_4C	Boron treatment
Titanium boride	TiB_2	Grain refinement
Graphite	C	Fluxing tubes, rotor wear
Chlorides	NaCl, KCl, $MgCl_2$, etc.	Chlorine or fluxing treatment
Alpha alumina	α-Al_2O_3	Entrainment after high temperature melting
Gamma alumina	γ -Al_2O_3	Entrainment during pouring
Magnesium oxide	MgO	Higher Mg containing alloys
Spinel	$MgOAl_2O_3$	Medium Mg containing alloys
Fluorides	Na_6AlF	Flux material

2.2.2 Control of inclusions in Aluminium Alloys

Good industrial practice is required to control the cleanliness of aluminium alloys, especially non-metallic inclusions. Agitation by electromagnetic stirring has been shown to enhance inclusion agglomeration and / or segregation out of the bulk metal and cast products [34, 38]. Also, minimising turbulence and the overlapping of the liquid metal surface reduces the number of oxide film defects.

In shape castings proper gating and pouring practice is also known to minimise inclusion problems. If exogenous inclusions leave the ladle because of inadequate upstream control, the gating system should be designed to remove such inclusions in the pouring basin or in the runner system. [14]. When a pouring basin is not designed to fill easily or to remain filled, there is risk or forming oxide film defects which could transform into inclusions in the casting. Whirl gates can also be used to trap these inclusions, but there is no evidence of their effectiveness.

Intermetallic inclusions can be controlled by making manganese additions to the melt, to change the morphology of the needle-like, Fe,Mn and Si-rich intermetallic inclusions into a less harmful globular morphology [38, 39].

2.3 The Effects of Inclusions on Mechanical Properties

The detrimental effect of an inclusion on mechanical properties is a function of their morphology and size; spherical inclusions are less harmful than angular ones and larger inclusions are more harmful than smaller ones [27, 42, 43]. A comparison between the types of inclusions found in a C-Cr bearing steel and their stress raising / void forming potential is shown in figure 14.

Figure 14 shows that calcium aluminate inclusions have the highest stress raising potential and are therefore the most detrimental to fatigue properties. These are followed by alumina, spinels (the aluminates Mn,Mg and Fe), nitrides and most silicates respectively, in descending order of their stress raising potential. Oxides such as MgO, CaO, FeO and MnO have been shown to have lower stress raising potentials due to their globular morphology and were therefore considered to be less detrimental to the previously mentioned inclusions. MnS inclusions were reported to have the highest void forming potential due to its coefficient of thermal expansion being higher than that of the steel matrix.

Alumina will be used as an example to illustrate the effect of inclusions on fatigue in steel. Figure 15 shows a comparison of axial fatigue data for typical constructional steel and one that was calcium treated. The calcium treated sample showed a significant improvement in the number of cycles to failure at various alternating stress levels. Additions of calcium to the steel melt react with the angular alumina inclusions to produce spherical particles, composed of a (Ca,Mn)S ring surrounding the alumina inclusion [43], see figure 10. These calcium

aluminates are more deformable at temperatures greater than 1000°C than the undeformable alumina and hence, the stress concentration around alumina inclusions is significantly reduced, which improves fatigue life, see figure 15.

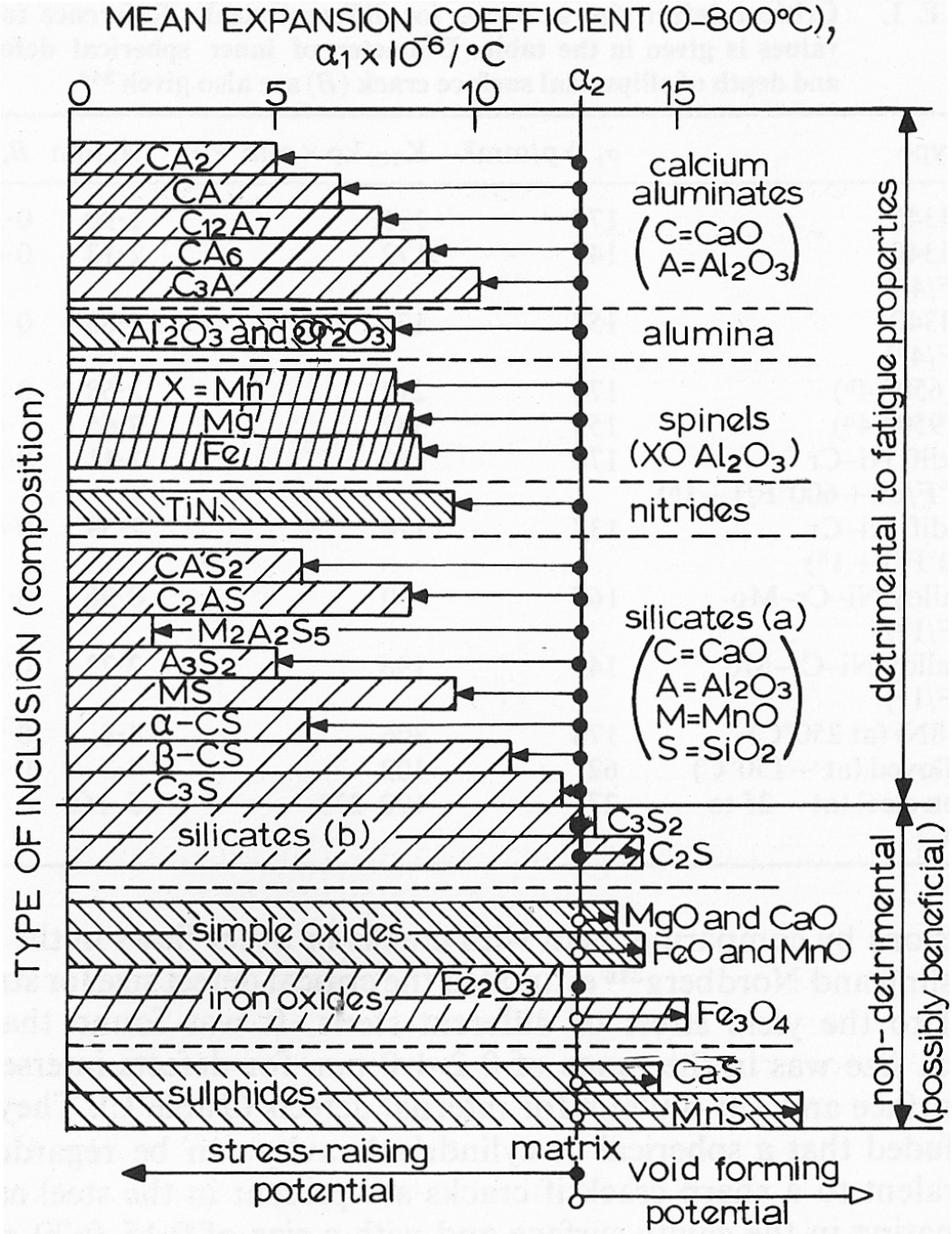

Figure 14. A graph showing the stress-raising and void forming properties of inclusions in 1% C-Cr bearing steels [16]

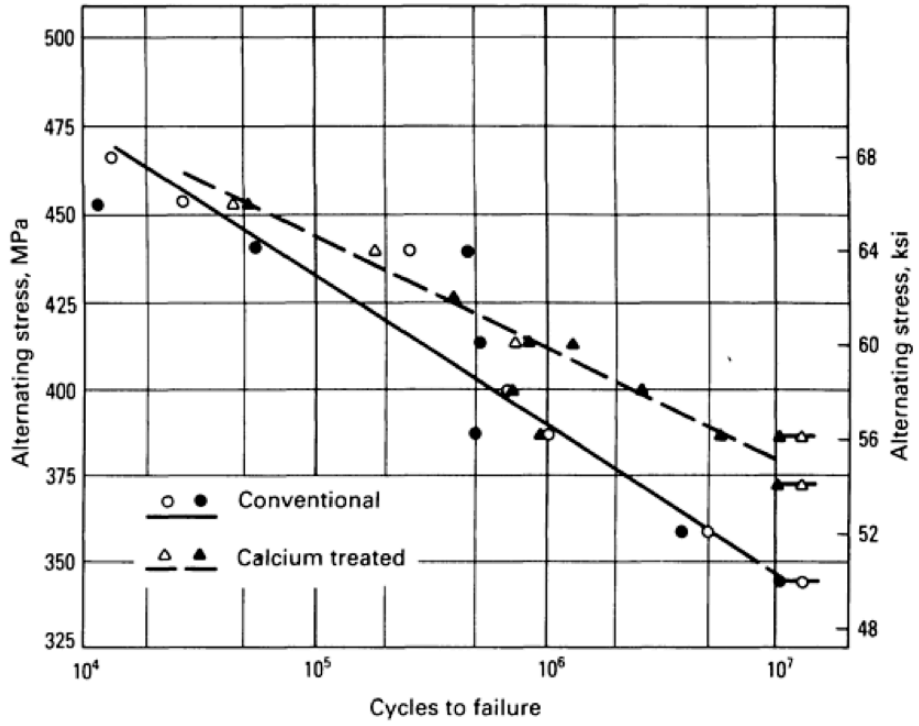

Figure 15. A graph showing a comparison between axial fatigue data for untreated and calcium treated rolled ASTM A516 steel. 51mm thick plates tested with alternating stress ratio of 0.1 [13]

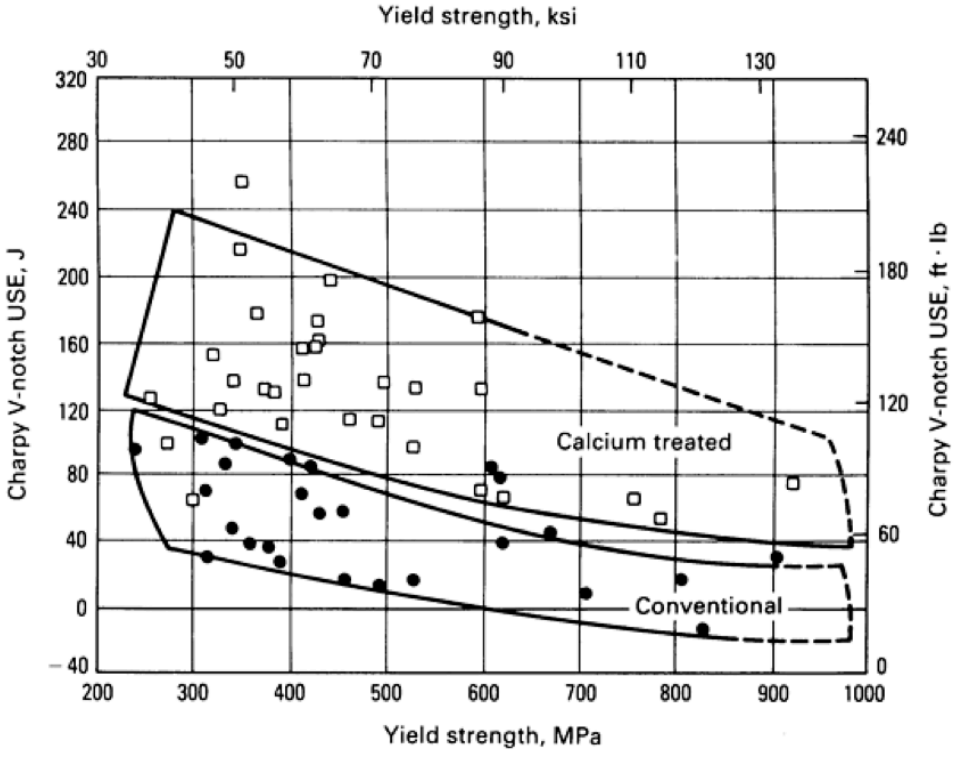

Figure 16. A graph showing a comparison between charpy V-notch upper shelf energies for several grades and thickness of untreated and calcium treated steel [13]

Similarly, MnS inclusions have high indexes of deformability at all temperatures. No cracks are developed at the inclusion/steel interface during working of the steel and the inclusions participate in different stages of steel deformation, changing their shape with the surrounding steel matrix [1]. Thus these inclusions serve better than other indigenous oxide inclusions during steel working [17] (e.g machining-MnS enables swarfing). However MnS inclusions still result in brittle fractures because their elongated shapes, provide an easy path for cracks to grow after rolling i.e. they are only better than some oxide and complex inclusions in terms of machinability but they are still, like any other inclusions, generally undesirable.

Work presented by Hollappa *et al*. also showed that the detrimental effects of inclusions on tool life during machining can be significantly minimised by the Ca treatment described earlier. The calcium aluminate inclusions enveloped by (Ca,Mn)S rim form a protective layer on TiN-coated cutting tools, as well as on TiC-containing cemented carbide tools during machining, which results in improved tool lives [44]. Figure 17 shows the effects of inclusions on the machinability of Al-killed, case hardened, quenched and tempered steel grades with TiN-coated cemented carbide tools, where clearly higher cutting speeds were achieved with the Ca-treated steel, indicated by M on figure 17 [44].

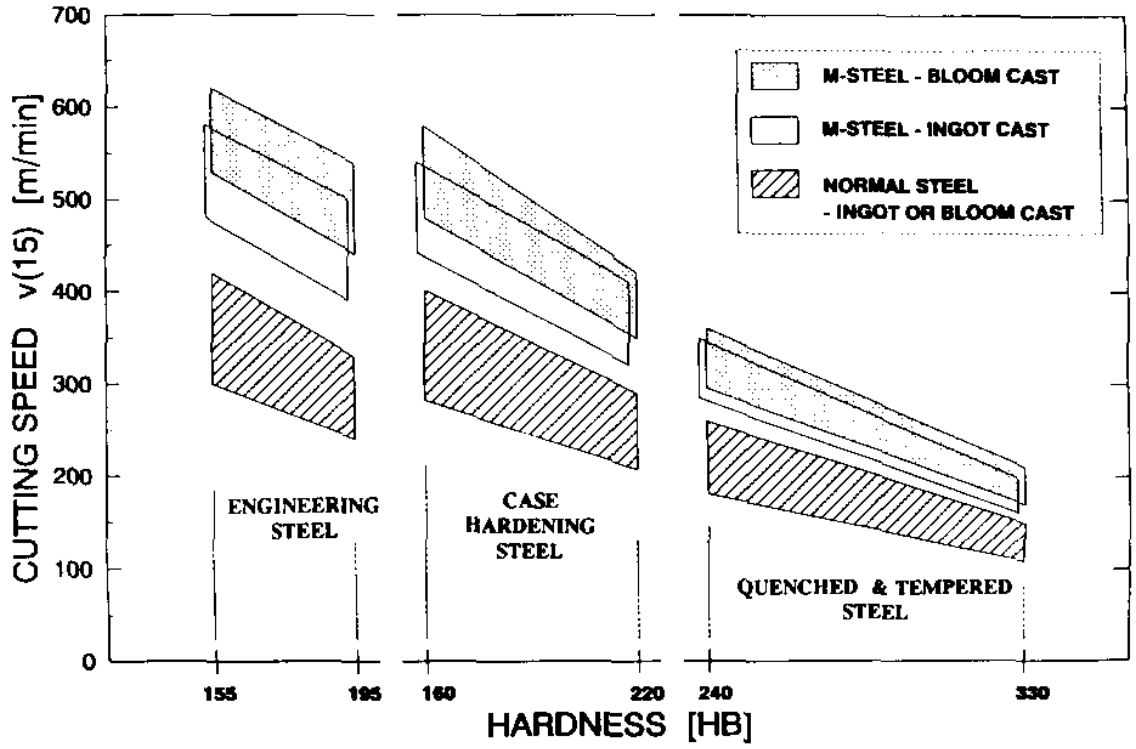

Figure 17. A graph showing the influence of inclusion control by calcium (M) on machinability compared with respective normal steel. The diagram shows the cutting speed corresponding to a tool life of 15 min in turning. Cutting parameters: depth of cut 2.5mm, feed 0.4mm/r, tool TiN coated carbide [44]

2.4 Techniques of Inclusion Detection and Quantification

There is a need to find a reliable method that could be used to determine the size of inclusions present in a metal. The critical size is defined as the size above which inclusions are dangerous and may cause failure to metallic products [45], and can be different depending on the service conditions of the product. For example, the critical inclusion size for fatigue failure of a bearing steel is 10μm if the inclusion is below the surface and 30μm if the inclusion is 100μm below the surface [45].

The available inclusion detection and evaluation techniques can be categorised into direct and indirect direct techniques. Direct techniques are usually more accurate but costly and time consuming while indirect ones are quick and inexpensive but can only be reliable as rough indicators of the type and quantity of inclusions present [46].

Direct techniques include simple optical microscopy, where inclusions are identified and counted manually in 2-D. This is obviously not ideal due to their small size, which may not include rare but large inclusions. It can also be difficult to identify correctly large numbers of smaller inclusions, which can be confused with complex inclusions and vice versa. Using image analysis and computers attached to optical microscopes does allow for a larger number of inclusions to be counted and identified using their difference in colours and contrast between the inclusion and the metal matrix. However these image analysis techniques are prone to errors due to stains, pitting or scratches that can be falsely identified as an inclusion [46]. Scanning electron microscopy (SEM) allows for 3-D examination of inclusion

morphology and more accurate identification by measuring the composition of a target area using Energy Dispersive X-ray Spectroscopy (EDS) or Electron Probe Micro Analysis (EPMA) [46]. But SEM analysis of inclusions requires extensive sample preparation to find and expose these inclusions.

Another commonly used technique for steels is sulphur printing, where sulphur rich areas are etched to reveal sulphide rich inclusion clusters [24, 46]. This 2-D technique does not provide quantitative results and is only really suitable for macroinclusions. Other techniques involve dissolving a sample in acid and filtering the solute to collect the inclusions that were contained in that sample [47]. The size distribution of these extracted inclusions can then be determined using Coulter Counter Analysis, where the particles flow into a sensor that identifies the particles by measuring the electrical conductivity across a gap, which varies with the size of the inclusion passing through that gap [46, 48].

Some direct inclusion detection techniques are also available for liquid metals, such as ultrasonic techniques where the reflections from ultrasound pulses are used to determine the size distribution of inclusions in a liquid metal, in real time [49]. But this technique does not provide any information about composition and is very limited to the physical range of the ultra sound waves, which cannot scan a whole industrial size vessel, used to transport the liquid metal.

Porous Disc Filtration Apparatus (PoDFA) is also commonly used to evaluate the inclusion content in aluminium. In this technique a large sample of approximately 1.5kg is melted in a

preheated crucible which has a fine-grade filter in the bottom. The metal is forced through the filter and inclusions present in the melt are collected [50]. The filter cake is then examined metallographically to determine metal cleanliness.

Another similar technique is the Liquid Metal Cleanliness Analyser (LiMCA), where a melted aluminium sample is pushed through a tube with the potential difference across that tube recorded [51]. As an inclusion enters the tube the voltage drops by a certain value proportional to the inclusion size. This technique has been reported to be limited to inclusions of size 10-140μm [14, 51] and currently can only be applied to liquid metals at temperatures upto about 800^{o}C . LiMCA is currently being developed for use at higher temperatures, with steels and nickel alloys [46] as well as more reactive metals such as molten magnesium [52].

Indirect inclusion evaluation techniques have been used in industry as rough indicators of metal cleanliness. One example in the case of steel making is measuring the total oxygen in a disc sample extracted at the various steel making stages. This is used as an estimation of the total oxide inclusions present in the steel. The equilibrium equation of deoxidation, equation 5, is used to determine the number of oxide inclusions per unit volume of steel. Similarly, measuring nitrogen pickup is also used as an index of the amount of nitride inclusions present in the steel [46].

2.5 Positron Emission Particle Tracking (PEPT)

2.5.1 Theory and Types of Radiation

2.5.1.1 The Stability of Atoms

Isotopes are nuclides that have the same atomic number and are therefore the same element, but differ in the number of neutrons. Most elements have several unstable, radioactive isotopes as well as their stable ones. [53]

Figure 18 shows the distribution of the stable nuclides plotted using the number of protons versus the number of neutrons. Every atom has a certain neutron to proton ratio, for example oxygen-16 has 8 protons and 8 neutrons with a ratio of 1. Indium-115 has 49 protons and 66 neutrons with a ratio of 1.3. The heavier the atom, the higher the neutron to proton ratio [53].

If a heavy nucleus were to split into two fragments, each fragment would form a nucleus that would have approximately the same neutron-to-proton ratio as the heavy nucleus. This high neutron-to-proton ratio places the fragments below and to the right of the stability curve displayed in figure 18. The instability caused by this excess of neutrons is generally rectified by radioactive decay events, each of which converts a neutron to a proton and moves the nucleus toward a more stable neutron-to-proton ratio [53].

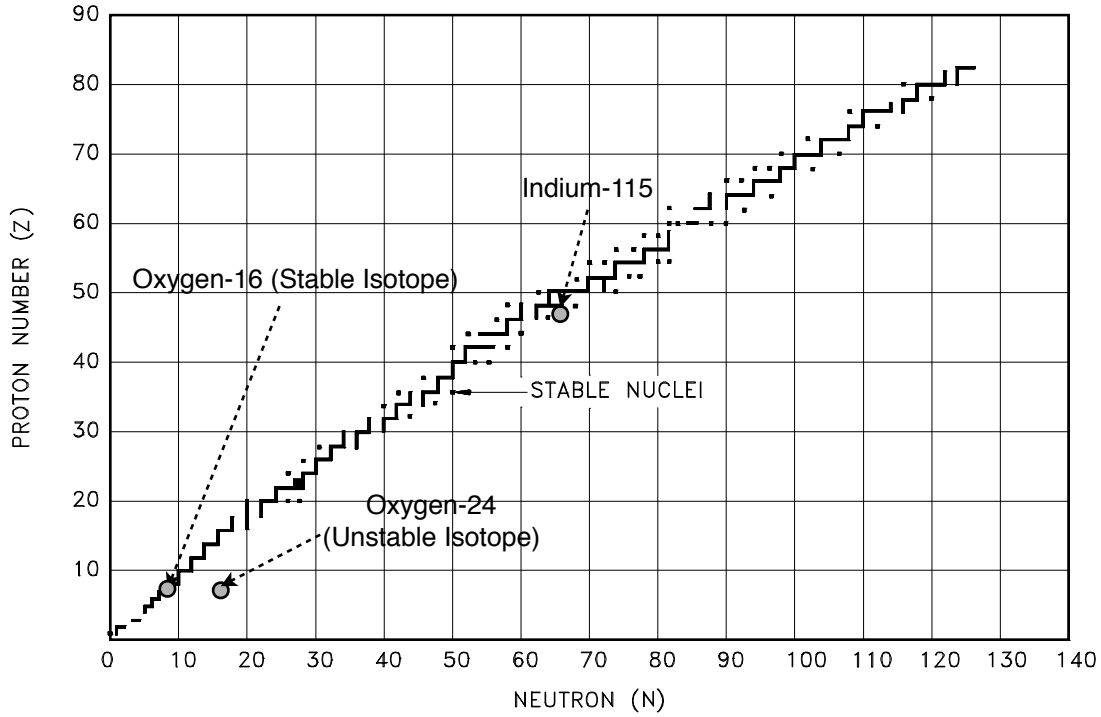

Figure 18. A graph showing the distribution of the stable nuclides plotted on the same axes as the Chart of the Nuclides [53]

2.5.1.2 Types of Radioactive Decay and Measures of Radioactivity

Radioactive decay can be defined as the process in which an unstable nucleus loses energy by emitting ionising particles and radiation to reach a more stable state [53, 54]. Radioactivity is measured by counting how many atoms decay spontaneously each second. The Curie is a commonly used unit that represents 37×10^9 disintegrations per second [54]. Another unit is the Becquerel which is 1 disintegration per second [54]. The half-life of a given mass is the amount of time required for half the atoms to disintegrate;

$$A_E = A_0(\frac{1}{2})^{\frac{t}{t_{1/2}}} \text{ ----------Equation 11}$$

A_E is the amount of substance left, A_0 is the original amount of the substance, t is the elapsed time and $t_{1/2}$ is the half-life.

There are three types of radioactive decay, alpha (α), beta (β) and gamma (ɣ). Alpha (α) decay occurs when a neutron emits an α−particle, which is essentially a helium nucleus, 2 protons and 2 neutrons. These α-particles however do not have much penetration depth and can be stopped by, e.g paper.

Beta decay occurs when unstable nuclei have a surplus or deficiency of neutrons. There are 2 types of β-decay. When the nucleus suffers from an excess in the number of neutrons, β-decay occurs where a neutron is converted into a proton by emitting an electron and an antineutrino ($\underline{\nu}_e$), ($n \rightarrow p + e^- + \underline{\nu}_e$) [53]. However, when a nucleus suffers from a deficiency in the number of neutrons, β^+ decay occurs, where a positively charged electron and a neutrino are emitted ($energy + p \rightarrow n + e^+ + \underline{\nu}_e$) [53]. β^+ decay requires energy due to the heavier mass of a neutron compared to a proton.

Gamma decay occurs when a nucleus changes from a higher level energy state to a lower level. This is similar to the concept of shells of electrons at different energies surrounding an atom nucleus. When an electron moves from a higher energy shell to a lower one, a few eV of energy are emitted due to the energy difference between those shells. However, in a nucleus, differences in energy between levels are typically a few hundred keV. Therefore, the photons emitted are gamma ray photons.

2.5.2 The Principles of PET and PEPT

2.5.2.1 PET and PEPT

Positron Emission Tomography (PET) refers to applications of nuclear medicine imaging where a three-dimensional image of a functional process in the body is generated [55-57]. Positron Emission Particle Tracking (PEPT) uses the principles of PET to obtain information about industrial processes by tracking single or multiple radioactively labelled particles in industrial conditions.

The basis of PET and PEPT is the detection of photons emitted when a positron is produced by the β decay of an unstable nucleus. During β^+ decay, the emitted positrons are annihilated by electrons from the surrounding material. This annihilation process, and conservation of energy and momentum requires that 2 ɣ-ray photons, of energy 511 keV, are emitted back to back (180^o apart) [58] as shown in figure 19. A PET scanner, comprising rings of small ɣ-ray detectors (Bismuth Germanate scintillators)[59] operating in coincidence, is used to detect these back-to-back ɣ-ray pairs [58, 60]. Simultaneously detecting both photons defines a line with the annihilation occurring somewhere along this line, figure 20.

The location of a positron emitting medium can be determined as the point of intersection of several lines, defined by the detection of the 2 ɣ-ray photons.

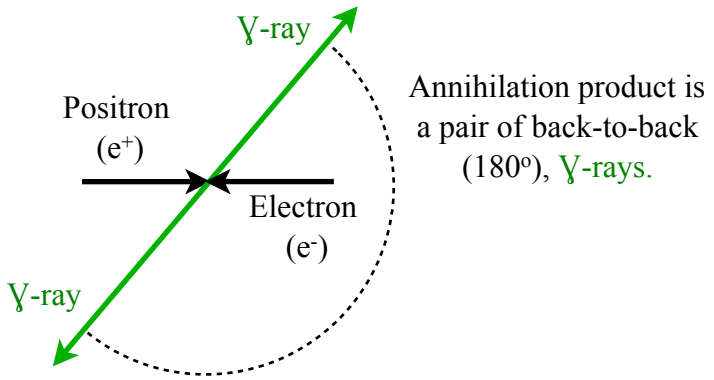

Figure 19. A schematic diagram showing the production of 2 back to back ɣ-rays due to positron annihilation with an electron.

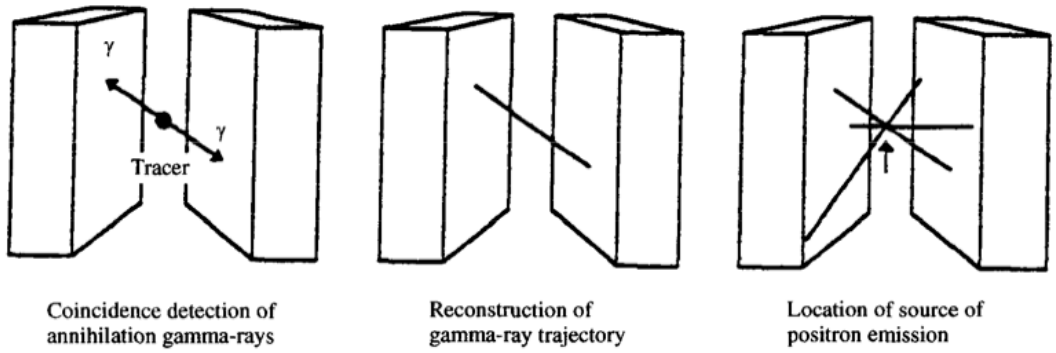

Figure 20. A schematic diagram showing the positron electron annihilation, gamma ray detection and reconstruction of the tracer location between the 2 detection camera faces. [5]

2.5.2.2 Labeling Tracer Particles

There are two main irradiation techniques that are used to label tracer particles for PEPT, direct activation and ion exchange. In direct activation an oxide particle can be used, such as alumina or silica, provided the particles can withstand the high temperature generated during activation (up to 1500°C)[61, 62]. The particle is sealed in a target and is directly struck by a 33MeV ^{3}He beam in a Cyclotron (where the ^{3}He is accelerated using electro magnets to reach high energies) for a certain period of time [62-64]. During this time the oxygen atoms within

the particle are converted to the radioactive isotope ^{18}F via reactions $^{16}O(^{3}He,p)^{18}F$ and $^{16}O(^{3}He,n)^{18}Ne \rightarrow ^{18}F$ [63]. This ^{18}F produced has a half life of 110 minutes and decays by β^+ decay [3, 5, 8, 58, 65, 66].

The activity achieved in a particle by this technique is determined by the product of the beam current density from the cyclotron (ions per unit area per second) and the cross sectional area of the particle [3]. The value of the radioactivity achieved is described by equation 12.

$$A = f_0(I,S,t) = f(I,d^2,t) \text{ ----------Equation 12 [63]}$$

A is the radioactivity achieved (μCi), I is the electric current of the target (μA), S is the cross sectional area of the particle (mm^2), d is the particle diameter (mm) and t is the irradiation time (min) [63]. This relationship is depicted in figure 21. Therefore particles have to have a sufficient volume of oxygen atoms for the ^{3}He beam to penetrate and irradiate, which means that particle size can be a limitation (small volume of oxygen atoms) when high radioactivities are required from oxide particles, particularly those with diameters less than 1mm [62]. The main advantage of direct irradiation is that the radioactivity is structurally bound to the body of the tracer particle [62]. Other factors that affect the magnitude of the radioactivity achieved are the holding time in the cyclotron and the particle material. Other types of particles can also be directly irradiated, such as ^{63}Cu via the reactions $^{63}Cu(d,p)^{64}Cu$, where d refers to deuteron particles, an isotope of hydrogen [3, 67]. Other positron emitting isotopes are listed in section 2.5.6.

Small particles (<100μm) can be made radioactive using an indirect technique, based on an ion exchange mechanism between ^{18}F in distilled water and anions present at the surface of a particle [3, 64]. The ^{18}F present in the distilled water was produced by directly irradiating the water to form a dilute fluoride solution, which is then attached to the surface of the tracer particle [62, 64, 66, 68]. Particles of strong base anion exchange resin as small as 60μm can be labelled by an ion exchange technique via reactions $RCH_2N(CH3)_2+H_2O\leftrightarrow RCH_2NH(CH_3)+OH^-$ [62, 64]. Other materials that cannot be labelled by ion exchange, are surface modified by adding Fe^{3+} ions that act as a bridge that binds to the ^{18}F ions [62, 64].

Radioactivities obtained via the ion exchange technique can be significantly higher than those obtained by direct activation, as shown in figure 22, for quartz (SiO_2). Figure 23 shows the difference between radioactivities achieved by ion exchange before and after surface modification was developed, where a maximum of 800 μCi was recorded [64].

The resolution of any PET imaging system is a factor of both the finite range of the positron before annihilation and the effect of the slight acollinearity of the two photons (the ɣ-ray photons are not exactly back to back). If a pair of detectors separated by 50 cm is used to detect the photons then the uncertainty in location arising from this acollinearity is around 1mm, comparable to the range of travel of the emitted positrons before annihilation [69]. In practice, detector systems never achieve this level of precision. For PET, the best resolution achievable is around 8mm with the original Birmingham camera or 5mm with the current one [69]. However in PEPT, a stationary tracer can be located accurately by using large numbers of events [69].

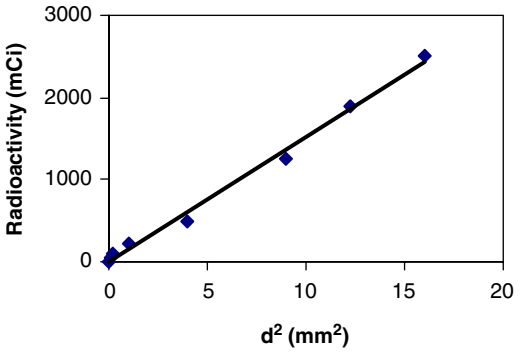

Figure 21. A graph showing the effect of particle size on radioactivity achieved through direct activation (33 MeV ^{3}He beam at a target current of 10mA for 60 min) [62].

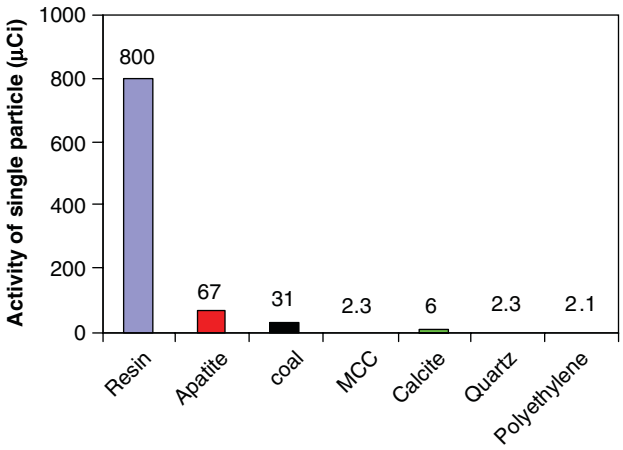

Figure 22. A graph showing the uptake of radioactivity on a single particle with a size range 215-250µm (initial radioactivity approximately 6mCi, 6 particles used in each experiment) [64]

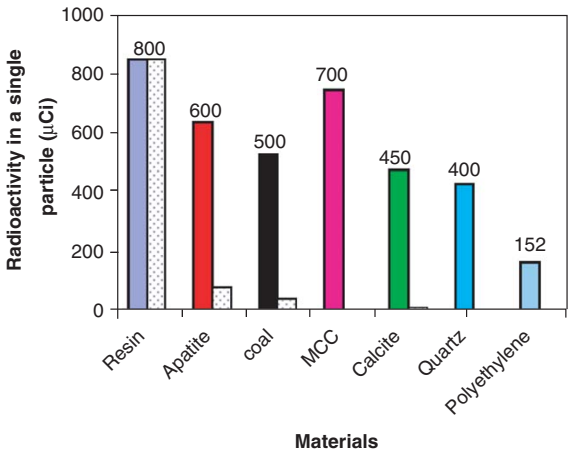

Figure 23. A graph showing the radioactivities achieved in a single particle using the surface modification technique [64]

2.5.3 The PEPT Algorithm

Typically, ɣ-rays strike the detectors at thousands of times a second. The location algorithm relies on the principle that one positron emitter produces back-to-back ɣ-rays with trajectories crossing each other at the same exact point, which is where the positron emitter is located. Other trajectories are discarded by performing iterations using the following method.

Firstly, pairs of ɣ-rays are determined by assessing where the ɣ-ray strikes are occurring on the pairs of detectors either side of the experiment. These are recorded as a set of trajectories N(S). The algorithm then calculates the position of the point to which the perpendicular distance from all trajectories is a minimum. This sum is given for that point m by equation 13.

$$D(S) = \sum_{x} \delta_i(m)$$ ----------Equation 13 [70, 71]

Where δ_i is the distance of the i th trajectory from point m. The mean deviation of these trajectories is given by equation 14.

$$d(S) = D(S) / N(S)$$ ----------Equation 14 [70, 71]

The algorithm then discards the events with perpendicular distance δ_i that is greater than kd (S), where k is a fixed parameter that represents the trajectory rejection rate, usually between 1 and 1.5 s^{-1} [70]. These trajectories are rejected because they may not be pairs of ɣ-rays from the same event, but only appear as pairs due to, for example, Compton scattering, (a reduction in energy of a ɣ-ray due to passage through a material), coincidental strikes between ɣ-rays from different decay events, and cosmic rays.

This procedure is carried out iteratively until a specified f fraction of N(s) events is left [71], usually 20% to 33% of the original data set [63] or alternatively until d(s) is less than some specified value. Figure 24 is a schematic diagram showing the positron emitting particle identified as the intersection point of the back-to-back ɣ-ray pairs.

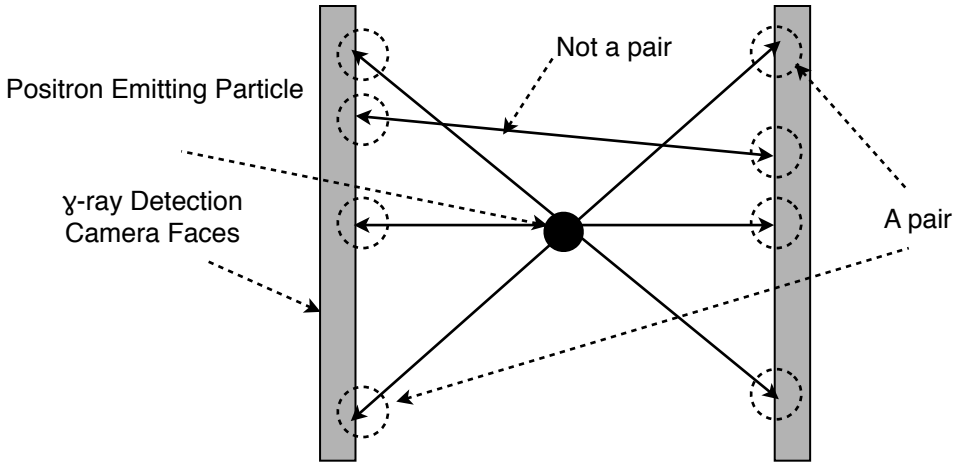

Figure 24. A schematic diagram showing how the PEPT algorithm defines the valid data set and discards the invalid events.

If multiple particles were to be tracked, (for example 3), a modified version of this algorithm is used where the same process is carried out but in this case the largest portion of the acquired events is used to identify the location of the strongest particle first. Afterwards a smaller data set (that was not previously used to locate the strongest particle), is used to locate the second particle and finally the weakest particle is located from the remaining data [70, 72].

2.5.4 Applications of PET and PEPT

PET and PEPT have been widely used in diverse fields; from studying the lubrication of aero-engines, by Rolls Royce in the early 1980s [3] to researching the metabolism of the human brain [57]. This is owing to the ability to radioactively label different types of tracer particles, and the accuracy with which real time data can be obtained about moving particles, particularly in the chemical, medical and food industry [8, 9, 73-80]. Some of these applications are briefly outlined in this section to demonstrate the capabilities of PET and PEPT.

PET has been used to study specific reactions of the human brain, by using tracers to radioactively label blood, sugars or medicine [57]. Lars *et al*. used krypton-77.$H_2{}^{15}O$, $CH_3{}^{18}F$, ^{18}F-flouroantipyrine and ^{11}C-iodoantipyrine as tracers to study cerebral blood flow (CBF) to better understand brain processes and quantify the effect of certain pharmaceuticals on these processes. The uptake of radioactivity in a group of cells was used to reflect the metabolic rate or the extent a particular brain region is involved in a certain mental or physiological process. The substrate that was used in this case was 2-deoxy-2-[^{18}F] fluoro-D-glucose (18F-FDG), recently replaced by ^{11}C-deoxyglucose [57]. This is because ^{11}C-deoxyglucose is chemically identical to natural glucose and it can therefore be transported and metabolised via the same reactions and at the same rate as the natural substrate [57]. The ^{11}C-glucose was produced by photosynthesis from $^{11}CO_2$ using unicellular algae [57]. Data obtained from this work was used to create mathematical models of brain processes.

Another application of positron emission imaging was to study the kinetics of heterogeneous catalytic reactions under actual process conditions [79]. ^{13}N-labeled NO was used to investigate the selective catalytic reduction of NO by NH_3 over vanadia / titania [79]. The results obtained showed that the activation energy calculated from the PET data was in fair agreement with those measured by more conventional methods. Similarly, work was carried out to model the reactions occurring in a tubular plug-flow reactor under normal process conditions. Model automotive exhaust catalysts of Pt- and Rh- loaded CeO_2/Al_2O_3 were used in these experiments. Radio-tracers such as ^{11}CO, $^{11}CO_2$, ^{13}NN, ^{15}OO, $C^{15}O$ and $C^{15}OO$ were injected into the feed of the reactor under steady state conditions. The residence time of these tracers was of the order 10-500s allowing a successful 3D PET image to be produced.

PEPT has been widely used in industry to study the motion of fluids, pastes or granules of material during different processes. Wildman *et al*. used PEPT to investigate the die entry behaviour of a clay-based paste during extrusion [78]. A directly irradiated silica glass ball of 2 mm diameter was inserted into a paste undergoing flow, in a simple barrel and die arrangement for extrusion as shown in figure 25, a) [78].

The PEPT results obtained not only provided useful rheological information about the paste but it also showed the tracer location and the paste speed at different locations within the die / barrel. Figure 25 (b) showed the particle paths of the tracer, plotted with a normal parallel to the axis of the barrel, where it was clear that the particle moved from the outside of the barrel into the die, and that there was probably no tangential motion occurring, only radial motion towards the axis of the barrel [78]. The speed of the tracer and consequently the paste was

calculated by a running average of the tracer position with time. Figure 25, c) and d) show the calculated speed of the tracer plotted versus time and height within the barrel.

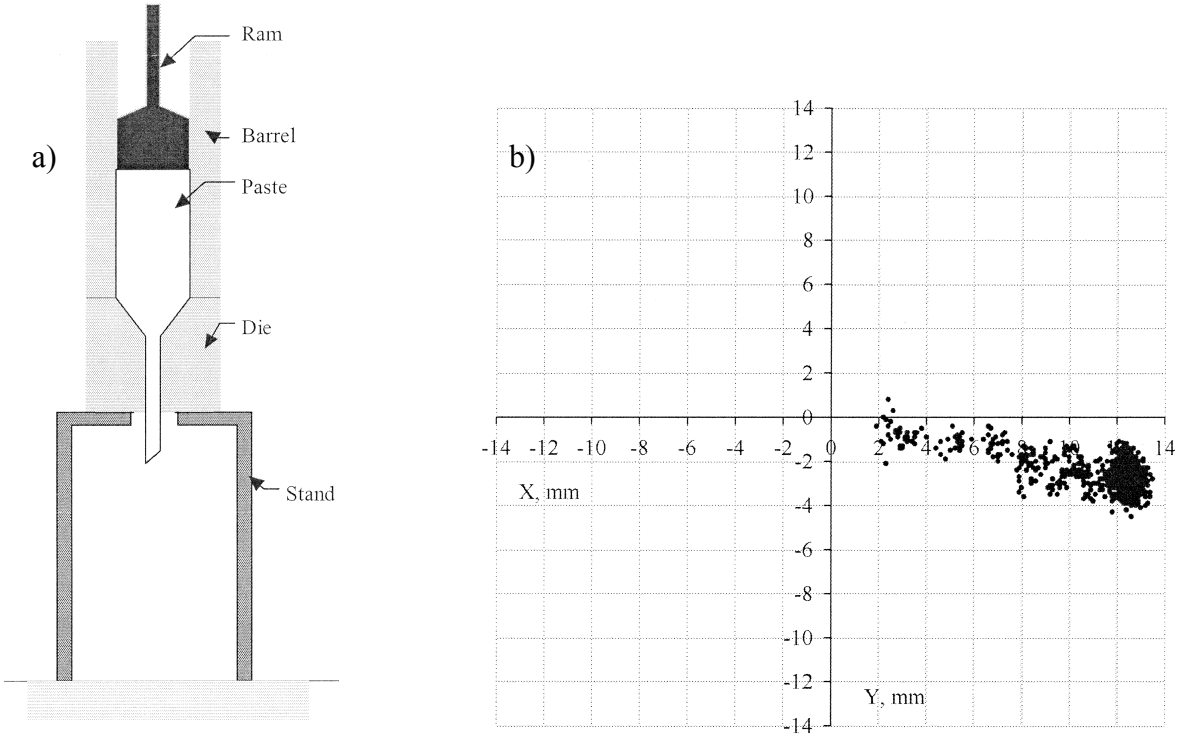

Figure 25. a) A schematic diagram showing the barrel and die arrangement for extrusion b) A projection of the particle track in the x-y plane.[78]

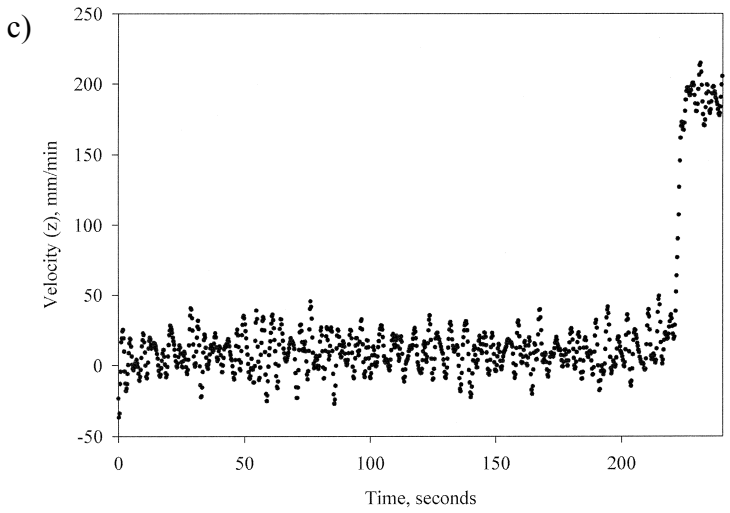

Figure 25.c) The speed of a particle with time during extrusion. [78]

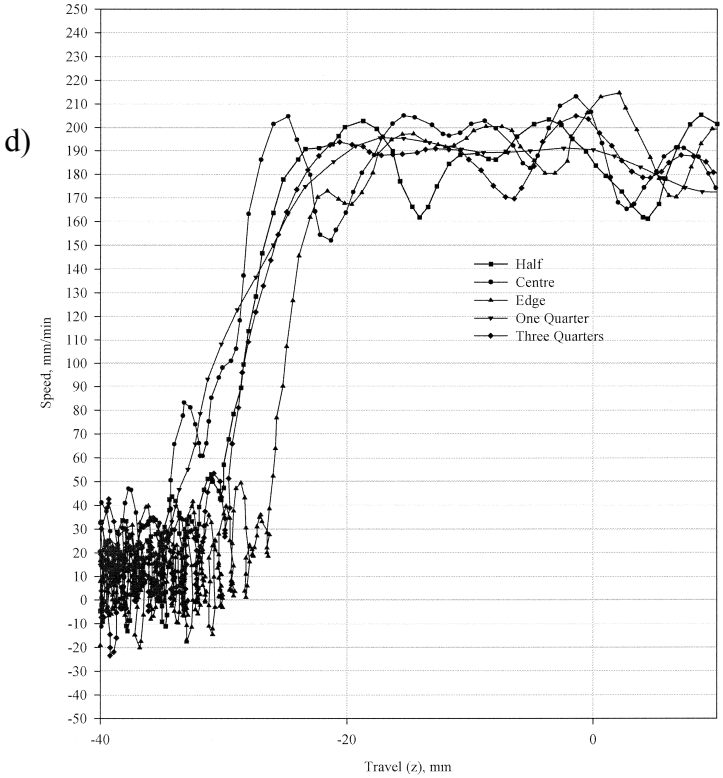

Figure 25. d). Variation of the speed of particles with different starting positions with height above the die exit, for extrusions performed at a ram speed of 10 mm min^{-1}.[78]

No industrial use of PEPT to track multiple particles has been reported in the literature, but the experimental application was investigated. Parker *et al*. developed an algorithm that could be used to detect multiple tracer particles within a system [72]. This algorithm relies on differentiating the particles by their different radioactivities and therefore the greater the difference in radioactivities, between 2 or more particles, the more accurate the particle tracking results can be. The use of multiple particles however, has been limited to where the separation distance between the tracer particles can be controlled, as in the following example.

Figure 26 shows 3 positron emitting particles of radoiactivites, 326μCi, 198μCi and 97μCi, attached to the vertices of a cube, mounted on a turntable rotating at a constant speed. The full

rotation of the cube could be reconstructed from the particle trajectories as shown in figure 26 (b). The maximum recorded location error was 6 mm at a particle speed of 240 mm/s [81]. Figure 27 shows the location errors obtained versus the particle speeds.

Parker *et al*. stated that tracking multiple particles successfully requires the particles to be at least 5 mm apart [70, 81] otherwise the multiple particle location algorithm has great difficulty in determining the particle locations and distinguishing between each of them.

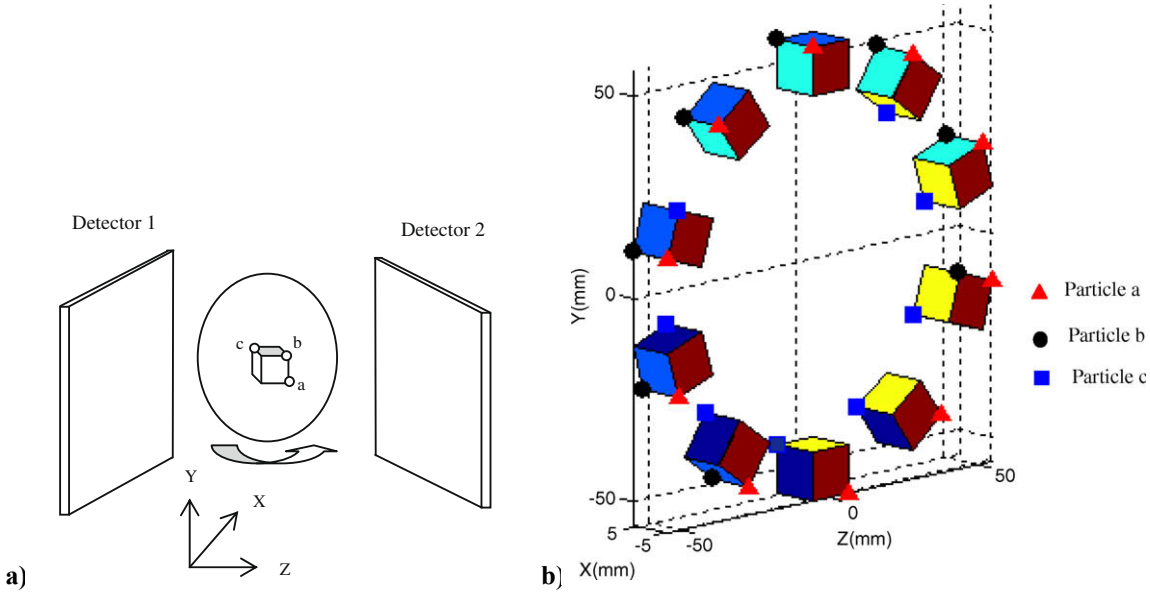

Figure 26 (a) A schematic diagram showing the cube mounted on a turntable between the camera faces with 3 tracer particles fixed to its vertices. (b) A reconstruction of the cubes rotation using all the 3 tracer particle tracks. [81]

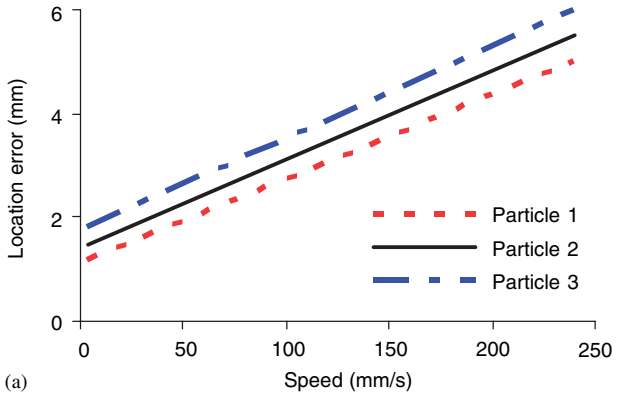

Figure 27. A graph showing the calculated location error of all 3 particles versus the calculated speed. [70]

2.2.5 PET/PEPT compared to other particle imaging techniques

The main difference between PEPT and other more established imaging techniques such as laser doppler velocimetry (LDV) and particle image velocimetry (PIV) is that it can be applied to determine particle movement in 3-D in dense opaque systems [73, 74, 82]. LDV and PIV are limited to dilute systems and can only produce 2-D results.

Pianko-Oprych *et al*. compared the results obtained from PEPT to those obtained by PIV for single-phase flow of a salt solution, where it was found that the results obtained were in good agreement, as shown in figure 28 [82]. This work not only validated PEPT as capable of producing results of similar accuracy to a well established technique such as PIV, but it also demonstrated the potential of PEPT in applications where PIV cannot be used.

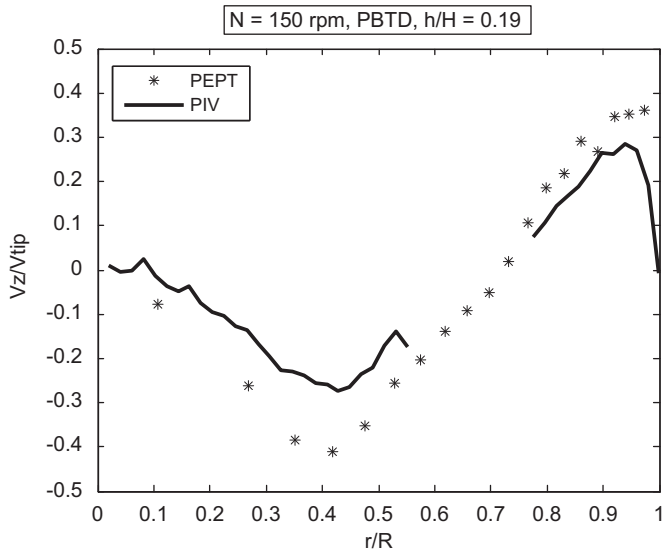

Figure 28. A graph showing the radial profiles of dimensionless axial velocity from PIV and PEPT at 150 rpm for the PBTD at a h/H plane=0.19 for single-phase flow (salt solution without surface aeration). [82]

2.5.6 Positron Emitting Isotopes

Table 5 is a list of positron emitters that can be produced using a cyclotron, where a suitable target is bombarded by high energy hydrogen, helium or deuterium nuclei. Positron emitters with shorter half lives are favoured in medical applications where human exposure and dosage are of great concern, while longer lived tracers can be used in industrial applications where human exposure can be reduced.

For example ^{11}C has a half life of 20.3 minutes which makes it suitable for medical applications but not for industrial applications, where 20 minutes would be insufficient to transport the tracer and carry out the experiment. On the other hand tracers with very long half lives, such as ^{22}Na (half life 2.6 years), are also not favourable for industrial application for safety reasons. Therefore for many industrial PEPT applications a half-life in the range of

110 minutes to 5 hours would be reasonable, but this ultimately depends on the experiment to be carried out.

Table 5. Some of the positron emitting isotopes. [83]

Nuclide	Half-life	Production Route
^{82}Rb	78 s	From ^{82}Sr Generator
^{15}O	122 s	$^{14}N(d,n)^{15}O$
^{13}N	10 min.	$^{12}C(d,n)^{13}N$
^{11}C	20.3 min.	$^{14}N(p,\alpha)^{11}C$
^{68}Ga	68 min.	From ^{68}Ge generator
^{18}F	110 min.	$^{18}O(p,n)^{18}F$ or $^{16}O(^{3}He,p)^{18}F$ and $^{16}O(^{3}He,n)^{18}Ne \rightarrow ^{18}F$
^{45}Ti	3.1 h.	$^{45}Sc(p,n)^{45}Ti$
^{62}Zn / ^{62}Cu	9.2 h.	$^{63}Cu(p,2n)^{62}Zn$
^{66}Ga	9.7 h.	$^{66}Zn(p,n)^{66}Ga$
^{64}Cu	12.7 h.	$^{64}Ni(d,2n)^{64}Cu$ or $^{63}Cu(n,\gamma)^{64}Cu$
^{140}Nd / ^{140}Pr	3.4 days.	$^{141}Pr(p,2n)^{140}Nd$
^{124}I	4.2 days.	$^{124}Te(d,2n)^{124}I$
^{82}Sr / ^{82}Rb	25 days	Abundant Fission Product
^{68}Ge / ^{68}Ga	271 days	$^{66}Zn(\alpha,2n)^{68}Ge$
^{22}Na	2.6 years.	$^{24}Mg(d,\alpha)^{22}Na$

2.6 Mathematical Modelling of Castings

2.6.1 Types of models

There are two types of commercial packages available, “open” models and “closed” models. “Open” models are ones where most understanding of the physical process is required. The user has to provide some guidance as to how the model is to be constructed, while incorporated in the model are the mathematical equations to be solved for each case. An example of an open model would be Flow-3D™, a widely used commercial modelling package. There, a description of the body to be cast is provided while, for example, the user chooses to consider the effect of surface tension during casting or ignore it in the model setup. “Open” models are very flexible but require a good understanding of the physics of the process being modelled. “Closed” models on the other hand, are models where the user does not require a deep level of understanding of the process, because the model is set up to contain only certain parameters.

“Open” and “Closed” models can be split into two categories, Eulerian and Lagrangian. Eulerian models are models where the material is allowed to flow through the mesh describing the volume to be modelled. The mesh dimensions are fixed and hence such models are suitable to describe fluid flow problems. Flow-3D™, Fluent™ and PHEONICS™ are examples of this type of commercial software. Lagrangian models allow the mesh to distort as the material it contains deforms and therefore this type of software is more suited for modelling stress and plastic deformation, (e.g ABAQUS)

2.6.2 The Theory of Modelling Fluid Flow

There are two categories that can describe the computational techniques incorporated in Eulerian models. These are Energy balance techniques and Momentum balance techniques [84].

Energy is a scalar quantity and therefore energy balance techniques are useful in determining flow rates through sprues and runner bars, where the direction of the flow is decided by the system configuration [84]. The Bernoulli equation is used for calculating the flow in completely filled channels such as sprues, while the Saint-Venant continuity equations are used for partially filled channels such as non-pressurised runners. Equations 15 and 16 are the Bernoulli and continuity equations respectively. For the Bernoulli equation, P is the pressure, V is the mean velocity and z is the elevation (b is a velocity distribution factor, 0.5 for laminar flow and 1.0 for highly turbulent flow), g is the acceleration due to gravity and $E_{f_{i,j}}$ is the friction energy loss between positions i and j. Figure 29 is a schematic diagram of a gravity-filled casting system analysed by the Bernoulli equation approach. Numbered planes on figure 29 correspond to the subscripts used in Eq 15. For the continuity equation, W_T is the width of the channel at flow depth Y, t is time and VA is the volumetric flow rate [84].

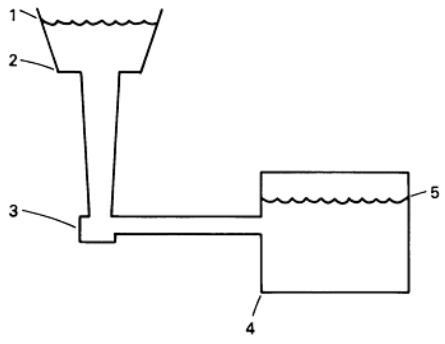

Figure 29. A schematic diagram showing a gravity-filled casting system analysed by the Bernoulli equation approach. Numbered planes correspond to the subscripts used in Eq 1. [84]

Bernoulli equation:

$$\frac{P_j - P_i}{\rho} + \frac{V_j^2}{2b_j} - \frac{V_i^2}{2b_i} + g(z_j - z_i) + E_{f_{i,j}} = 0 \text{ ----------Equation 15}$$

Saint-Venant continuity equation:

$$W_T \frac{\partial Y}{\partial t} + \frac{\partial (VA)}{\partial X} = 0 \text{ ----------Equation 16}$$

Momentum balance techniques are another type of Eulerian model, where fluid flow problems are solved by a finite-difference scheme for mathematical analysis. This is very useful when the filling of the mould cavity is being modelled where the amount and location of the liquid changes rapidly. The finite-difference technique divides the configuration of the casting cavity into rectangular cells. Then a set of imaginary markers or fluid function values are introduced into the system to represent the location of the fluid at any time [84]. Figure 30 shows a flow pattern obtained 3.95s after the pouring begins showing the marked cells divisions [84] while figure 31 shows a portion of the fluid domain with the fluid function [84]. Markers are moved or the fluid function is updated according to the calculated velocity fields as the fluid proceeds, in order to represent the new location of the fluid domain [85]. This procedure is repeated until the mould cavity is full.

In the fluid function technique, the numbers shown in figure 31, F represents the fraction of volume of a cell that is filled with fluid. F can have values from 0 to 1. F is one for a full cell, 0 for an empty cell and a fractional value for surface cells. Therefore, the full cells are either interior region cells or surface region cells [84, 85].

After the flow domain and the corresponding interior and surface regions of the domain have been identified, the velocity and pressure fields within the flow domain are calculated. The physical conditions that control the flow behaviour differ between the interior and surface regions. This is the principle of the marker and cell (MAC) technique and the more advanced and widely used volume of fluid (VOF) techniques [85, 86].

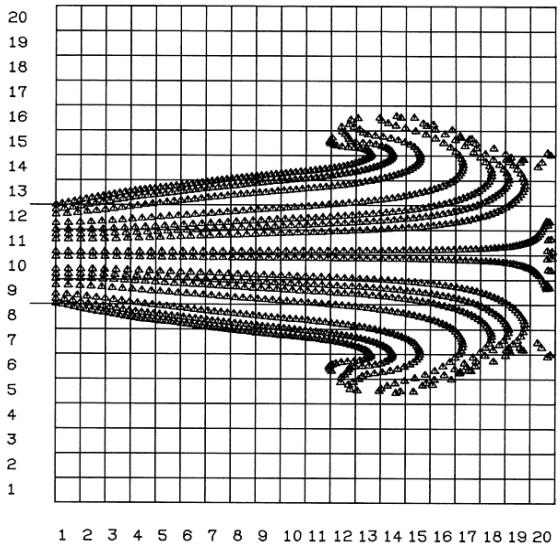

Figure 30. A graph showing the flow pattern obtained 3.95s after pouring begins showing MAC cell divisions and fluid domain locations (indicated by triangular markers) [84] .

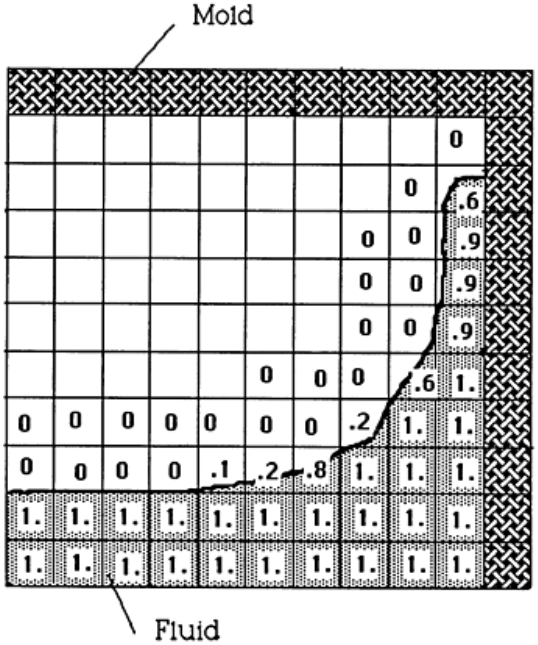

Figure 31. A graph showing the fluid domain plot obtained with the fluid function F using SOLA-VOF technique. F=1.0, 0.0 < F < 1.0, and F=0 indicate full, surface, and empty cells respectively [84].

Because liquid metals are incompressible fluids, for the previously described interior regions, the governing principles are the conservation of mass and momentum [84]. The conservation of mass is solved using the continuity equation solved is as follows:

$$\frac{\partial u}{\partial x} + \frac{\partial v}{\partial y} = 0 \text{ ----------Equation 17}$$

Where "u" and "v" are the velocity components in the x- and y-directions.

Secondly, the conservation of momentum which is commonly known in the mathematical form as the Navier-Stokes equation [84, 87], is represented as follows:

In the x-direction:

$$\frac{\partial u}{\partial t} + u\frac{\partial u}{\partial x} + v\frac{\partial u}{\partial y} = -\frac{\partial p}{\partial x} + v\left(\frac{\partial^2 u}{\partial x^2} + \frac{\partial^2 u}{\partial y^2}\right) + g_x \text{ ----------Equation 18}$$

In the y-direction:

$$\frac{\partial u}{\partial t} + u\frac{\partial v}{\partial x} + v\frac{\partial v}{\partial y} = -\frac{\partial p}{\partial y} + v\left(\frac{\partial^2 v}{\partial x^2} + \frac{\partial^2 v}{\partial y^2}\right) + g_y \text{ ----------Equation 19}$$

t is time, p is pressure/density, v is viscosity/density and g is the acceleration of gravity. In case of turbulent flow, v is replaced by the effective viscosity. Therefore the Navier-Stoke's equations in the x- and y- and z- (for 3-D models) directions together with the continuity equation are how the velocity pressure fields for the interior region are calculated [84].

Finally, in the surface region the momentum balance principle still applies and hence the Navier-Stoke's equations apply. However the continuity equation used for the surface region is not valid because the mass within the cells of this region is changing [84].

2.6.4 Modelling of Turbulence in Fluid Flow

Turbulence is the unstable motion of fluids that takes place due to the lack of stabilising forces, namely viscosity. Reynolds number (Re) is a dimensionless number that has been used to estimate the flow regime of a fluid and is given in equation 20 [14]. Where "ρ" is the density, "V" is the fluid velocity, "L" is the hydraulic diameter and "μ" is the dynamic viscosity. The Reynolds number predicts only bulk turbulence i.e. turbulence within the fluid itself, not free surface turbulence [88]. A Re value greater than 2000 was reported to indicate bulk turbulence in liquid steels [89]. Figure 32 shows a map of expected flow regimes in castings.

$$R_e = \frac{\rho V D}{\mu}$$ ----------Equation 20

The accurate mathematical modelling of turbulence has always been a limitation due to the complexity of the process and the limited capabilities of the currently available computing hardware [90, 91]. This is because turbulence involves 3-D motions of a wide range of eddy sizes and thus extremely fine meshes are required to solve the conservation of momentum equations accurately across the whole range of eddy sizes [89]. This cannot be carried out feasibly with the current computing technology and consequently, various approximations are currently employed by commercial modelling packages such as MAGMAsoft™ and

Flow-3D™ [91, 92]. The principle of these models is the substitution of the viscosity terms in the continuity equation with an eddy viscosity, which is equal to the sum of molecular and turbulent viscosities, (known as the k-ε model) [91, 93, 94].

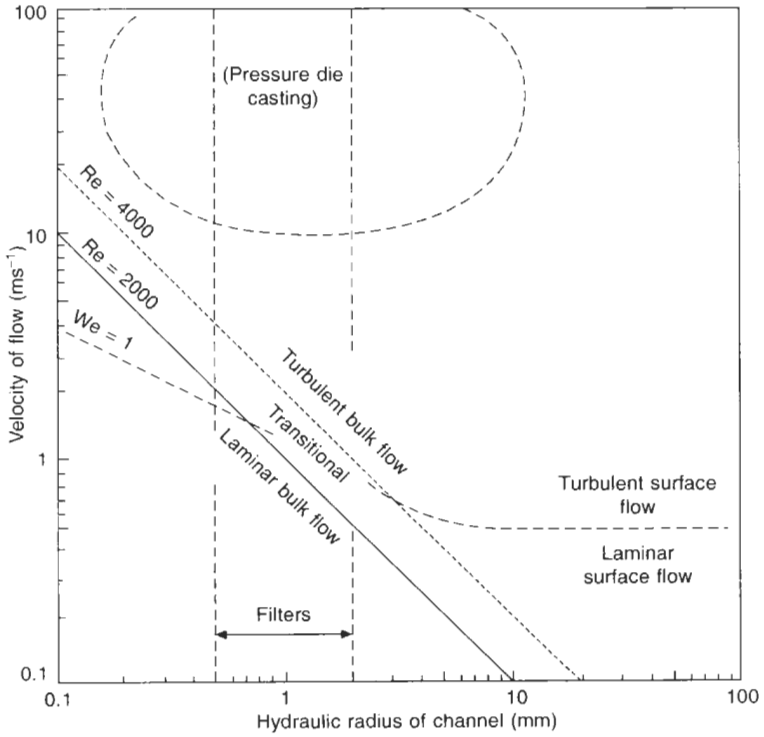

Figure 32. A graph showing a suggested map of flow regimes in castings [14].

Although, the use of these k-ε model models has enabled commercial modelling packages to make reasonably accurate predictions of fluid flow [95, 96], their effects on modelling particles such as non-metallic inclusions that are present in the liquid metal has not yet been validated due to the lack of experimental methods to achieve this [97].

2.6.5 Modelling of Non-Metallic Inclusions in Castings

Most work found in the literature where the movement and behaviour of non-metallic inclusions in castings was modelled, was validated using water models which are not an identical representation of the problem being modelled [98-103]. This is believed to be due to the lack of experimental techniques by which such models could be validated, owing to the opacity and high temperatures involved in shape castings. State of the art X-ray techniques that were employed in the validation of various types of fluid flow models are only in 2-D and have limited resolution, and do not allow for particles smaller than 2-5 mm in diameter to be detected. Even for large particles a full particle path cannot be obtained during casting due to the restricted field of view of the X-rays.

Commercial modelling packages available such as MAGMAsoft™ and Flow-3D™ have different capabilities to track particles within a casting. MAGMAsoft™ for example can introduce one or a stream of dimensionless particles into a casting from a user defined initial position [92]. These tracer particles have no mass or size but are merely a visual representation of the possible behaviour of these particles [92]. Any interaction between the particle and the moving fluid due to drag or buoyancy is completely ignored.

Flow-3D™ also has a particle tracking feature but in this case a particle size and density can be specified [91]. This feature was mainly developed for predicting the behaviour of large particles (e.g. >5 mm) in the stream of a river, and therefore only drag and buoyancy of the particle were implemented in the calculation.

Chapter 3
EXPERIMENTAL PROCEDURE

3.0 Experimental Summary

Various castings were produced to develop the PEPT technique for use with tracking single and multiple particles in castings. The final locations of single particles were determined in steel cast in sand and investment moulds while a full particle path was obtained for low melting point alloy castings that could be produced *in situ* between the positron camera faces. The effects of changing casting parameters such as particle density and the use of ceramic foam filters, on the entrained particle behaviour were studied. Some of the results obtained were compared to those predicted by commercial modelling packages, such as MAGMAsoft™ and Flow-3D™.

The available multiple particle tracking algorithm was also assessed and the possibilities of using the modular camera to track multiple particles in a foundry environment were explored.

3.1 Particle Preparation and Handling

3.1.1 Direct Irradiation of Oxide Particles

Initially, experiments were carried out with particles of Al_2O_3 and SiO_2, that were directly irradiated using the Radial Ridge Cyclotron, at the University of Birmingham. The particles were first sieved to obtain a size range of 355-600 μm, and then wrapped in aluminium foil and placed into a cyclotron target. This was then exposed to a 35 MeV ^{3}He beam for 2-3 hours. This allowed some of the oxygen atoms in the oxide particles to be converted to the radioactive isotope ^{18}F via the following reactions, where p is a proton and n is a neutron.

$$^{16}\mathrm{O} + (^3\mathrm{He}, \mathrm{p}) \rightarrow {}^{18}\mathrm{F}$$

$$^{16}\mathrm{O} + (^3\mathrm{He}, \mathrm{n}) \rightarrow {}^{18}\mathrm{Ne} \rightarrow {}^{18}\mathrm{F}$$

The radioactivities obtained ranged from 15-135 μCi with a half-life of 110 minutes.

3.1.2 Ion Exchange

The ion exchange technique was used to make smaller particles, of size range 63-100 μm, but still with sufficient radioactivity for PEPT. In this case the target contained distilled water which was also exposed to a 35 MeV ^{3}He beam for 2-3 hours, causing some of the oxygen atoms of the water to be converted to ^{18}F via the reactions mentioned previously. Alumina particles and particles of an ion exchange resin were then mixed with the radioactive water for a further 2 hours, after which the particles were dried using a continuous stream of N_2 and an infrared lamp. The particles became radioactive due to adsorption of radioactive water onto

their surface, a process that was significantly enhanced if the particle surface was modified prior to the mixing with the radioactive water. This surface modification consisted of introducing Fe^{3+} ions onto a particle surface, which act to enhance the adsorption of ^{18}F onto the particle surface. Much higher radioactivities could be achieved than by direct activation of the whole particle, despite the smaller volume of the particles [64].

3.1.3 Introduction of the radioactive Particles

Various handling techniques were used depending on the casting process in which the radioactive particles were used. With particles of size range 355-600 μm, introduced into the steel castings, initially handling was carried out by applying a thin film of glue to a pin head, which was then used to pick up the particles. In the case of sand castings, the pins carrying the particles were fixed between the pouring basin and the mould while for the investment castings these pins were placed onto a stainless steel mesh, as shown in figure 33, which was fixed in position using fireclay.

In the case of the low melting point alloy castings, small 63-100 μm particles were used and, vacuum tweezers were used (a fine glass tube 30-40 μm in diameter connected to a vacuum pump), to pick up particles, under an optical microscope. This was then placed in a 1 mm depression created in a 100-400 μm thick sheet of the same alloy as was used in the experiment. This Field's metal / Lensalloy-136 film was produced by casting the metal between two Perspex™ blocks after which it was cut in to 10 mm x 25 mm strips. A thin film of oil was applied to the 1 mm depression to ensure that the particles stayed in place. This

method of inserting the particle into the metal stream was developed further, by placement of the particle in a 3 mm diameter, 1.5 mm deep hole drilled in a 3 mm diameter rod, cast from the same alloy used for the casting. The hole was sealed by inserting another 3 mm diameter rod so that it was flush with the surface and the rod was inserted through the Perspex™ die wall, so that the particle's initial position was 35 mm below the centre of the downsprue opening.

In the experiments to evaluate multiple particle tracking the directly irradiated particles ranged in size from 90-150 μm. They were placed into a 1 mm depression in a 0.6 mm thick aluminium disc, or a 2 mm diameter, 1.5 mm deep hole, drilled in an aluminium rod. This approach allowed multiple particles to be introduced simultaneously.

In the case of tracking multiple particles in a stirred low melting point alloy bath, alumina particles of size 63-100μm were used and irradiated by ion exchange. Lensalloy-136 rods of length 280-320 mm and diameter 8 mm were drilled to produce 3 mm in diameter and 4 mm deep holes so that a particle can be placed along the centre line of the rod. A thin film of oil was spread inside the holes and a radioactive particle was placed into each hole using vacuum tweezers. The holes were then sealed using 3 mm diameter Lensalloy-136 rods that were inserted on top of the particle and clipped short.

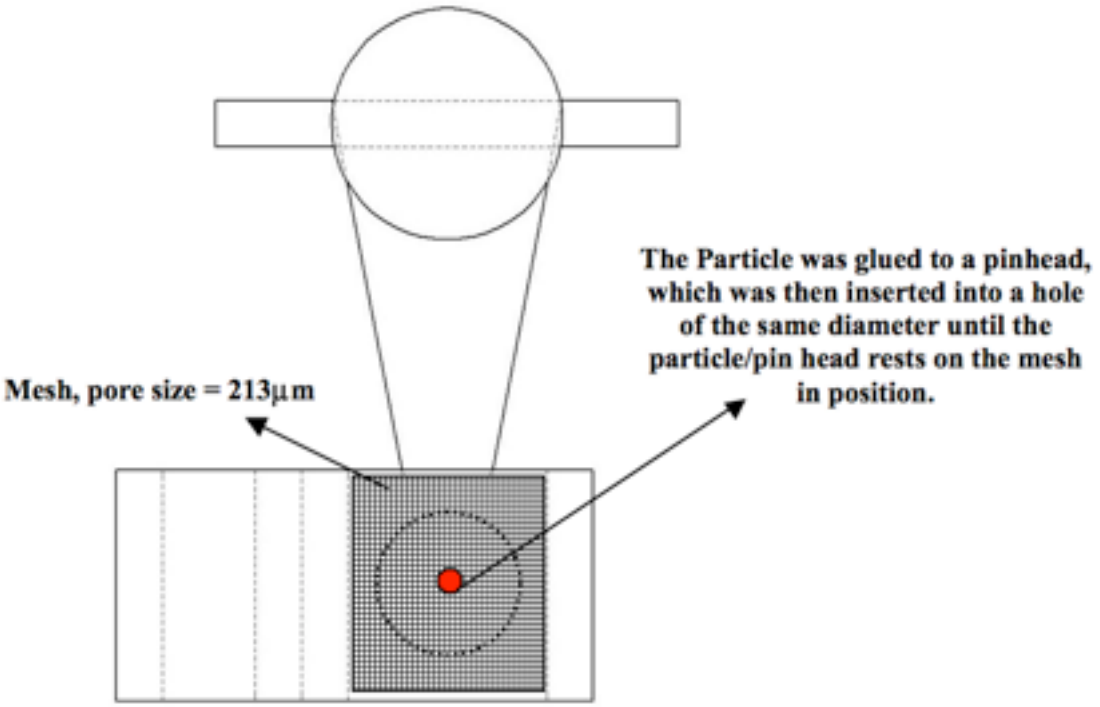

Figure 33. A schematic diagram showing how the particle was inserted at a known initial position onto the stainless steel mesh.

3.2 Single Particle Tracking Experiments

3.2.1 Steel Cast in Sand Moulds

En3B steel with composition shown in table 6 was used to investigate the applicability of PEPT to study the behaviour of inclusions in castings. A 5 kg charge of was melted in a 45 kW EMA induction furnace in a Morganite E300 clay graphite crucible, and cast at approximately 1700ºC into two sand moulds to make plate-shaped castings. The moulds were made from Kings Lynn, grade 60 silica sand bonded with 1.2 mass % Pepset^{TM} 5112 and 5230 two-part resin. The faces of the mould were then glued together using a nitrocellulose refractory adhesive. The geometry of the castings is depicted in figure 34. The initial particle positions for the sand castings were the centre of the downsprue opening at the top of the mould, (see figure 35).

Table 6 The chemical composition of EN3B steel. [104]

Element	C	Si	Mn	P	S
Wt %	0.15-0.25	0-0.35	0.3-0.9	0-0.05	0-0.05

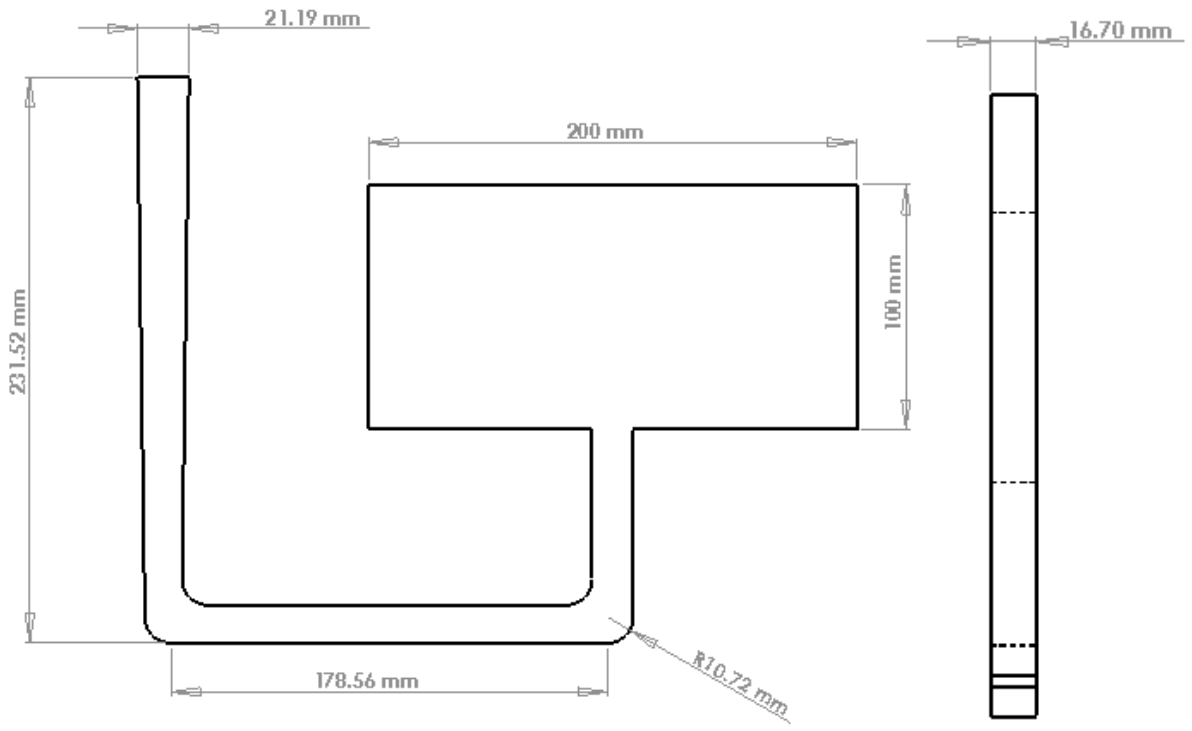

Figure 34. A schematic diagram showing the sand cast plate and its dimensions.

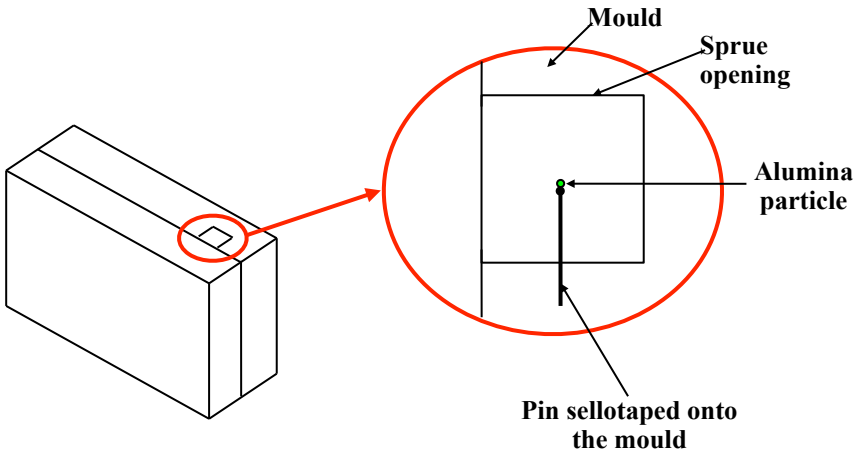

Figure 35. A schematic diagram showing the Alumina particle setup. The Alumina particle is glued to the pinhead so that it is at the centre of the downsprue opening. The pin was sellotaped onto the mould between the mould and the pouring basin.

After pouring the castings were quenched in water to room temperature and then taken to the Birmingham University positron camera where the final locations of the embedded alumina particles were determined. Figure 36 shows the casting between the camera faces. The back to back ɣ-rays produced by the positron-electron annihilation, taking place at the location of the embedded particle, were recorded on a computer and translated to coordinates with respect to the camera datum. To determine the particle's exact position within the casting, another radioactive particle was placed at known positions on the casting and the coordinates of both particles recorded with reference to the camera datum. This reference particle was glued to a pinhead, which was then temporarily stuck to the corners of the plate as shown in figure 37. The co-ordinates of the embedded particle were determined, relative to the reference particle, with an accuracy of ±2-3mm.

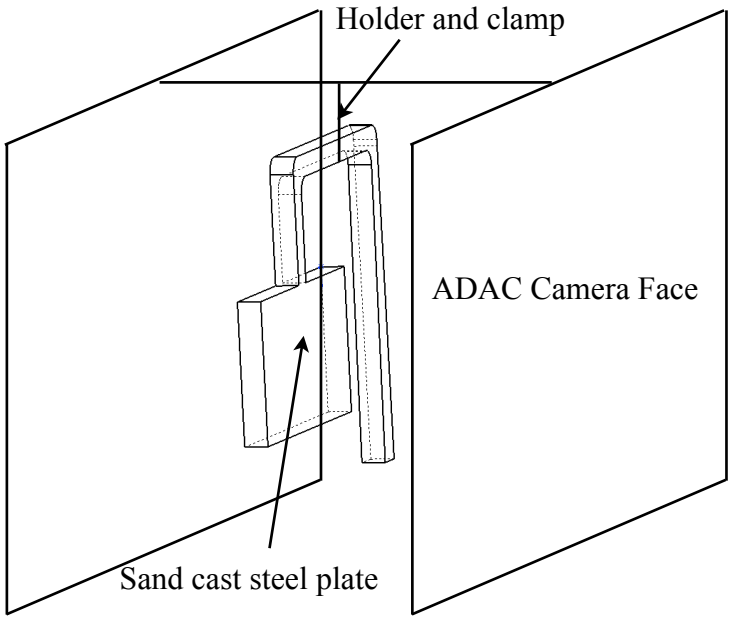

Figure 36. A schematic diagram showing the cast steel plate setup between the (ADAC) positron camera faces.

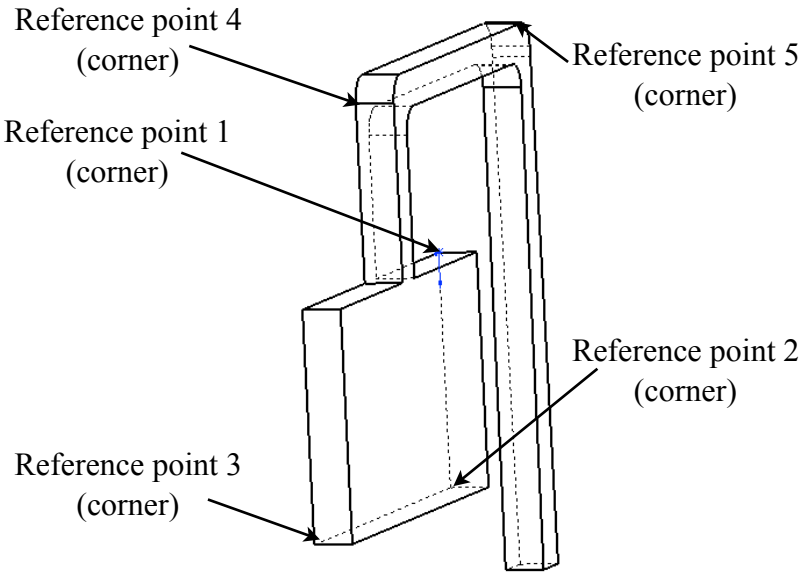

Figure 37. A schematic diagram showing the reference points where the radioactively labelled alumina particles (reference particles) were fixed.

3.2.2 Steel Cast in Investment Shell Moulds

3.2.2.2 Moulding and Casting procedures

The sand moulds previously used to cast steel were not sufficiently robust as the resin used resulted in significant gas porosity in the castings which may have significantly affected the particle path and its final location. As a result it was decided that ceramic shell moulds, used for investment casting, should be used.

The ceramic shell moulds were built in layers using a zircon primary coating followed by Molochite 30/80 and Molochite 16/30 stucco respectively. The secondary slurry was an Al_2O_3-SiO_2 based slurry and the final shell moulds had a thickness of 15-20mm. The geometry used for these experiments is shown in figure 38 and table 7 is a summary of the

experiments carried out with these investment castings, where the effects of changing particle size, density, initial position and presence of a ceramic foam filter on the particle final location were investigated.

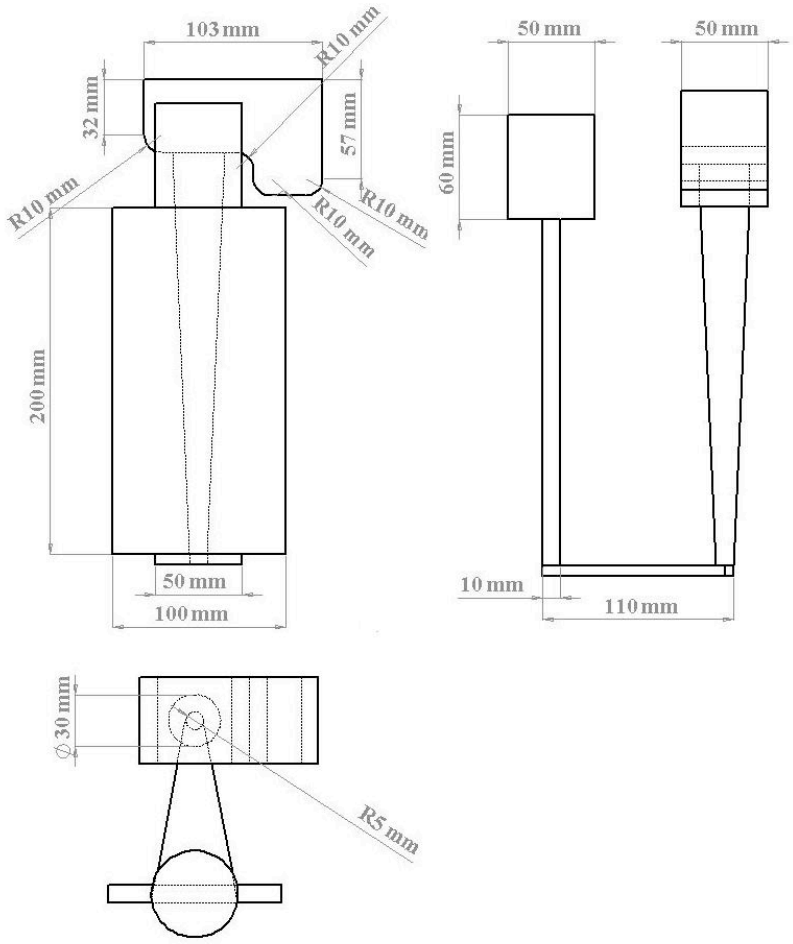

Figure 38. A schematic diagram showing the investment cast steel plates and its dimensions.

3.2.2.1 Determining the final location

The accuracy of determining the final particle location for these sets of castings varied with the method employed to place the reference particles. This was a continuous development from the sand castings where an adhesive was used to fix the pins carrying the reference particles in position to determine the location of the embedded particle relative to the known position of the reference particle. Initially the methods employed to attach the reference particles in position led to contamination of the reference position (reference particle shattering and leaving a fragment behind at the previous reference position) and accordingly inaccurate results were obtained. The technique which brought the most accurate results used a reference particle glued to a pin head fixed in place using small magnets placed on the castings. This technique minimised the risk of contamination from one reference point to the next, as well as minimising any movements of the casting between the camera faces due to handling of the reference particle.

3.2.2.3 Experiments Performed

Eight moulds were cast at room temperature with En3B steel, directly poured from an induction furnace at 1700ºC. Before casting, the moulds were preheated to 500ºC to remove any moisture, and then allowed to cool down. Experiments were carried out to determine the effects of changing the particle type, initial position, and the use of a zircon ceramic foam filter (pore size10-15 ppi).

Some castings showed a substantial amount of pores and gas bubbles due to the turbulent pouring method used, as the steel was poured directly from the furnace as fast as possible. It

was considered that the trapped gas bubbles may have significantly affected the particles' motion, and therefore the results obtained from these castings were rejected. In subsequent experiments the molten steel was transferred from the furnace into a preheated graphite crucible, at approximately 1700ºC, then poured from the crucible into the ceramic shell moulds to lower the pouring speed and minimise turbulence and air entrainment.

This experiment was repeated, and four moulds were cast with EN3B steel in the same manner. But in this case the casting was video recorded to obtain accurate modelling parameters such as the metal stream diameter pouring, head height and filling time.

A final experiment was carried out to eliminate all known sources of error in the particle location, in order to obtain accurate tracking results that would enable the SEM and EDX identification of the particle at its final location. Three investment casting moulds were produced with an alumina particle placed at the centre of the sprue opening. The irradiated alumina particles were of a much higher radioactivity, approximately 10 times (400 μCi), the standard particles (10-40 μCi). After the castings cooled down, the castings were fixed, facing exactly the centre of the positron cameras using a ratchet clamp. The reference particles were glued to pin heads, and those pins were fixed in position by the aid of magnets. Therefore the casting did not move at all during changing the reference particle location and hence minimum error was to be expected. However, no tracking results were obtained for all 3 castings. The positron camera was unable to detect any of the embedded radioactive particles despite them being much more radioactive than those used in previous experiments.

Table 7. A summary of the experiments carried out and the parameters used for each casting.

Exp	Casting No.	Particle	Particle Size (µm)	Radioactivity (µCi)	Initial Position	Mould Thickness (mm)	Mould Temp (°C)	Cast Metal	Cast Temp (°C)	Filter Size (ppi)
1	7 castings	Al_2O_3	355-425	64-135	Centre	7 - 8 mm	600	En3B	1723	-
2	1	Al_2O_3	355-425	22	Centre	15.9	20	En3B	1732	-
	3	Al_2O_3	355-425	38.8	Centre	15.3	20	En3B	1723	-
	4	Al_2O_3	355-425	24.3	Edge	15.6	20	En3B	1700	-
	5	Al_2O_3	355-425	56	Edge	17.4	20	En3B	1718	-
	6	SiO_2	355-425	24	Centre	17.2	20	En3B	1732	-
	8	Al_2O_3	355-425	41	Centre	17.6	20	En3B	1720	10
	9	Al_2O_3	355-425	41	Centre	17.1	20	En3B	1735	10
3	10	Al_2O_3	355-425	11	Centre	17.1	20	En3B	1706	-
	11	Al_2O_3	355-425	10	Centre	18.4	20	En3B	1750	10
	12	SiO_2	355-425	15	Centre	18	20	En3B	1766	-
	14	Al_2O_3	355-425	14	Edge	18	20	En3B	1709	-
	16	Al_2O_3	355-425	10	Centre	17.8	20	En3B	1708	10
4	17	Al_2O_3	355-425		Centre	20	20	En3B	1725	10
	18	5 x Al_2O_3	355-425		5 mm around the centre	20	20	En3B	1725	-
	19	SiO_2	355-425		Centre	20	20	En3B	1725	-
5	21	Al_2O_3	355-425	200	Centre	20	20	En3B	1740	-
	22	Al_2O_3	355-425	360	Centre	20	20	En3B	1740	-
	23	Al_2O_3	355-425	400	Centre	20	20	En3B	1740	-
6	21	ZrO_2	355-425	1.2	Centre	20	20	En3B	1740	-
	22	Al_2O_3	355-425	27.6	Centre	20	20	Cast Iron	1410	-
	23	SiO_2	355-425	30	Centre	20	20	En3B	1746	-
	24	Al_2O_3	355-425	24.3	Centre	20	20	En3B	1752	10
	25	Al_2O_3	355-425	26.6	Centre	20	20	En3B	1752	10
	27	Al_2O_3	560-630	111	Centre	20	20	En3B	1752	-

3.2.3 Low Melting Point Alloy Castings

The next stage of the investigation used low melting point alloys in order to use smaller inclusions of size range 63-100μm, which are more representative of the most abundant inclusion sizes in industrial castings [1]. Since such inclusions can only be irradiated sufficiently by ion exchange as explained earlier in the literature survey (2.5.2.2), low melting point alloys, Field's metal and Lensalloy-136 were used, (which had melting points of 335 K (62ºC) and 330.8 K (57.8ºC) respectively), in order to avoid driving the radioactive water from the particles surfaces.

3.2.3.1 Moulding and Casting procedure

Five sets of experiments (a summary of experimental parameters is shown in table 9) were carried out using the low melting point alloys, Field's metal and Lensalloy-136. The low melting point alloys meant that there was minimal risk of damaging the positron camera and casting could be carried out between the camera faces. The chemical compositions for both alloys are shown in table 8. Lensalloy-136 was used instead of Field's metal at a later stage of the project due to it's lower Indium content and hence reduced cost. Both alloys had similar (estimated) thermophysical properties, shown in table 15.

Table 8. The chemical compositions of Field's Metal and Lensalloy-136.

Element	In	Bi	Sn	Pb
Field's Metal	51	32.5	16.5	-
Lensalloy-136	21	49	12	18

Two acrylic (Perspex™) dies were machined from cast acrylic blocks with a tube shaped geometry, shown in figures 39 and 40 (with and without a filter). The low melting point alloys were melted in Pyrex beakers using a Fischer-Scientific hot plate and were cast at 87ºC (with an exception of one experiment cast at 110ºC).

3.2.3.2 Experiments Performed

Five sets of experiments were carried out. In the first set of experiments, 9 particles were irradiated by the ion-exchange method, in which 6 were porous alumina of size 63-100 μm, and 3 particles were of a strong base anion exchange resin [63] of size 63-73 μm. The radioactivities obtained ranged from 99-1035μCi. Figures 41 and 42 depict the placement of the Field's metal film, on which the radioactive particles were placed so as to introduce them into the liquid metal, and its arrangement between the acrylic mould and the pouring basin.

Once the particle was placed into the depression made into the Field's metal strips using vacuum tweezers, the film was fixed into position by the BlueTack™ used to fix the 50 mm diameter pouring basin on top of the mould. The Field's metal charge was then melted in a Pyrex® beaker and left to cool down for a few minutes to be cast into the pouring basin at 87ºC. Table 9 is a summary of the experimental parameters used in these castings. In the initial bench mark experiment, the particle was placed at the centre of the downsprue opening and the metal cast at 87ºC. This was carried out 5 times, in order to test reproducibility.

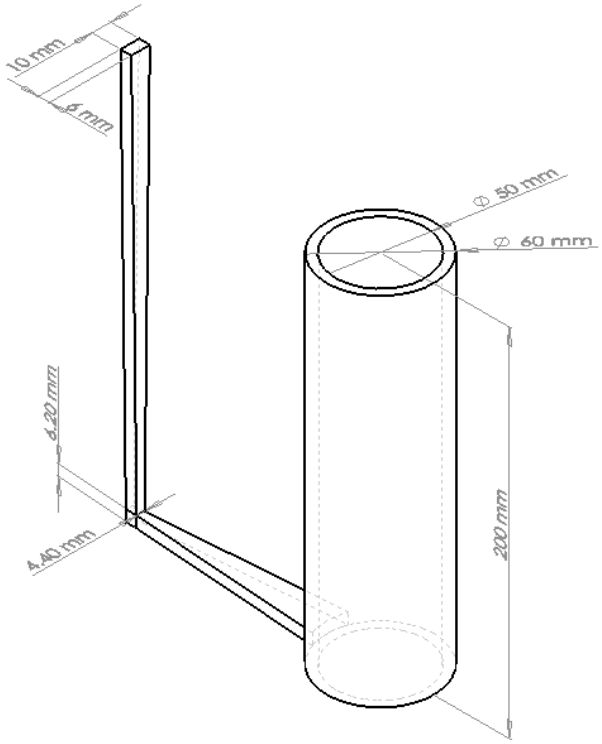

Figure 39. An isometric view showing the geometry and dimensions of the cast tube used in the low melting point alloy experiments.

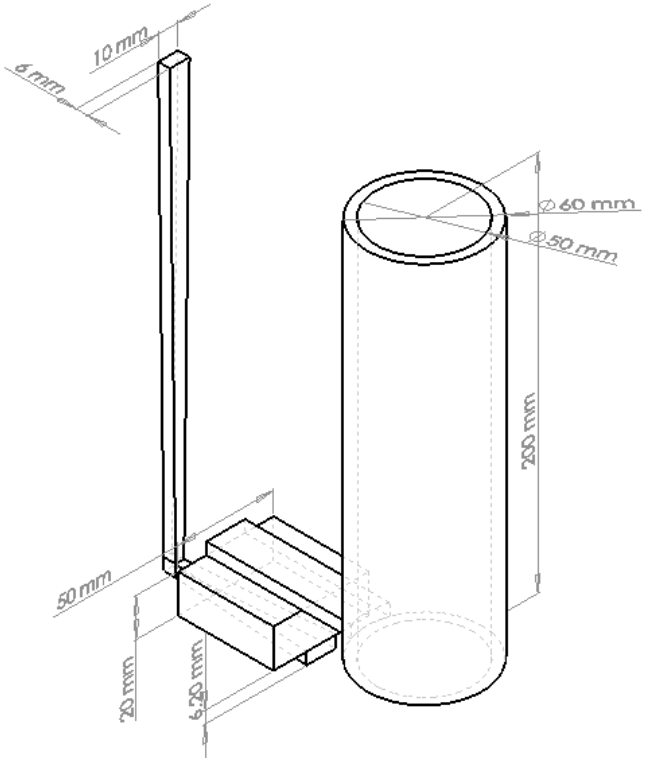

Figure 40. An isometric view showing the geometry and dimensions of the second low melting point alloy casting where a filter was used. Filter dimensions were 50x50x20 mm.

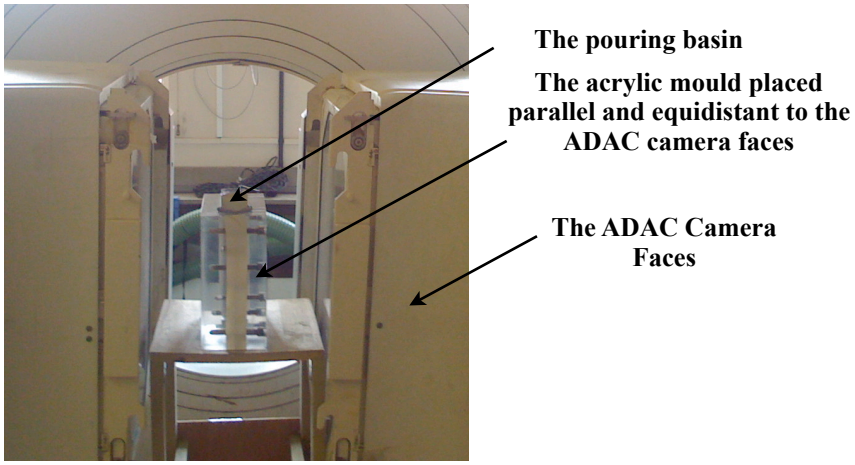

Figure 41. A photograph showing the setup of the Perspex™ mould in between the (ADAC) positron camera faces.

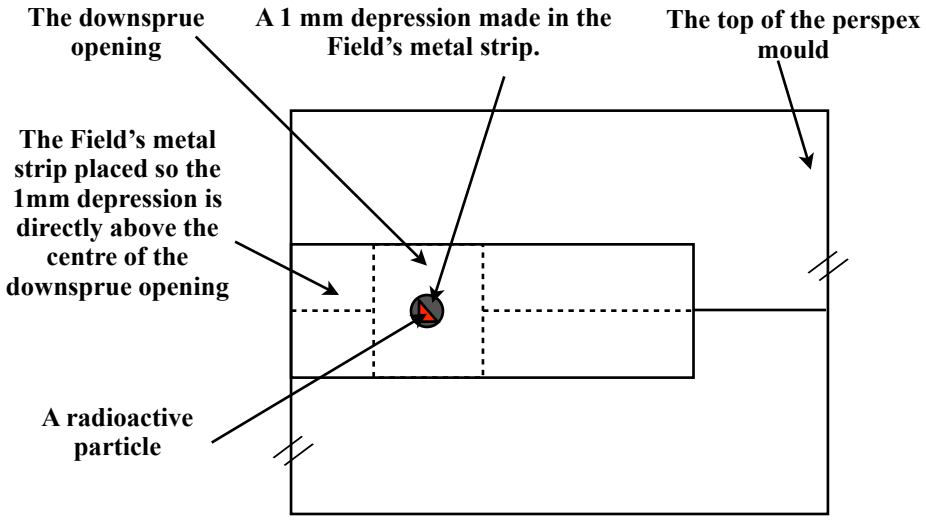

Figure 42. A schematic diagram showing the initial particle location in the Field's metal casting with emphasis on the placement of the Field's metal strip carrying the particle.

In a subsequent set of experiments the effects of having a ceramic foam filter (10, 20 and 30ppi) in the running system were investigated. Nine castings were produced in which the radioactive particles were ɣ-alumina of size 63-100 μm and the radioactivities achieved were in the range 130-532 μCi. This time the cast alloy was Lensalloy-136, cast at 87^{o}C.

Another set of experiments were dedicated to investigate the effects of preheating the acrylic die, for which the mould temperature at casting was above the pouring temperature (87^{o}C).

This was to enable a clearer understanding of how the growth of the solidification front of the metal in the mould cavity might affect the particle path, and whether eliminating this factor would improve reproducibility of results. Five castings were produced for which the mould was preheated to a transfer temperature of 84-90^{o}C after which it was assembled, aligned between the camera faces and cast within about 5 minutes. Two thermocouples were used to obtain the mould temperature 2 mm away from the surface of the cast metal at the top of the runner bar and 100 mm parallel to the length of the cast tube (see figure 43). Measured mould temperatures ranged from 48-77^{o}C and 50-85^{o}C before and after casting respectively. The radioactivities achieved for the alumina particles used in these castings were between 24-406 μCi.

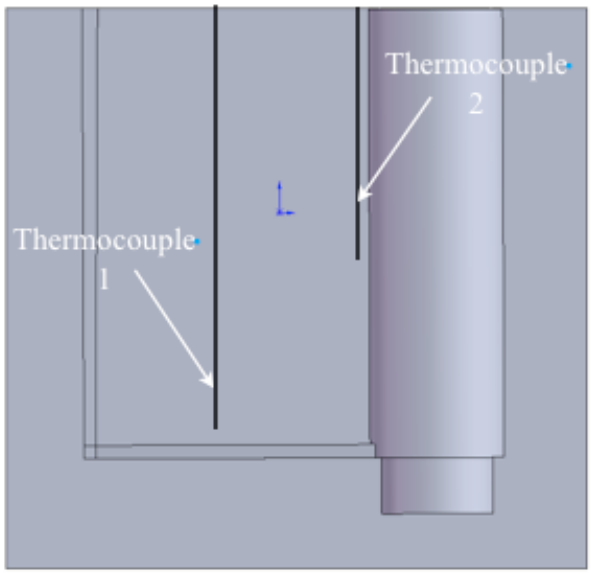

Figure 43. A schematic diagram showing the positions where the thermocouple grooves were machined into the mould. One thermocouple measured the temperature 2 mm away from the metal surface half way along the runner bar and the other also 2 mm away from the surface of the metal half way along the length of the tube.

A further set of 4 castings, were produced to determine whether a reproducible particle path could be obtained, by eliminating all the sources of error learned from previous experiments. The radioactive particles used were also alumina of size 63-100 μm but they were placed and

sealed into a hole which was drilled through the tip of a 3 mm diameter Lensalloy-136 rod. The rod was then inserted through the Perspex™ die wall so that the radioactive particle was 35 mm below the centre of the downsprue opening to ensure that the particle would be released into the metal stream without prior movement in the pouring basin, (an observation made from the results of previous experiments). To maximise reproducibility an upper pouring basin was fixed on top of the lower pouring basin using a silicone adhesive and a rubber stopper rod was used, see figure 44. This meant that the whole melt could be poured into the upper pouring basin after which the stopper rod was removed. Hence the mould filling procedure was very similar in all experiments. The metal was cast at 87°C and the radioactivities of the alumina particles used in these experiments were 178-822 μCi.

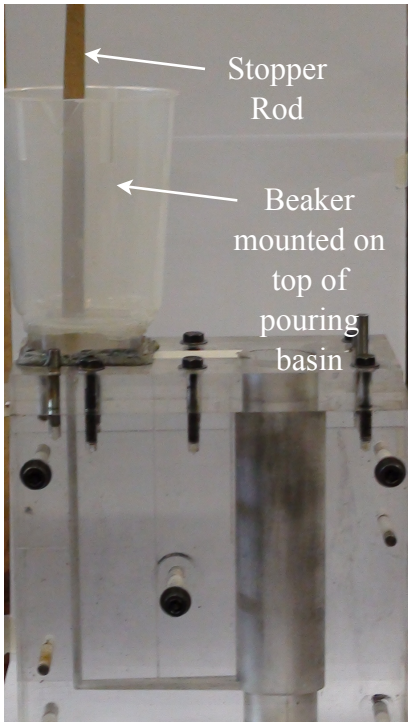

Figure 44. A photograph showing the pouring arrangement and the stopper rod used to maximise reproducibility.

The filling of the Perspex™ mould was video recorded to measure the filling time, record the mould filling behaviour and validate the mathematical models of mould filling, using a digital high definition SONY® video camera. The frames captured in this video were extracted and

have been presented in the results section; a copy of the video is on a CD inserted into this thesis.

Table 9. A summary of the experimental variables used in the low melting point alloy castings.

Casting Number	Filter Size (ppi)	Cast Metal	Particle Type	No. of Ptcls	Particle Size (μm)	Initial Position	Rad. (μCi)	Casting Temp. (°C)	Mould Temp. (°C)	Average Ptcl Holder Thickness (mm)
1	-	Field's Metal	Al_2O_3	1	63-100	Centre	1035	85	Ambient	0.31
2	-	Field's Metal	Al_2O_3	1	63-100	Centre	607	87	Ambient	0.37
3	-	Field's Metal	Al_2O_3	1	63-100	Centre	335	86	Ambient	0.36
4	-	Field's Metal	Al_2O_3	1	63-100	Centre	274	85	Ambient	0.405
5	-	Field's Metal	Al_2O_3	1	63-100	Centre	168	110	Ambient	0.41
6	-	Field's Metal	Al_2O_3	1	63-100	Centre	99	87	Ambient	0.415
7	-	Field's Metal	Resin	1	63-73	Centre	418	86.6	Ambient	0.38
8	-	Field's Metal	Resin	1	63-73	Centre	250	86.5	Ambient	0.44
9	-	Field's Metal	Resin	2	63-73	Centre	183	86	Ambient	0.395
10	30	Lensalloy-136	Al_2O_3	1	63-100	Centre	532	87.4	Ambient	0.205
11	-	Lensalloy-136	Al_2O_3	1	63-100	Centre	390	87.4	Ambient	0.19
12	10	Lensalloy-136	Al_2O_3	1	63-100	Centre	240	87	Ambient	0.17
13	20	Lensalloy-136	Al_2O_3	1	63-100	Centre	130	87.5	Ambient	0.19
14	10	Lensalloy-136	Al_2O_3	1	63-100	Centre	497	87.3	Ambient	0.31
15	30	Lensalloy-136	Al_2O_3	1	63-100	Centre	351	87	Ambient	0.2
16	30	Lensalloy-136	Al_2O_3	1	63-100	Centre	190	87.2	Ambient	0.2
17	20	Lensalloy-136	Al_2O_3	1	63-100	Centre	150	87.5	Ambient	0.2
18	30	Lensalloy-136	Al_2O_3	1	63-100	Centre		87	Ambient	0.2
19	-	Lensalloy-136	Al_2O_3	1	63-100	Centre	123	87	From Oven, 90, Long: 56, 63; Short: -, -	0.23
20	10	Lensalloy-136	Al_2O_3	1	63-100	Centre	240	86.6	Ambient	0.24
21	10	Lensalloy-136	Al_2O_3	1	63-100	Centre	141	88	Ambient	0.255
22	-	Lensalloy-136	Al_2O_3	1	63-100	Centre	97.7	83	From Oven, 86, Long: 48, 50; Short: 56, -	0.225
23	20	Lensalloy-136	Al_2O_3	1	63-100	Centre	211	86	Ambient	0.22
24	20	Lensalloy-136	Al_2O_3	1	63-100	Centre	64	88	Ambient	0.195
25	-	Lensalloy-136	Al_2O_3	1	63-100	Centre	24	85.6	From Oven, 85, Long: 66, -; Short: 54, -	0.19
26	-	Lensalloy-136	Al_2O_3	1	63-100	Centre	406	86	From Oven, 86, Long: 62, 65; Short: 52, 58	0.155
27	-	Lensalloy-136	Al_2O_3	1	63-100	Centre	66	96	From Oven, 90, Long: 77, 80; Short: 58, 61	0.115
28	-	Lensalloy-136	Al_2O_3	1	63-100	35 mm below Centre (b.c)	822	87	Ambient	-
29	-	Lensalloy-136	Al_2O_3	1	63-100	35 mm b.c	235	87	Ambient	-
30	-	Lensalloy-136	Al_2O_3	1	63-100	35 mm b.c	240	87	Ambient	-
31	-	Lensalloy-136	Al_2O_3	1	63-100	35 mm b.c	178	87	Ambient	-

3.3 Multiple Particle Tracking

The algorithm that was previously used to process the particle tracking data was limited to 2 particles only. The experiments described in this section were carried out to assess and apply a newer multiple particle detection algorithm that was theoretically capable of tracking a larger number of particles at one time.

3.3.1 Assessment of The Multiple Particle Tracking Algorithm

To assess the feasibility of using this algorithm a square arrangement of grooves was machined into a piece of wood, (the width of the grooves was 4 mm and the depth was 2.7mm), see figure 45. Seven spherical alumina particles of 4 mm diameter were irradiated by the ion-exchange technique to radioactivities in the range of 35-63 μCi. Table 10 is a list of the designated particle numbers and their radioactivities. The piece of wood was placed at approximately 30^{o} between the positron camera faces, to enable the vertical coordinate of particles at opposite ends of one line to be distinguished. The arrangement is shown in figure 46.

Table 10. The designated particle numbers for the 4 mm alumina tracers and their radioactivities.

Particle Number	1	2	3	4	5	6	7
Radioactivity (μCi)	63	43	35	63	61	58	56

Figure 45. A photograph showing the groove / path of the 4 mm alumina particles used to assess the multiple particle tracking algorithm.

Figure 46. A photograph showing the sheet of wood placed approximately 30^{o} in between the (ADAC) positron camera faces.

Initially the seven particles were placed in the different positions shown in figure 47, and their stationary locations were recorded and processed using the "NTrack" algorithm. The particles were then removed and the following placement sequence was carried out to assess the algorithm's ability to determine the locations of multiple particles, and assess its ability to recognise agglomerated particles.

Particle 1 was placed in the centre as shown in figure 47 and its stationary location recorded. Afterwards particle 2 was placed in the upper right corner, figure 48, and manually pushed towards particle 1 in the centre at an approximately constant speed of 0.5 cms^{-1}. The recording was then stopped and particle 3 was placed at the upper right corner (see, figure 49) after which the data was recorded again to mark the initial location of particle 3 which was then moved towards particles 1 and 2 that were already in the centre, again at roughly 0.5 cms^{-1}. This was repeated as depicted in figures 48-53 until all 7 particles became an agglomerate in the centre (note that the size of the particles in figures 47-53 has been exaggerated for clarification). The "NTrack" algorithm successfully recorded the positions of all 7 particles and the results are presented and discussed in subsequent sections.

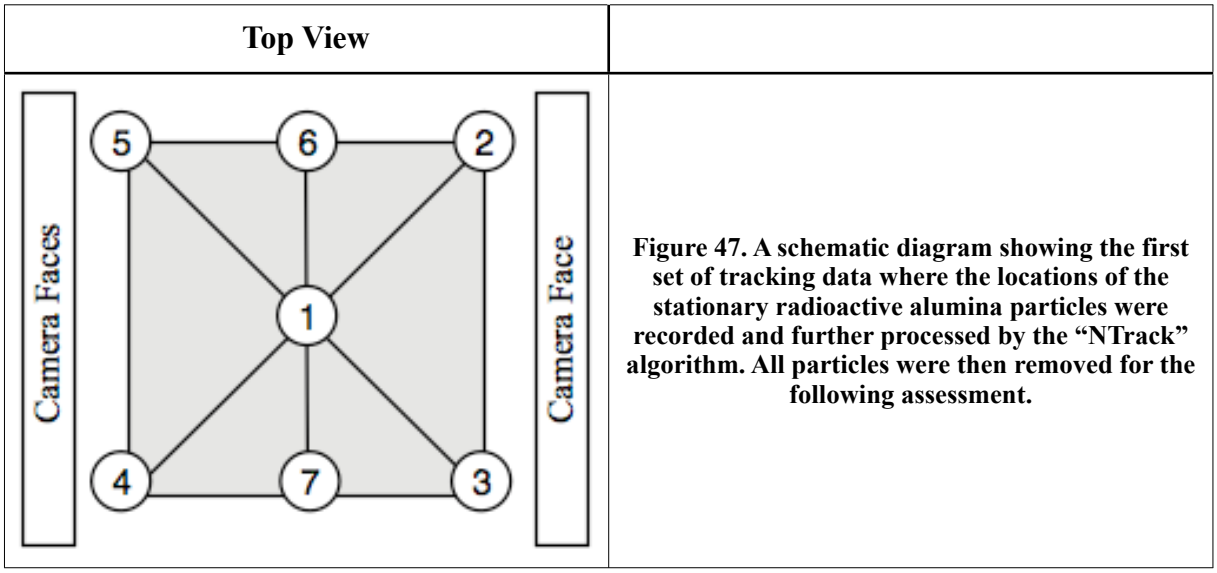

Figure 47. A schematic diagram showing the first set of tracking data where the locations of the stationary radioactive alumina particles were recorded and further processed by the "NTrack" algorithm. All particles were then removed for the following assessment.

Top View	
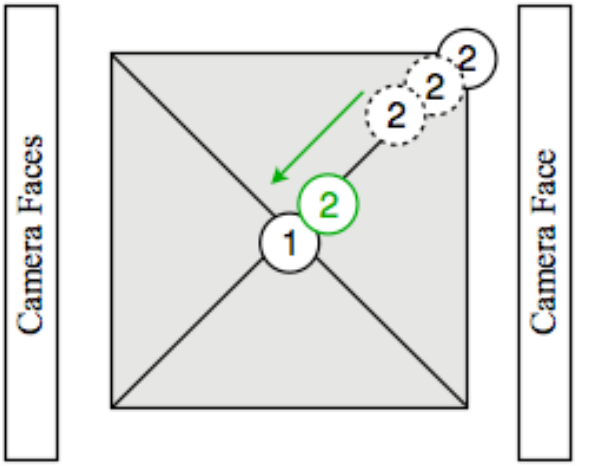	**Figure 48. A schematic diagram showing particle 2 being manually pushed towards particle 1 to form an agglomerate in the centre.**
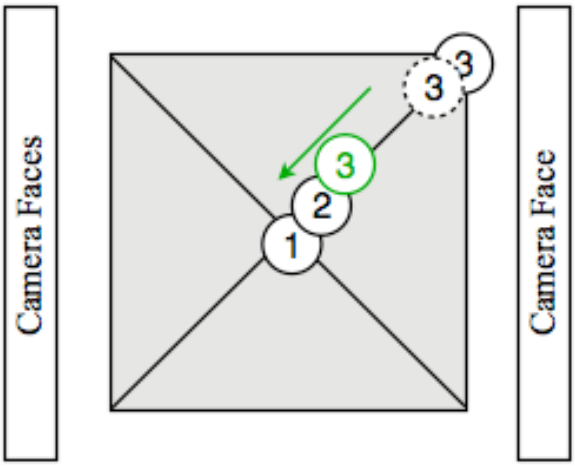	**Figure 49. A schematic diagram showing particle 3 being manually pushed from its initial position in the lower right corner towards particles 1 and 2 in the centre.**
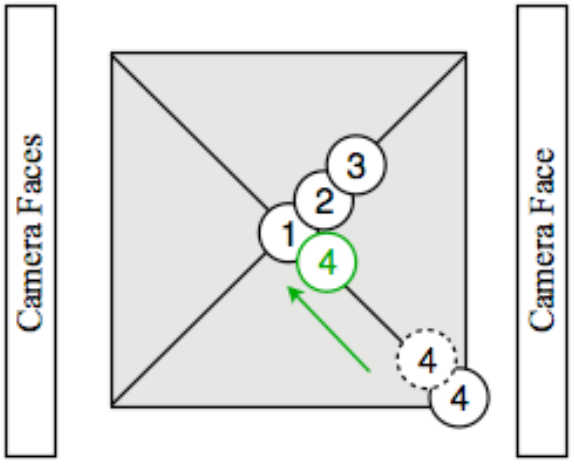	**Figure 50. A schematic diagram showing particle 4 being manually pushed from its initial position in the lower left corner towards particles 1, 2 and 3 in the centre.**

Top View	
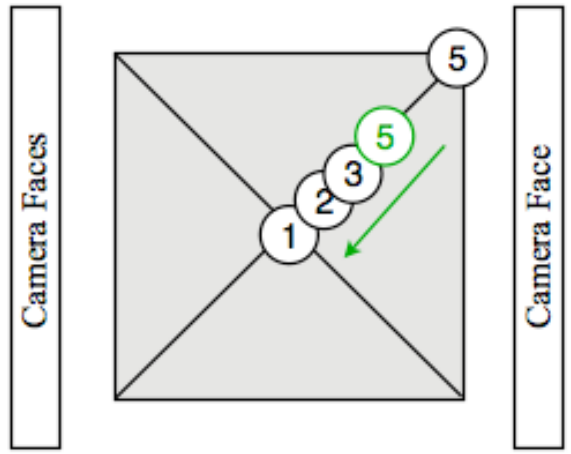	**Figure 51. A schematic diagram showing particle 5 being manually pushed from its initial position in the lower right corner towards particles 1, 2 ,3 and 4 in the centre.**
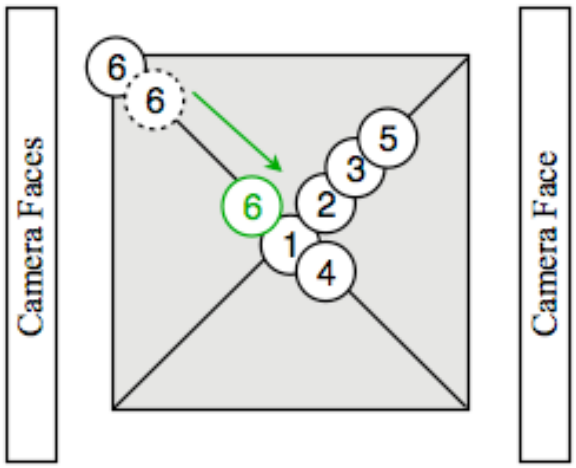	**Figure 52. A schematic diagram showing particle 6 being manually pushed from its initial position in the lower left corner towards particles 1-5 in the centre.**
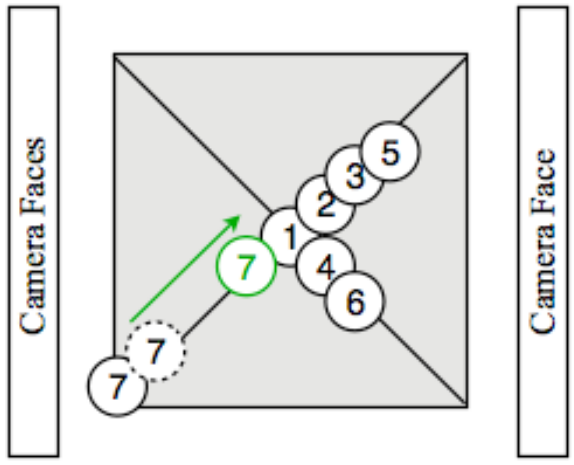	**Figure 53. A schematic diagram showing particle 7 being manually pushed from its initial position in the upper right corner towards particles 1-6 in the centre.**

3.3.2 PEPT of Multiple Particles in a Stirred Liquid Metal Bath

Three experiments were carried out where radioactive particles were introduced into a stirred bath of Lenssllloy-136, a 44 mm diameter tube of 240 mm length, mounted on a flat acrylic sheet, (figure 54). This was carried out to investigate the ability of the algorithm to differentiate between multiple particles in a continuously stirred liquid metal bath, a situation that is common in many industrial liquid metal processing routes. The small cross section of the bath was chosen to minimise the attenuation of the ɣ-rays to obtain better tracking data.

Lensalloy-136 was melted in a Pyrex™ beaker and poured into the tube at transfer temperatures of 101-106^{o}C. When the metal was poured into the tube, a magnetic stirrer was operated at the highest setting, at which a small vortex could be seen at the metal surface. The temperature of the liquid metal at this stage was recorded to be 83-85^{o}C. Lensalloy-136 rods carrying the radioactive particles, which were previously prepared as explained in section 3.1.3, were lowered into the tube using a wooden guide, machined to fit the tube (see figure 54). Two experiments were carried out where 2 particles were introduced in a single rod, (see figure 55), so that they were 15 mm apart in the Y-direction, with the particle nearest the tip of the rod being 20 mm above the bottom of the tube. In a third experiment, 2 particles were introduced using 2 rods (1 particle in each), which were 15 mm apart in the Z-direction (see figure 54), and 35 mm above the base of the tube. The PEPT data was recorded for 5 minutes and the radioactivities of the particles used were between 8-67μCi.

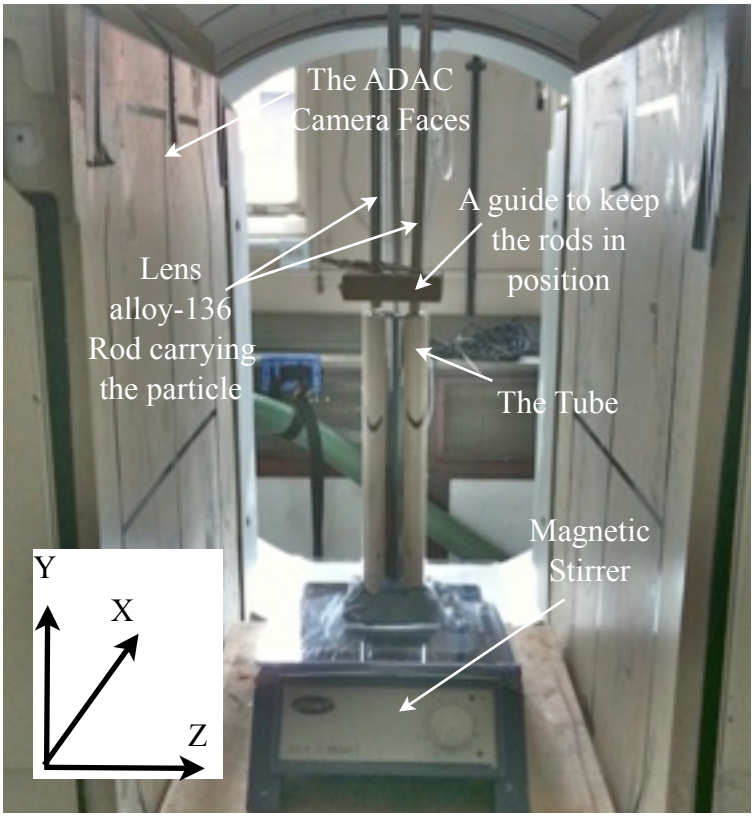

Figure 54. A photograph showing the tube arrangement in between the (ADAC) positron camera faces, when two particles were inserted using, two separate Lensalloy-136 rods.

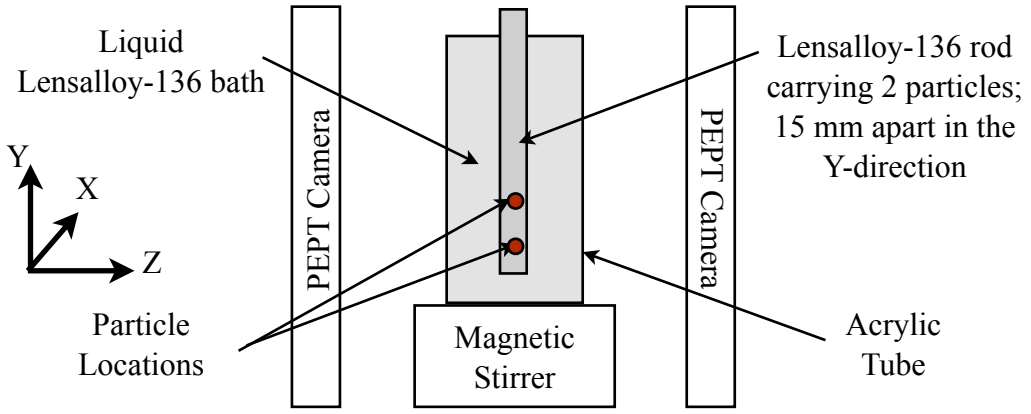

Figure 55. A schematic diagram showing the tube arrangement in between the (ADAC) positron camera faces, when two particles were inserted using the same Lensalloy-136 rod.

Table 11. The radioactivities of the particles used for the tube experiments.

Casting	Rods	Particles	Radioactivity (μCi)
1	1	2	23 and 31
2	1	2	33 and 67
3	2	1 in each rod	20 and 8

3.3.3 Sand Casting of Aluminium

This experiment was aimed at applying the technique to track multiple radioactive alumina particles in an aluminium sand casting. In this case a modular camera was used which was set up around the sand mould that was cast with the camera *in situ*, see figure 56.

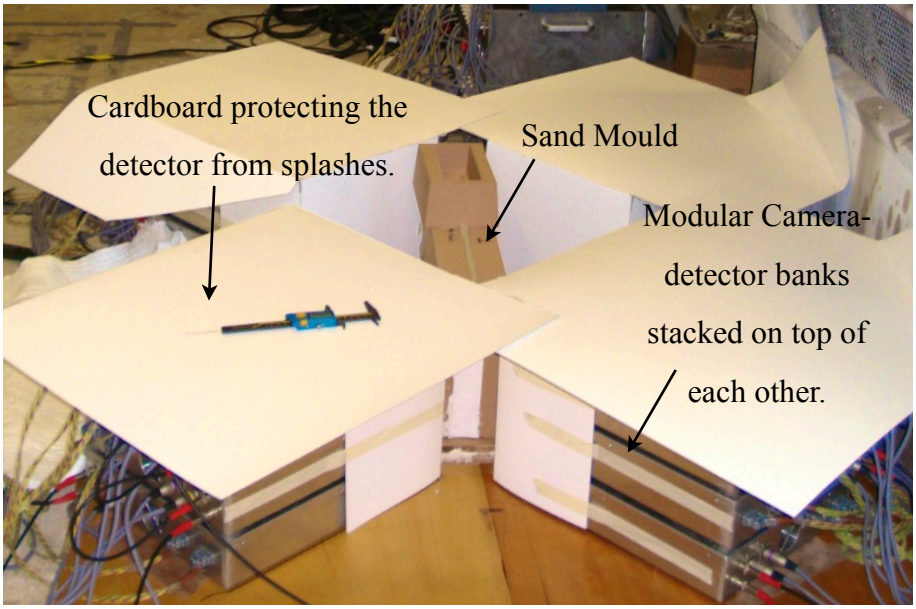

Figure 56. A photograph showing the setup of the sand moulds in between the 4 modular camera detectors that are covered by thick cardboard to protect them from metal splashes.

3.3.3.1 Moulding and Casting

The sand moulds were again made using Kings Lynn, grade 60 silica sand, with a 1.2 mass % 2 part addition Pepset^{TM} resin. The resin addition rate is that used for cast iron and was used in this case to increase the robustness of the mould and therefore minimise the risks of mould failure leading to damage of the modular camera. The faces of the mould were glued together using a nitrocellulose refractory adhesive. The geometry of the casting was identical to that used for the sand castings in steel, and is shown in figure 34. Four moulds were prepared with

various provisions for introducing the particles, (see section 3.3.3.2). The Al alloy used was LM29 (composition shown in table 12), melted in a 45 kW EMA induction furnace, and cast at 720^{o}C into the sand moulds from a Morganite E300 clay graphite crucible.

Table 12. The chemical composition of Aluminium, LM29 [105].

Element	Cu	Mg	Si	Fe	Mn	Ni	Zi	Pb	Sn	Ti	Cr	Co	Al
Weight%	0.8-1.3	0.8-1.3	22-25	0.7 max	0.6 max	0.8-1.5	0.2 max	0.1 max	0.1 max	0.2 max	0.6 max	0.5 max	Bal.

3.3.3.2 Particle Handling

Alumina particles of size 90-150 μm were directly irradiated as explained earlier in section 3.1.1, and placed in a 2 mm diameter hole, drilled in a 2.7 mm diameter aluminium rod, held in position by a thin film of oil previously placed in the hole. These rods were then inserted through the mould wall so the particles were released at different heights along the downsprue, as shown in figure 57. Some of the radioactive particles were placed in 1 mm depressions made in 0.6mm thick aluminium disks, and sealed in position by a thin strip of Sellotape™. These disks were used to introduce the particles at the centre of the downsprue opening, and at the same time acted as a stopper at the junction of the pouring basin and the downsprue. Figure 58, shows one of the disks, carrying 2 particles, in its position on top of the downsprue opening.

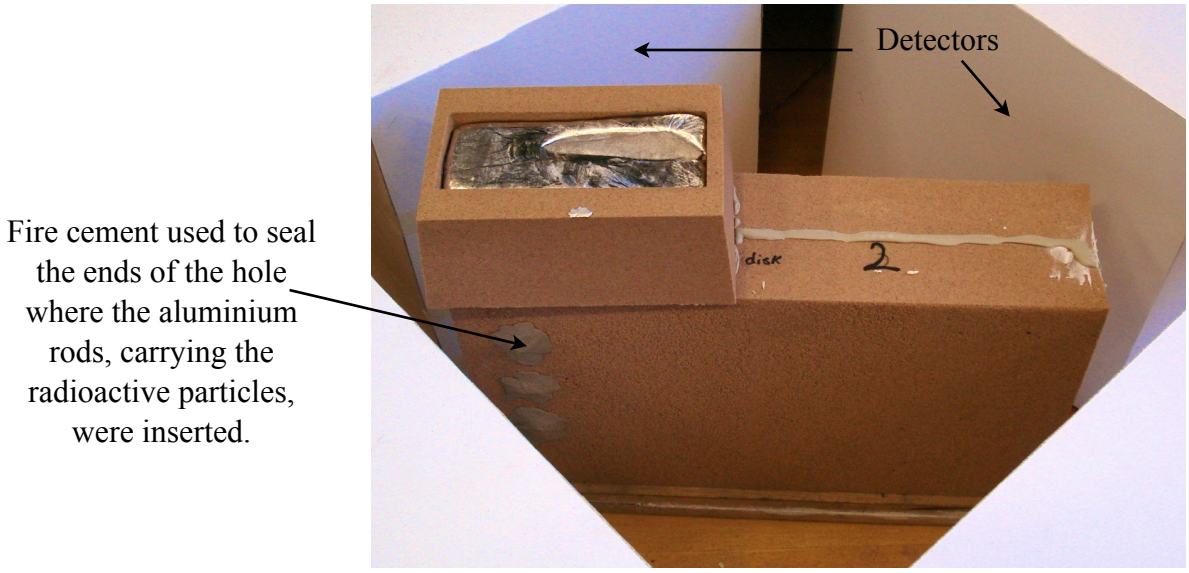

Figure 57. A photograph showing the arrangement of the mould and the locations of the rods carrying the radioactive particles along the length of the downsprue.

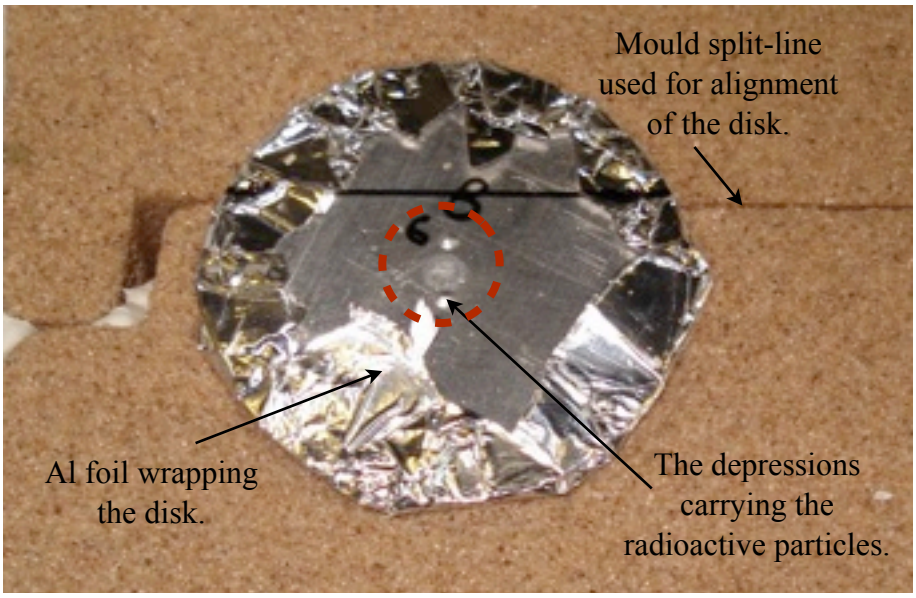

Figure 58. A photograph showing the aluminium disk carrying 2 particles that are 2 mm apart, 1 mm from the centre of the downsprue opening. The particles were sealed in place using Sellotape™ after which the disk was flipped and wrapped with AL foil and placed in position.

3.3.4 Other Attempts Using Multiple Particles

A steel investment casting similar to those described in section 3.2.2 was cast with En3B steel, with 4 directly irradiated alumina particles (size 355-425 μm) placed 5 mm around the centre of the downsprue opening and a 5th particle placed at the centre of the downsprue opening. The steel was cast at 1700^{o}C, and the final casting quenched in water before being taken to the positron camera to determine the final locations of the particles. The result obtained is shown in figure 294.

Another attempt to use multiple particles, involved a Lensalloy-136 casting, where 2 alumina particles of size 63-73μm were initially placed 2 mm apart, 1 mm one either side of the centre of the downsprue opening. The results obtained were poor due to the inability of the algorithm available at the time to determine the particle position with reasonable error. The result obtained is shown in figure 295.

3.4 Validation Experiments

3.4.1 Locating a Particle in an Investment Steel Casting

An attempt was carried out to locate an alumina particle of size 355-425 μm, after it's final location was determined using the PEPT technique. A cube of volume 2.25 cm^3 (which accounted for the reported tracking errors) was removed from the casting and manually ground at 30-50 μm steps using P240 SiC grinding paper. The sample was examined using an optical microscope after every grinding pass.

3.4.2 Locating a Particle in a Low Melting Point Alloy Casting

A tracked particle in a low melting point alloy casting, where the recorded errors were minimal, was located, to demonstrate the accuracy of the PEPT technique. The particle used in the low melting point alloy castings was of size 63-100 μm. The sample of choice was one where the particle came to rest in a 30 ppi filter. The whole filter was mounted and precision ground in 15μm steps. The surface was also examined using a 100-200x USB microscope after every grinding pass.

3.4.3 Locating a Particle in an Aluminium Plate Casting

Two particles of size 90-150 μm were also located after being tracked using the portable modular camera. A cube of size 15 mm X 5 mm X 16.7 mm was removed from the plate,

mounted and machined in 50 μm steps. The surface was examined using a 100-200x USB microscope after every milling step.

3.4.4 Real Time X-ray Examination of an Al Casting

A real time X-ray unit was used to record the mould filling of the Al plate cast in a sand mould. The sand mould was placed between an X-ray source and a detector (as shown in figure 59), containing a high speed camera capable of recording images at up to 100 frames/ second. As the liquid aluminium was being automatically poured into the mould, a video of the mould filling was generated with a maximum resolution of 800x600 pixels, and a maximum field of view of approximately 250x188 mm. This video of the liquid metal flow was used to help interpret the PEPT results obtained for the filling of the aluminium castings.

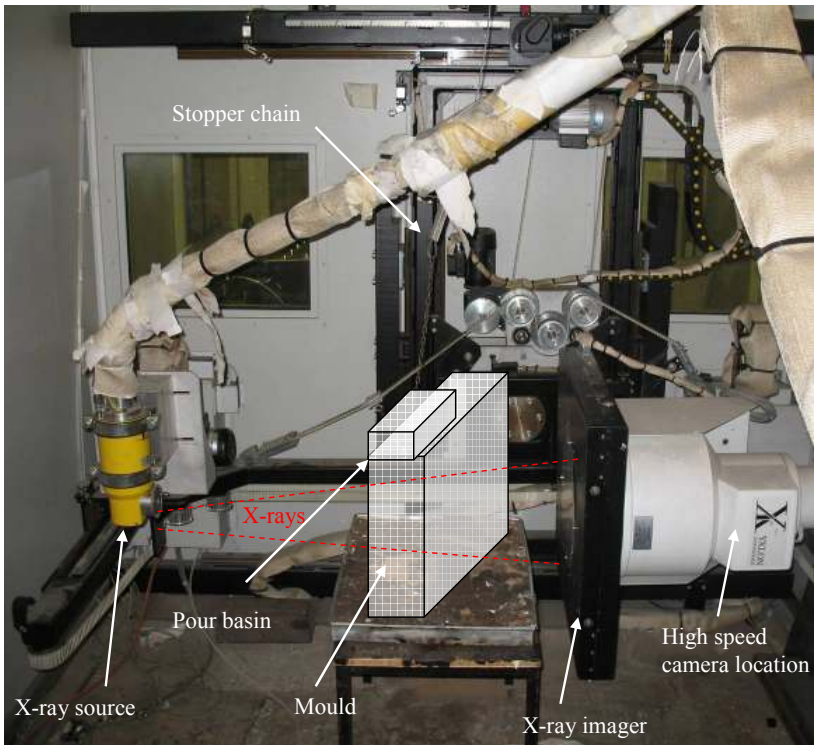

Figure 59. A photograph showing the X-ray casting unit located in the Metallurgy and Materials Department, The University of Birmingham.

3.4.5 New Radioactive Tracer for Industrial Applications

One of the targets of the project was to develop a technique that could be applied in an industrial environment. One problem was the thicknesses of the metal that would be encountered, and that the ɣ -rays would have to penetrate in order to be detected by the modular camera. Therefore a Zircon (zirconiumsilicate) particle was directly irradiated for 30 minutes, to investigate the possibilities of creating a longer lived, much stronger tracer. In this case the high energy ^{3}He beam converted some of the Zr atoms to ^{90}Nb, which has a half life of 14 hours, three times more than ^{18}F (0.511 MeV), and leads to the emission of ɣ-rays which have an energy of 1.5 MeV. (Note, Nb^{90} does not decay by positron emission, but decays by emitting ɣ-rays).

Two experiments were carried out to determine the penetration depth of the high energy ɣ-rays emitted from zircon particles, in steel and aluminium. Cylindrical pieces of steel or aluminium were stacked on top of one another, above one radioactive particle of size 1 mm and a Geiger counter was used to measure the level of radiation passing through the metal. Measurements were made of radiation passed through the metal in 50 mm increments, up to 550 mm.

3.5 Mathematical Modelling

MAGMAsoft™ and Flow-3D™ are two commercial modelling packages widely used in the foundry industry. Each of these packages has their strengths and weaknesses with regard to predicting an inclusion's behaviour in a casting, and their sensitivity to the users' input parameters.

3.5.1 MAGMAsoft™

Four types of model were carried out of the filling of the sand cast plate, shown in figure 34, with the first being the assessment of the sensitivity of the particle location to variations in thermophysical properties used. In this model a massless marker particle was introduced at the centre of the downsprue opening, and for simplicity a constant head pressure of 3825 Pa was used to describe the pouring of the liquid metal. Models were run with varying density, thermal conductivity, viscosity and specific heat capacity, as shown in table 13. A coarse mesh of 250,000 cells was used to model the running system and the cast plate to minimise computational time, but care was taken that a minimum of three cells described the thinnest sections of the casting, as recommended by MAGMAsoft™. Table 14 shows the temperature dependant thermophysical properties of steel, obtained from the MAGMAsoft™ database.

The ranges with which the thermophysical properties were varied, shown in table 13, were used as an exaggeration of the accuracy with which these thermophysical properties are known.

Table 13. The variations applied to the thermophysical properties of steel.

Property	Varied to:
Initial (pouring) temperature	± 100°C
Specific heat, C_p	± 25%
Thermal conductivity, λ	± 25%
Kinematic Viscosity, υ	± 25%
Density, ρ	± 5%
Initial position of the particle	± 1 mm

The effects of modelling the pouring basin and angling of the metal stream into the mould was also examined. Two models were produced in which the predicted final particle location was compared when a pouring basin was and was not included in the model. A finer mesh was used in this case, (500,000 cells), in an attempt to maximise the model accuracy. It was not feasible to use a finer mesh at the time due to the capabilities of the computational hardware available.

Finally, MAGMAsoft™ was used to model the filling of the steel investment casting. A massless marker particle was again introduced at the centre of the downsprue opening and its final location was predicted. The pouring basin was modelled together with the correct metal stream diameter, which was obtained from a video recording of the experiment.

Table 14. The thermophysical properties of steel used in the MAGMAsoft™ sensitivity analysis. [106]

Temperature (°C)	Thermal Conductivity ($W.m^{-1}.K^{-1}$)	Specific Heat Capacity ($J.Kg^{-1}.K^{-1}$)	Density ($Kg.m^{-3}$)
25	46.97	422	7850
100	46.63	496	7829
200	45.29	544	7801
300	43.11	580	-
400	40.35	620	7734
500	37.34	683	-
600	34.01	780	7661
700	30.84	931	-
750	-	871	-
760	27.1	-	-
800	25.8	716	7604
850	-	577	-
900	26.9	591	7547
1000	-	617	7503
1100	29	644	7460
1200	-	670	7413
1300	31.1	-	7369
1400	-	-	7323
1420	-	-	7315
1430	-	-	7313
1440	-	-	7308
1448	32.3	746	7297
1460	-	-	7284
1470	-	-	7258
1480	-	-	7211
1490	-	-	7158
1526	28.6	800	7080
1600	-	-	6960
2000	30	800	6480

3.5.2 Flow-3D™

Several models were carried out using Flow-3D™ to model the Lensalloy-136 castings, where an alumina particle was introduced at the centre of the downsprue opening, with the mass and density of the particle being specified. The available thermophysical properties of Lensalloy-136 were obtained from the literature [107] while viscosity was estimated using a weighted average of values of viscosity for the pure elements in its composition. Table 15 shows the thermophysical properties of Lensalloy-136 used in these models.

In the first model the behaviour of an 80μm particle with density 3.73 gcm^{-3}, particle was modeled. The coefficient of restitution, which describes the amount of energy lost by the particle upon impact with the mould surface, was assumed to be 0.5. (A restitution coefficient of 0 means the particle would lose all of its energy when it touches the mould wall and a value of 1 means that the particle would retain all of its energy). A heat transfer coefficient of 10,000 $W.m^{-2}.K^{-1}$ was used to describe the heat transfer between the Lensalloy-136 and the smooth Perspex™ mould surface. Table 15 is a summary of the parameters used in this simulation.

Finally, a series of models were carried out to investigate the effects of variations in modelling parameters that were believed to have an impact on the predicted particle's path and its final location. These parameters were the coefficient of restitution and the particle initial position. Table 16 shows the variations investigated.

Table 15 The thermophysical properties of Lensalloy-136 and the modelling parameters used to model the Lensalloy casting using Flow-3D™

Flow-3D™ Modelling Parameters		
Physics	Heat Transfer	Second Order, Full energy equation
	Particle	Diameter 80E-6 m, Density 3730 $Kg.m^{-3}$
	Coefficient of Restitution	0.5
	Drag Coefficient	1
	Dynamic Viscosity	0.0024 Pa.s
Fluid	Density	8800 $Kg.m^{-3}$
	Specific Heat Capacity	133.9 $Joule.Kg^{-1}.K^{-1}$
	Thermal Conductivity	36 $Watt.m^{-1}.K^{-1}$
	Surface Tension coefficient	0.4 $Newton.m^{-1}$
	Contact angle	160^{o}
	Liquidus Temp	331 K
	Solidus Temp	331 K
	Latent Heat of Fusion	18608 $Joule.Kg^{-1}$
	Turbulent Length (TLEN)	0.35 mm
Perspex™ Mould	Heat Transfer Coefficient	10,000 $Watt.m^{-2}.K^{-1}$
	Thermal Conductivity	0.19 $Watt.m^{-1}.K^{-1}$
	Density*Specific Heat Capacity	1.764e6 $Joule.m^{-3}.K^{-1}$
	Initial Temperature	293 K
Boundaries	Stagnation Pressure	1771.2 Pa

Table 16. The variations made to the Flow-3D™ models of the Lensalloy-136 casting.

Variable	Values
Coefficient of restitution	-1, 0, 0.5
Initial particle position	± 1 mm in the X and Y directions.

Chapter 4
RESULTS

4.0 Results Summary

The results chapter contains particle tracking results, mathematical modelling results and the results obtained from auxiliary experiments that were carried out to clarify / validate the tracking and modelling results. Particle tracking results have been split into 2 categories, static and moving particles. The static particle tracking results will be described for sand castings and investment castings respectively, while commenting on the effects of various experimental variables such as the use of ceramic foam filters, different particle sizes and particle density. Dynamic particle tracking results, which were carried out using low melting point alloys, will also be described in a similar manner. Finally the multiple particle tracking results will be described both for steel (static) and the low melting point alloy (dynamic).

Mathematical modelling of the experiment has also been split into 2 sections, for MAGMAsoft™ and Flow-3D™, respectively. The effects of the various thermophysical properties on a particle's path, and the accuracy required to model a particle's movement in a casting have been examined.

Results obtained from auxiliary experiments using X-Rays to monitor the filling by aluminium of a sand moulded plate casting; and from experiments to locate and verify tracked particles using SEM and EDX are presented at the end of this chapter.

4.1 Final Particle Locations in Steel Sand Castings:

The particle tracking results obtained for the two sand cast plates, are shown in figures 60 and 61 respectively, with an isometric view shown to clearly illustrate the final location of the entrained particles. Each point shown in the figures represents an estimated position of the entrained particle in the casting, with respect to the location of a reference particle, placed at a known position. As the reference particle was moved to a new position on the casting, repeated 5 times for every casting, a new estimated position for the radioactive particle inside the casting was obtained.

Figure 60 suggests that the particle came to rest half way along the runner bar, confirmed using a Geiger counter after the casting cooled down. The particle location results, however, show 3 unrealistic, spurious points (in red) that indicate that the particle came to rest outside the body of the casting. The recorded error obtained from the PEPT camera data was an average of ± 2.5 mm in the X, Y and Z directions. Figure 61 shows the results obtained from the second plate, which were similar with the particle again coming to rest half way along the runner bar. Again spurious points (in red) were found. The recorded error in the particle location was an average of ± 2.4 mm in the X, Y and Z directions.

This suggests that, in both castings, the particles moved down the downsprue with the liquid metal and became trapped along the left hand side of the runner bar, at the mould wall. One explanation as to why the particles did not reach the cast plate could be that, due to the high temperature at which the steel was cast, the liquid metal evolved a large amount of gas, from the burning / evaporating of the resin binder. These gas bubbles could have affected the

particle path because, as they were trying to escape from the mould cavity, they may have pushed the particles towards the mould wall. Both castings showed good reproducibility with a similar final particle location.

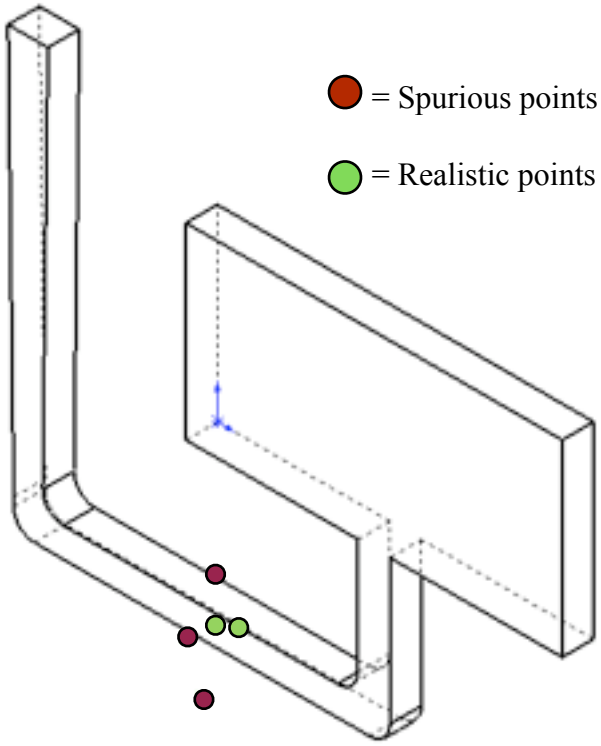

Figure 60. An isometric view of the sand cast plate A, showing the particle's final location halfway along the runner bar. Note: Spurious points were shown in red while realistic points which were shown in green.

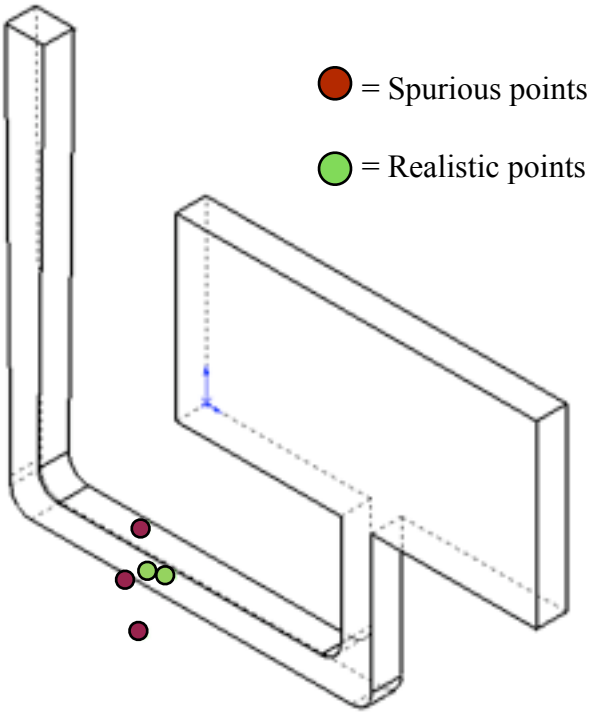

Figure 61. An isometric view of the sand cast plate B showing the particle's final location halfway along the runner bar. Note: Spurious points were shown in red while realistic points were shown in green.

4.2 Final Particle Locations in Steel Investment Castings:

To avoid the problem of gas evolution, moulds were made using the investment casting process, and cast with steel. Experiments were carried out to assess the effects of different experimental variables on the final particle location, as well as to develop the experimental technique. The first experiment to be carried out used an alumina particle placed at the centre of the downsprue opening, and became the baseline test of this technique. The effects of changing the initial position of the alumina particle on its final position were then studied. The effect of using a ceramic foam filter was also investigated, as well as the effect of varying the radioactive particle size and density.

4.2.1 Particles Placed at The Centre of The Downsprue Opening - Baseline Casting

Figures 62 and 63 show the particle positions for the casting where an alumina particle was placed at the centre of the sprue opening. The results shown in figure 62 show a significant scatter in the predicted particle position, where the particle came to rest, centrally in the cast plate, somewhere between the 3 scattered points shown in this location. This scatter was an error that occurred due to the method employed to handle the reference particles. Two of these points were outside the body of the casting, which was found to be an error due to the attenuation of the ɣ-rays as will be explained in more detail in section 5.4.1.

The reference particles were glued to pins which were then held in position using Bluetack™ which meant that the reference particle was up to 10mm away from where it was supposed to be (due to the thickness of the Bluetack™) which significantly increased the errors in the determined particle location. This type of error was found to affect the accuracy of the results obtained from experiments carried out in the early stages of developing the technique and the method used to handle the reference particles was therefore improved in later experiments. The 2 points recorded to be in the bottom left corner of the plate are a result of leaving behind a reference particle in this position.

Figure 63 shows a more accurate result where 3 of the points obtained, lay within a 20mm x 20 mm x 10 mm cube at the top right hand corner of the plate. This is one of the more accurate results obtained as this experiment was carried out at a later stage of the development of the technique, after some of the sources of error were identified. The final locations of the

alumina particles showed the randomness of the process and that it is a matter of running system design and casting practice, where the particle's movement stops. The estimated final particle locations were also approximately verified using a Geiger counter.

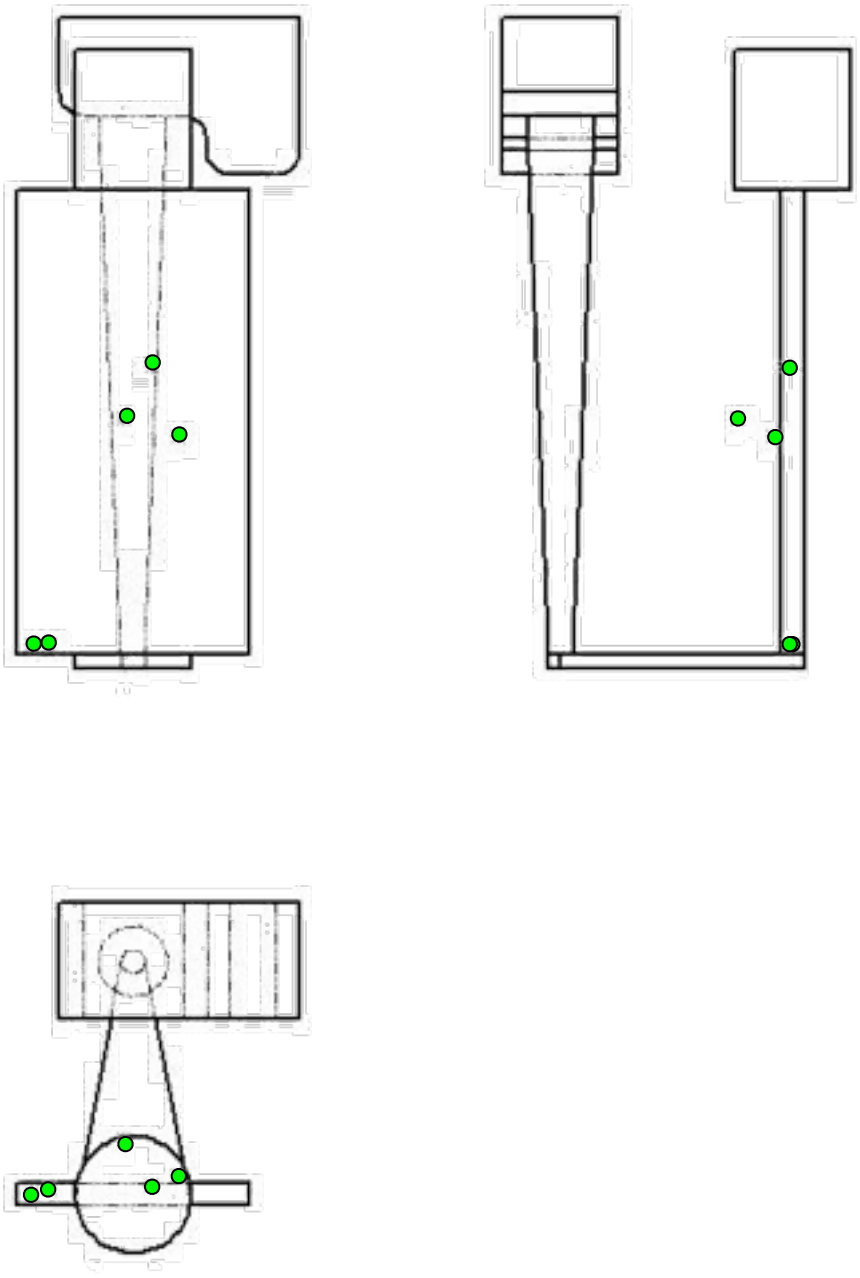

Figure 62. Three engineering views showing the final particle location, determined using PEPT, when a directly irradiated Al2O3 particle (38.8µCi) was initially placed at the centre of the sprue opening. En3B steel was cast at 1723°C.

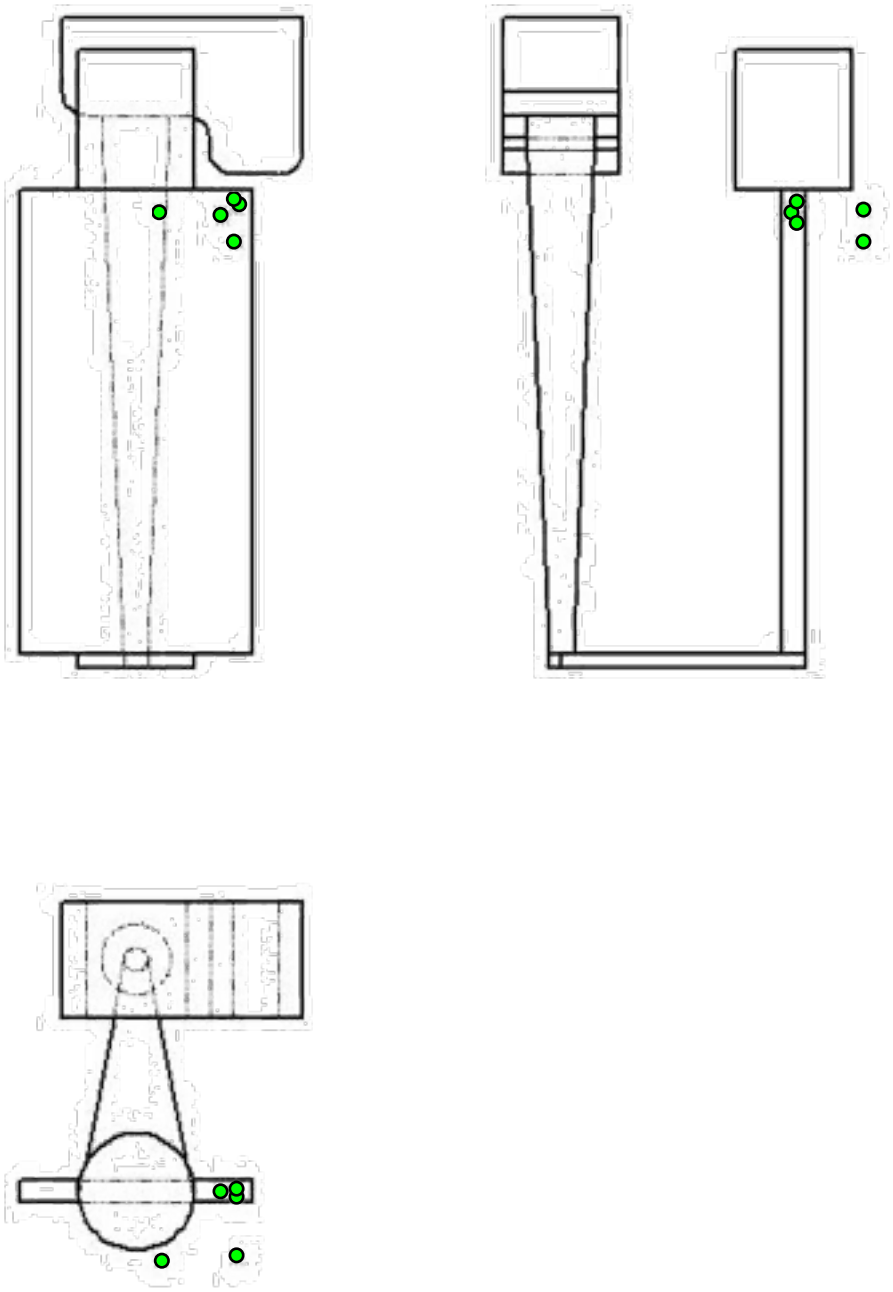

Figure 63. Three engineering views showing the final particle location, determined using PEPT, when a directly irradiated Al_2O_3 particle (11μCi) initially placed at the centre of the sprue opening. En3B steel was cast at 1706°C. (A later experiment)

4.2.2 The Effect of Changing The Particle's Initial Position

Figure 64 shows the results obtained when the particle's initial position was changed from the centre of the downsprue opening to its edge (The downsprue opening was 30 mm in

diameter). In this case 3 of the points obtained for the final particle position were in agreement. Two points were found to be outside the casting with one being very far from the detected particle location in the cast plate, near the downsprue. This spurious point could be due to a corrupt event as will be explained later in the discussion section. Changing the initial particle position by 1mm resulted in a different final particle location, which demonstrates the practical difficulty in reproducing the castings.

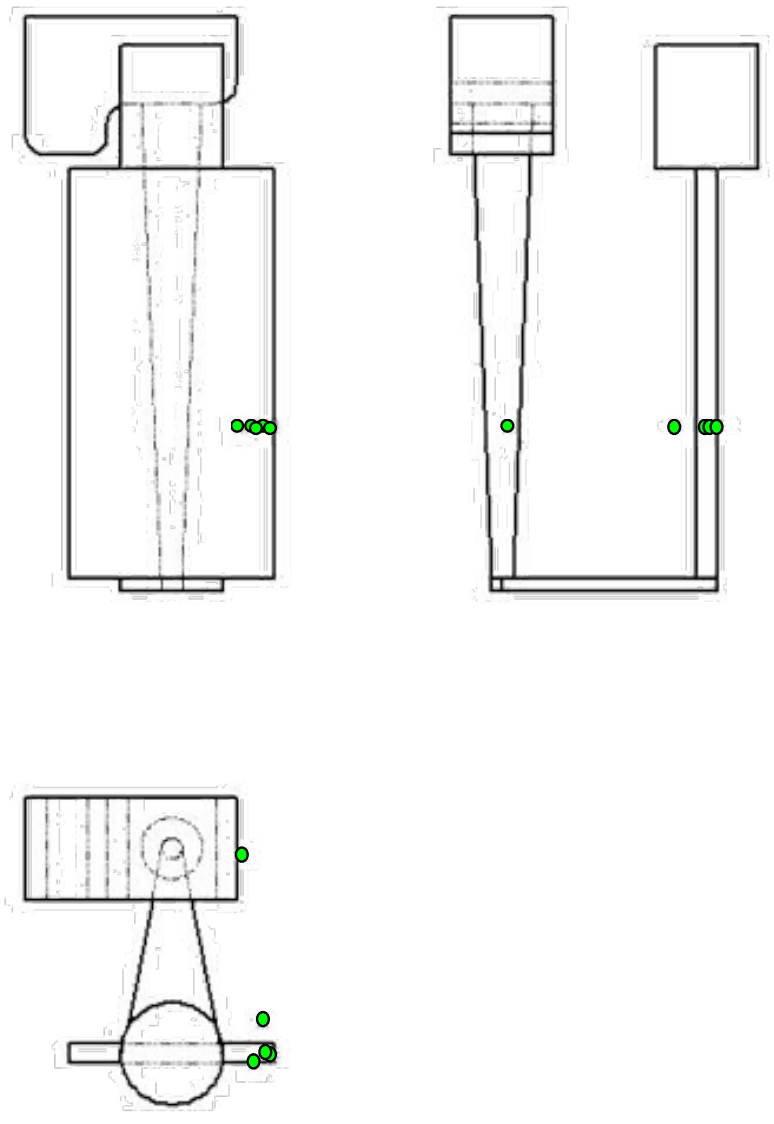

Figure 64. Three engineering views showing the final particle location, determined using PEPT, when a directly irradiated Al_2O_3 particle (56µCi) initially placed at the edge of sprue opening, which was 15 mm away from the centre. En3B was cast at 1732°C.

4.2.3 The Effect of Using Ceramic Foam Filters

Figures 65-67 show the final particle positions obtained for castings where the alumina particle was placed at the centre of the sprue opening and a ceramic foam filter was used. Figure 65 is the result obtained when a 20 mm thick, 10ppi filter was used. The final location of the particle was within the pouring basin, and could not be determined, due to the limited ability of the γ-rays to penetrate large steel thicknesses. This experiment was repeated using a different ceramic filter (15 mm thick 10 ppi) and the results obtained are shown in figures 66 and 67, where the particle again remained in the pouring basin.

One interpretation of these results could be that the particle followed the metal flow as it was advancing through the mould, but when this was slowed by the filter, the particles rose back up the downsprue and came to rest somewhere in the pouring basin. Another interpretation is that the particle did not enter the mould at all but floated into the pouring basin. The filters were successful in preventing the irradiated particles from coming to rest in the cast plate, but the exact method by which this was achieved could not be determined.

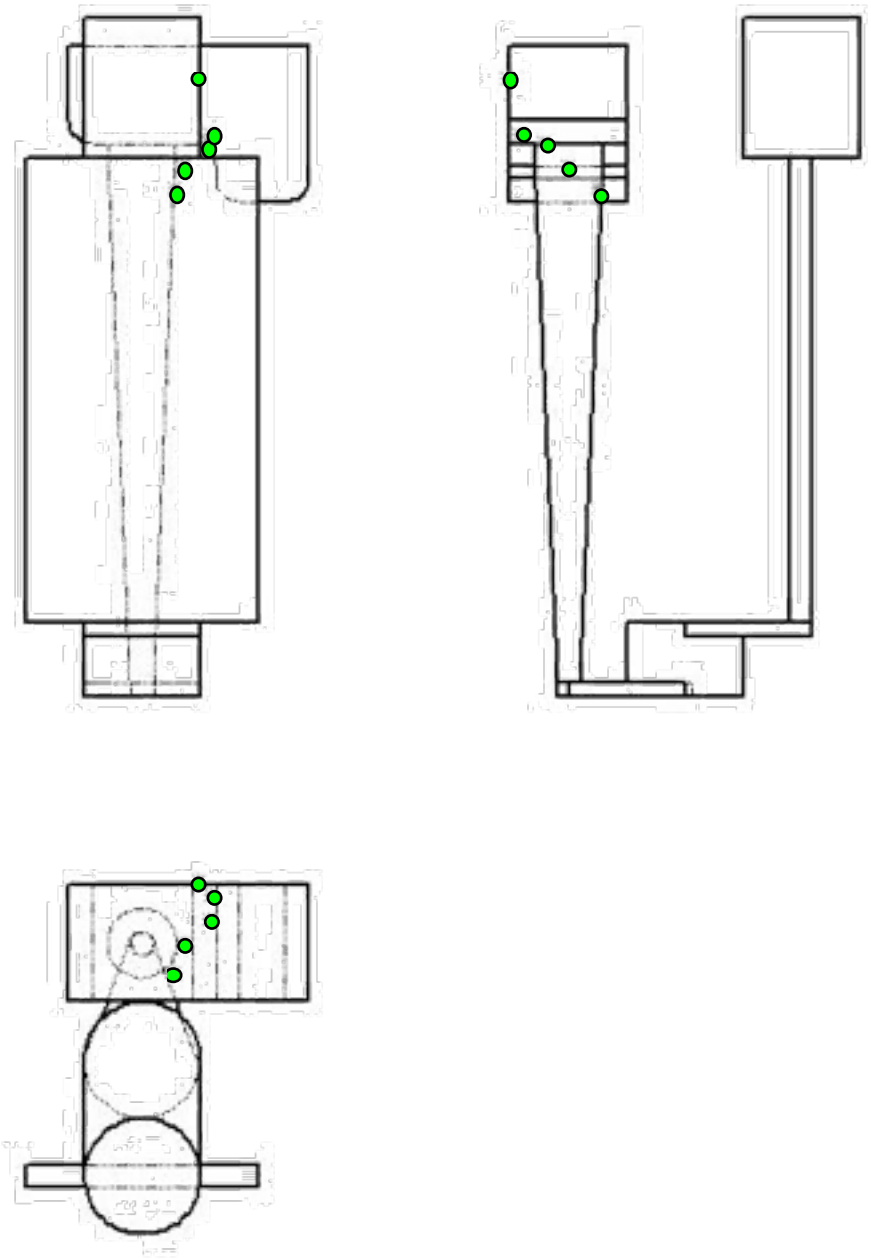

Figure 65. Three engineering views showing the final particle location, determined using PEPT, when a a 20 mm thick, 10ppi filter was used, average error ± 3.5mm. The particle was irradiated to 41µCi and En3B steel was cast at 1720°C.

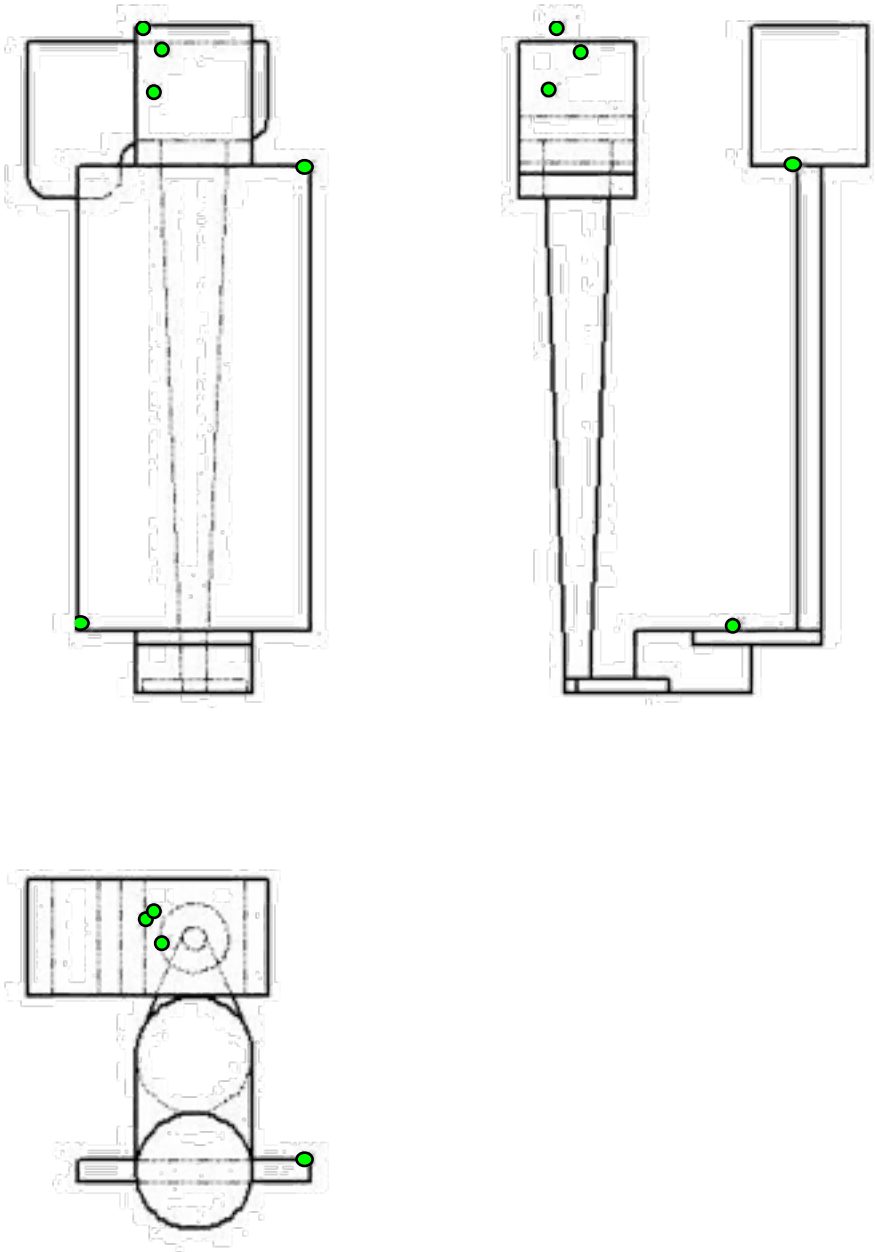

Figure 66. Three engineering views showing the final particle location, determined using PEPT, when a 15mm thick, 10ppi filter was used, average error ±6.2mm. The particle was irradiated to 26.6µCi and En3B steel was cast at 1752°C.

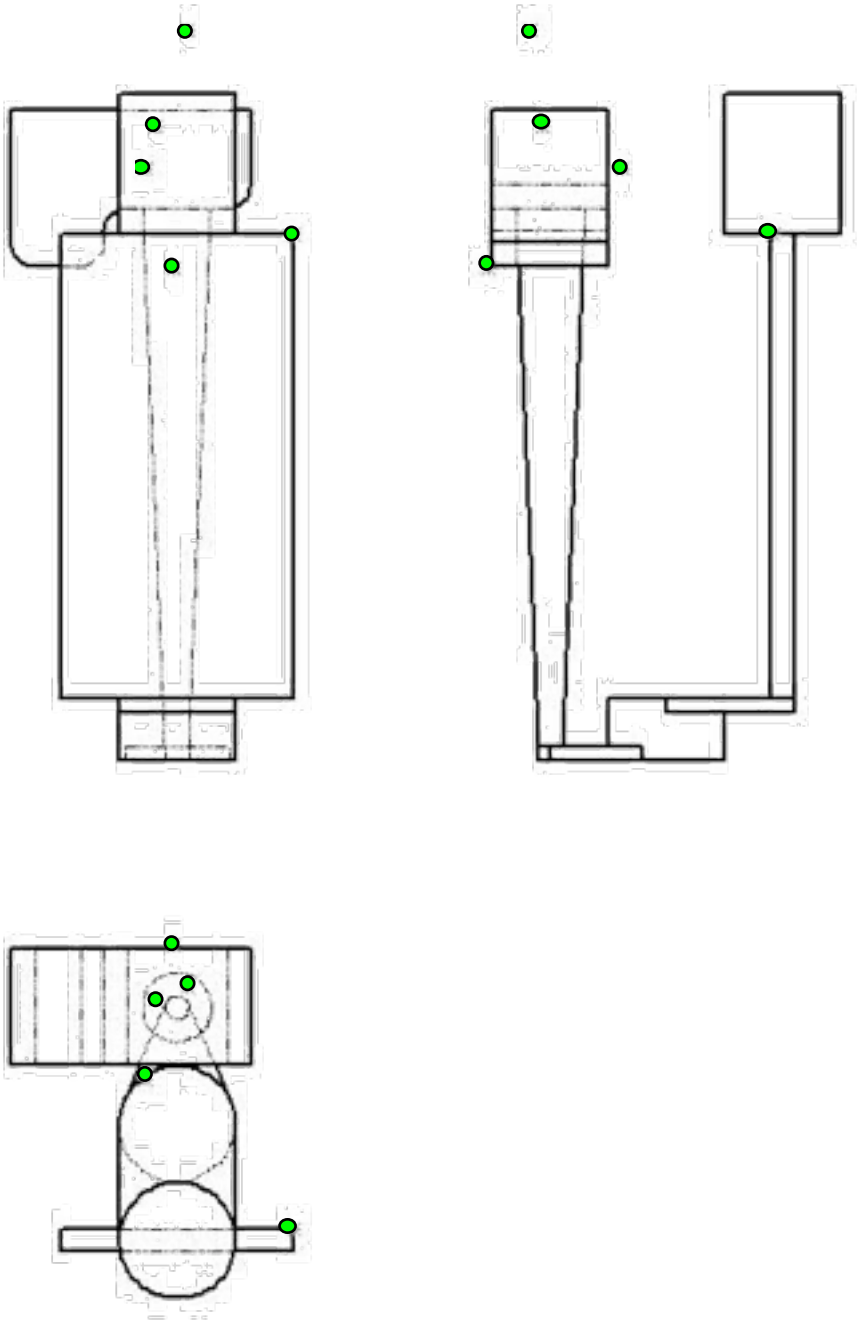

Figure 67. Three engineering views showing the final particle location, determined using PEPT, when a 15mm thick, 10ppi filter was used, average error ±6.5mm. The particle was irradiated to 24.3µCi and En3B steel was cast at 1752ºC.

4.2.4 The Effects of Changing Particle Density

The 2 castings shown in figures 68 and 69 were produced after placing a silica particle of size 355-425µm (density = 2.65 g/cm^3) at the centre of the downsprue opening, to compare with a denser, alumina particle (density = 3.7 g/cm^3) used in the baseline experiments.

Figure 68 showed that the final particle position was at the beginning of the runner bar and approximately in its centre. The 4 points obtained agreed very well. In comparison, the repeated experiment in figure 69 showed a different final location, with slightly less accuracy in the determined final particle location, which was roughly the centre of the cast plate.

It was reasonable to expect that the less dense silica particle would be likely to come to rest earlier in the running system, when compared to the baseline casting where the alumina particle was used, or higher up in the cast plate if it was forced into the plate by the metal flow. This was however contradicted by the result shown in figure 63 where the alumina particle came to rest at the top right hand corner of the cast plate.

Using the less dense silica particles resulted in different final particle positions when compared to the base line experiment but also showed different final particle locations when repeated. Therefore the effect of density could not be determined due to the lack of reproducibility and the randomness involved in the casting process, which will be discussed in more detail in the discussion section.

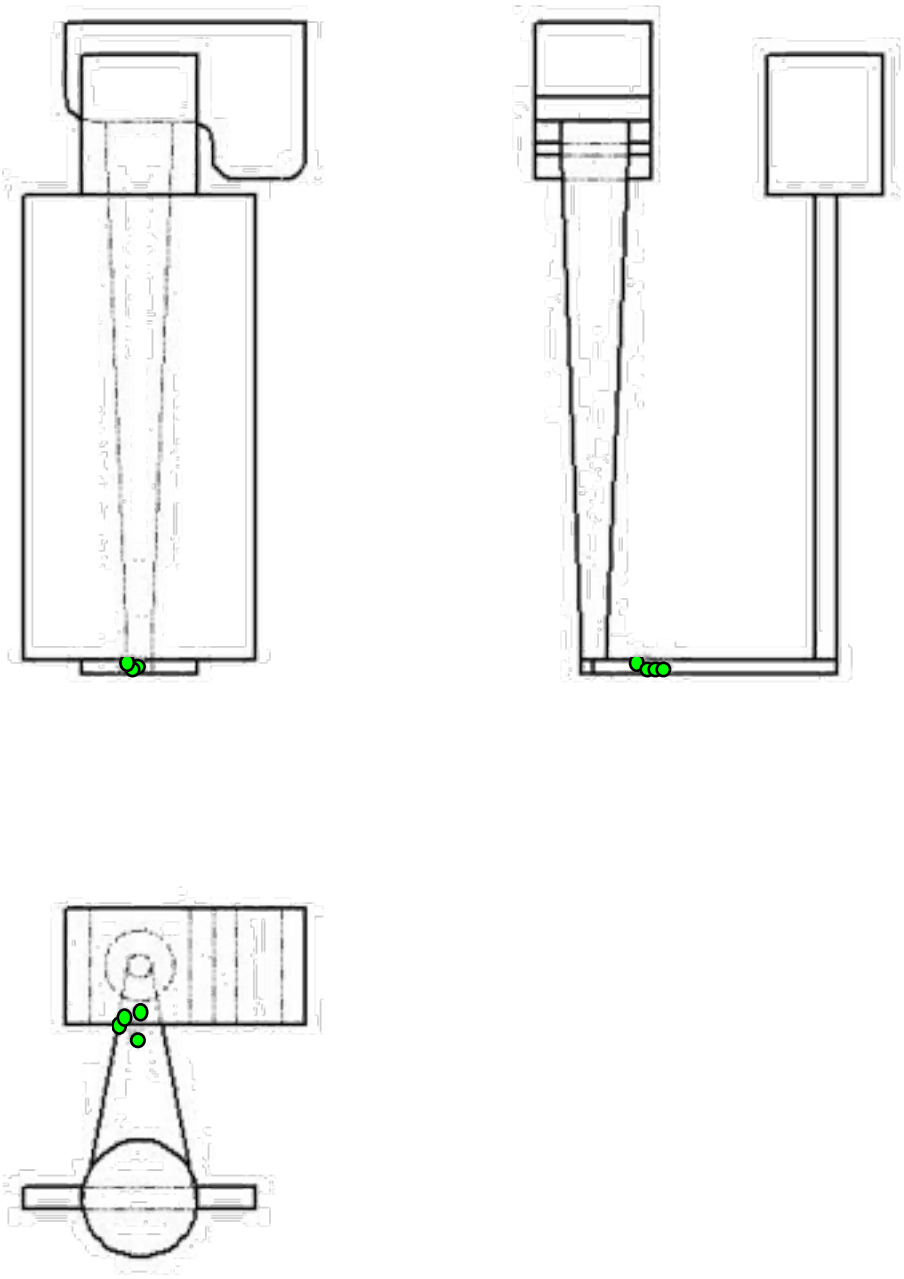

Figure 68. Three engineering views showing the final particle location, determined using PEPT, when a directly irradiated SiO_2 particle, initially placed at the centre of sprue opening.

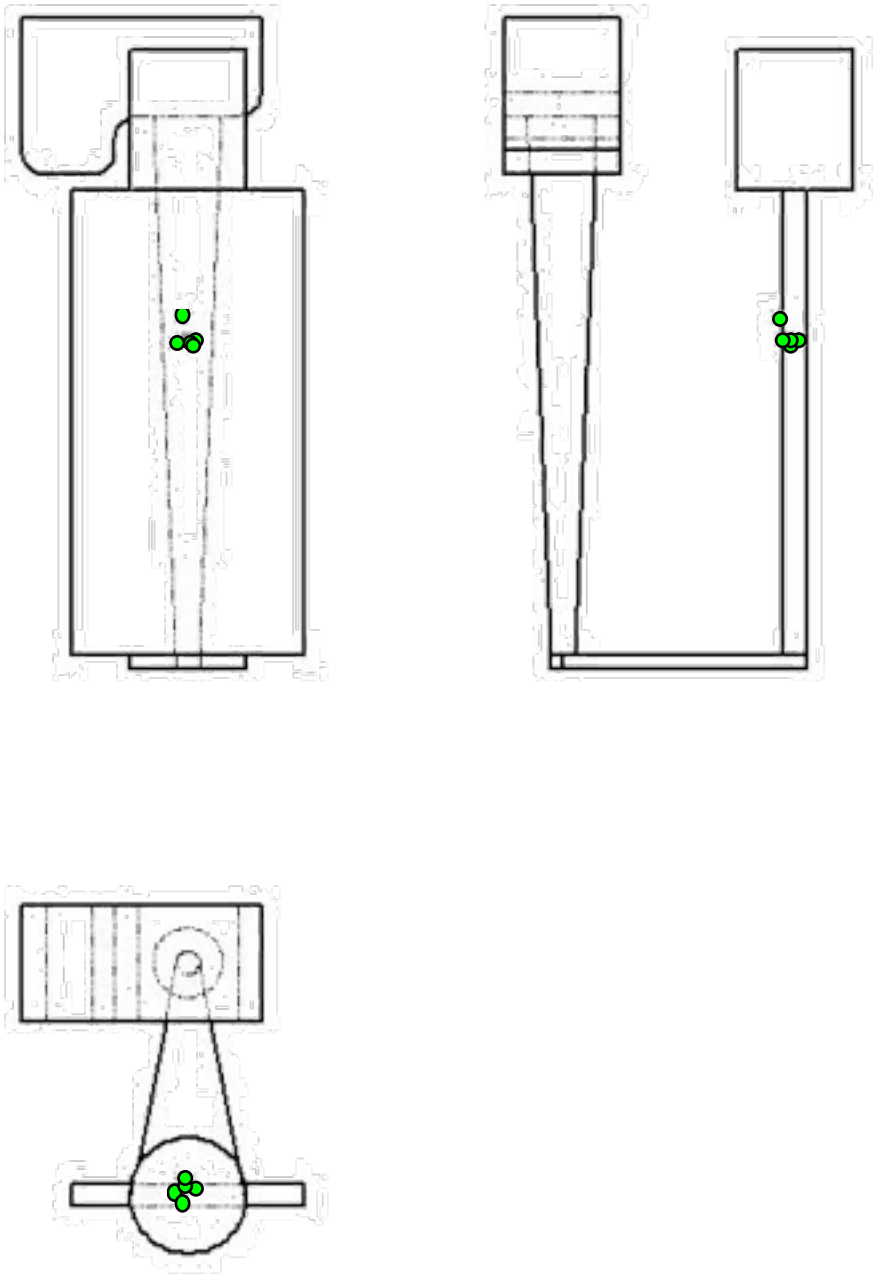

Figure 69. Three engineering views showing the final particle location, determined using PEPT, when a directly irradiated SiO_2 particle, initially placed at the centre of sprue opening.

4.2.5 The Effect of Using Particles of Different Size

The effect of particle size on the particles' final position was investigated by casting 2 moulds using alumina particles of sizes 450-560μm and 560-630μm respectively. The results from these experiments were then compared to the baseline experiment where an alumina particle of size range 355-425μm was used. Figure 70 shows the results from the casting with the 560-630 μm particle, which shows that the particle was in the pouring basin. The point shown at the top right hand corner of the plate, was due to a fragment of the reference particle that shattered when pressure was applied to fix it in position. The casting with, a 450-560 μm particle used a particle with radioactivity lower than that detectable by the positron cameras.

These experiments demonstrated that the larger particles, with sizes comparable to the exogenous inclusions that could occur due to mould or refractory erosion, are likely to remain or float out to the pouring basin and are therefore less critical than smaller particles.

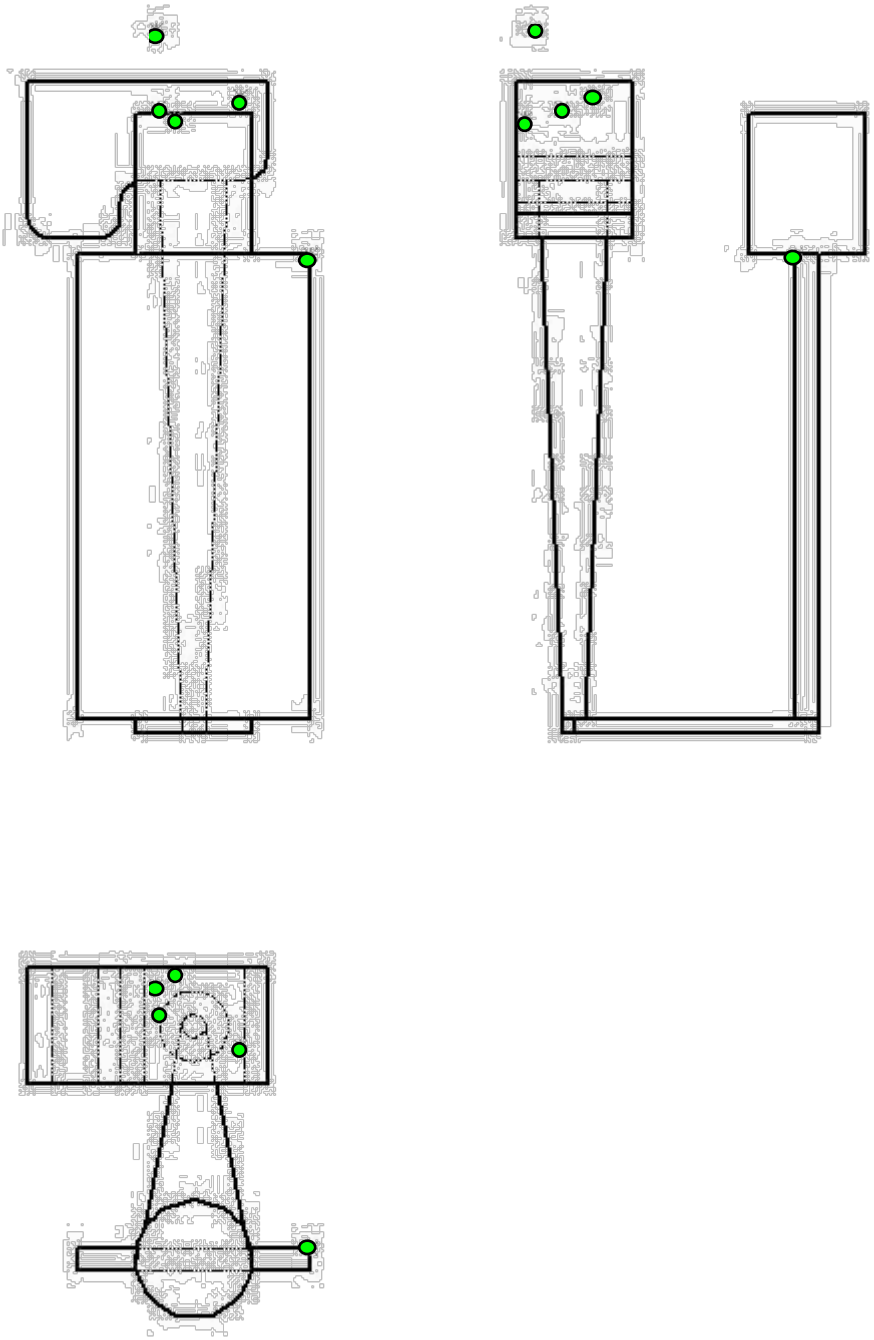

Figure 70. Three engineering views showing the final particle location, determined using PEPT, when a directly irradiated Al_2O_3 particle, 560-630 μm in diameter, initially placed at the centre of the sprue opening. The particle had a radioactivity of 111μCi and En3B steel was cast at 1752°C.

4.2.6 Errors and Particle Decay

The reported error in the final particle location coordinates, obtained for the investment castings has been shown in figure 71. These errors are the reported positron camera detection errors, and therefore additional experimental errors should be added to these values. The reported errors varied from 2.65 mm to 7.85 mm in the X, Y and Z directions. The largest errors were associated with earlier experiments, where the handling of the reference particles was being developed, or the castings where the particle final location was in the thicker pouring basin, where high attenuations were observed. The reported errors were generally reduced due to improvements in the experimental procedure, such as methods employed to handle the reference particles.

These errors were also found to be a function of the radioactivity of the particle being tracked. The error bars shown in figure 71, represents the standard deviation of the reported error for each experiment. In cases where the radioactivity was high, and there was a small degree of attenuation, the reported error was low and the standard deviation varied from 0.65-0.1 mm. The lower the particle radioactivity, the higher the reported error in the particle location. This applies to the castings shown in blue in figure 71, where the particles came to rest in the cast plate and were therefore subject to an acceptable degree of attenuation.

On the other hand, in cases where attenuation was high, such as when the particles came to rest in the thick pouring basin, (see green bars in figure 71), a high radioactivity of the particles did not improve the accuracy of the data. This was because of the large attenuation

of the ɣ-rays due to the thick pouring basin. In these cases the standard deviation varied between 0.4-1.3 mm.

When the particle came to rest in the runner bar, there was a low level of attenuation, the reported error was minimum, with a standard deviation of 0.05 mm, despite the low radioactivity of the particle.

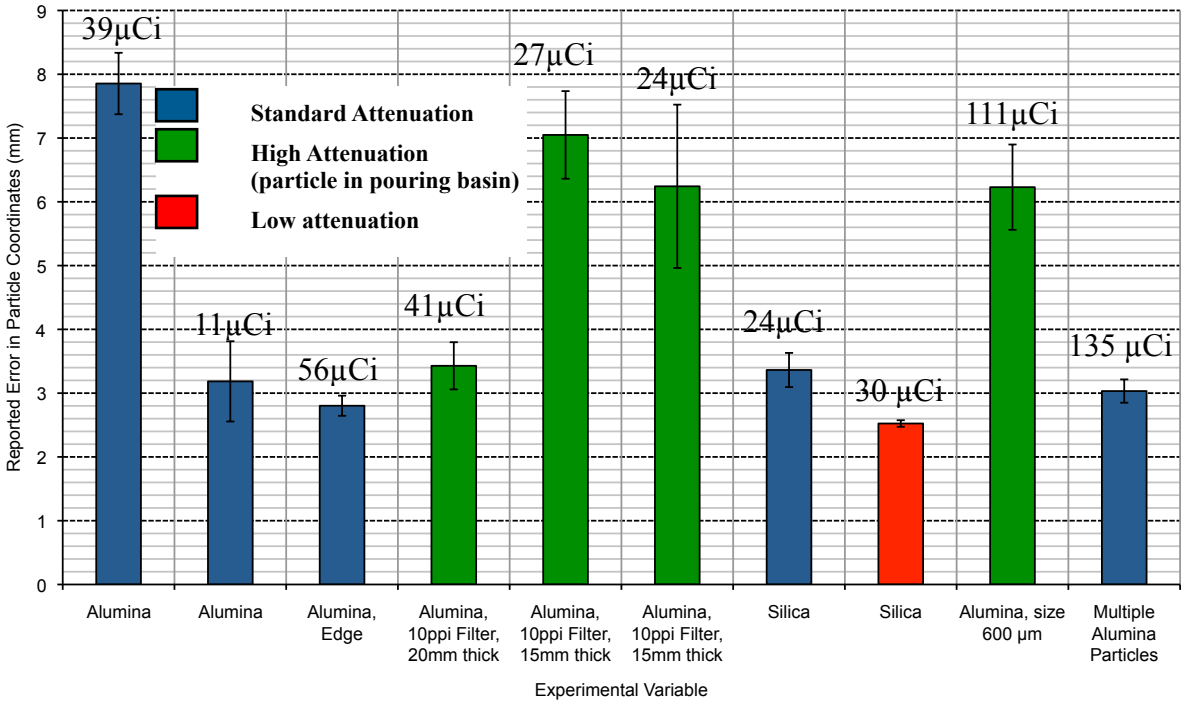

Figure 71. A graph showing the particle tracking errors recorded for the investment casting experiments. Note the bar representing the error obtained in a multiple particle experiment - this experiment will be described at a later section of this chapter.

The variation of accuracy in the particle position as reported by the positron camera as the radioactive particles decayed, was also investigated, and is shown in figures 72-74. This was achieved by placing a casting with a radioactive particle embedded within it, between the camera faces, and taking a reading of the particle's location every 20 minutes, for approximately 7 hours. Figures 72-74 showed no variation in the reported X, Y and Z coordinates as the particle decayed, and figure 75 also showed no variation in the recorded error of the particle position.

This showed that although the number of events recorded with time was declining rapidly as the particle decayed, the X, Y and Z coordinates showed negligible increase in error for the whole 7 hours. This meant that these experiments could be carried out with less time restrictions provided that the particle comes to rest in a thin section thickness. But the larger the metal thickness surrounding the particle, the quicker the particle would become undetectable and the larger the error.

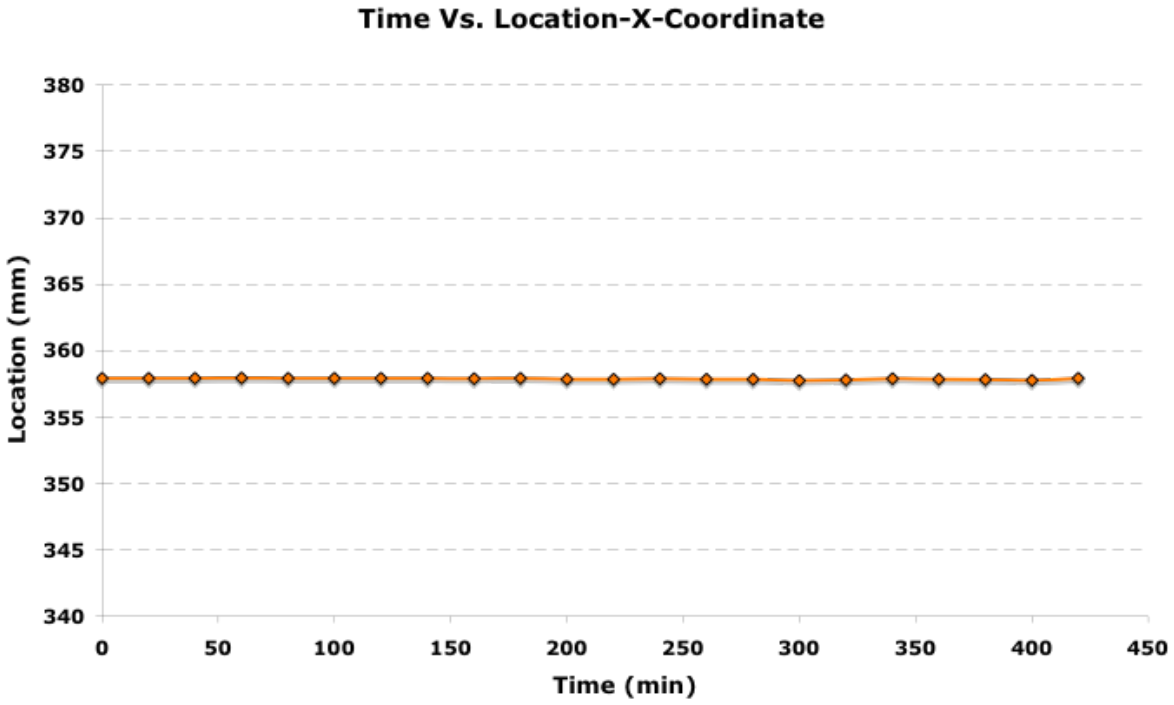

Figure 72. A graph showing the variation of the X-coordinates recorded for a stationary particle, embedded in a steel casting, in between the camera faces over 7 hours.

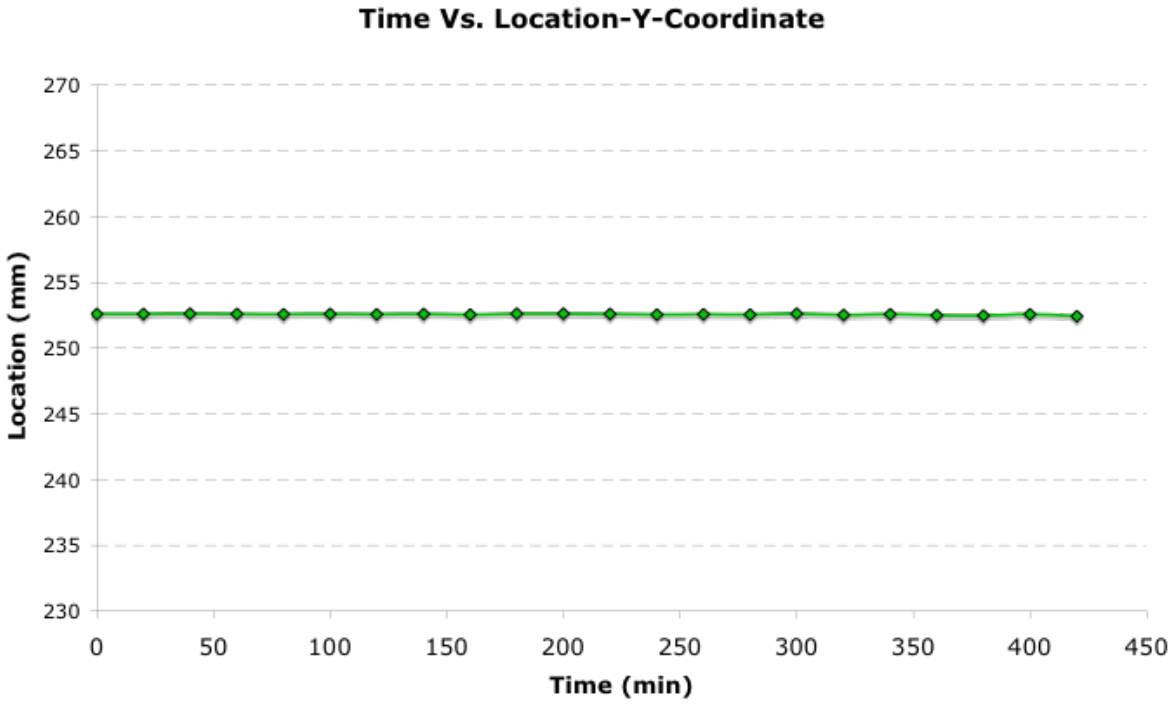

Figure 73. A graph showing the variation of the Y-coordinates recorded for a stationary particle, imbedded in a steel casting, in between the camera faces over 7 hours.

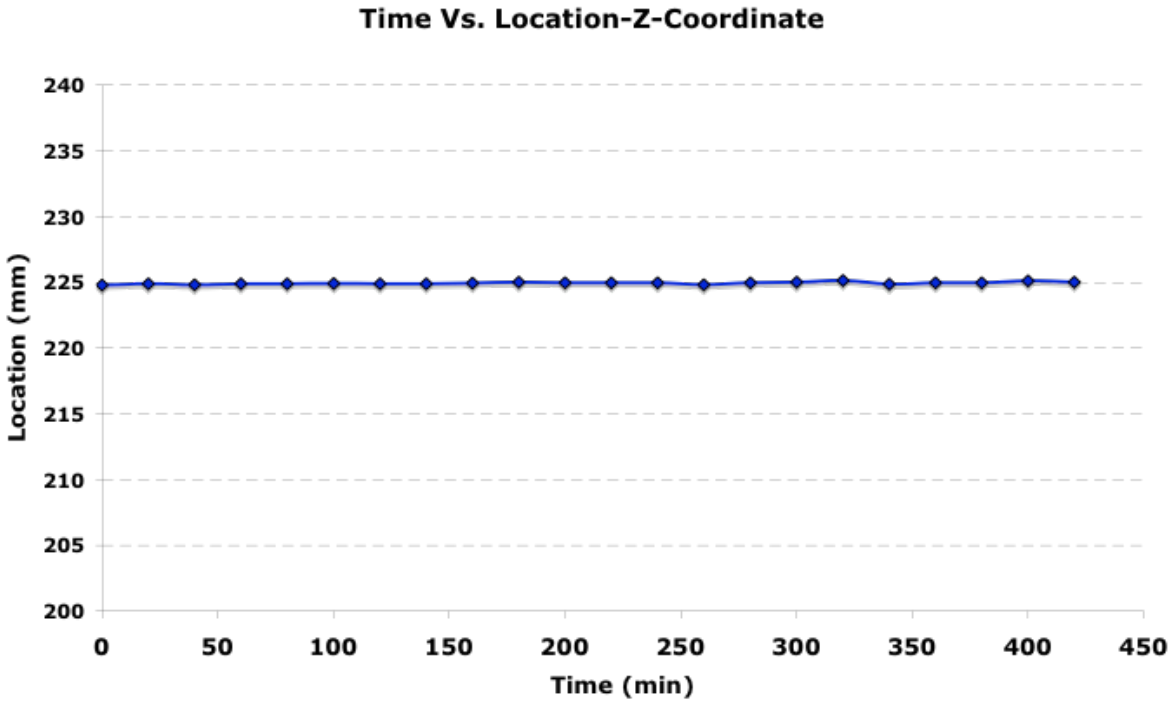

Figure 74. A graph showing the variation of the Z-coordinates recorded for a stationary particle, imbedded in a steel casting, in between the camera faces over 7 hours.

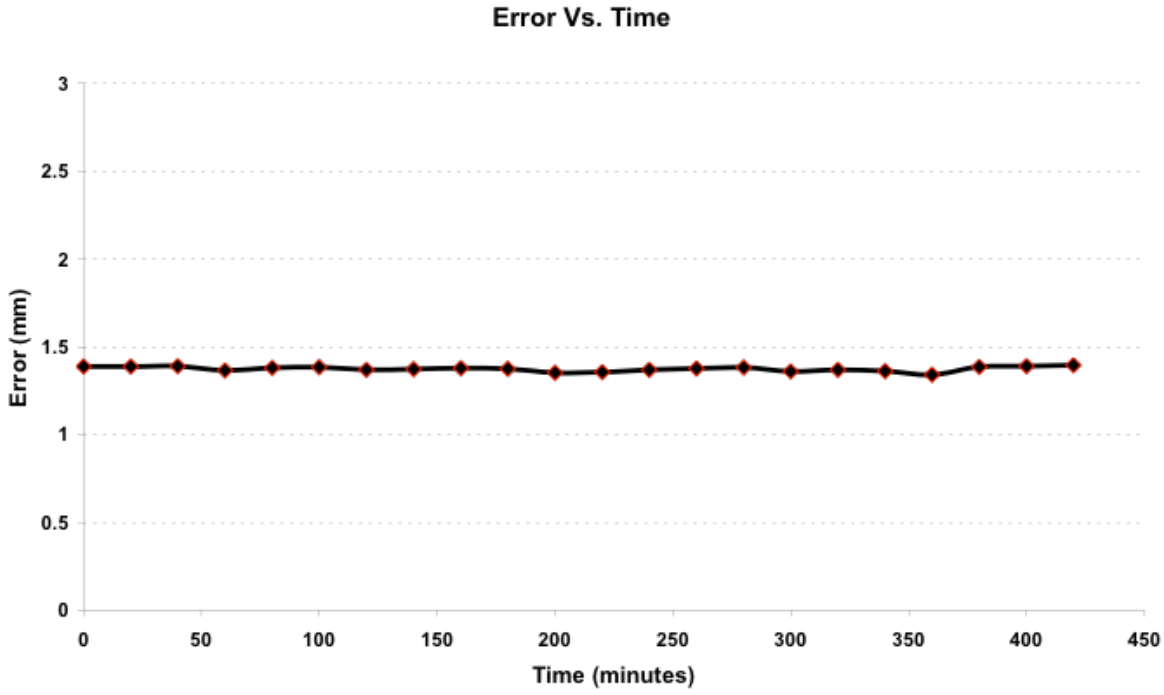

Figure 75. A graph showing the variation in the tracking errors recorded for a stationary particle, imbedded in a steel casting, in between the camera faces over 7 hours.

4.3 Mathematical Modelling of The Steel Castings using MAGMAsoft™

The plate geometry that was sand cast, see figure 34, was modelled using MAGMAsoft™. The reliability of the modelling results were assessed by investigating the sensitivity of the model to changes in the thermophysical properties. The effects of modelling the angled pouring and the pouring basin on the final particle location were also examined.

4.3.1 The effects of thermophysical properties on the final particle location

The results produced from the thermo-physical property assessment described earlier, have been summarised in figure 76 and are shown in detail in tables 17-22. Changes in the specific heat and thermal conductivity did not affect the particle path or final particle location. However, changes in density, viscosity, pouring temperature and the particle initial position (the vertical coordinate only) had a significant effect on the particle path and hence its final location. Figure 76 shows that reducing the density by 5% (table 17) had a similar effect to reducing the viscosity by 25% (table 19), where the particle came to rest near the top right hand corner of the plate. Increasing the viscosity by 25% resulted in the particle moving all the way to the top surface of the plate (table 20,b) and rapidly falling back with the bulk metal to the bottom left hand side surface of the plate (table 20,d). The particle then moved towards the left hand side wall (table 20,f) at which it started rising vertically upwards (table 20,h) where it looped around itself and came to rest at the left hand side of the plate (table 20,n).

When the pouring temperature was reduced, see figure 76 and table 21, the particle moved to the top surface of the plate (table 21,d), where it moved around (table 21,f-r) before it started

descending and coming to rest just on the left hand side of the plate (table 21,t). When the pouring temperature was increased to 1700^{o}C, see figure 76 and table 22, the particle moved near the top surface of the plate (table 22,d) and then came to rest further on the left hand side than it did when the pouring temperature was lower (table 22,t).

Finally, the particle final location was also changed when the initial position was lower by 1mm in the Y-axis (the vertical axis). The initial position was varied in the other coordinates, but no changes were observed in the final particle location in these models.

It was found that pouring temperature, density and viscosity were critical thermo-physical properties that had a direct effect on the fluid flow within the mould and consequently the final particle location. Note, that in all cases the predicted final particle location was different to that obtained experimentally, which was half way along the runner bar, as shown in figures 60 and 61. But this is probably attributable to the large amount of gas that evolved during casting (due to the resin) that was not modelled in this assessment.

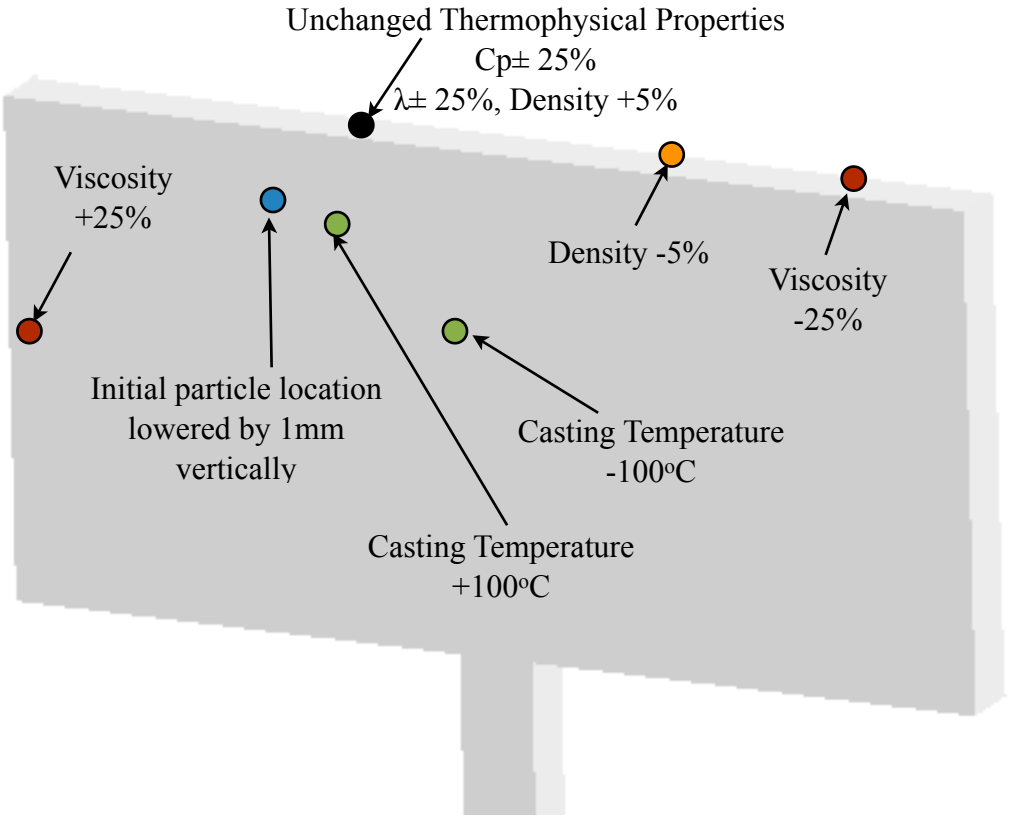

Figure 76. A schematic diagram showing the obtained final particle locations from each simulation, superimposed on the same casting for comparison.

Table 17. MAGMAsoft™ results showing the effect of reducing the density of steel by 5%, on the predicted particle path.

Density -5%	
Mould Filling	Particle Path
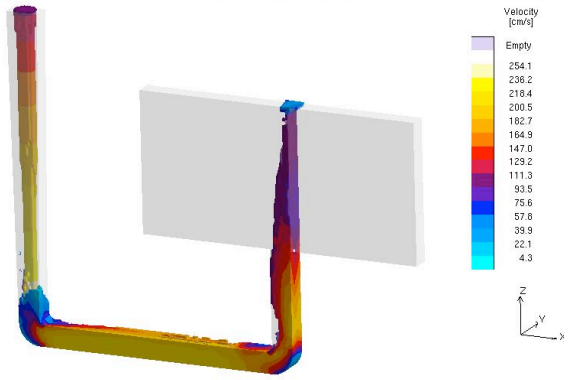	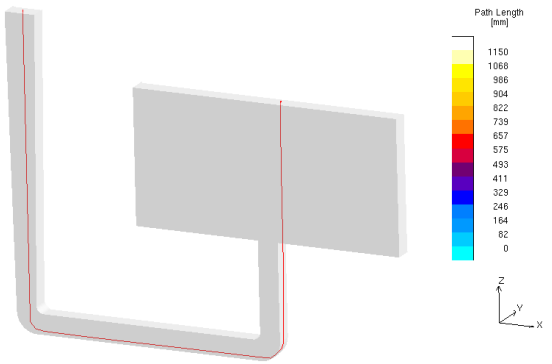
A) Fluid flow at filling time, 473 ms	**B) Particle path at filling time, 473 ms**
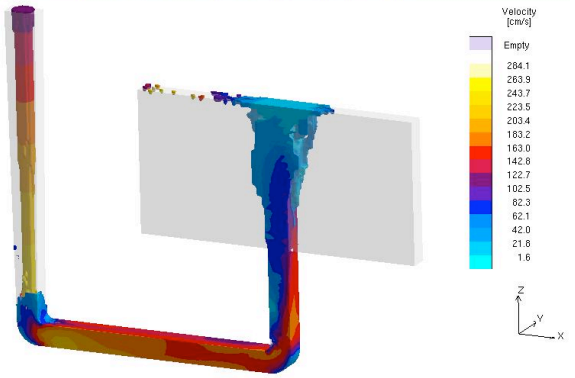	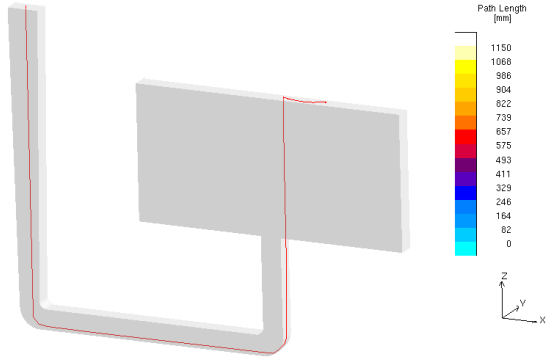
C) Fluid flow at filling time, 715 ms	**D) Particle path at filling time, 715 ms**
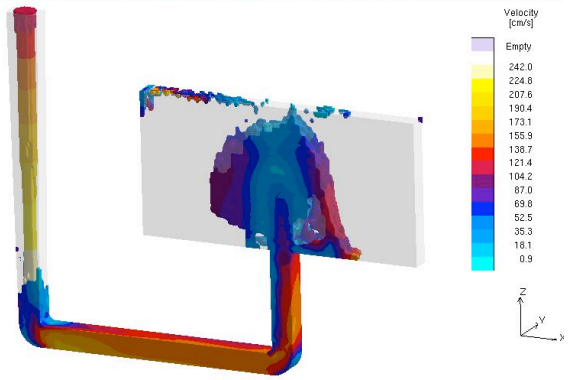	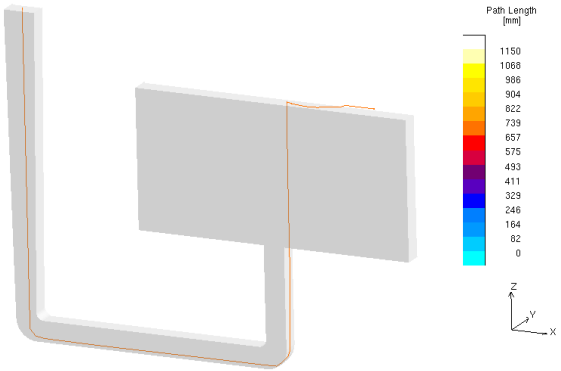
E) Fluid flow at filling time, 959 ms	**F) Particle path at filling time, 959 ms**

Density -5%	
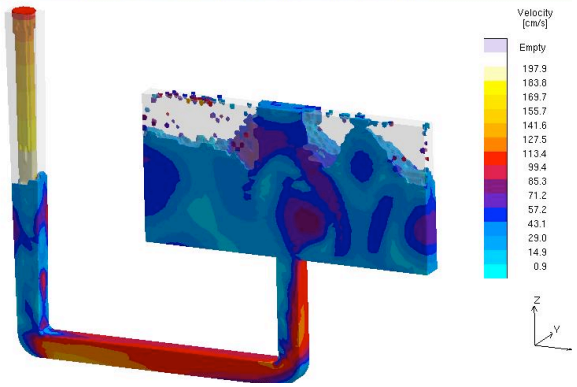	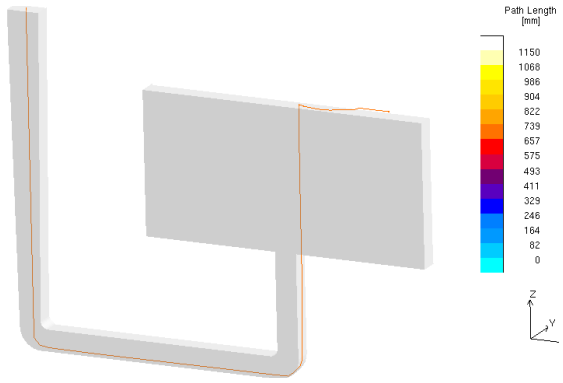
G) Fluid flow at filling time, 1930 ms	**H) Particle path at filling time, 1930 ms**
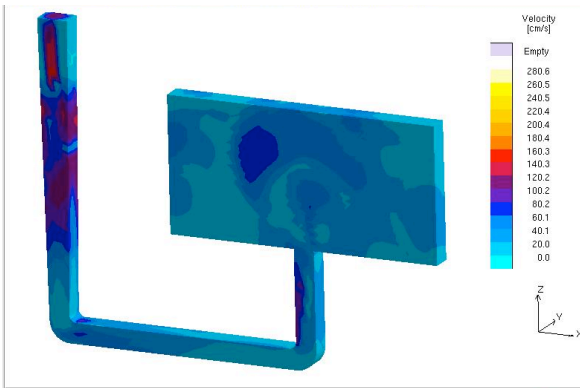	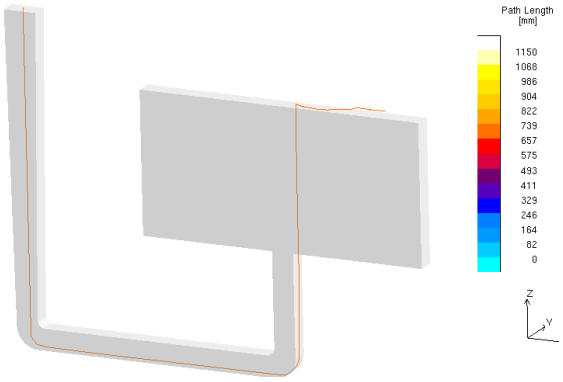
I) Fluid flow at filling time, 2415 ms	**J) Particle path at filling time, 2415 ms**

Table 18. MAGMAsoft™ results showing the effect of increasing the density of steel by 5%, on the predicted particle path.

Density +5%	
Mould Filling	Particle Path
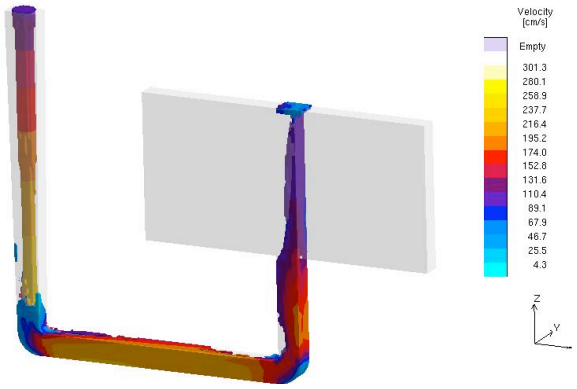	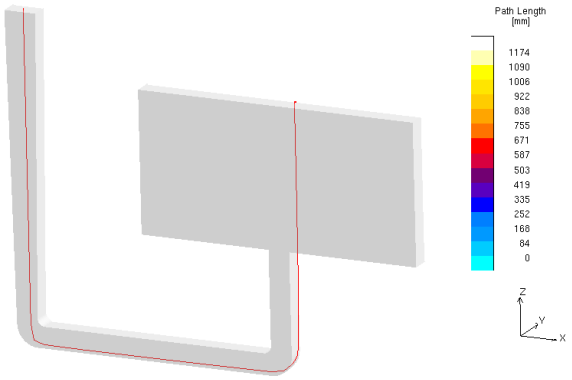
A) Fluid flow at filling time, 485 ms	**B) Particle path at filling time, 485ms**
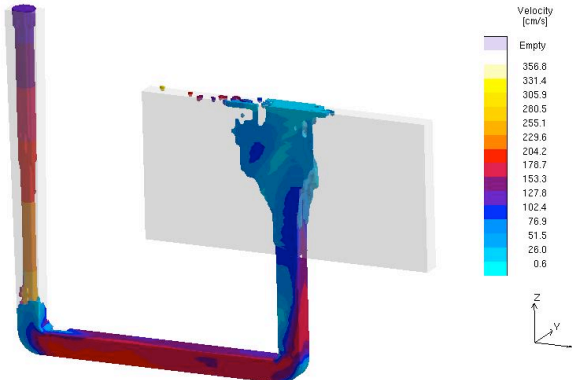	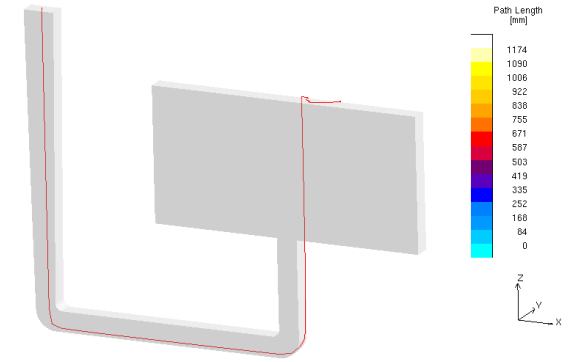
C) Fluid flow at filling time, 883 ms	**D) Particle path at filling time, 883ms**
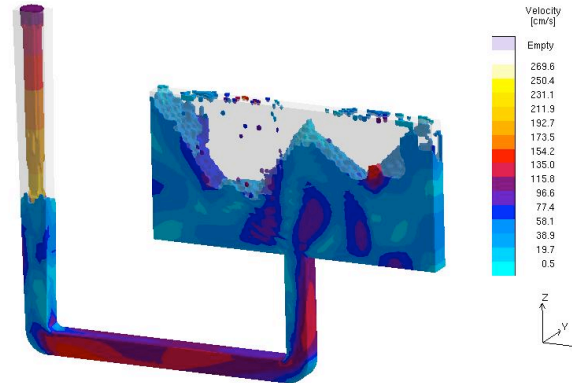	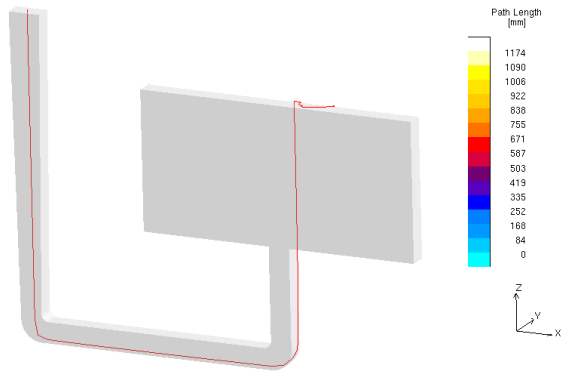
E) Fluid flow at filling time, 1822 ms	**F) Particle path at filling time, 1822ms**

Density +5%	
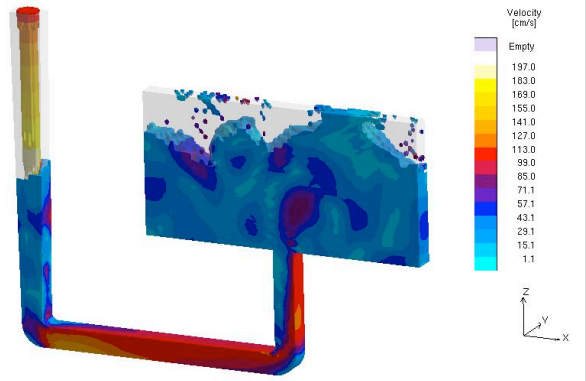	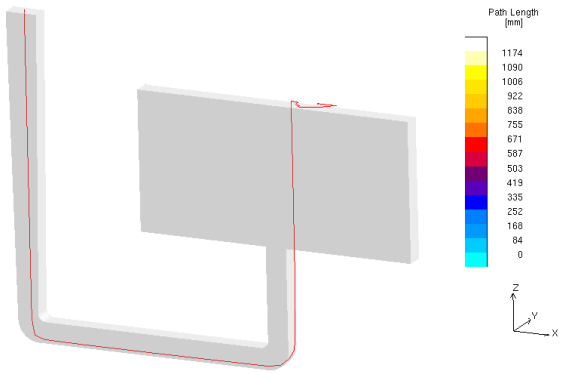
G) Fluid flow at filling time, 1980s	**H) Particle path at filling time, 1980ms**
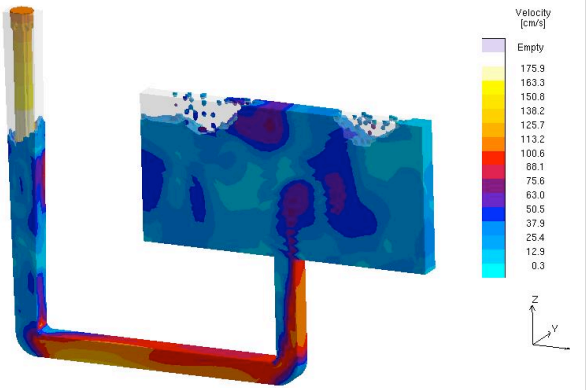	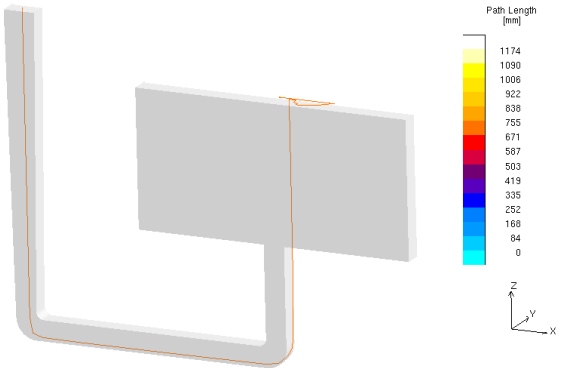
I) Fluid flow at filling time, 2229 ms	**J) Particle path at filling time, 2229ms**
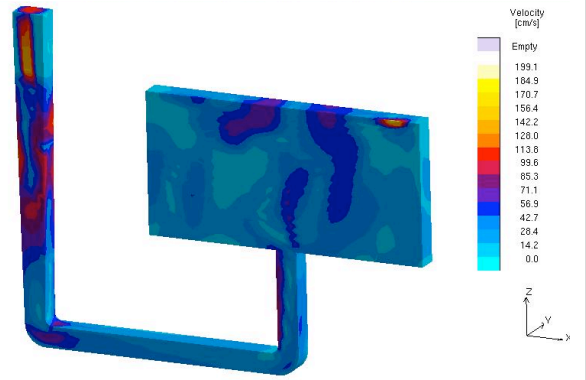	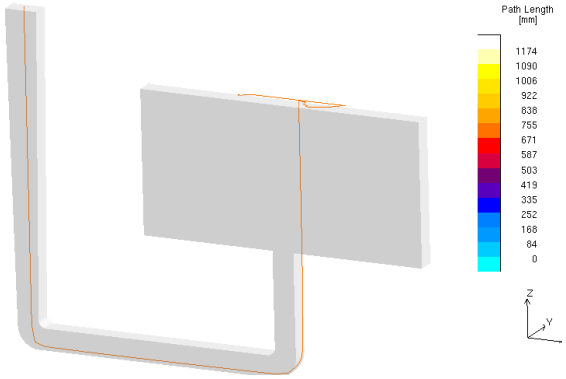
K) Fluid flow at filling time, 2478 ms	**L) Particle path at filling time, 2478ms**

Table 19 MAGMAsoft™ results showing the effect of reducing the viscosity of steel by 25%, on the predicted particle path.

Viscosity -25%	
Mould Filling	Particle Path
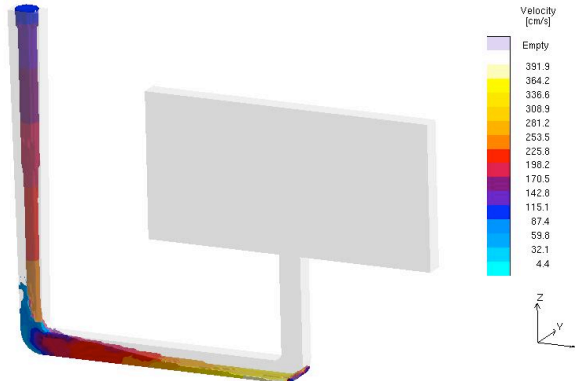	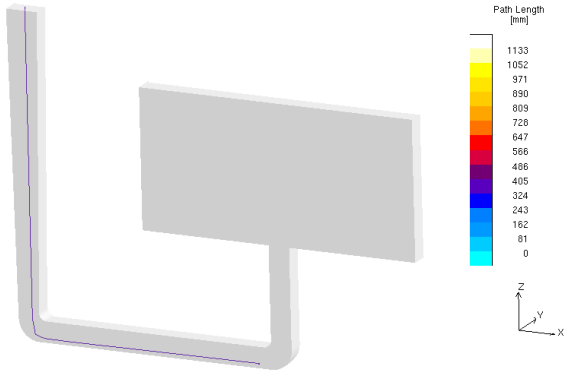
A) Fluid flow at filling time, 236 ms	**B) Particle path at filling time, 236**
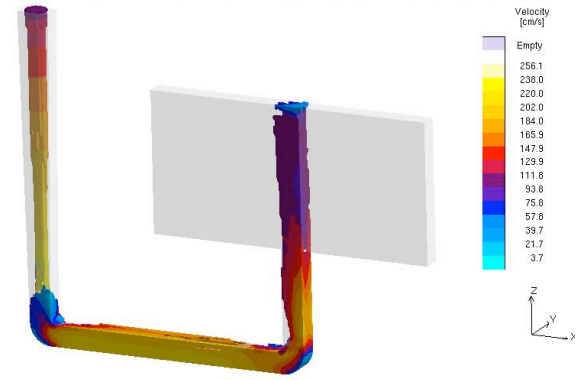	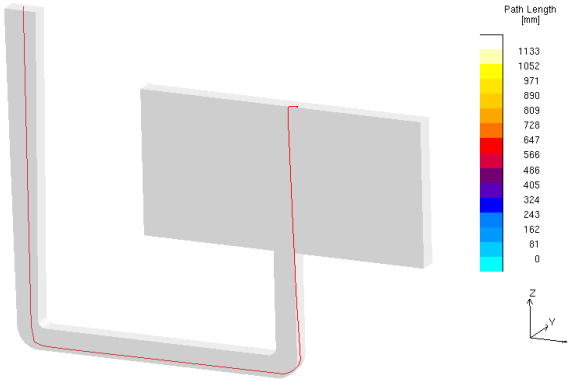
C) Fluid flow at filling time, 485 ms	**D) Particle path at filling time, 485ms**
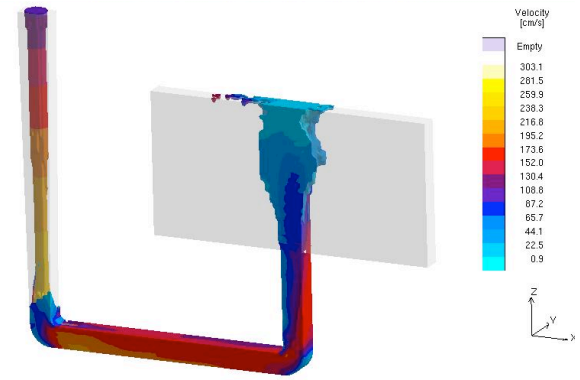	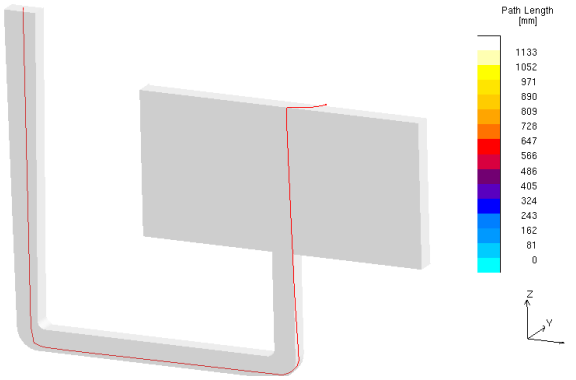
E) Fluid flow at filling time, 734 ms	**F) Particle path at filling time, 734ms**

Viscosity -25%	
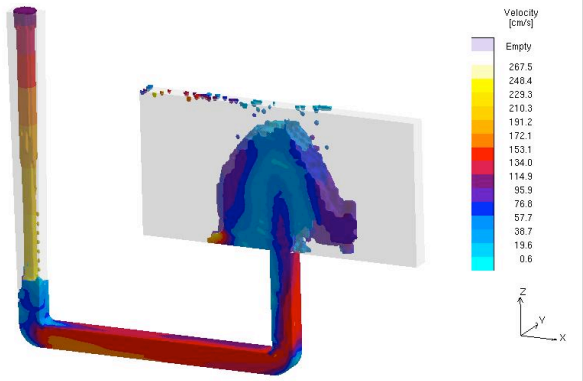	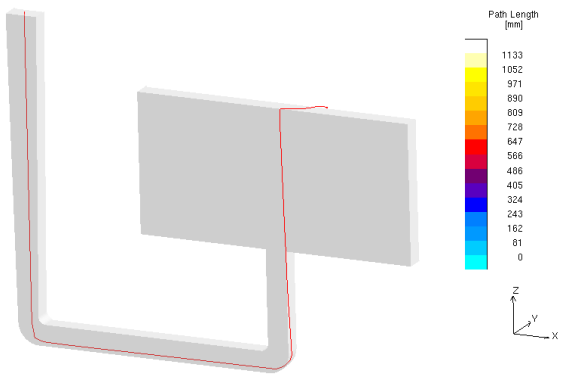
G) Fluid flow at filling time, 984 ms	**H) Particle path at filling time, 984ms**
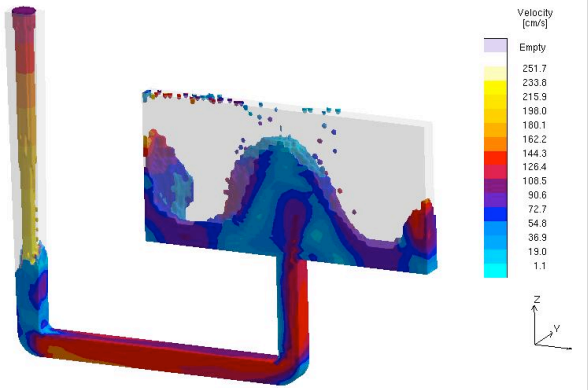	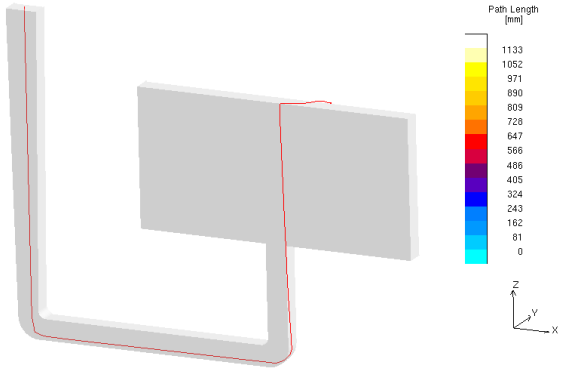
I) Fluid flow at filling time, 1232 ms	**J) Particle path at filling time, 1232ms**
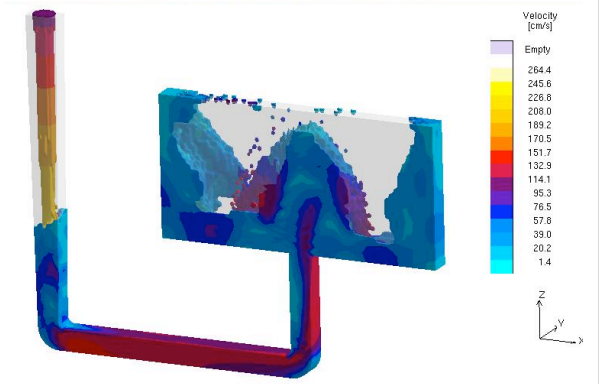	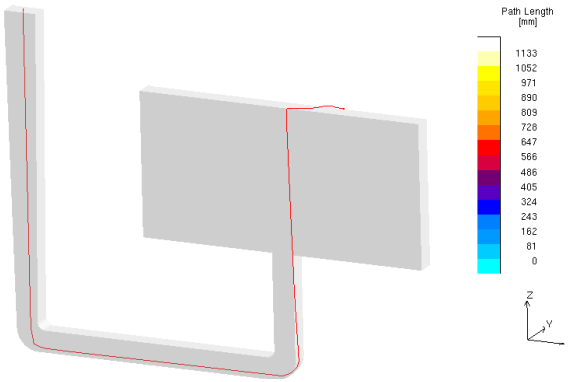
K) Fluid flow at filling time, 1482 ms	**L) Particle path at filling time, 1482ms**

Viscosity -25%	
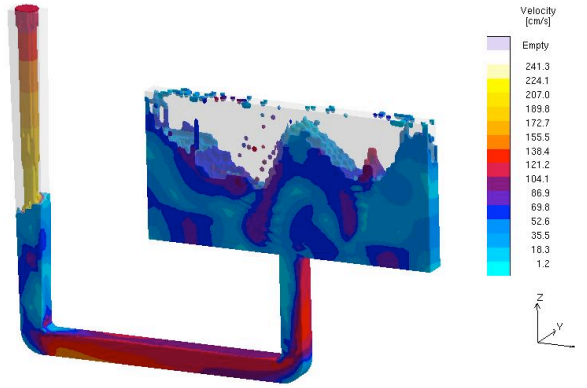	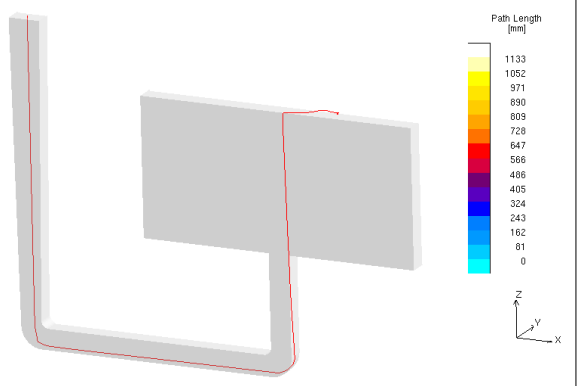
M) Fluid flow at filling time, 1731 ms	**N) Particle path at filling time, 1731ms**
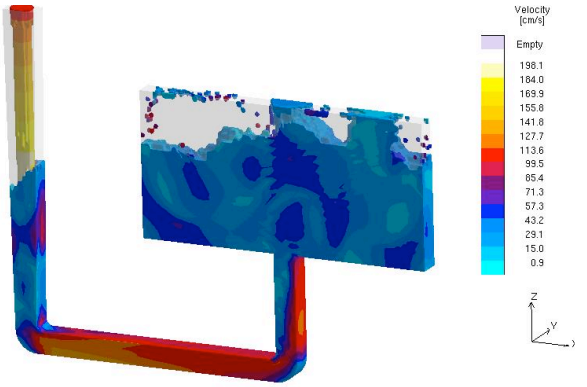	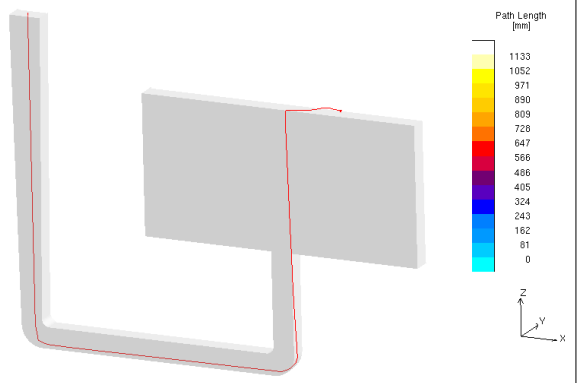
O) Fluid flow at filling time, 1980 ms	**P) Particle path at filling time, 1980ms**
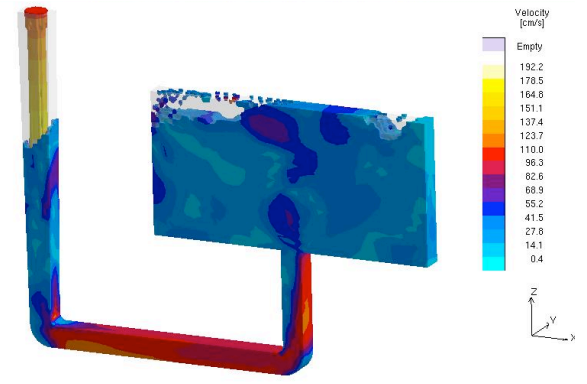	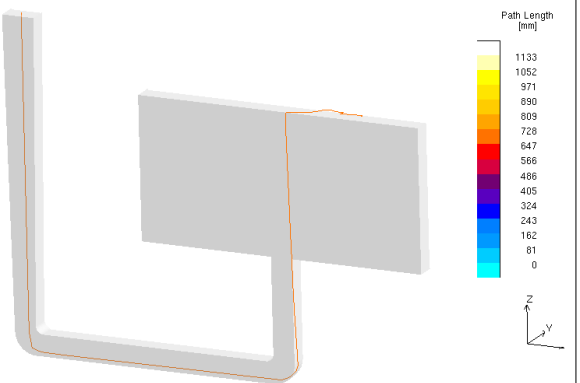
Q) Fluid flow at filling time, 2229 ms	**R) Particle path at filling time, 2229ms**

Viscosity -25%	
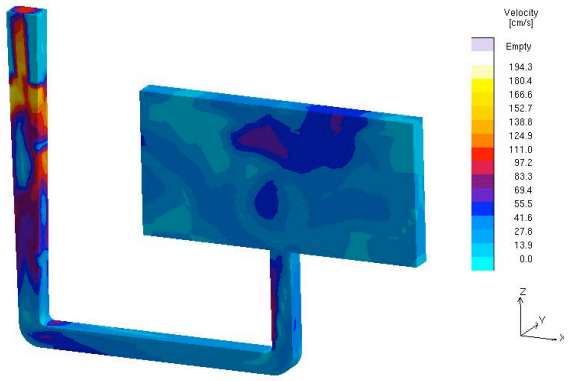	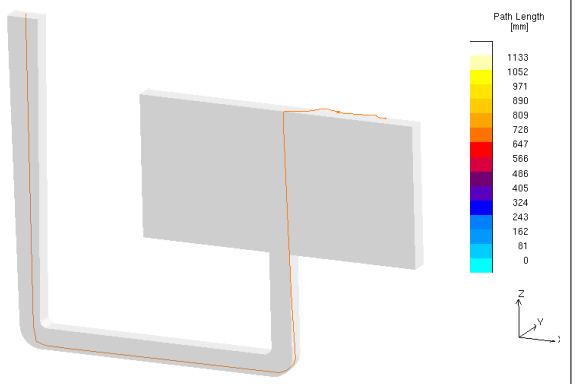
S) Fluid flow at filling time, 2478 ms	**T) Particle path at filling time, 2478ms**

Table 20. MAGMAsoft™ results showing the effect of increasing the viscosity of steel by 25%, on the predicted particle path.

Viscosity +25%	
Mould Filling	Particle Path
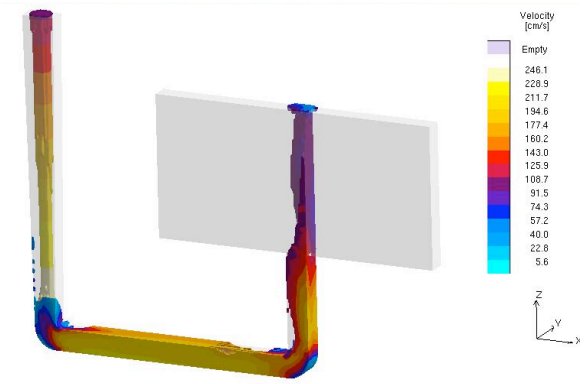	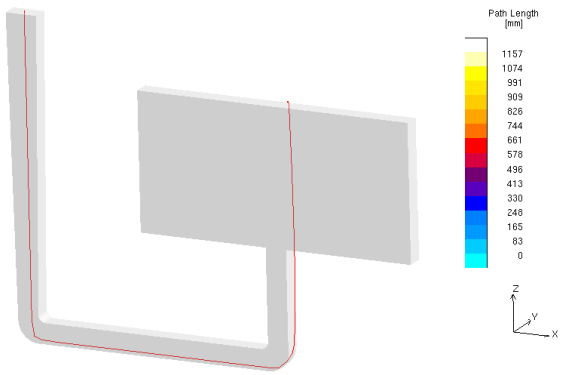
A) Fluid flow at filling time, 485 ms	**B) Particle path at filling time, 485ms**
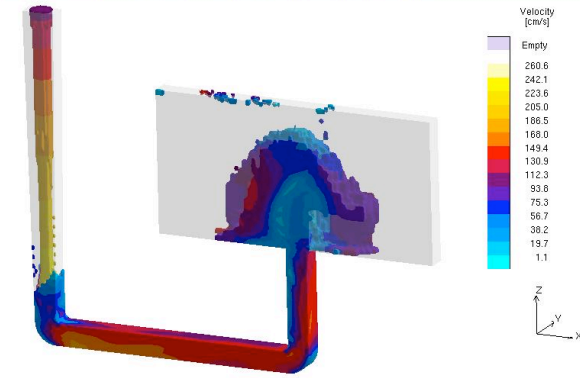	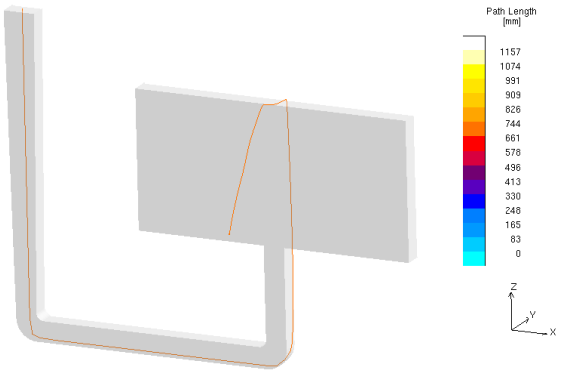
C) Fluid flow at filling time, 985 ms	**D) Particle path at filling time, 985ms**
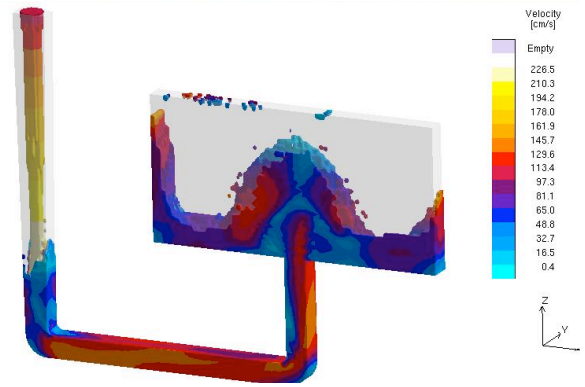	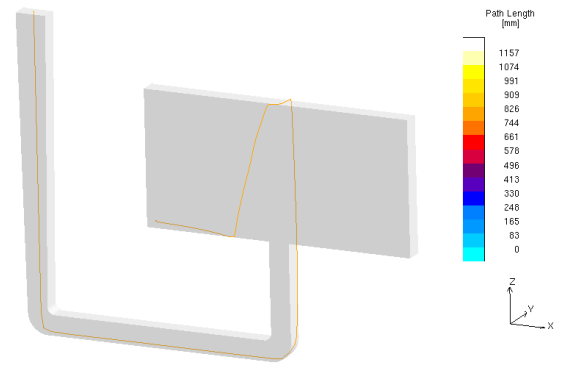
E) Fluid flow at filling time, 1232 ms	**F) Particle path at filling time, 1232ms**

Viscosity +25%	
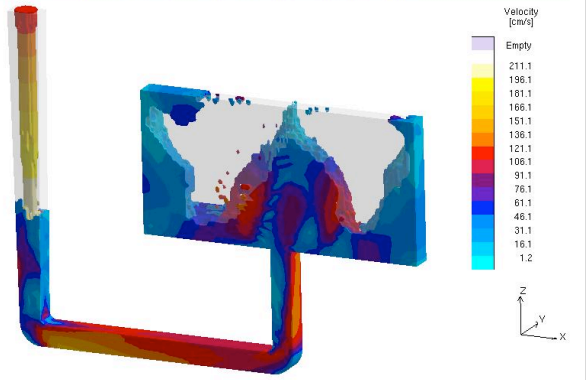	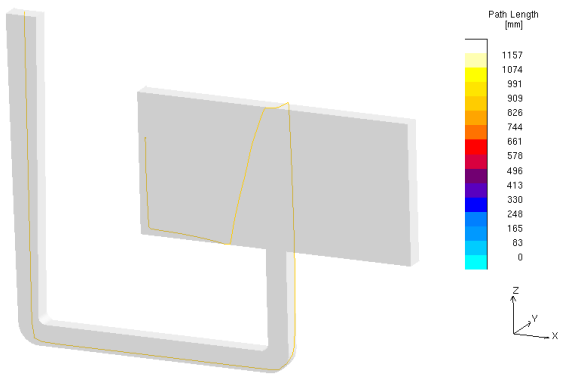
G) Fluid flow at filling time, 1481 ms	**H) Particle path at filling time, 1481ms**
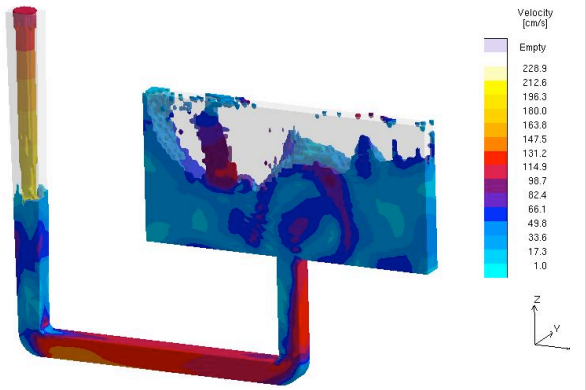	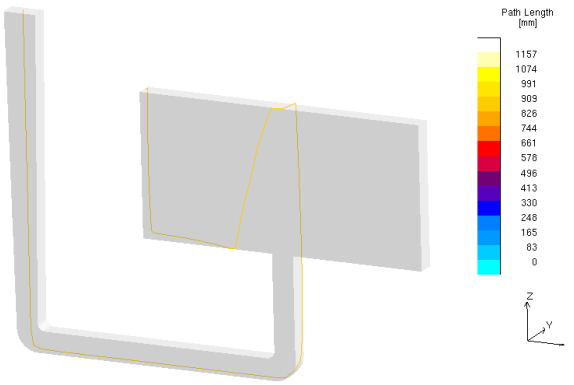
I) Fluid flow at filling time, 1730 ms	**J) Particle path at filling time, 1730ms**
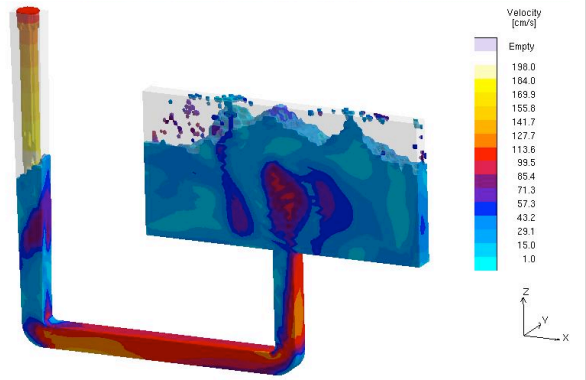	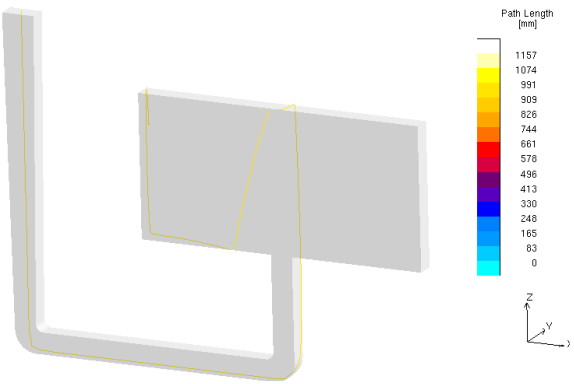
K) Fluid flow at filling time, 1980 ms	**L) Particle path at filling time, 1980ms**

Viscosity +25%	
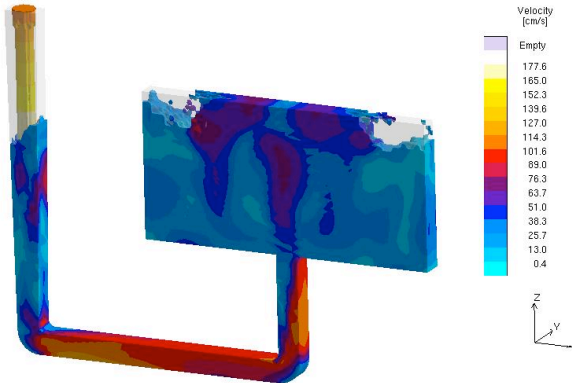	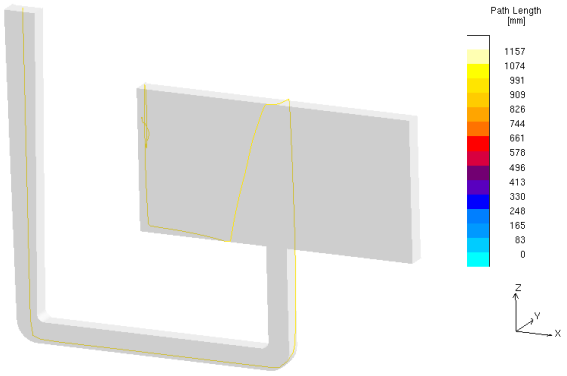
M) Fluid flow at filling time, 2230 ms	**N) Particle path at filling time, 2230ms**

Table 21. MAGMAsoft™ results showing the effect of reducing the casting temperature by 100°C, on the predicted particle path.

Temperature -100°C	
Mould Filling	Particle Path
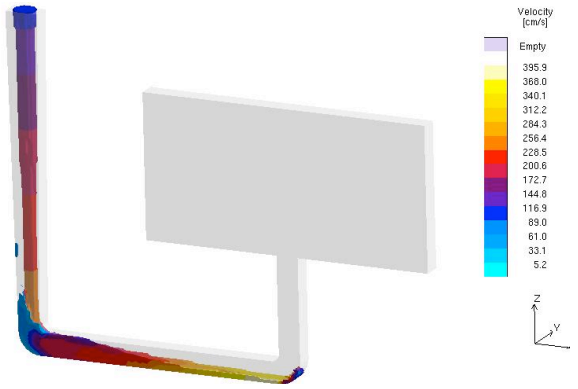	
A) Fluid flow at filling time, 238 ms	**B) Particle path at filling time, 238ms**
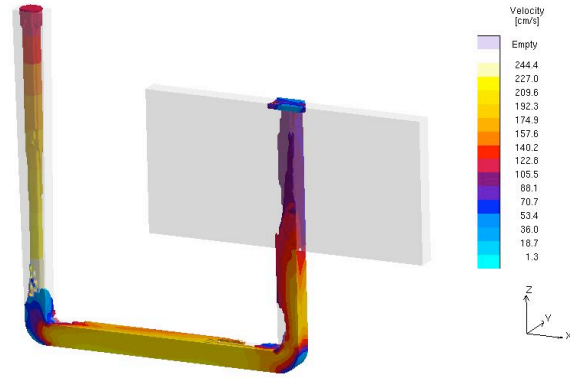	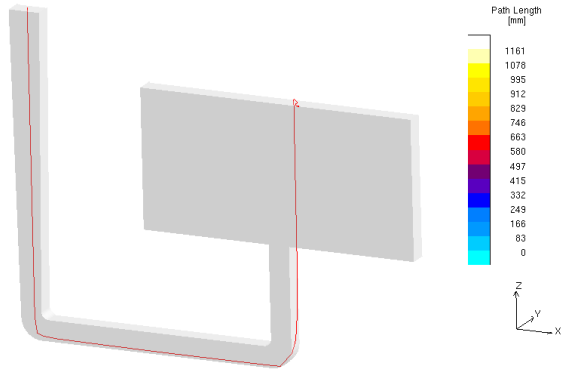
C) Fluid flow at filling time, 489 ms	**D) Particle path at filling time, 489ms**
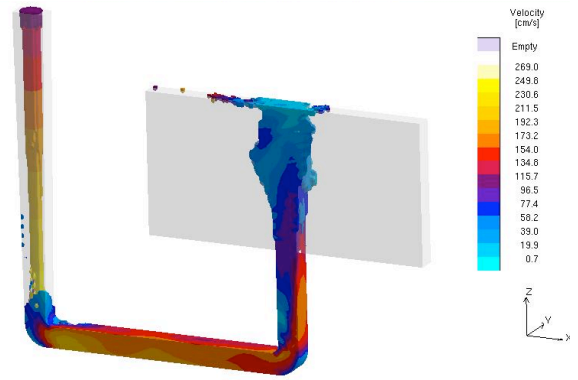	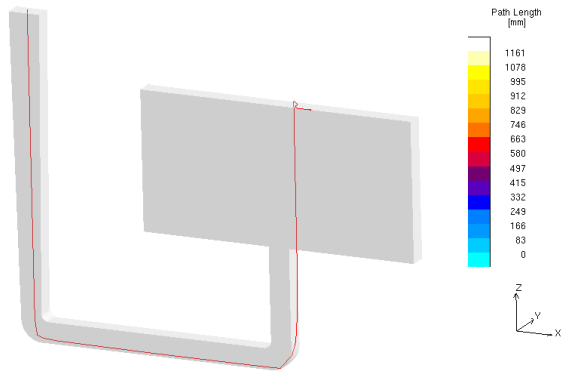
E) Fluid flow at filling time, 714 ms	**F) Particle path at filling time, 714ms**

Temperature -100°C	
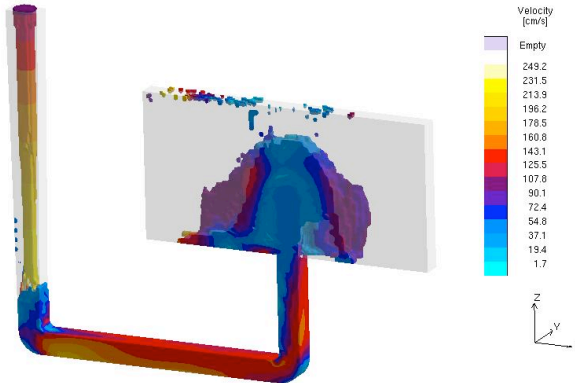	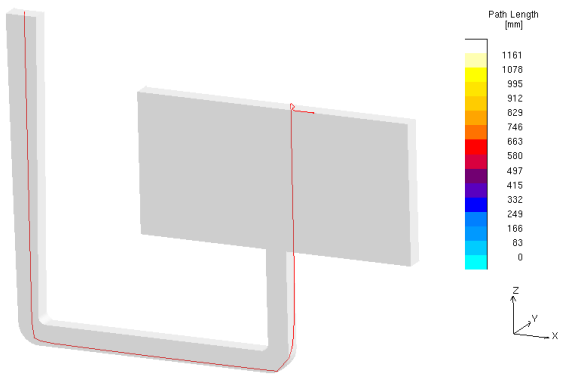
G) Fluid flow at filling time, 922 ms	**H) Particle path at filling time, 922ms**
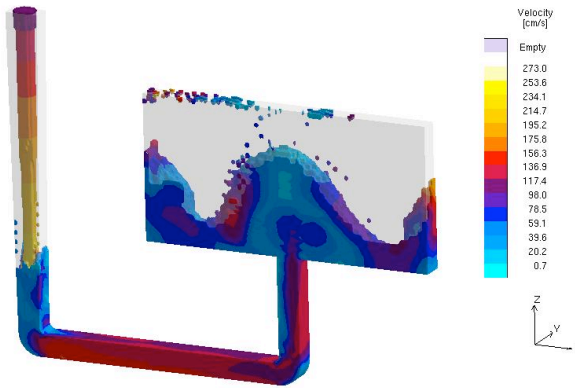	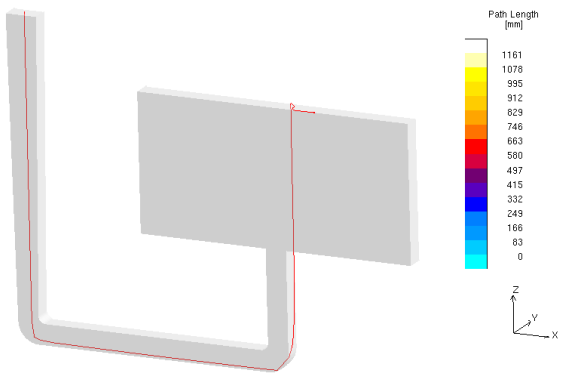
I) Fluid flow at filling time, 1243 ms	**J) Particle path at filling time, 1243ms**
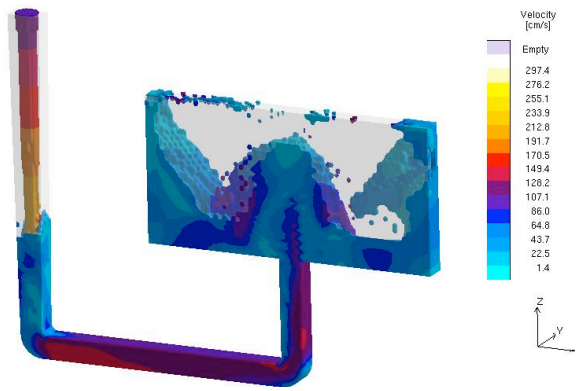	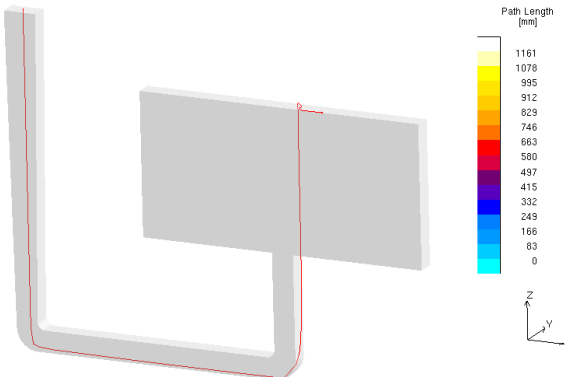
K) Fluid flow at filling time, 1494 ms	**L) Particle path at filling time, 1494ms**

Temperature -100°C	
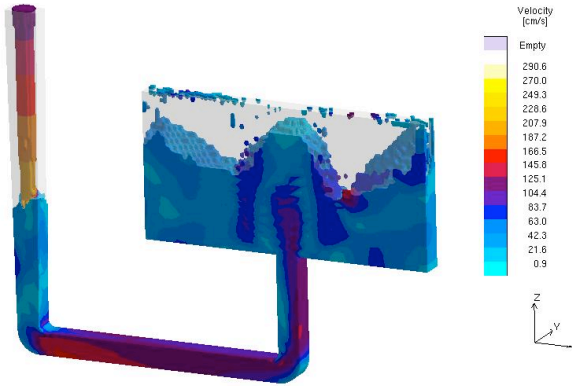	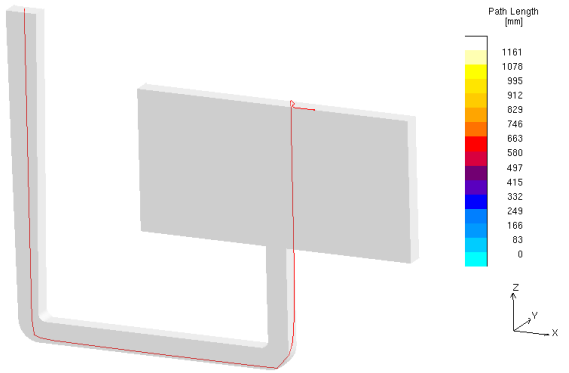
M) Fluid flow at filling time, 1746 ms	**N) Particle path at filling time, 1746ms**
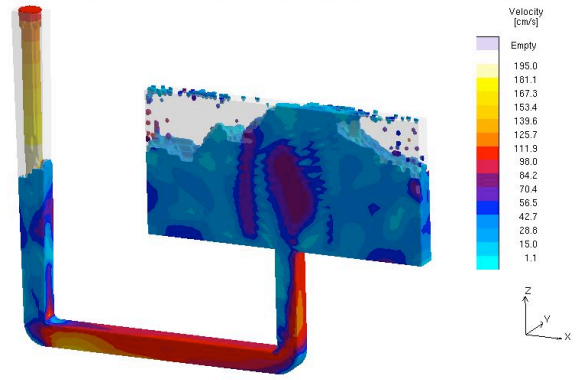	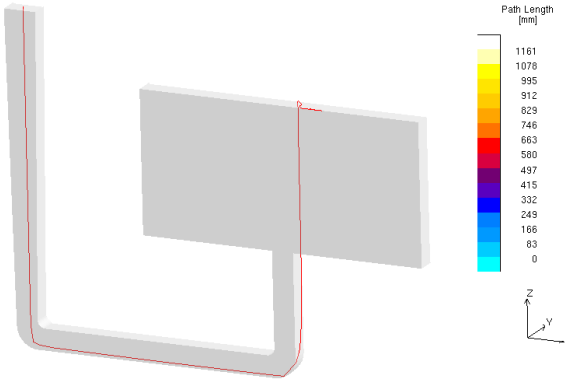
O) Fluid flow at filling time, 1998 ms	**P) Particle path at filling time, 1998ms**
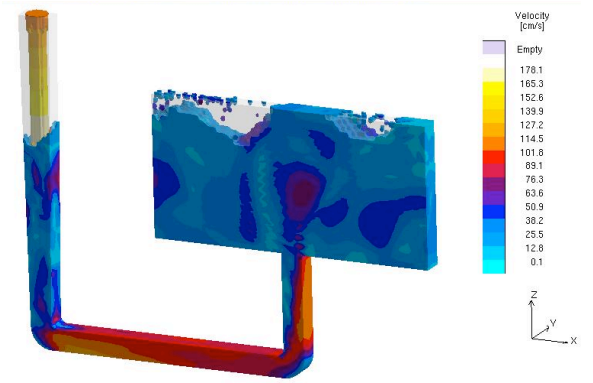	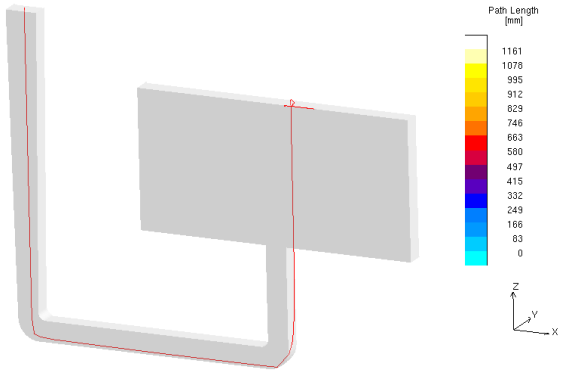
Q) Fluid flow at filling time, 2248 ms	**R) Particle path at filling time, 2248ms**

Temperature -100°C	
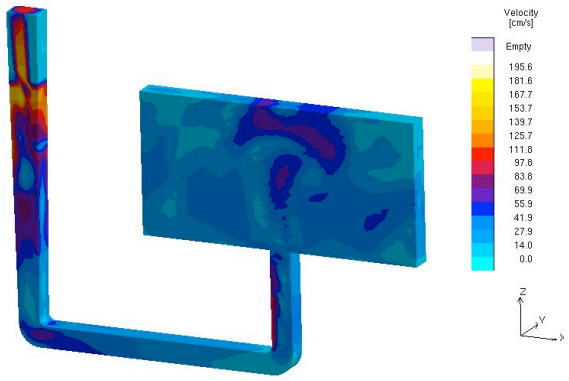	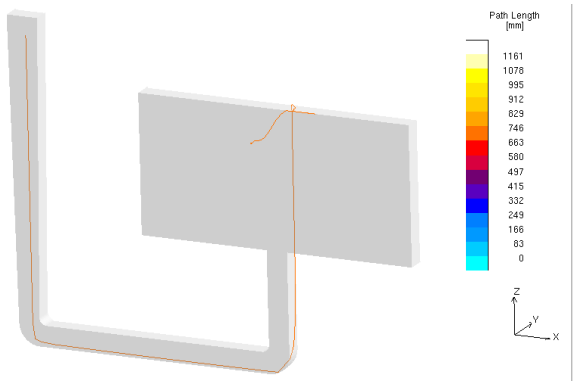
S) Fluid flow at filling time, 2500 ms	**T) Particle path at filling time, 2500ms**

Table 22. MAGMAsoft™ results showing the effect of increasing the casting temperature by 100°C, on the predicted particle path.

Temperature +100°C	
Mould Filling	Particle Path
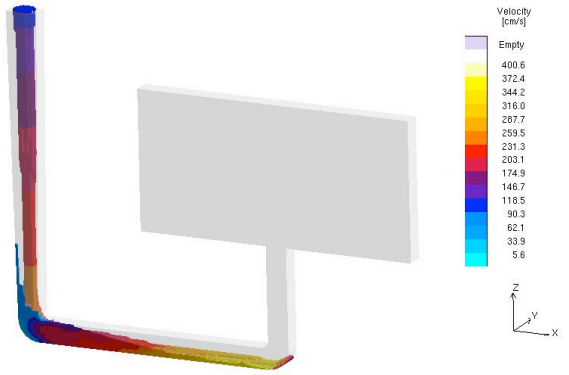	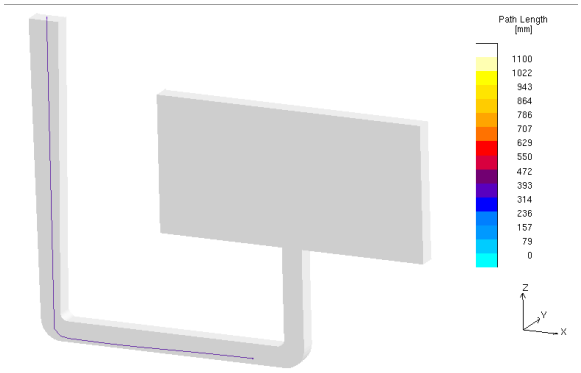
A) Fluid flow at filling time, 234 ms	**B) Particle path at filling time, 234ms**
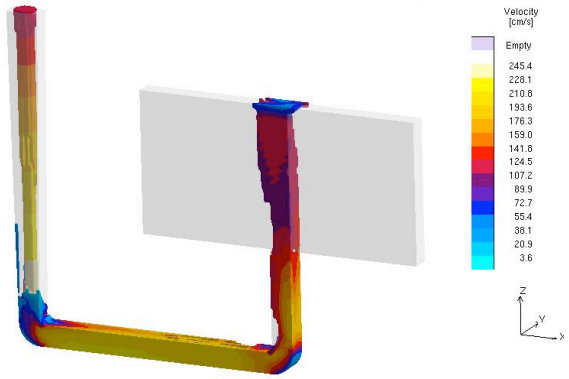	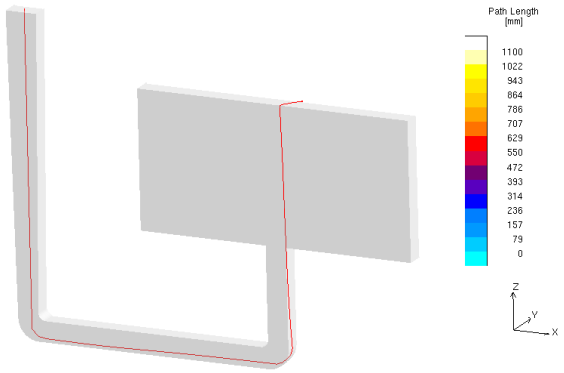
C) Fluid flow at filling time, 481 ms	**D) Particle path at filling time, 481ms**
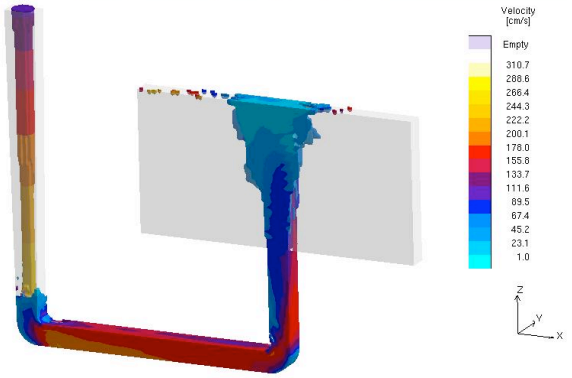	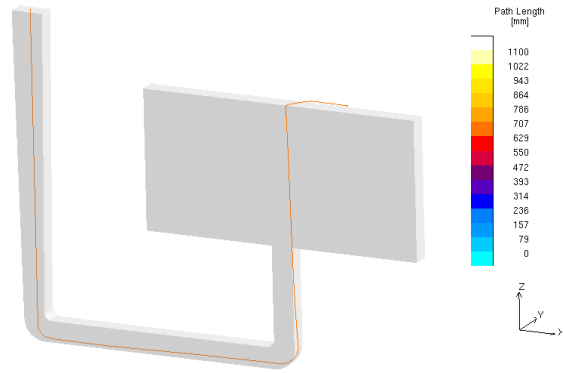
E) Fluid flow at filling time, 728 ms	**F) Particle path at filling time, 728ms**

Temperature +100°C	
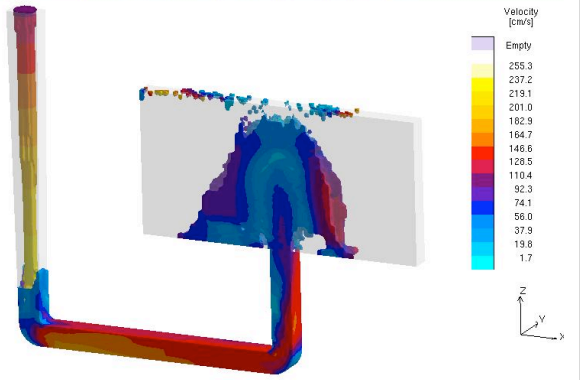	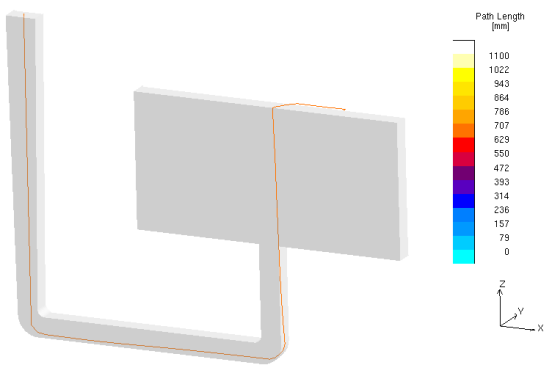
G) Fluid flow at filling time, 974 ms	**H) Particle path at filling time, 974ms**
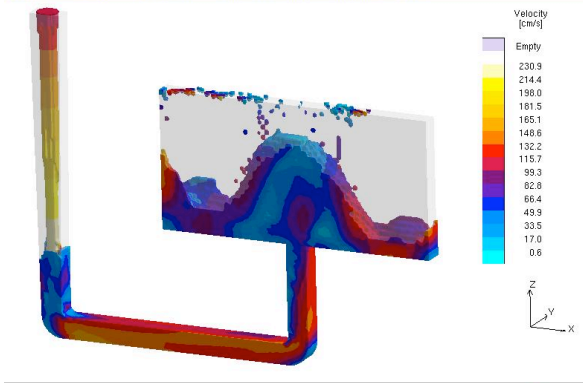	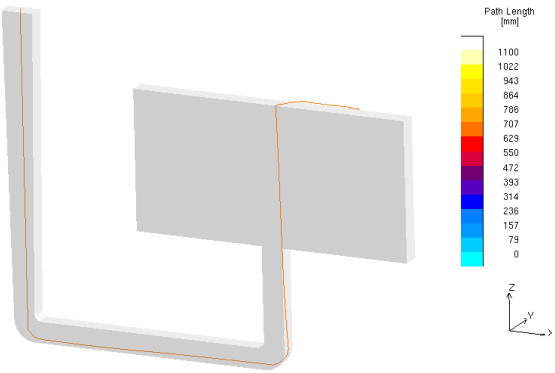
I) Fluid flow at filling time, 1222 ms	**J) Particle path at filling time, 1222ms**
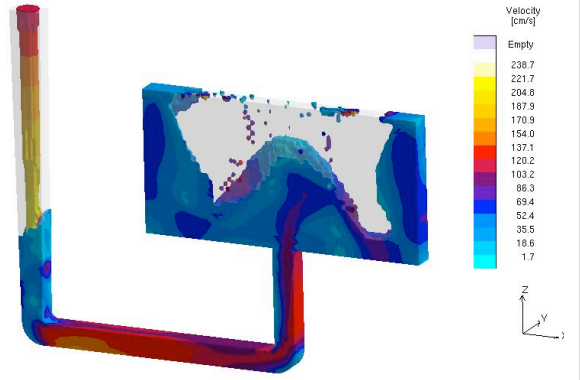	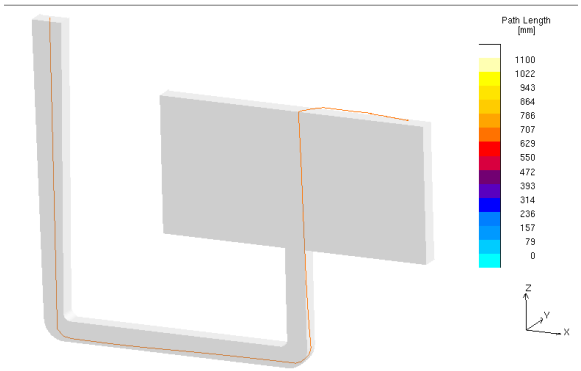
K) Fluid flow at filling time, 1468 ms	**L) Particle path at filling time, 1468ms**

Temperature +100°C	
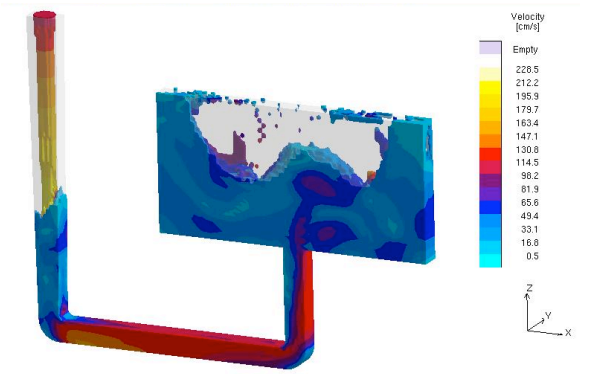	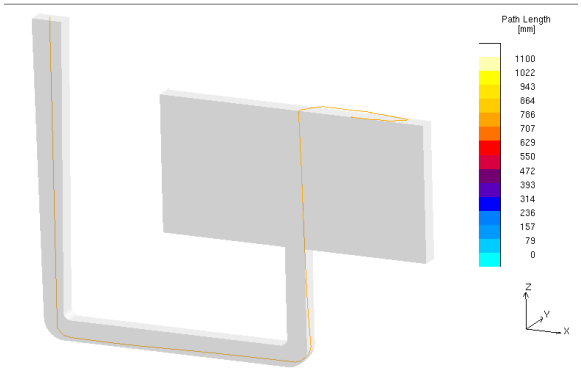
M) Fluid flow at filling time, 1716 ms	**N) Particle path at filling time, 1716ms**
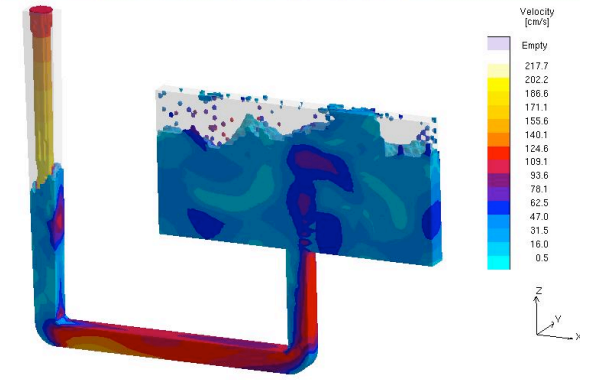	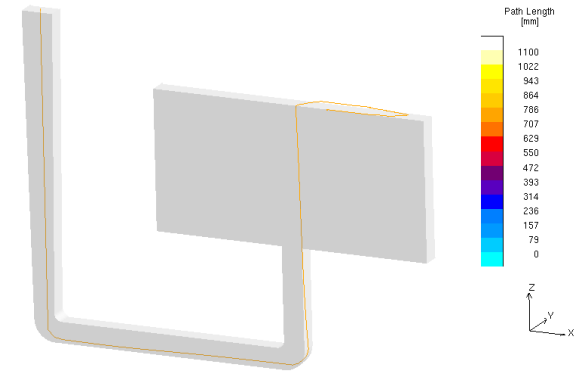
O) Fluid flow at filling time, 1962 ms	**P) Particle path at filling time, 1962ms**
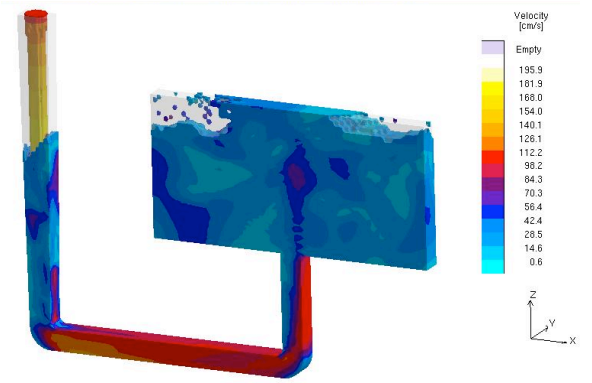	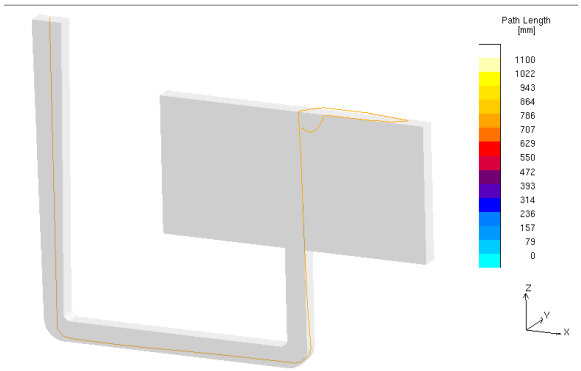
Q) Fluid flow at filling time, 2209 ms	**R) Particle path at filling time, 2209ms**

Temperature +100°C	
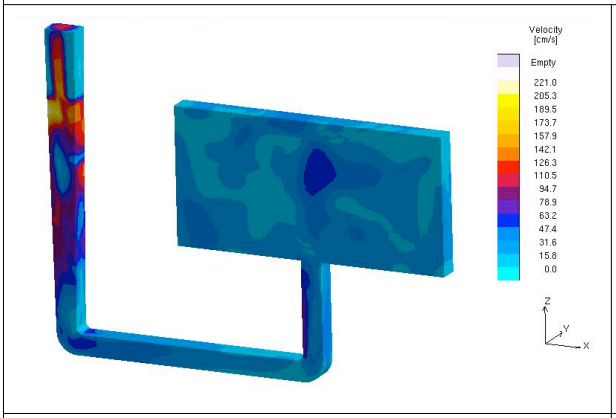	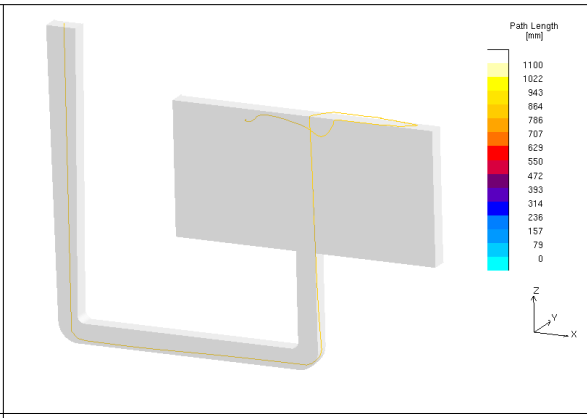
S) Fluid flow at filling time, 2456 ms	**T) Particle path at filling time, 2456ms**

4.3.2 The Effects of Modelling the Pouring Basin and Angled Pouring

Two types of models were produced to study the effect of the pouring practice details on the particle's final location, one in which effects from the pouring basin, pouring angle, metal stream diameter and head height were ignored and a second model that included consideration of these factors. The results produced from these models are shown in figures 77-89.

In the first model the metal was poured directly into the downsprue. The pouring basin was ignored in order to simulate the particle track when pure iron enters the sprue of a sand mould, in a uniform vertical manner. Figures 77-80 show simulation results describing the particle's movement until the mould was full. These figures suggest that the predicted track of the particle's movement is to follow the liquid metal front until 50% filling (figures 77 and 78), after which it became entrained and moved with the liquid metal, figures 79and 80.

Unfortunately, the effects of solidification on the particle's movement could not be simulated using the available licences for MAGMAsoft™. Therefore these particle-tracking results end when filling is complete, after approximately 2.62 seconds from pouring.

The results of the second model are represented in figures 81-89. The thermo-physical properties of pure Fe were also used for this model and the filling time was 3 seconds.

The results of this more accurate model show that the particle started moving along the walls of the sprue following the metal surface at 40% filling, see figure 84, unlike the first model

where it flowed straight down through the running system. At 46% filling the particle seems to have been carried by the liquid metal surface and entered the cast plate cavity at 53% filling as shown in figure 86. Figure 87 illustrates that at 73% filling the particle reached the top of the plate, after which it moved downwards as the mould cavity continued to be filled, 80% filling, figure 88. Finally when filling was complete the particle's final location was near the ingate.

The results obtained showed the sensitivity of the model to the inlet conditions and that modelling the angled pouring and the effects of having a pouring basin have led to different mould filling and final particle locations. However, these models did not account for any movement the particle may have undertaken during solidification which could not be modelled at the time. The model results did not agree with the final particle location obtained experimentally.

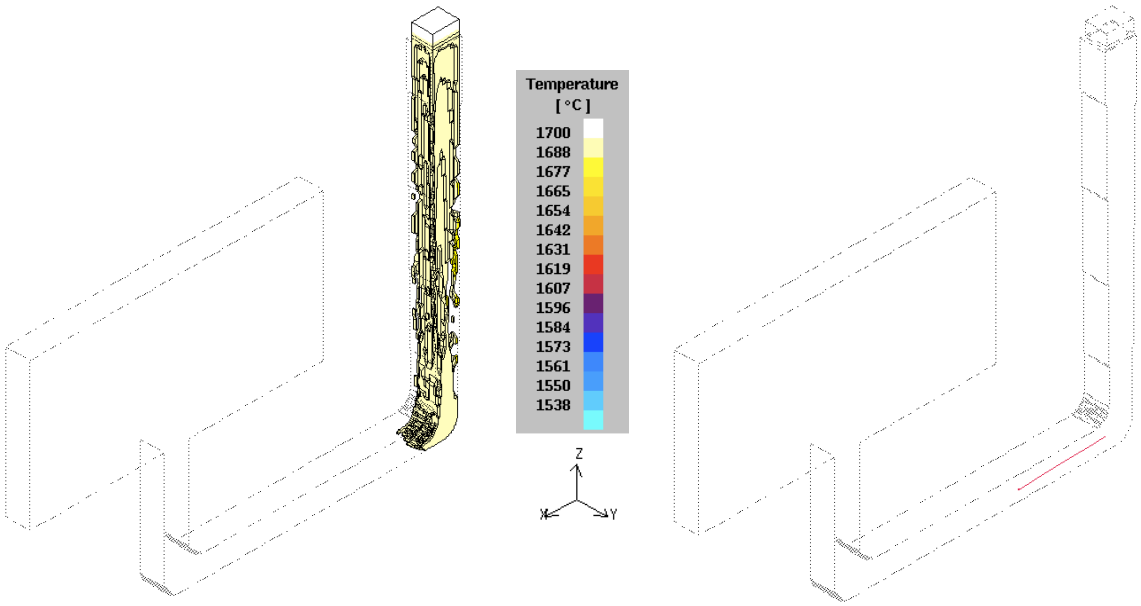

Figure 77. Two isometric views of the sand cast plate showing the MAGMAsoft™ model results, at 20% filling, when the pouring basin was ignored.

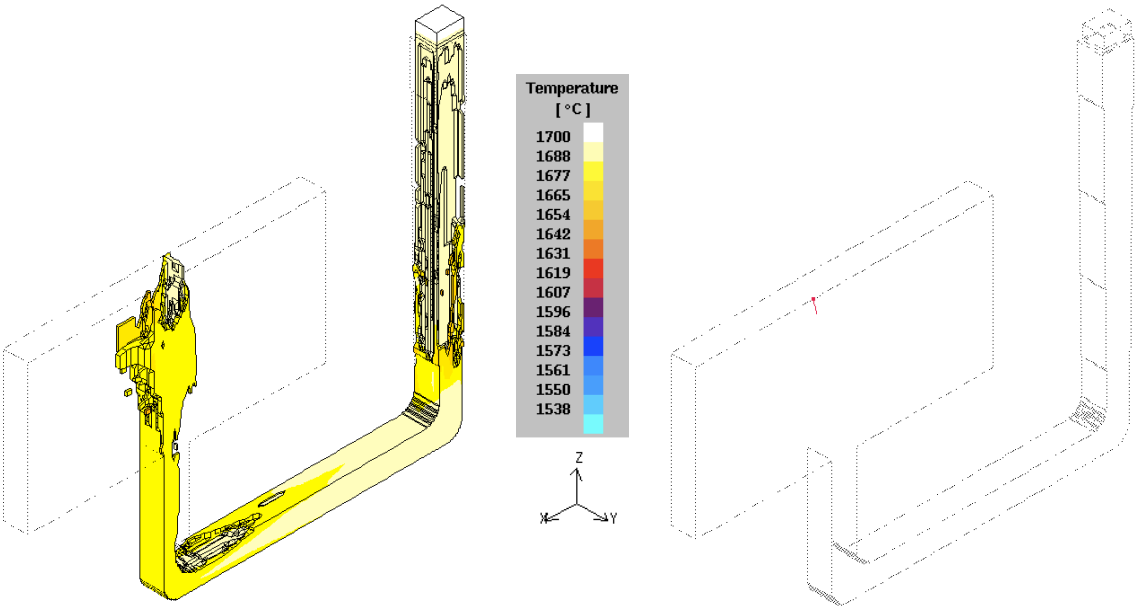

Figure 78. Two isometric views of the sand cast plate showing the MAGMAsoft™ model results, at 50% filling, when the pouring basin was ignored.

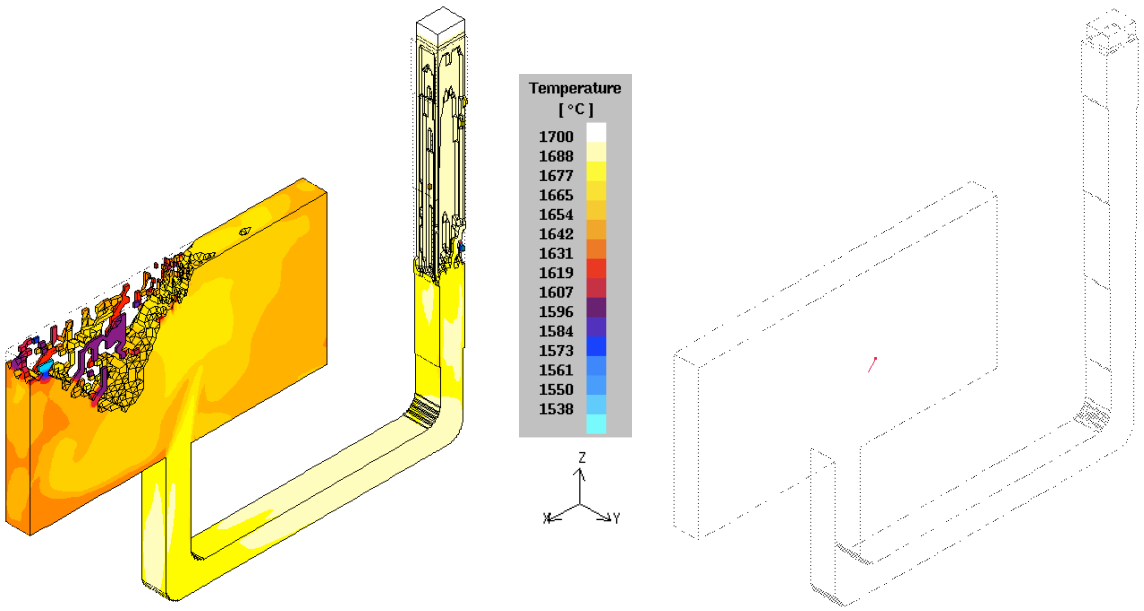

Figure 79. Two isometric views of the sand cast plate showing the MAGMAsoft™ model results, at 80% filling, when the pouring basin was ignored.

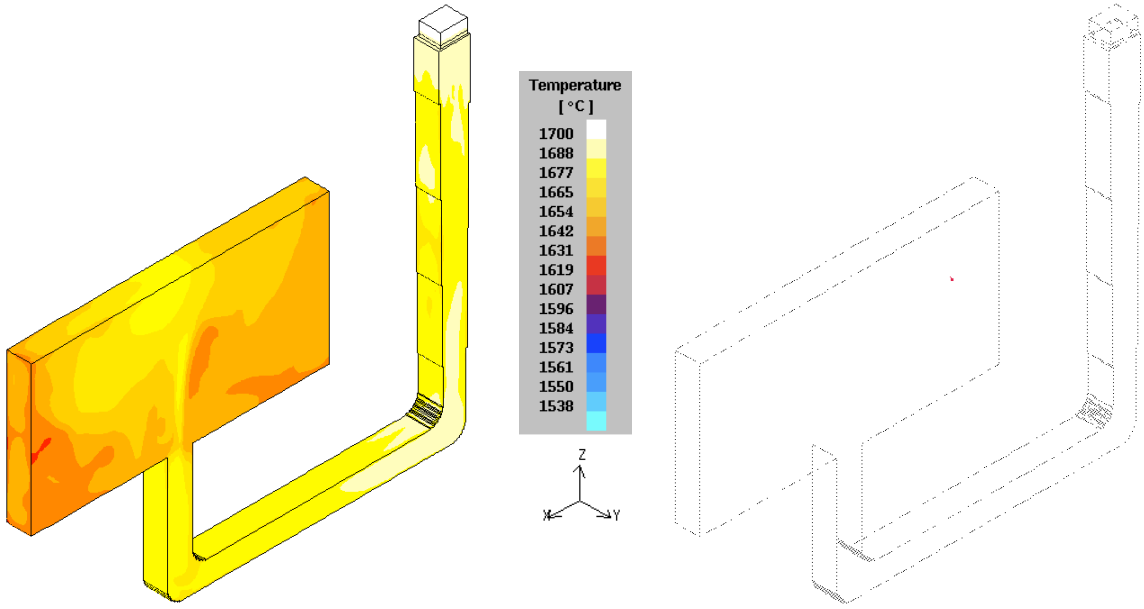

Figure 80. Two isometric views of the sand cast plate showing the MAGMAsoft™ model results, at 100% filling, when the pouring basin was ignored.

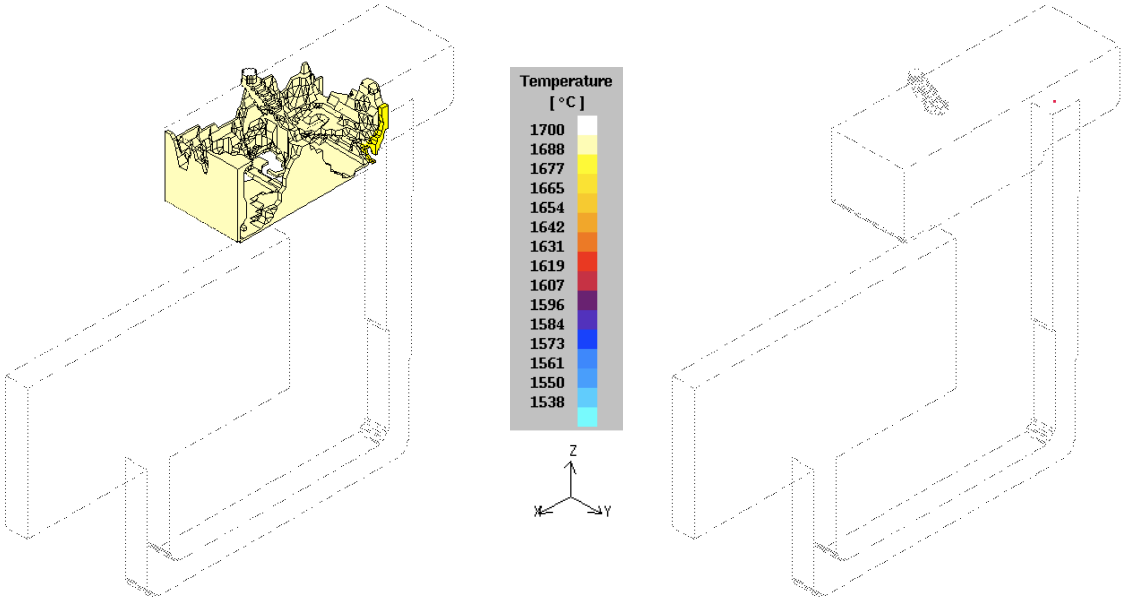

Figure 81. Two isometric views of the sand cast plate showing the MAGMAsoft™ model results, at 10% filling, when the pouring basin and pouring angle were modelled

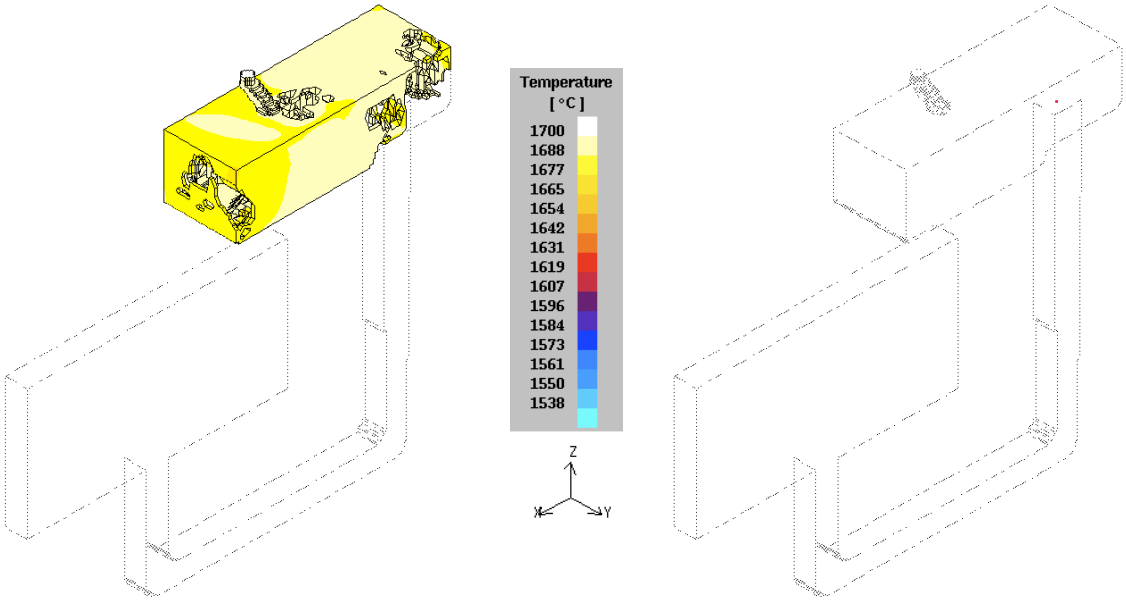

Figure 82. Two isometric views of the sand cast plate showing the MAGMAsoft™ model results, at 20% filling, when the pouring basin and pouring angle were modelled.

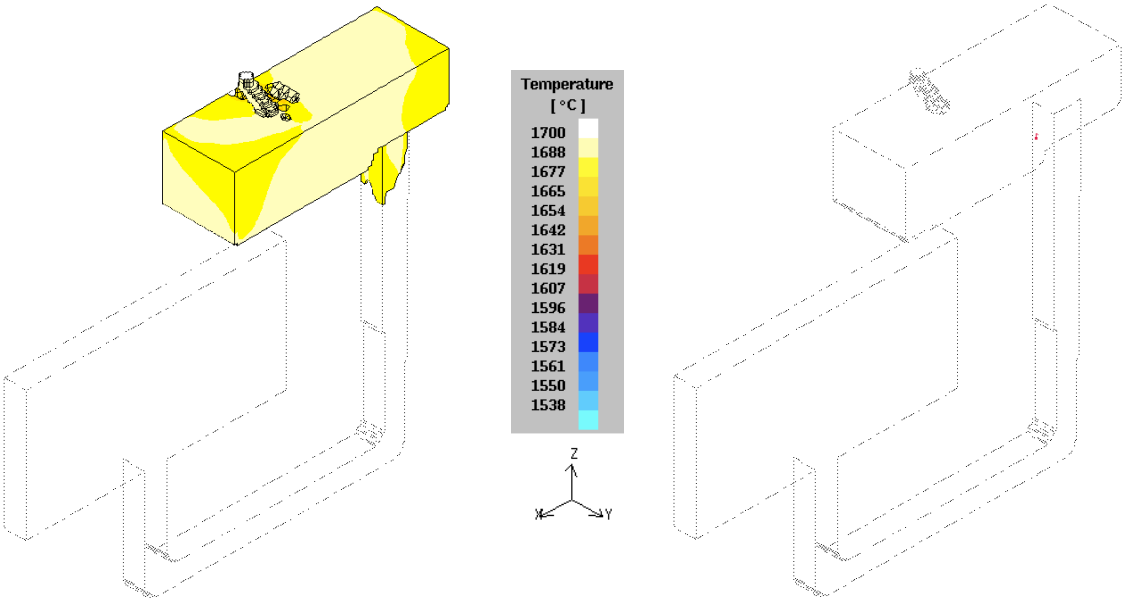

Figure 83. Two isometric views of the sand cast plate showing the MAGMAsoft™ model results, at 30% filling, when the pouring basin and pouring angle were modelled.

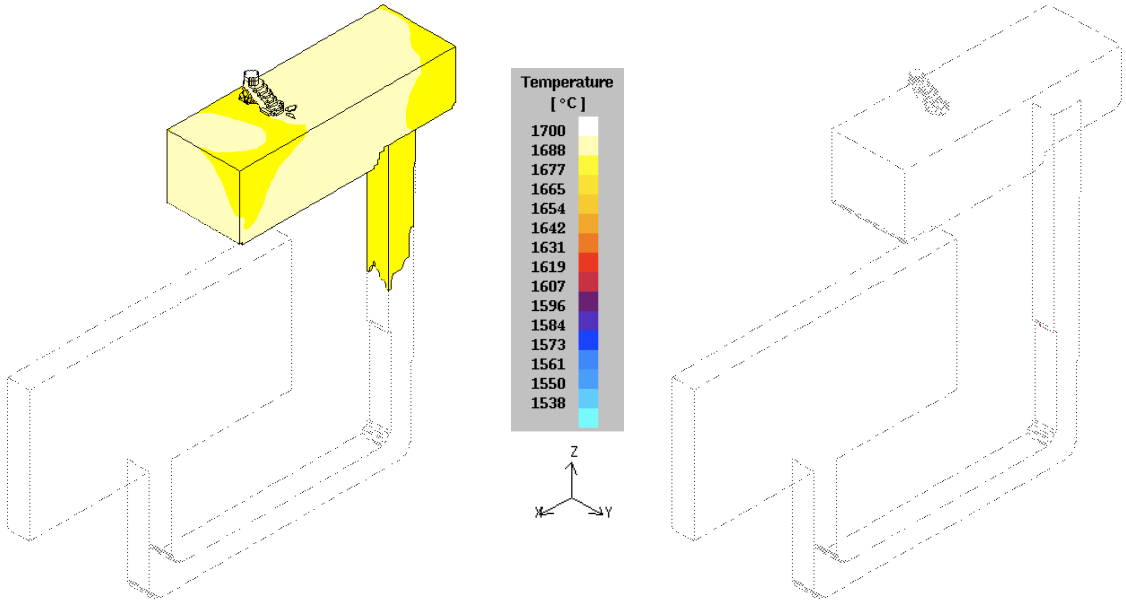

Figure 84. Two isometric views of the sand cast plate showing the MAGMAsoft™ model results, at 40% filling, when the pouring basin and pouring angle were modelled.

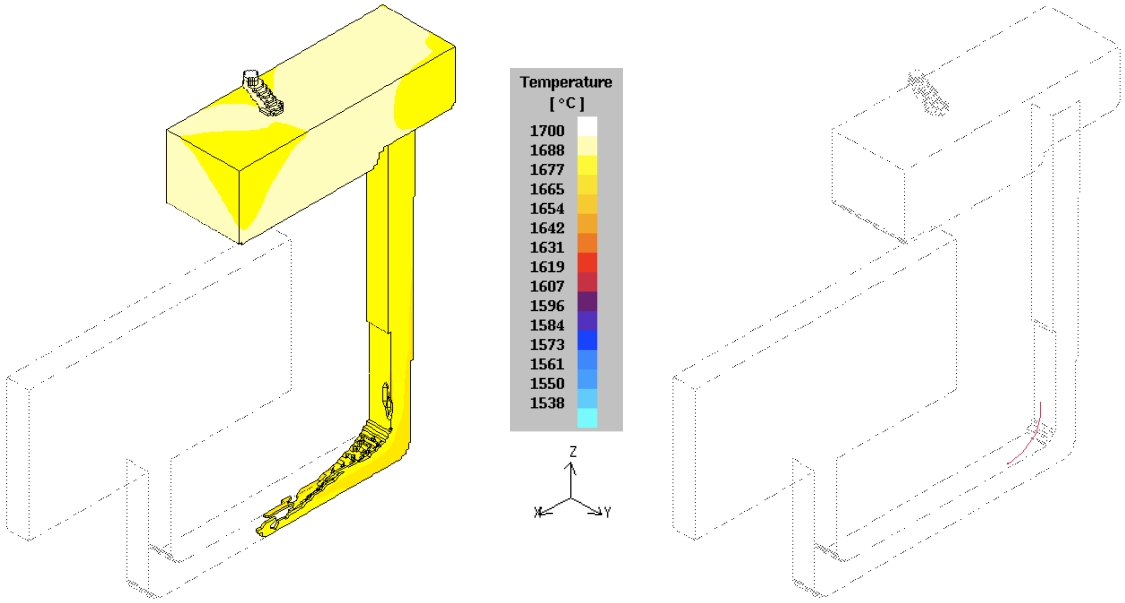

Figure 85. Two isometric views of the sand cast plate showing the MAGMAsoft™ model results, at 46% filling, when the pouring basin and pouring angle were modelled.

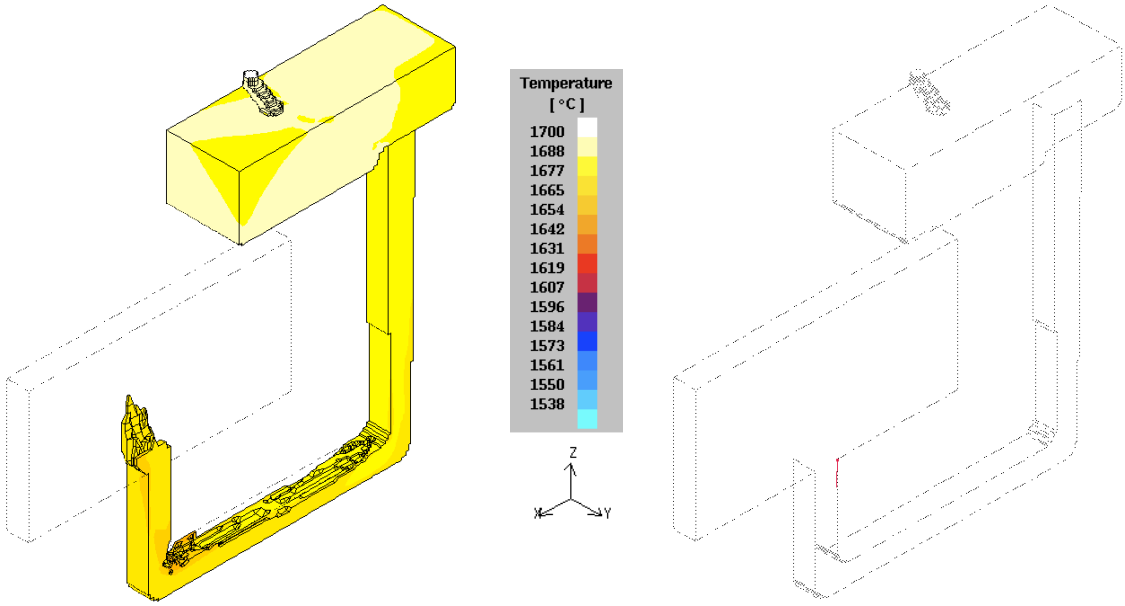

Figure 86. Two isometric views of the sand cast plate showing the MAGMAsoft™ model results, at 53% filling, when the pouring basin and pouring angle were modelled.

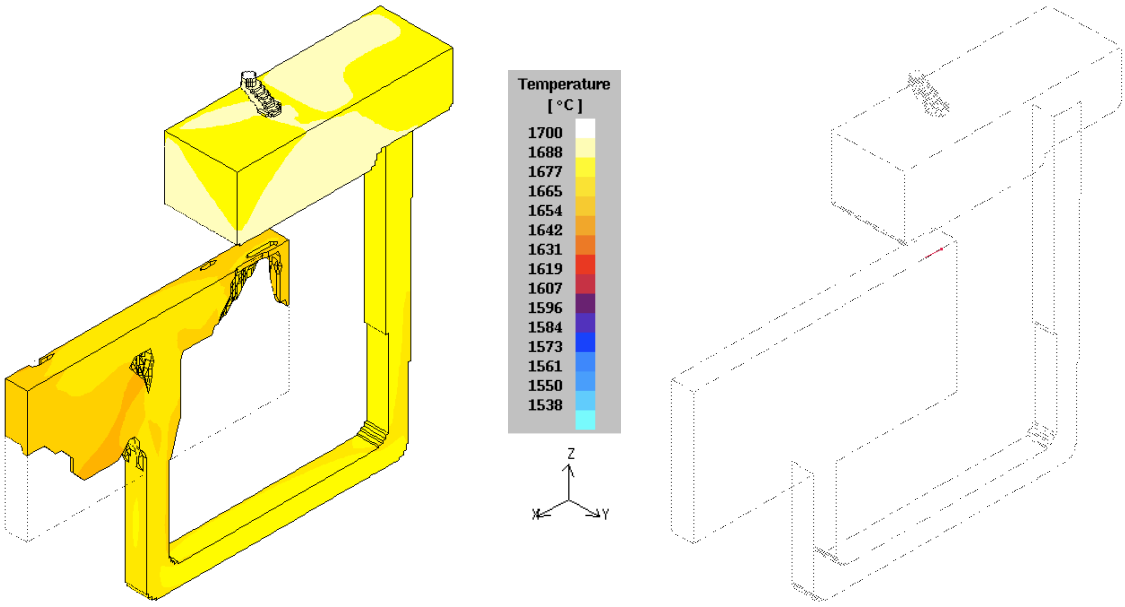

Figure 87. Two isometric views of the sand cast plate showing the MAGMAsoft™ model results, at 73% filling, when the pouring basin and pouring angle were modelled.

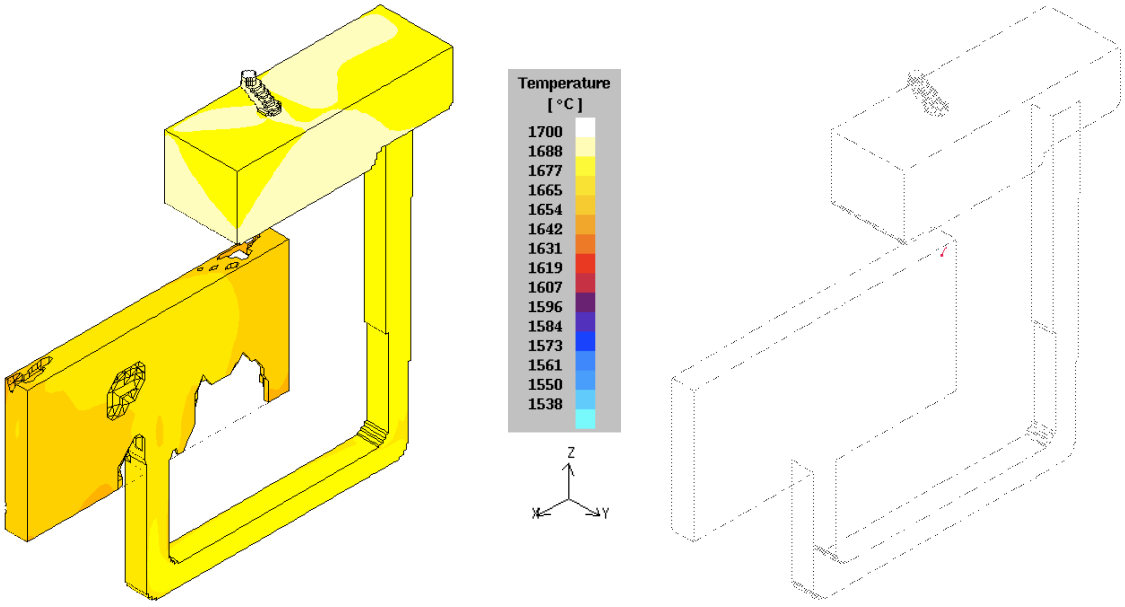

Figure 88. Two isometric views of the sand cast plate showing the MAGMAsoft™ model results, at 80% filling, when the pouring basin and pouring angle were modelled.

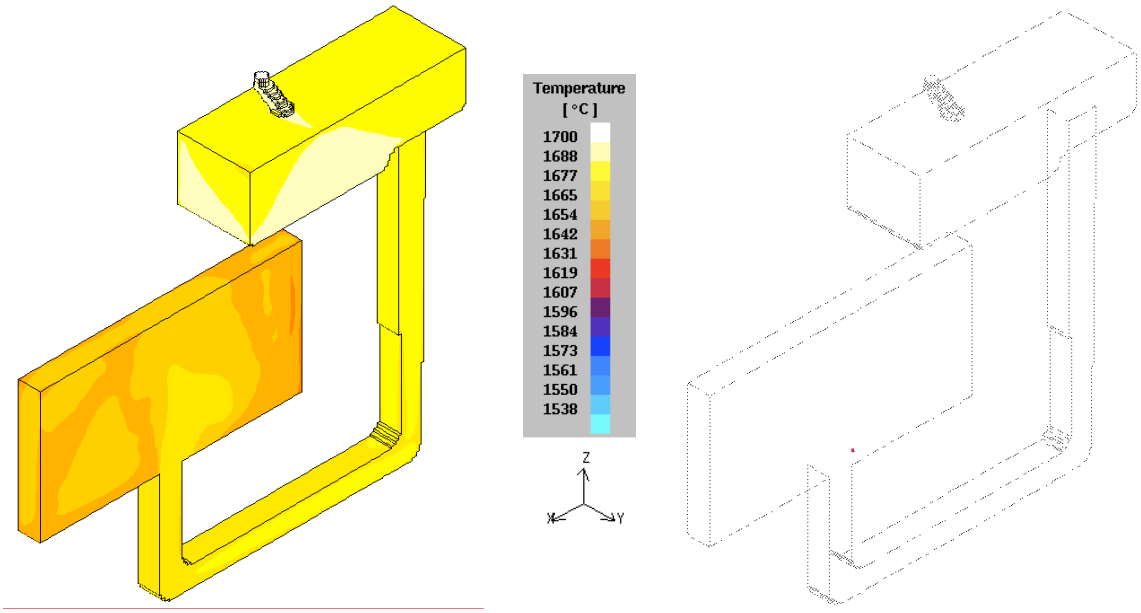

Figure 89. Two isometric views of the sand cast plate showing the MAGMAsoft™ model results, at 100% filling, when the pouring basin and pouring angle were modelled.

4.3.3 Investment Casting of Steel

The investment casting, where the irradiated alumina particle was placed at the centre of the downsprue opening, see figure 38, was also modelled using MAGMAsoft™. The thermo-physical properties of pure iron were used in this model and figures 90-101 show the results obtained.

The particle became entrained in the liquid metal at 8% filling as shown in figures 91. As the metal accelerated through the downsprue, the particle was entrained in the liquid metal and entered the cast plate cavity at 30% filling, figure 95, after which it moved in a loop near the bottom left corner of the plate, (see figures 96,97 and 99,c), at approximately 8 $cm.s^{-1}$. When the casting was 70% full the particle started to float upwards at roughly 34 $cm.s^{-1}$ and eventually came to a stop in the centre at the lower part of the plate as shown in figure 99. As explained earlier due to the limitation of the available MAGMAsoft™ licenses, further information about the particle's movement during solidification could not be obtained.

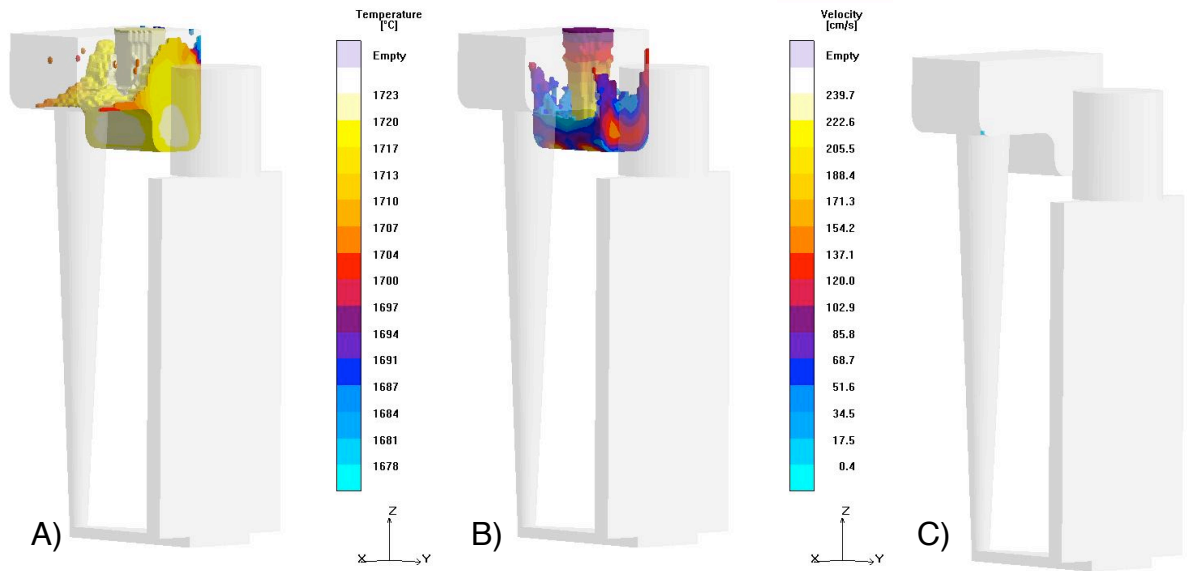

Figure 90. The baseline investment casting, where an alumina particle was placed at the centre of the downsprue opening, at 5% filling; A) fluid coloured with respect to temperature, B) fluid coloured with respect to velocity and C) is the predicted particle location at the time.

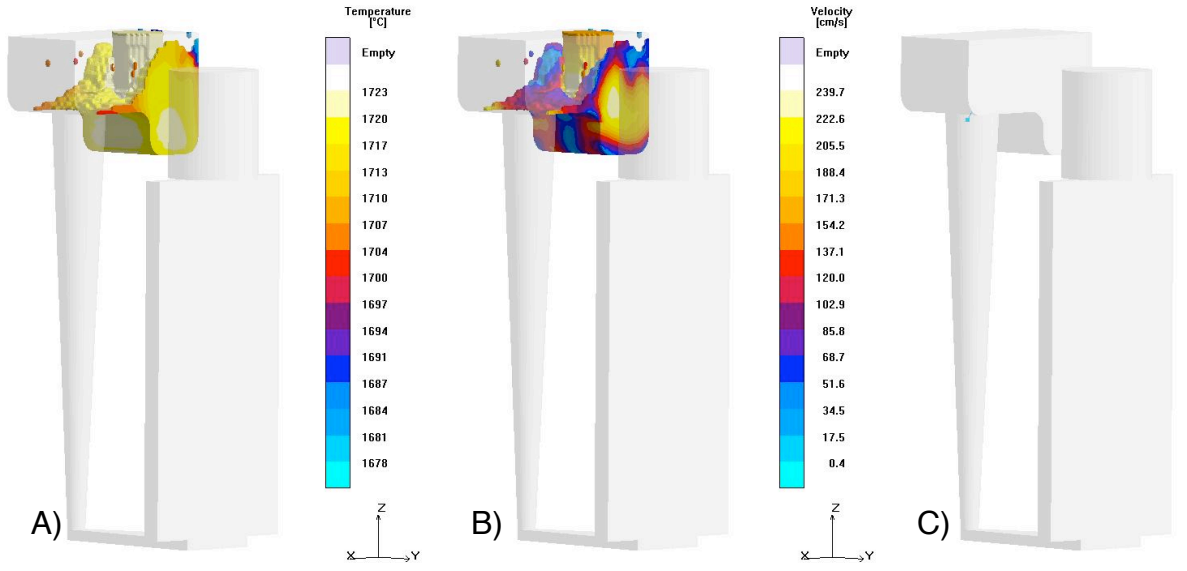

Figure 91. The baseline investment casting, where an alumina particle was placed at the centre of the downsprue opening, at 8% filling; A) fluid coloured with respect to temperature, B) fluid coloured with respect to velocity and C) is the predicted particle location at the time.

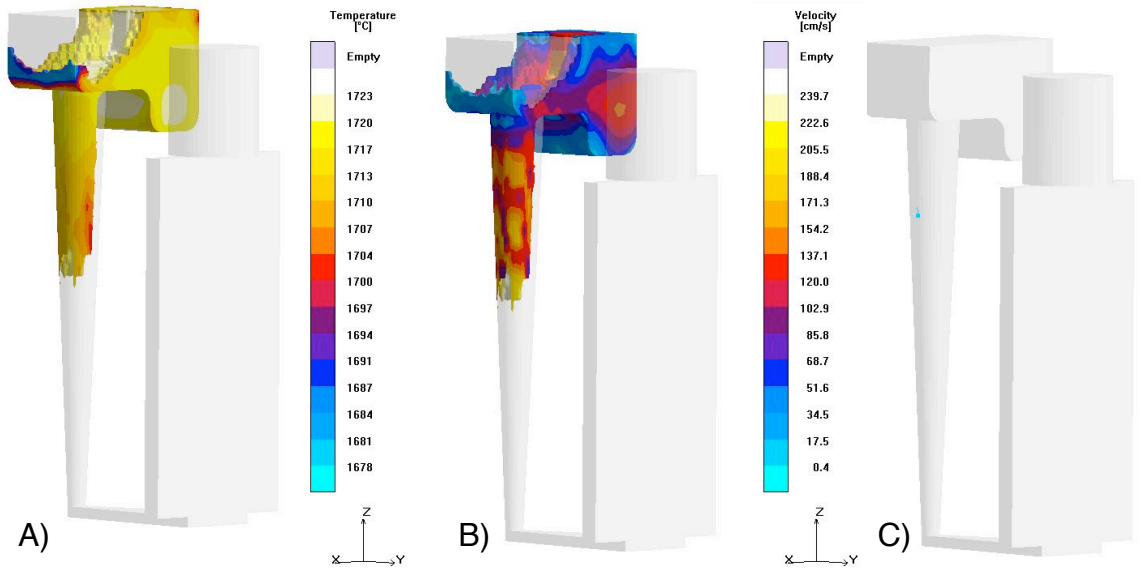

Figure 92. The baseline investment casting, where an alumina particle was placed at the centre of the downsprue opening, at 15% filling; A) fluid coloured with respect to temperature, B) fluid coloured with respect to velocity and C) is the predicted particle location at the time.

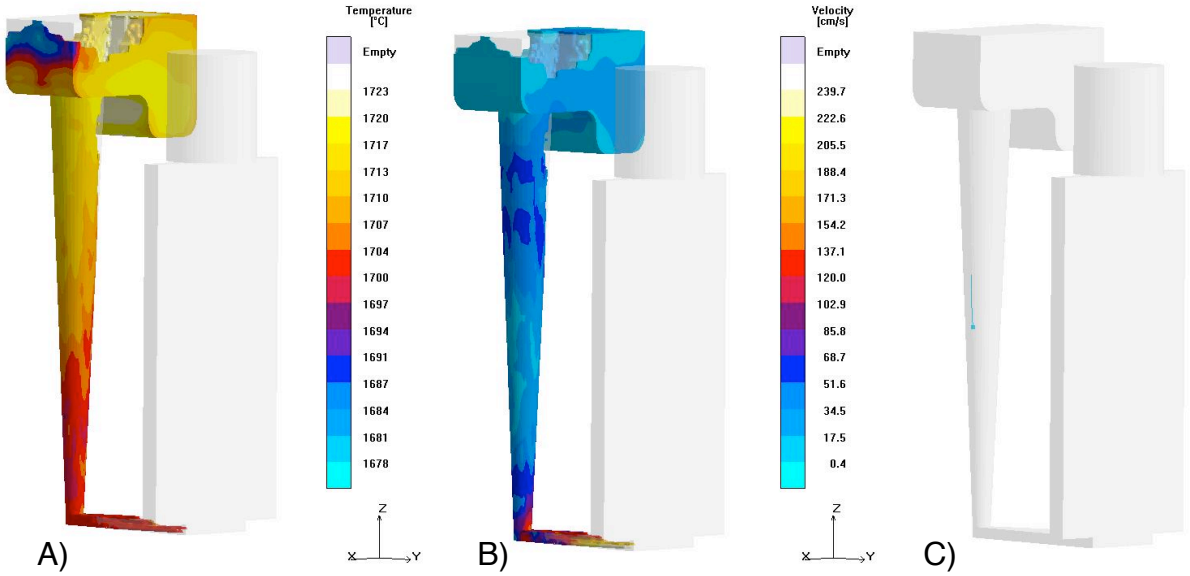

Figure 93. The baseline investment casting, where an alumina particle was placed at the centre of the downsprue opening, at 20% filling; A) fluid coloured with respect to temperature, B) fluid coloured with respect to velocity and C) is the predicted particle location at the time.

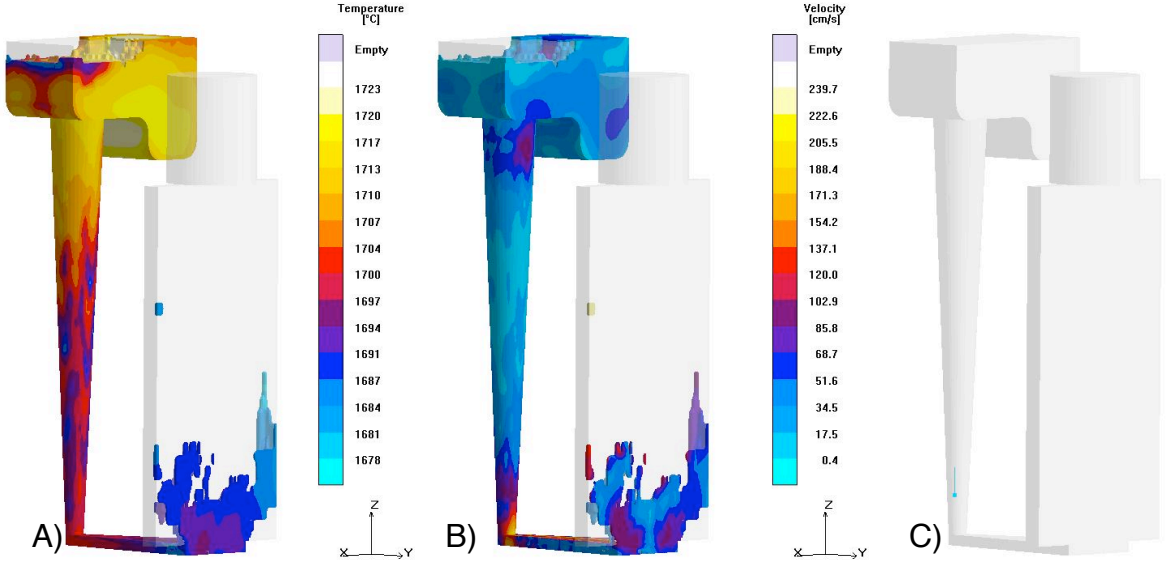

Figure 94. The baseline investment casting, where an alumina particle was placed at the centre of the downsprue opening, at 25% filling; A) fluid coloured with respect to temperature, B) fluid coloured with respect to velocity and C) is the predicted particle location at the time.

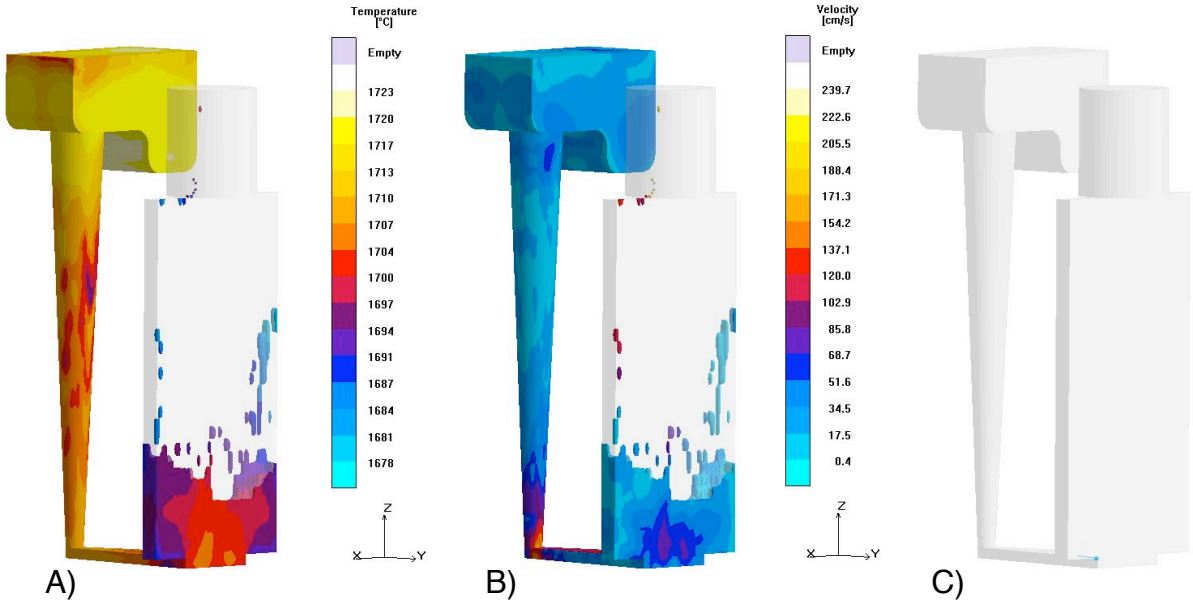

Figure 95.The baseline investment casting, where an alumina particle was placed at the centre of the downsprue opening, at 30% filling; A) fluid coloured with respect to temperature, B) fluid coloured with respect to velocity and C) is the predicted particle location at the time.

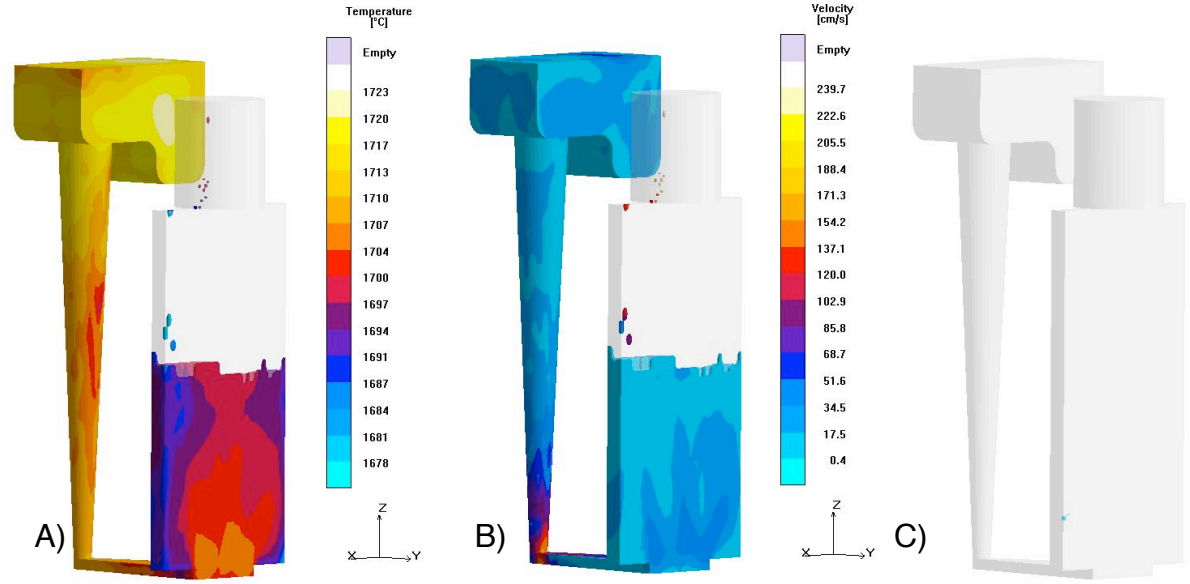

Figure 96. The baseline investment casting, where an alumina particle was placed at the centre of the downs pure opening, at 60% filling; A) fluid coloured with respect to temperature, B) fluid coloured with respect to velocity and C) is the predicted particle location at the time.

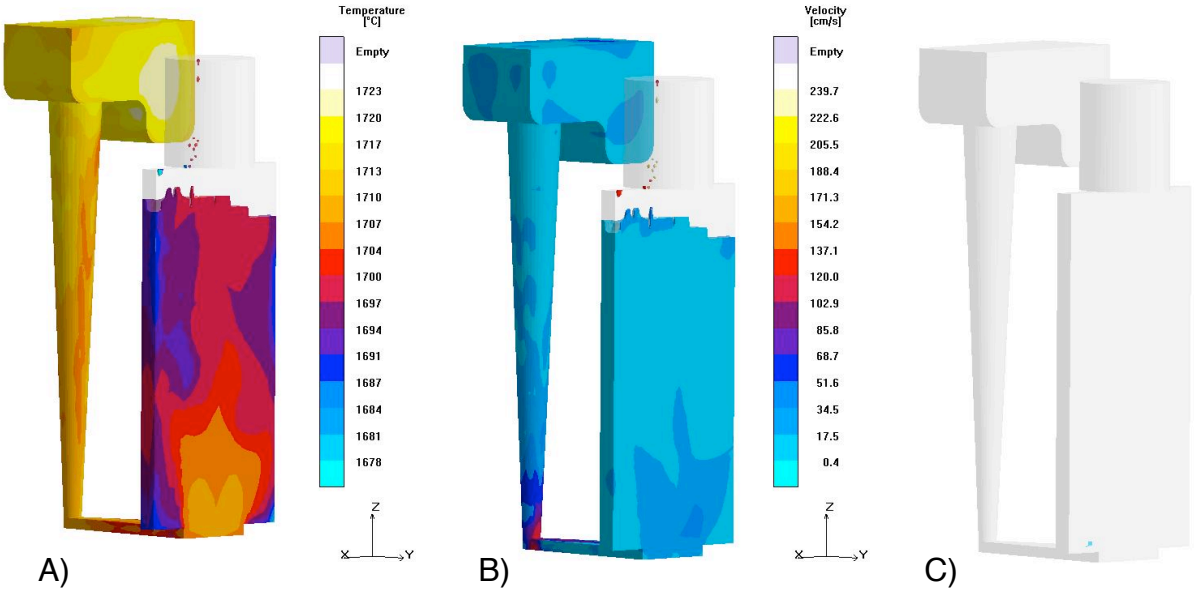

Figure 97. The baseline investment casting, where an alumina particle was placed at the centre of the downsprue opening, at 70% filling; A) fluid coloured with respect to temperature, B) fluid coloured with respect to velocity and C) is the predicted particle location at the time.

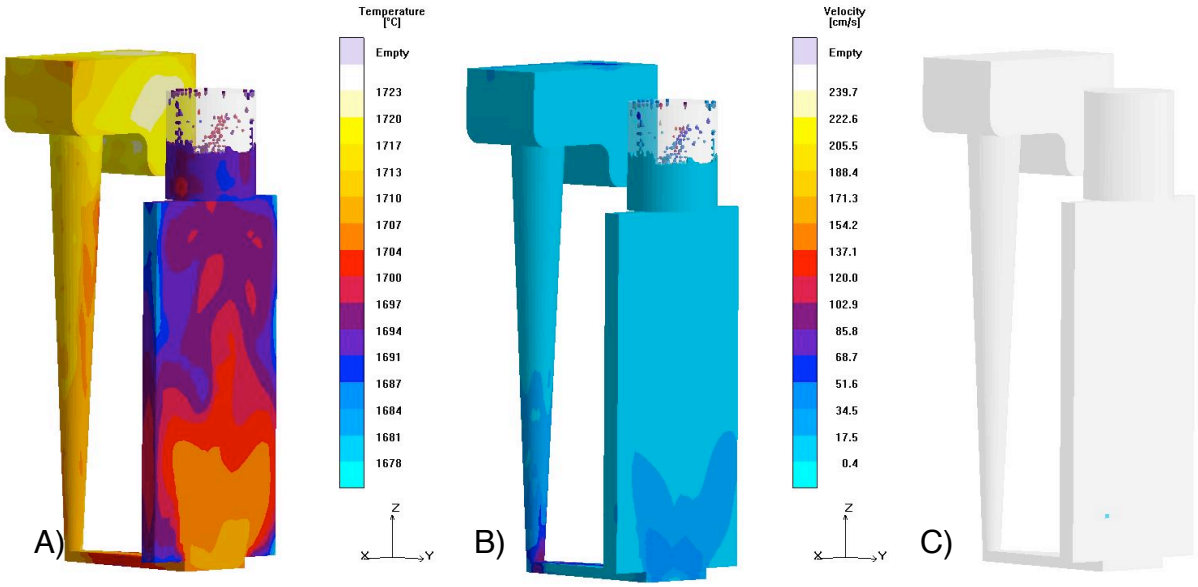

Figure 98. The baseline investment casting, where an alumina particle was placed at the centre of the downsprue opening, at 80% filling.; A) fluid coloured with respect to temperature, B) fluid coloured with respect to velocity and C) is the predicted particle location at the time.

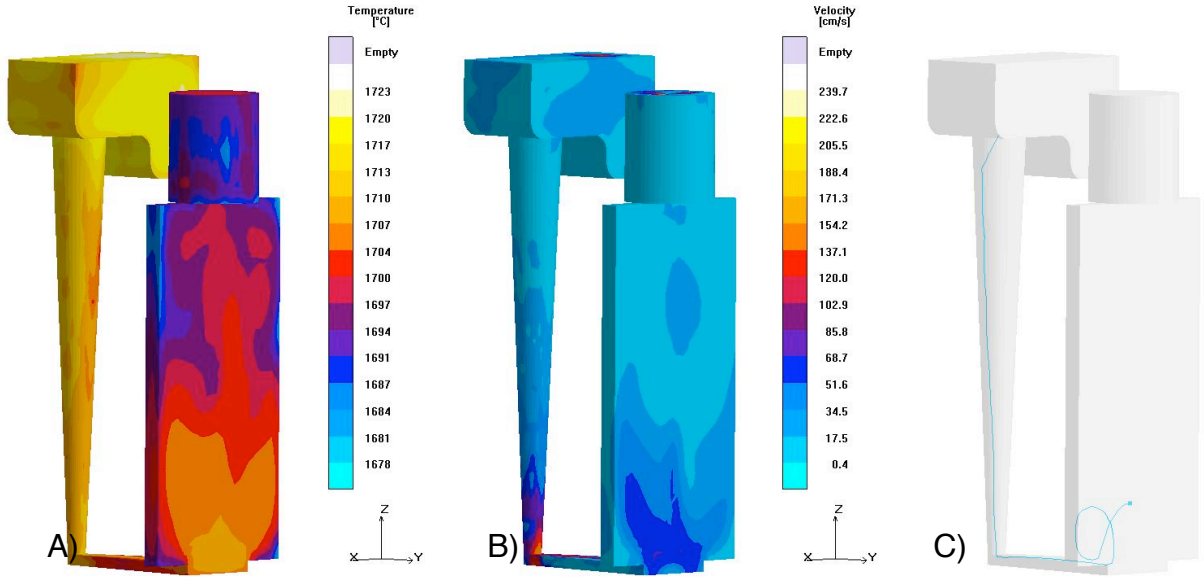

Figure 99. The baseline investment casting, where an alumina particle was placed at the centre of the downsprue opening, 100% full; A) fluid coloured with respect to temperature, B) fluid coloured with respect to velocity and C) is the predicted particle location at the time.

4.4 Particle Tracking Using Low Melting Point Alloy Castings

Low melting point alloys, such as Field's metal and Lensalloy-136 (melting points 62°C and 57.8°C respectively) were used for these experiments so that a full particle path could be obtained because the casting could now take place between the positron camera faces without the risk of damaging the equipment. This meant that smaller particles, of sizes 63-100μm, that are more representative of inclusions in castings could be used and irradiated by ion exchange to achieve higher radioactivities than those previously obtained by direct irradiation.

Figure 100 shows a top view of the low melting point alloy casting (shown in figure 39). The results presented in the following subsections will be described using the left hand side and right hand side directions as shown. The particle location within the tube is described using the angle with reference to the ingate to the tube casting.

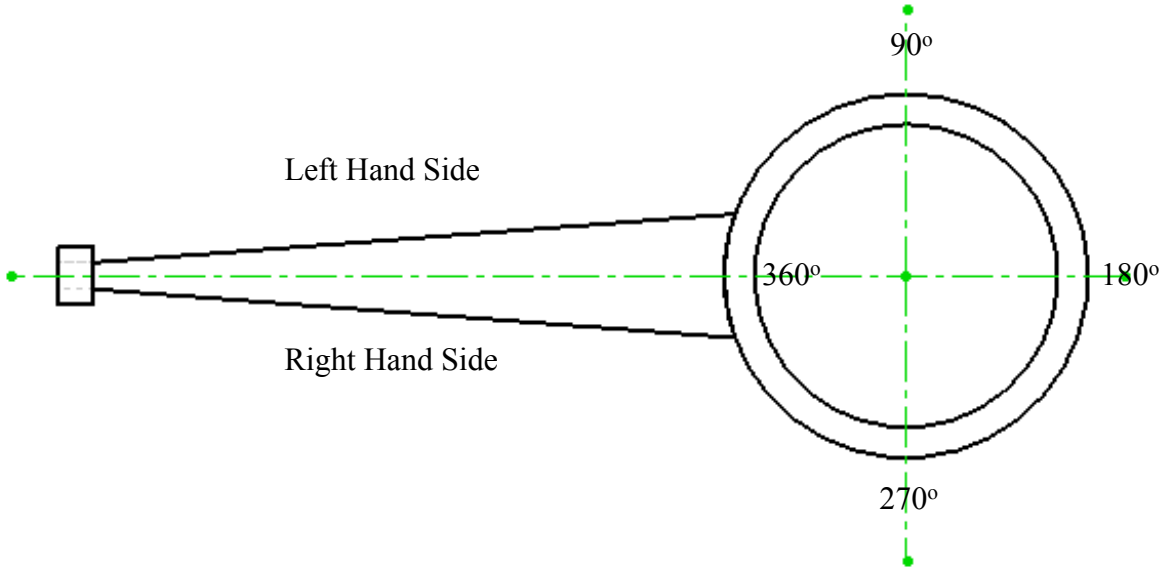

Figure 100. A schematic diagram showing the left and right hand side designation that will be used to describe the results in this section.

4.4.1 Video of the Lensalloy-136 filling the mould versus the PEPT results

Figures 101-118 showed the results obtained from the video of the filling in comparison to the particle track obtained using PEPT, when an alumina particle of size 63-100 μm was initially placed at the centre of the downsprue opening. The liquid metal descended the downsprue, from the right hand side as shown in figures 101 and 102, and advanced evenly along the bottom of the runner bar after which it entered the casting tube cavity. As the liquid metal rose against the acrylic core, the runner bar started to back fill, while the liquid metal passed either side of the core and met again at 180^{o} to the runner bar as shown in figure 103. Figure 104 shows that the particle was entrained within the liquid metal at this stage, 2s filling.

Figures 105 and 106 show that after 3 seconds of filling, the metal in the runner bar was sufficient to form a back-filling wave, while the particle seemed to be at the surface of the rising metal front in the cast tube cavity. The particle seemed to have remained at the surface of the rising metal front until the mould was filled completely after 9 seconds and the particle came to rest at the top surface of the cast tube. Metal flash occurred between the mould faces in the upper half of the mould, with more flash, on a lesser scale, at the exit of the runner bar. Small gas porosities were found at the bottom corners of the end of the downsprue and the upper corners of the runner bar due to the trapped air that failed to escape.

This comparison has shown that although the particle was entrained within the liquid metal at 2 seconds filling, it rose upwards to the rising metal front and came to rest at the top surface of the cast tube. However, due to the small cross section of the tube (5 mm in thickness) and

the expected error in location from the PEPT results (± 1.8 mm), it was difficult to determine wether the particle was at the walls of the cast tube or completely entrained within the liquid metal. Therefore the results obtained from the video recording of the mould could not be used to interpret the PEPT results that are presented in the following sections.

4.6 Numerical Modelling of The Lensalloy-136 Castings Using Flow-3D™

Flow-3D™ was chosen to model the following castings due to its capability of defining a mass and size for a particle, which was not possible with MAGMAsoft™. The models were fluid flow models only, and the simulations stopped when the casting was full.

4.6.1 The Baseline Low Melting Point Alloy Casting

In this model an alumina particle of size 80μm (an average of the size range used in the experiments 63-100μm) was initially placed 30 mm below the centre of the downsprue opening and the effects of having an upper pouring basin and using a stopper rod were simulated. The results obtained are shown in figures 160-189. The total filling time of the mould was 6 seconds, which is 3 seconds less than time used to fill the mould in reality, as demonstrated by the video of the mould filling (see figure 117).

Figure 160 shows the particle being instantly released as the liquid metal reaches the particle position. The alumina particle then descended on the surface of the metal front down the downsprue until the metal front entered the runner bar, as shown in figure 165. The liquid metal moved within roughly 2-3 mm from the bottom surface of the runner bar until it entered the casting tube cavity, where the particle followed after 0.02 seconds. It is difficult to determine whether the particle was within the liquid metal or at the surface due to its small size, which had to be enlarged in the post processor to be visible.

As the liquid metal struck the core forming the tube, it moved along either side of the core to meet again at 180^{o} from the runner bar exit. The particle remained stationary at 70^{o} for roughly 0.3 seconds, figure 174, after which it started moving around at the same level as the rising metal in the tube and reached 150^{o} after 0.8 seconds. At 1.34 seconds filling the particle carried on around the tube while the runner bar started back filling, figure 177. The runner bar was backfilled after 3.5 seconds when the particle was at roughly 250^{o} at the mould wall in the cast tube cavity. The mould was full after 6 seconds and the particle came to rest at 300^{o} at the top of the cast tube.

The pattern in which the liquid metal was predicted to fill the mould was somewhat similar to the real mould filling behaviour as shown in figures 190-207, where the video recording of the mould filling was compared to the modelling results in 2-D. Flow-3D^{TM} predicted a total mould filling time of 6 seconds which was less than the time required to fill the mould experimentally (9 seconds). This is probably attributable to the difference between manual pouring of the metal, where the head pressure can fluctuate in comparison to the constant head pressure considered in the model, which would result in a shorter filling time.

The particle behaviour predicted by the model was not the same as that obtained from the PEPT results. In most cases the particle either moved along the right hand side corner or the left hand side corner of the runner bar until it entered the casting tube cavity, which was similar behaviour to that predicted by the model. However, only two of the castings carried out had the particle come to rest in the top of the casting tube, as the model predicted, while in most cases it came to rest within the lower half of the tube.

The Baseline Casting					
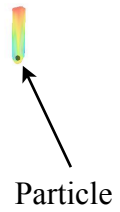	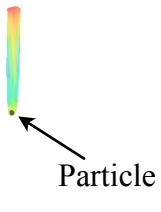	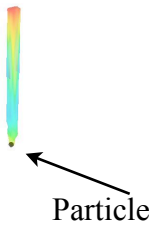	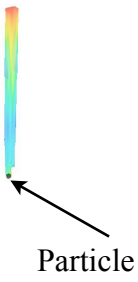	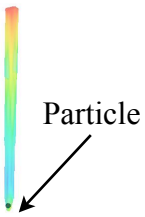	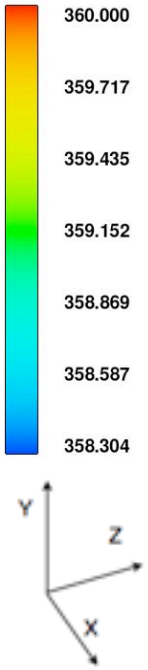
Figure 160 Filling at 0.06s.	**Figure 161 Filling at 0.1s.**	**Figure162 Filling at 0.12s.**	**Figure 163 Filling at 0.16s.**	**Figure 164 Filling at 0.19s.**	**Temperature in Kelvin**
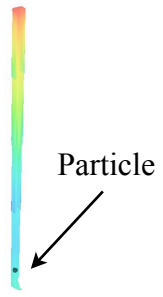	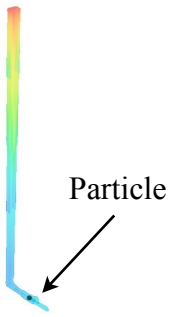	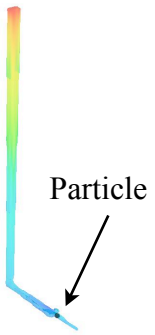	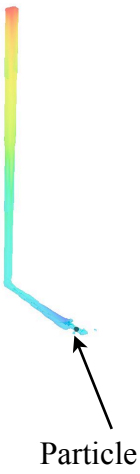		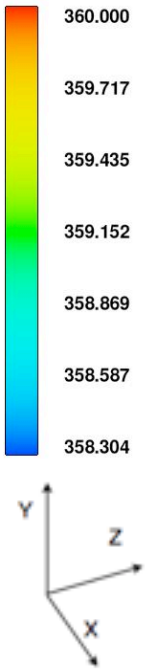
Figure 165 Filling at 0.22s.	**Figure 166 Filling at 0.24s.**	**Figure 167 Filling at 0.26s.**	**Figure 168 Filling at 0.28s.**	**Figure 169 Filling at 0.3s.**	**Temperature in Kelvin**

The Baseline Casting					
			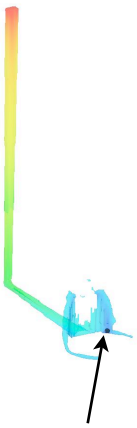		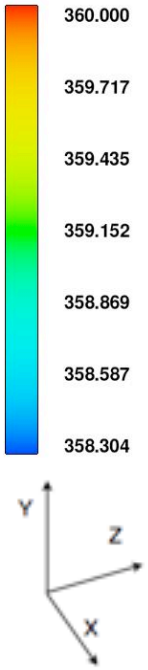
Figure 170 Filling at 0.32s.	**Figure 171 Filling at 0.34s.**	**Figure 172 Filling at 0.36s.**	**Figure 173 Filling at 0.48s.**	**Figure 174 Filling at 0.57s.**	**Temperature in Kelvin**
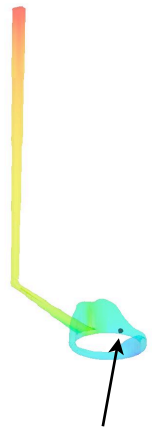	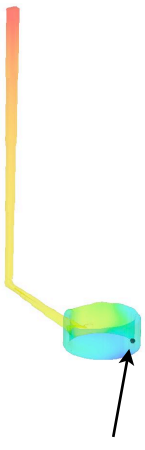	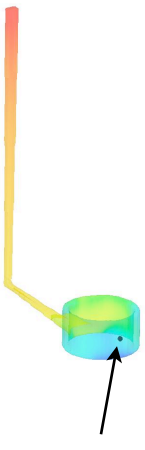	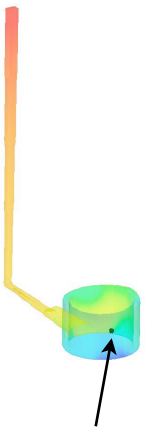		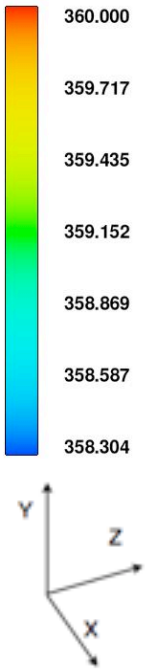
Figure 175 Filling at 0.89s.	**Figure 176 Filling at 1.1s.**	**Figure 177 Filling at 1.34s.**	**Figure 178 Filling at 1.56s.**	**Figure 179 Filling at 1.82s.**	**Temperature in Kelvin**

The Baseline Casting

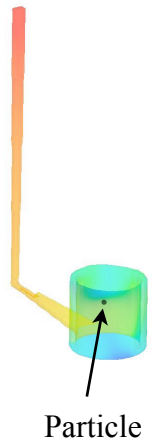

Figure 180
Filling at 2.04s.

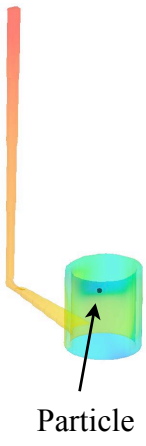

Figure 181
Filling at 2.5s.

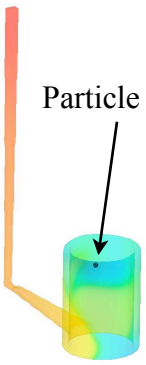

Figure 182
Filling at 2.8s.

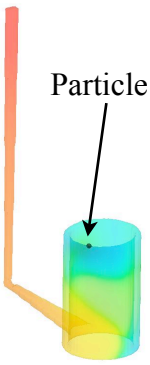

Figure 183
Filling at 2.94s.

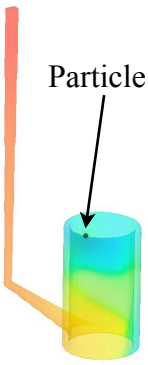

Figure 184
Filling at 3.5s.

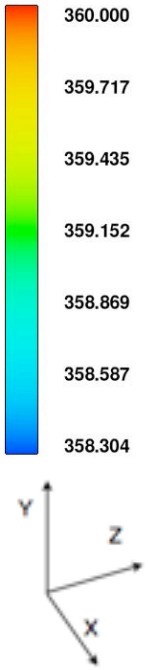

Temperature in Kelvin

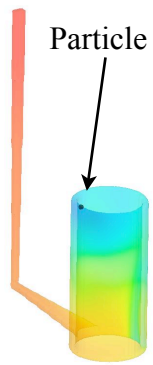

Figure 185
Filling at 4s.

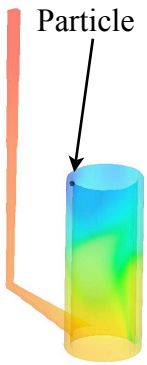

Figure 186
Filling at 5s.

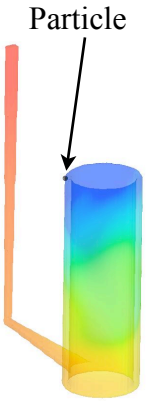

Figure 187
Filling at 5.5s.

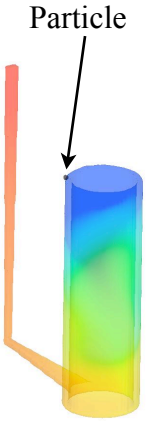

Figure 188
Filling at 6s.

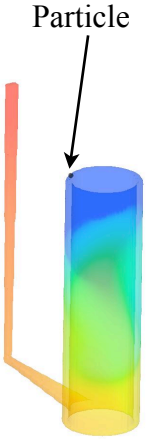

Figure 189
Filling at 6.1s.

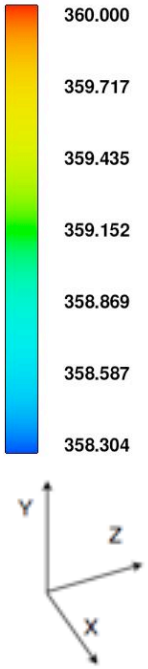

Temperature in Kelvin

Table 26. A comparison between the fluid flow behaviour observed from the video of the mould filling and the predicted fluid flow behaviour obtained from the Flow-3D™ model.x

Mould Filling Video	Modelling Results Obtained Using Flow-3D™	
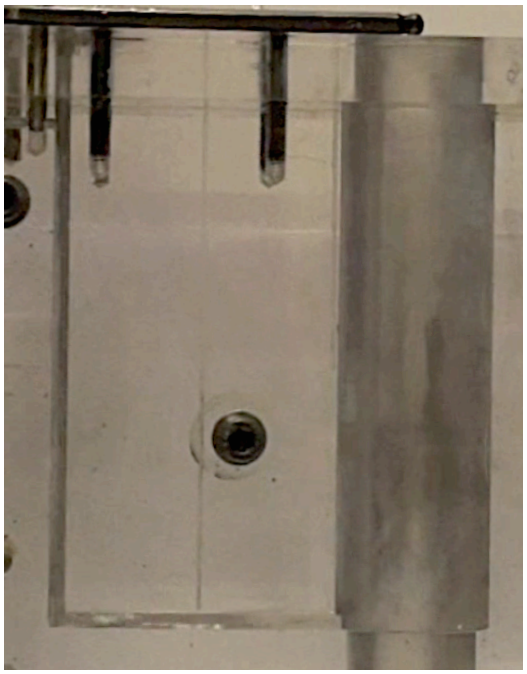	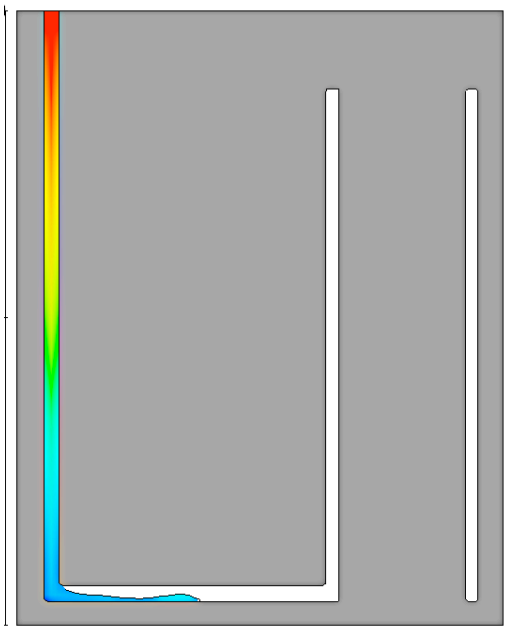	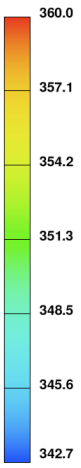
Figure 190. The acrylic mould filling at 1s.	**Figure 191. Flow-3D model of the filling at 0.22s.**	**Temp. (K)**
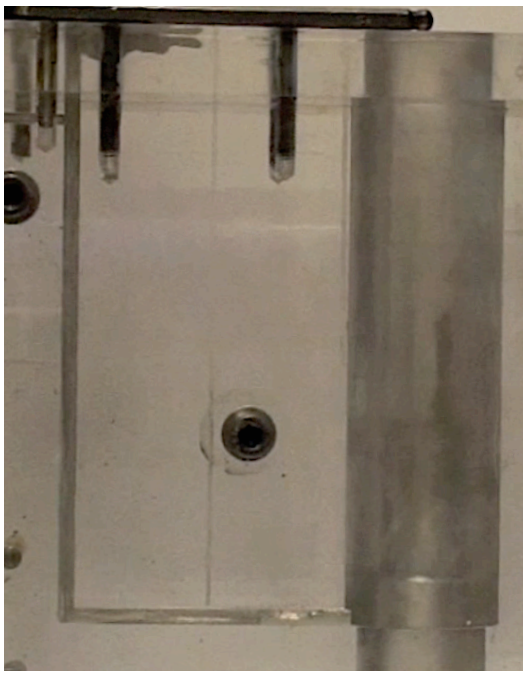	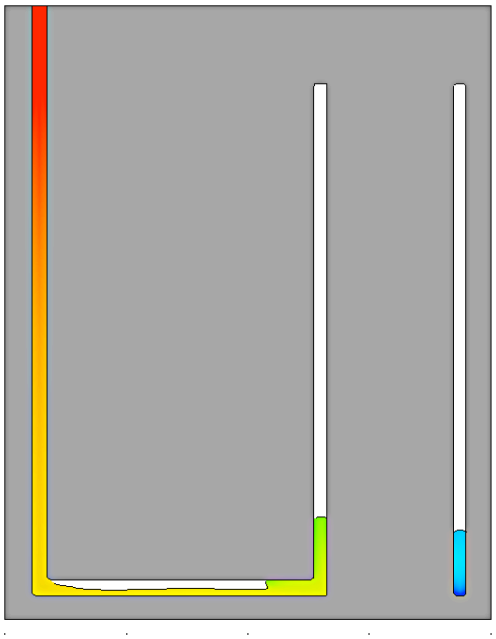	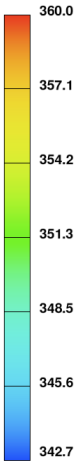
Figure 192. The acrylic mould filling at 2s.	**Figure 193. Flow-3D model of the filling at 1s.**	**Temp. (K)**

Mould Filling Video	Modelling Results Obtained Using Flow-3D™	
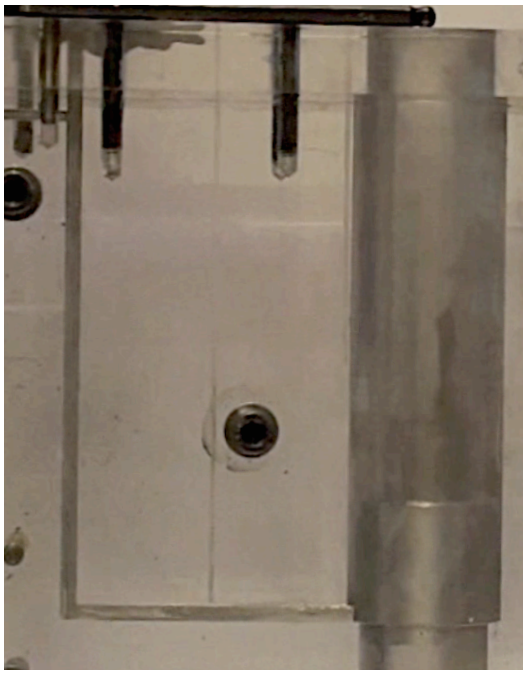	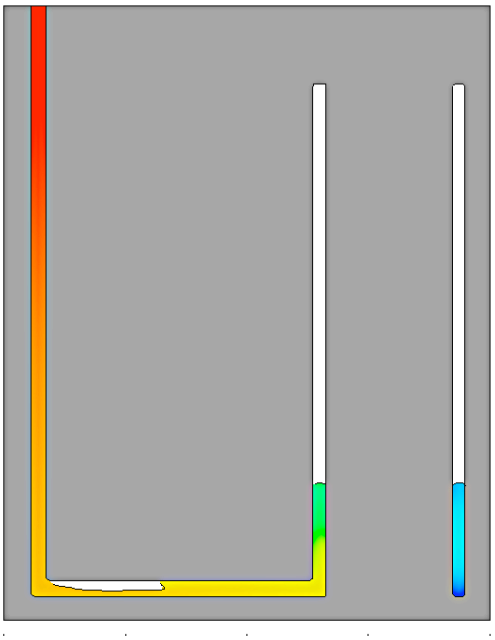	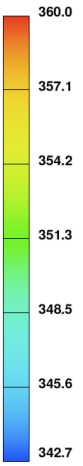
Figure 194. The acrylic mould filling at 3s.	**Figure 195. Flow-3D model of the filling at 1.5s.**	**Temp. (K)**
	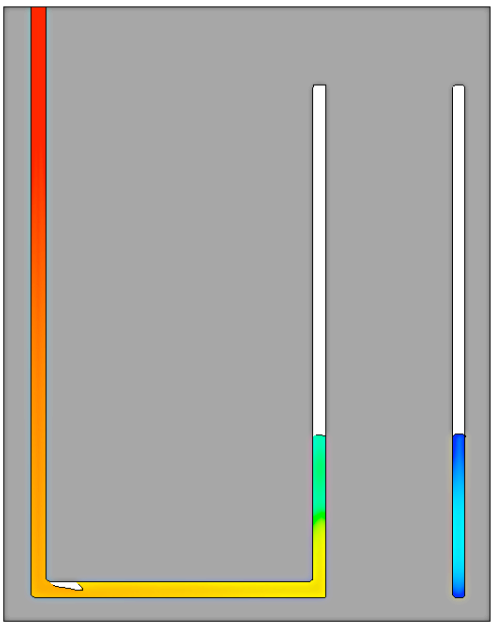	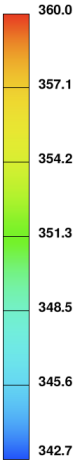
Figure 196. The acrylic mould filling at 4s.	**Figure 197. Flow-3D model of the filling at 2.01s**	**Temp. (K)**

Mould Filling Video	Modelling Results Obtained Using Flow-3D™	
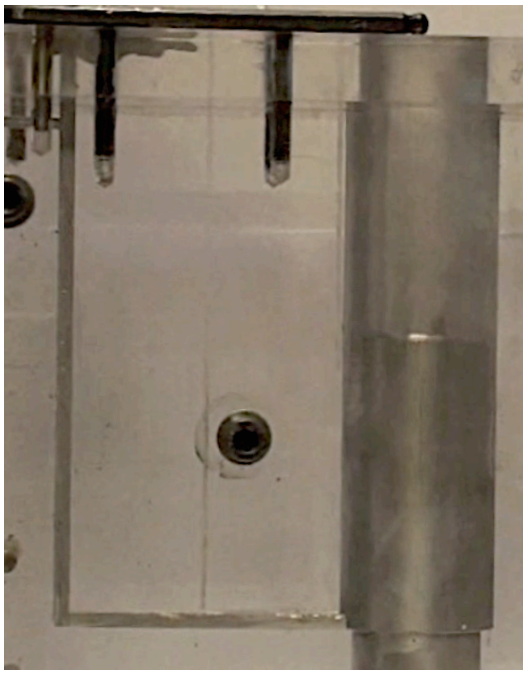	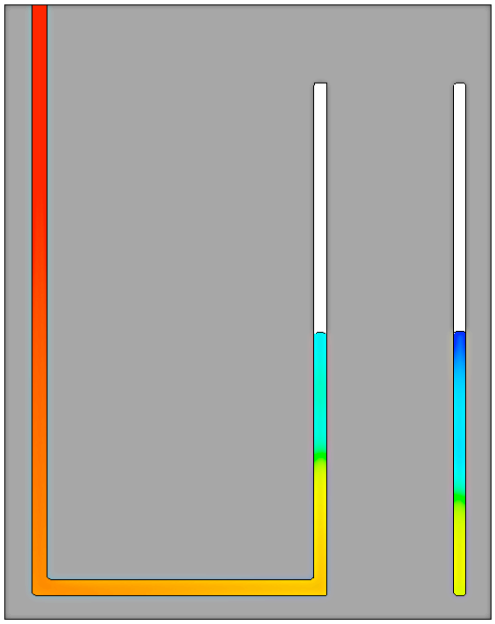	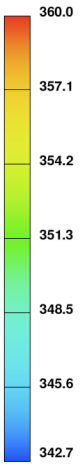
Figure 198. The acrylic mould filling at 5s.	**Figure 199. Flow-3D model of the filling at 3s.**	**Temp. (K)**
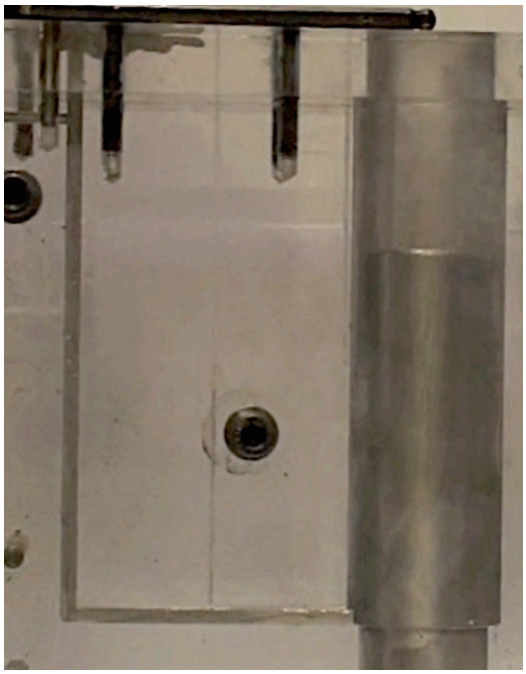	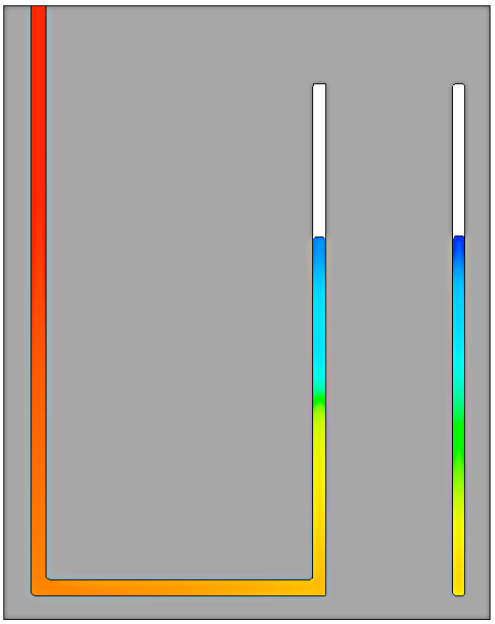	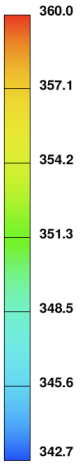
Figure 200. The acrylic mould filling at 6s.	**Figure 201. Flow-3D model of the filling at 4s.**	**Temp. (K)**

Mould Filling Video	Modelling Results Obtained Using Flow-3D™	
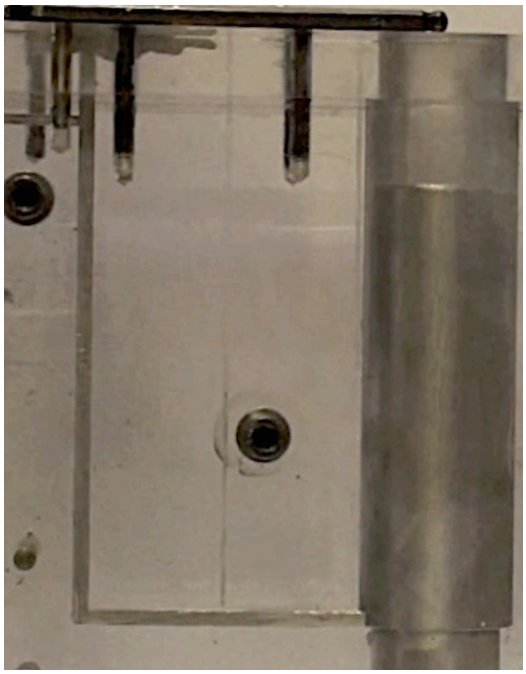	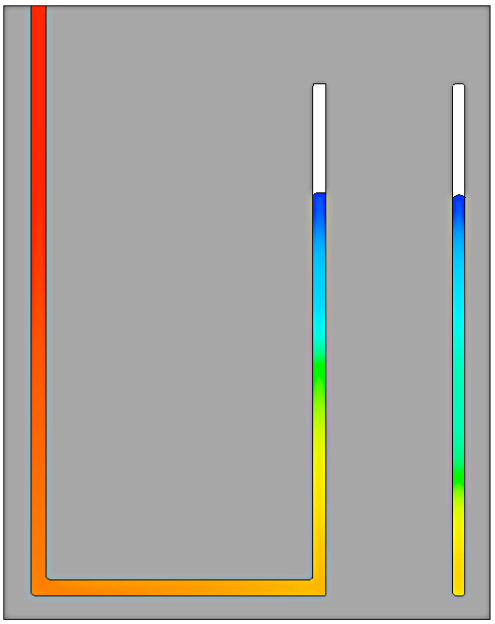	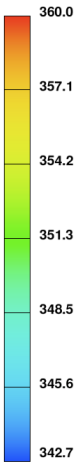
Figure 202. The acrylic mould filling at 7s.	**Figure 203. Flow-3D model of the filling at 4.5s**	**Temp. (K)**
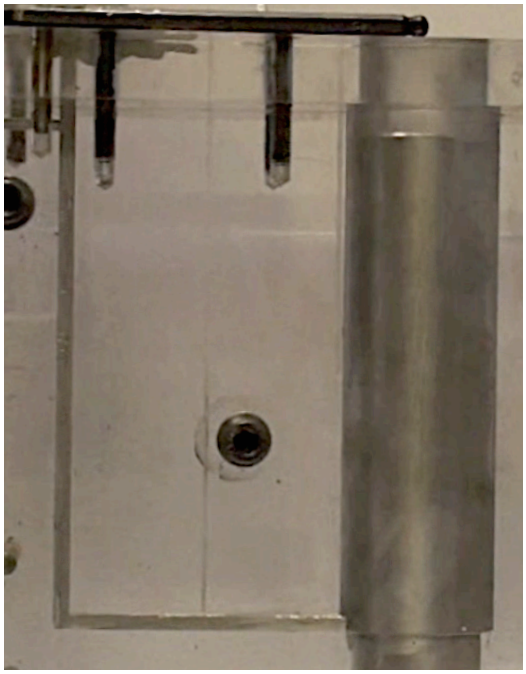	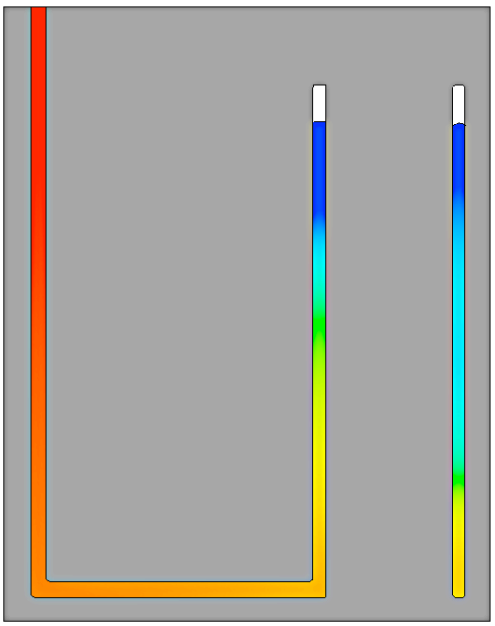	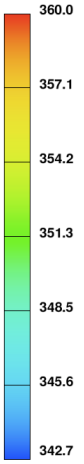
Figure 204. The acrylic mould filling at 8s.	**Figure 205. Flow-3D model of the filling at 5.5s.**	**Temp. (K)**

Mould Filling Video	Modelling Results Obtained Using Flow-3D™	
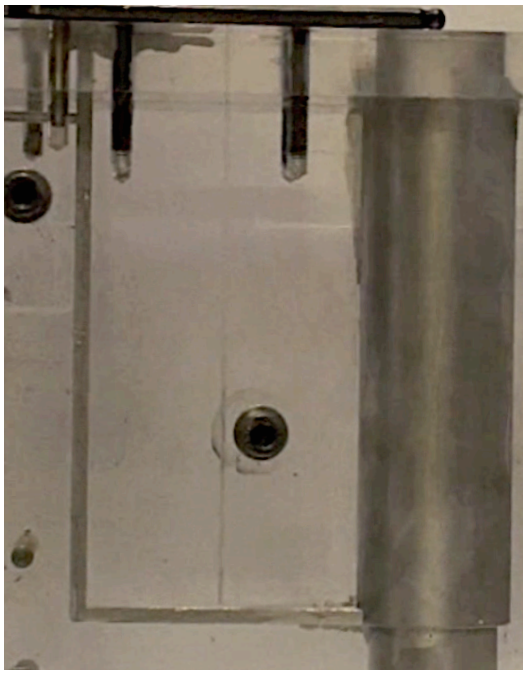	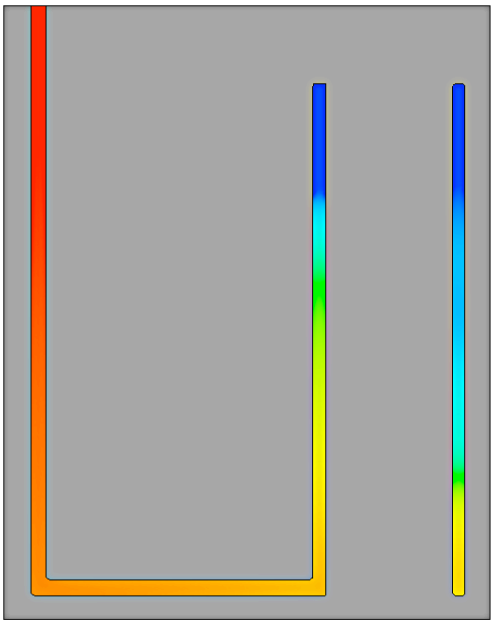	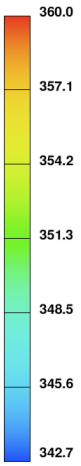
Figure 206. The acrylic mould filling at 9s.	**Figure 207. Flow-3D model of the filling at 6.1s.**	**Temp. (K)**

4.6.2 The Effects of Changing The Initial Position

The results obtained from the low melting point alloy casting that was modelled and described in the previous subsection, were compared to two other models where the particle initial position was varied in the X-direction and Y-direction respectively. Figures 208-247 show the modelled particle path during mould filling, when the X-coordinate was varied. The filling of the mould was not significantly changed, only the particle path and the particle final location were affected by changing the particle initial position.

A difference in particle path was first observed at 0.2 seconds, figure 208 where the particle seemed to be at the left hand side of the downsprue rather than in the centre. The particle then entered the runner bar and stayed on the left hand side while advancing towards the casting tube cavity as has been shown in figures 209-212. Figures 218-220 showed that as the metal started filling the tube cavity the particle moved around in a roughly 10mm circle until it started moving around the tube wall in a clockwise direction at 1.34s, figure 222. The particle maintained a clockwise direction while rising with the liquid metal where it moved from approximately 130^{o} to 190^{o} in approximately 0.6 seconds. The particle finally came to rest, at 290^{o}, at the top surface of the cast tube after 6 seconds, see figure 227.

The results obtained from the model where the Y-coordinate of the initial position was varied by 1mm is shown in figures 228-247. The particle behaviour in the downsprue and the runner bar was similar to the model where the X-direction was varied and different to the baseline model. As the particle entered the cast tube cavity at 0.3 seconds, it moved clockwise on the

left hand side until it reached 180° at 0.53 seconds, figure 236. The particle then moved anticlockwise while rising as the metal filled the mould and reached roughly 70° at 1 second. The particle then continued to rise with the metal while being between 110-120°, and finally came to rest when the mould was completely filled.

Therefore small changes in the particle's initial position were predicted to lead to a large difference to its final location. The particle's final location was roughly 180° different when the X and Y coordinates were changed by 1mm each and in both cases 10° and 190° different to the final location obtained from the baseline model. Figure 248 shows the superimposition of the final particle location predicted in the baseline model as well as that predicted when the initial position was varied by 1 mm in the X and Y directions, on one casting for comparison.

This suggests that to achieve reproducibility in the experiments, the initial particle location must be reproduced to better than ± 1mm. This is clearly very difficult to achieve practically and demonstrates the sensitivity of the available modelling packages to user input.

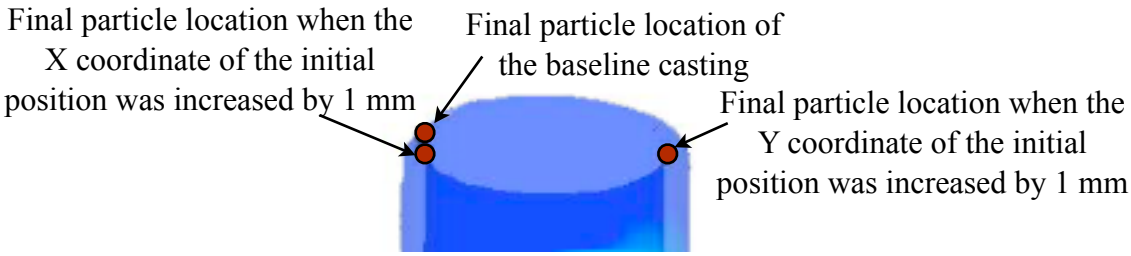

Figure 248. The final particle positions predicted for the baseline casting, as well as when the initial position was varied by 1 mm in the X and Y directions, superimposed on the same casting for comparison.

The Effect of Changing The Initial Particle Position in The X-Coordinate					
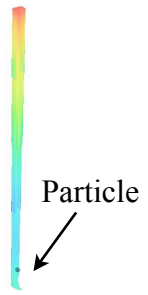	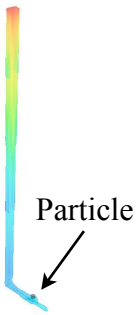		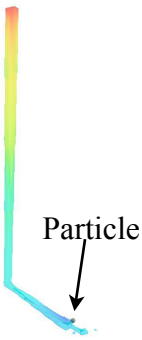		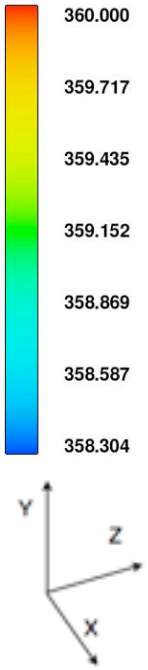
Figure 208 Filling at 0.2s.	**Figure 209 Filling at 0.22s.**	**Figure 210 Filling at 0.24s.**	**Figure 211 Filling at 0.26s.**	**Figure 212 Filling at 0.3s.**	**Temperature in Kelvin**
				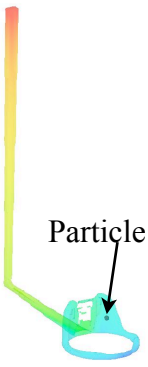	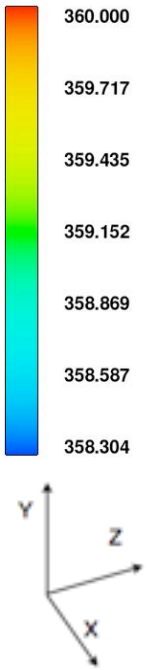
Figure 213 Filling at 0.32s.	**Figure 214 Filling at 0.34s.**	**Figure 215 Filling at 0.36s.**	**Figure 216 Filling at 0.37s.**	**Figure 217 Filling at 0.5s.**	**Temperature in Kelvin**

The Effect of Changing The Initial Particle Position in The X-Coordinate					
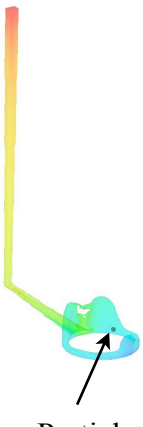	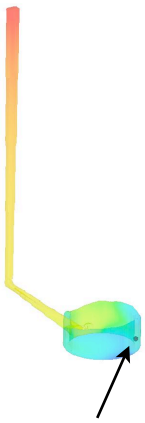		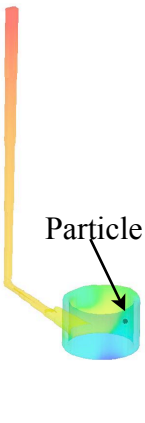		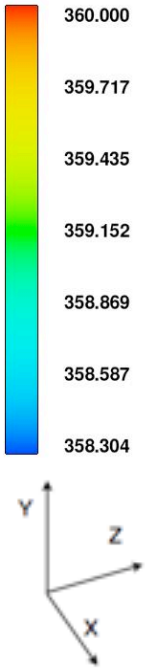
Figure 218 Filling at 0.56s.	**Figure 219 Filling at 0.9s.**	**Figure 220 Filling at 1s.**	**Figure 221 Filling at 1.2s.**	**Figure 222 Filling at 1.34s.**	**Temperature in Kelvin**
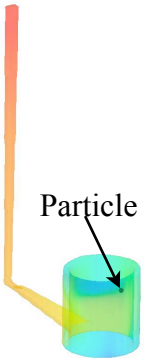	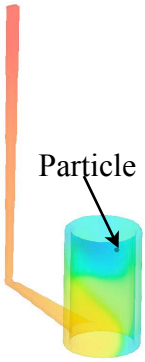	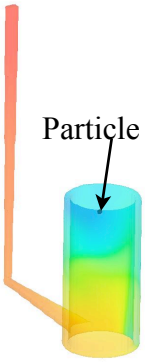	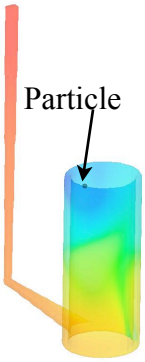	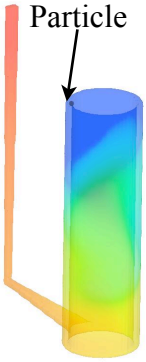	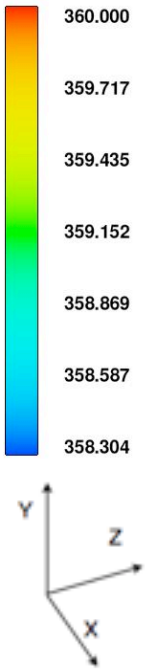
Figure 223 Filling at 1.8s.	**Figure 224 Filling at 2.5s.**	**Figure 225 Filling at 3.5s.**	**Figure 226 Filling at 4s.**	**Figure 227 Filling at 6.1s.**	**Temperature in Kelvin**

The Effect of Changing The Initial Particle Position in The Y-Coordinate					
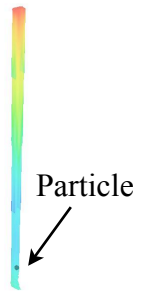	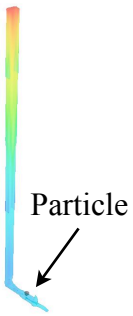				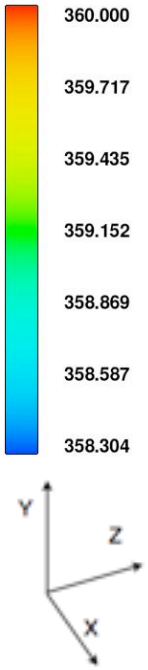
Figure 228 Filling at 0.2s.	**Figure 229 Filling at 0.22s.**	**Figure 230 Filling at 0.24s.**	**Figure 231 Filling at 0.26s.**	**Figure 232 Filling at 0.3s.**	**Temperature in Kelvin**
			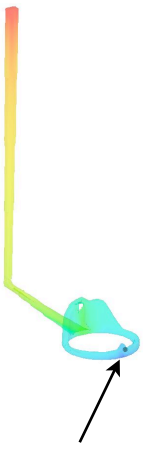	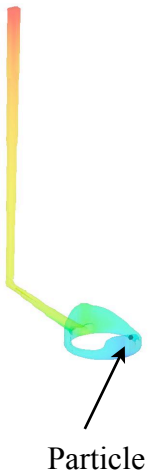	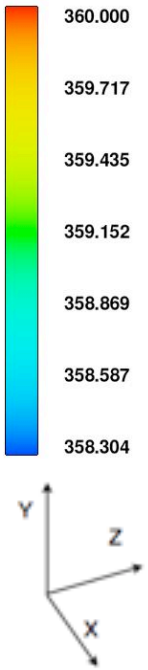
Figure 233 Filling at 0.33s.	**Figure 234 Filling at 0.38s.**	**Figure 235 Filling at 0.42s.**	**Figure 236 Filling at 0.53s.**	**Figure 237 Filling at 0.62s.**	**Temperature in Kelvin**

The Effect of Changing The Initial Particle Position in The Y-Coordinate					
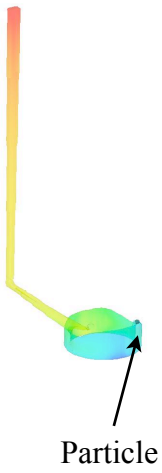	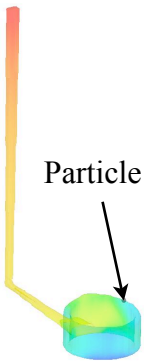	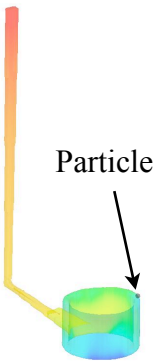	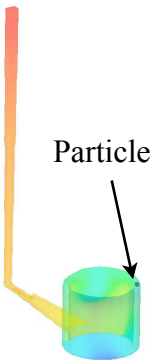	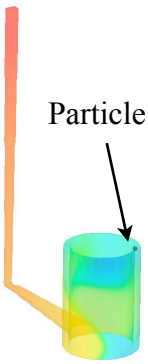	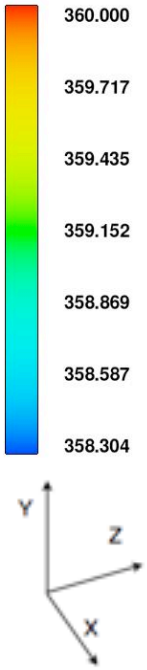
Figure 238 Filling at 0.73s.	**Figure 239 Filling at 1s.**	**Figure 240 Filling at 1.3s.**	**Figure 241 Filling at 1.7s.**	**Figure 242 Filling at 2.5s.**	**Temperature in Kelvin**
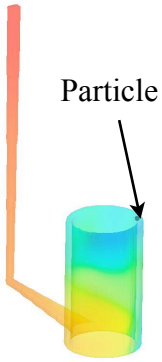	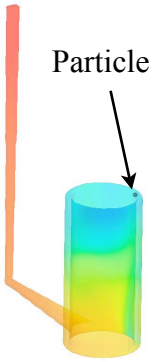	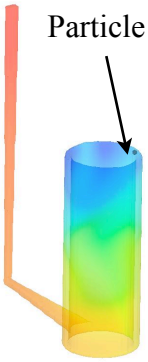	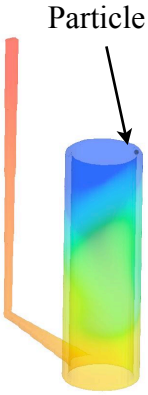	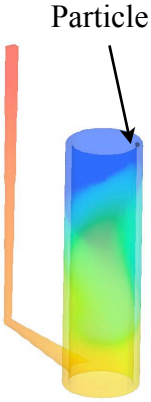	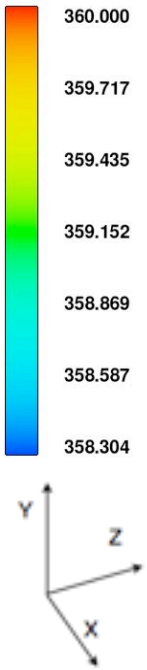
Figure 243 Filling at 3s.	**Figure 244 Filling at 3.5s.**	**Figure 245 Filling at 4.5s.**	**Figure 246 Filling at 5.5s.**	**Figure 247 Filling at 6s.**	**Temperature in Kelvin**

4.6.3 The Effects of Changing The Coefficient of Restitution

The coefficient of restitution is a number which describes how much kinetic energy is lost due to the collision of two objects in the 3D model. If the coefficient is high (close to 1.0), it means that a negligible amount of kinetic energy was lost. If the coefficient was very low (close to 0), it means that a large fraction of kinetic energy was lost due to the collision. Flow-3D™ allowed the user to input this value and hence the effects of changing it were investigated.

The coefficient of restitution was changed from the default value of 0.5 to -1 ,0 and 1 respectively. The results obtained from each model are shown in figures 250-265. When the coefficient of restitution was set to -1, (figures 249-250), the particle stopped on its first contact with the mould. However when the coefficient of restitution was set to 0, (figures 254-258), the particle behaved almost exactly as it did in the baseline experiment model, where it came to rest at roughly 290^{o} at the top surface of the cast tube.

Figures 259-264 show the results obtained when the coefficient of restitution was set to 1. The particle path was very similar to the initial model where the particle entered the casting tube cavity from the left hand side and continued to move clockwise while rising until it came to rest at roughly 320^{o} at the top of the cast tube.

This investigation showed that the coefficient of restitution is an important factor that is needed to be known in order to reproduce the real experiment in the model and obtain more reliable results.

The Effect of Changing The Coefficient of Restitution; R=-1					
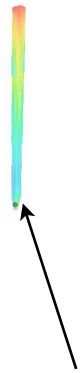	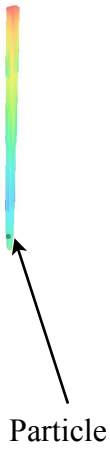	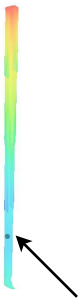	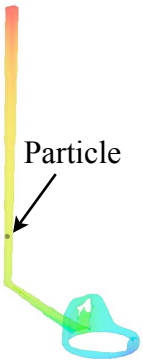	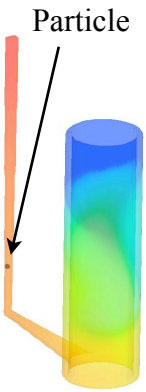	
Figure 249 Filling at 0.2s.	**Figure 250 Filling at 0.24s.**	**Figure 251 Filling at 0.26s.**	**Figure 252 Filling at 0.5s.**	**Figure 253 Filling at 6s.**	**Temperature in Kelvin**

The Effect of Changing The Coefficient of Restitution; R=0					
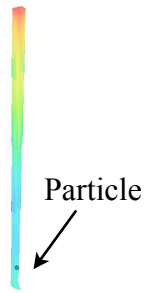		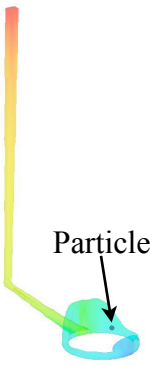	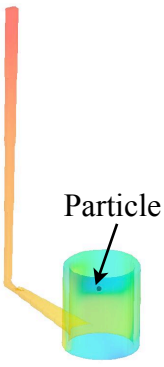	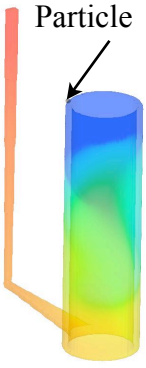	
Figure 254 Filling at 0.22s.	**Figure 255 Filling at 0.24s.**	**Figure 256 Filling at 0.5s.**	**Figure 257 Filling at 1.5s.**	**Figure 258 Filling at 6s.**	**Temperature in Kelvin**

The Effect of Changing The Coefficient of Restitution; R=1					
	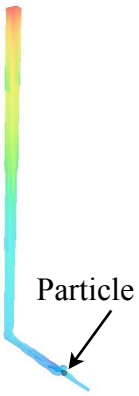		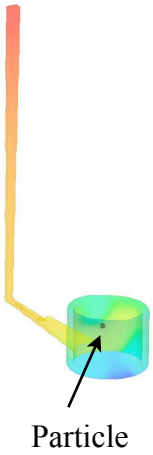	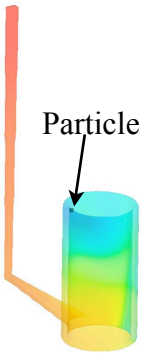	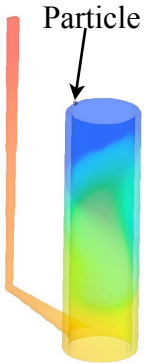
Figure 259 Filling at 0.2s.	**Figure 260 Filling at 0.24s.**	**Figure 261 Filling at 0.32s.**	**Figure 262 Filling at 1.5s.**	**Figure 263 Filling at 3.2s.**	**Figure 264 Filling at 6s.**

4.7 Multiple Particle Tracking

4.7.1 Assessment of the NTrack algorithm

The first assessment of the NTrack algorithm was carried out to verify whether a large number of particles, in this case 7, can be located accurately at the same time. The particles used were alumina particles, 4mm in diameter and were irradiated by ion exchange. Figure 265 shows the algorithm successfully determined the locations of 7 stationary particles. It is however clear that there is a large scatter near the central particle which demonstrates the difficulty in identifying particles when they were close to each other (the central particle was 25 mm from the nearest 2 particles).

A second assessment of the algorithm was carried out to determine the minimum separation distance between particles required to obtain accurate tracking results. Figure 266 showed the result obtained when a particle was moved from position 2 towards another stationary particle in position 1, the centre. Figures 267-269 are the X,Y and Z coordinates for both particles, plotted versus time. It was found that both particles were distinguishable, until they were about 4mm apart in the X direction and 2mm apart in the Y and Z directions. These values for the minimum separation distance were obtained by measuring the minimum distance h after which the particles became indistinguishable from each other (indistinguishable means having the coordinates of one particle assigned to the other and vice versa), as shown in figure 267. Figures 267-269 also showed some scattered points on the path of the stationary particle(s)

that were falsely assigned to the path of the moving particle by the algorithm. The recorded error was ± 1.3 and 1.6 mm for the stationary and moving particles respectively.

Figure 270 shows the results obtained when a third particle was placed at position 2 and moved towards the two stationary particles in the centre (the two particles that were previously pushed together in the centre). The moving particle was very faint (a lower detection events per second due to the lower radioactivity) compared to the two central particles. Figures 271-273 showed that the 2 stationary particles in the centre could not be distinguished from each other and that the moving particle was only distinguishable until it was 5mm apart in the X direction, 4mm apart in the Y direction and 6mm apart in the Z direction. Figure 273 also showed an increased scatter around the location of the 2 stationary particles.

A fourth particle was then introduced and initially placed at position 3 after which it was moved towards the 3 stationary particles in the centre. The tracking result obtained is shown in figure 274 where the moving particle is much fainter than the stationary particles in the centre. The moving particle was not clearly distinguishable when it was 10mm away from the stationary particles in the X direction, 5mm apart in the Y direction and 15mm apart in the Z direction.

Furthermore, a fifth particle was placed in position 2 and moved towards the 4 particles in the centre. The results obtained are shown in figures 278-281, where it was determined that the

minimum separation distance required to distinguish the moving particle clearly was in this case, 10mm, 5mm and 10mm in the X,Y and Z directions respectively.

Figure 282 depicts another iteration where a sixth particle was placed in position 3 and moved towards the 5 particles at the centre. The moving particle in this case was distinguishable only in the X and Z directions, as shown in figures 283 and 285, when it was 20mm and 10mm apart respectively. The particle's location could not be differentiated in the Y-Direction.

Finally, a seventh particle was placed in position 5 and moved towards the 6 stationary particles in the centre where the tracking results are shown in figures 286-289. Again the particle's location could only be differentiated in the X and Z directions, figures 287 and 289, where the minimum separation distance was determined to be 15mm and 10mm respectively.

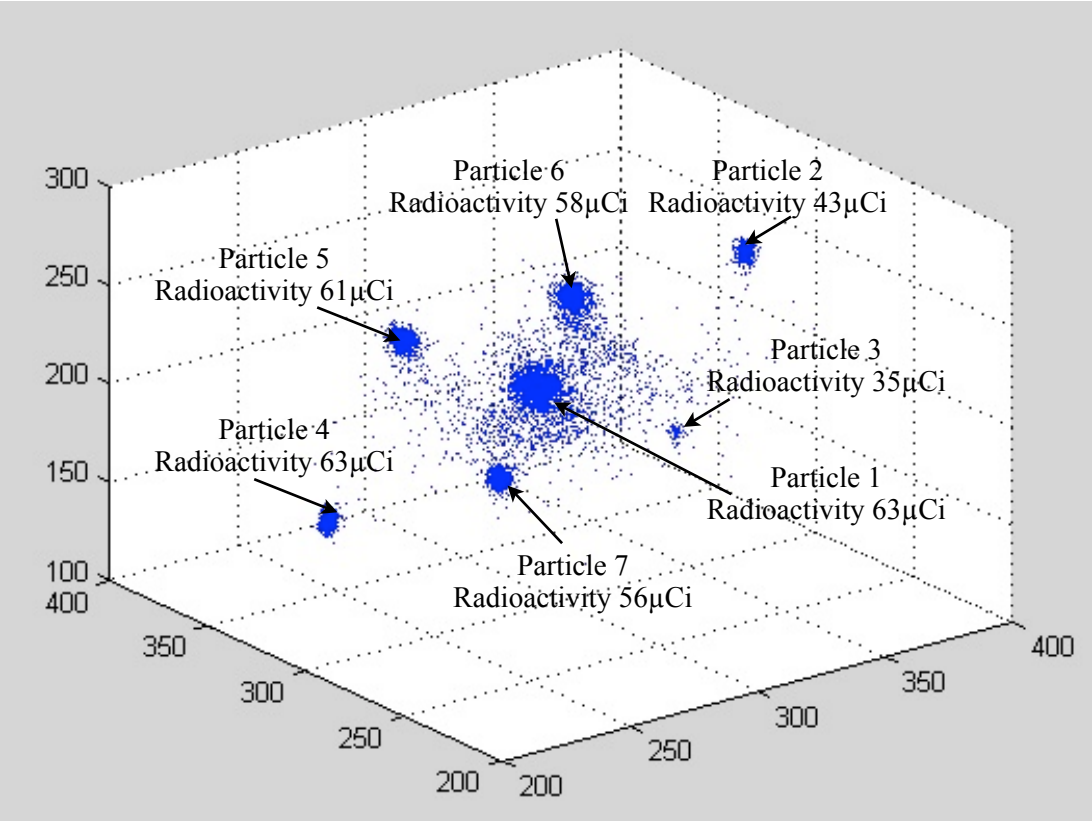

Figure 265. The tracking result obtained showing all of the 7 stationary particles in their positions.

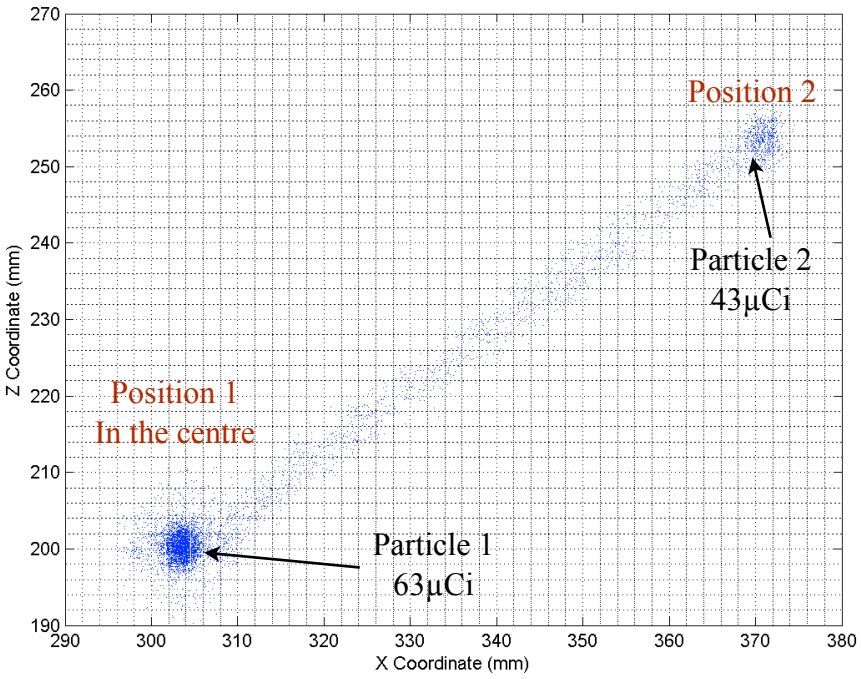

Figure 266. A 2D plot of a particle moved from position 2 towards the stationary particle in the centre.

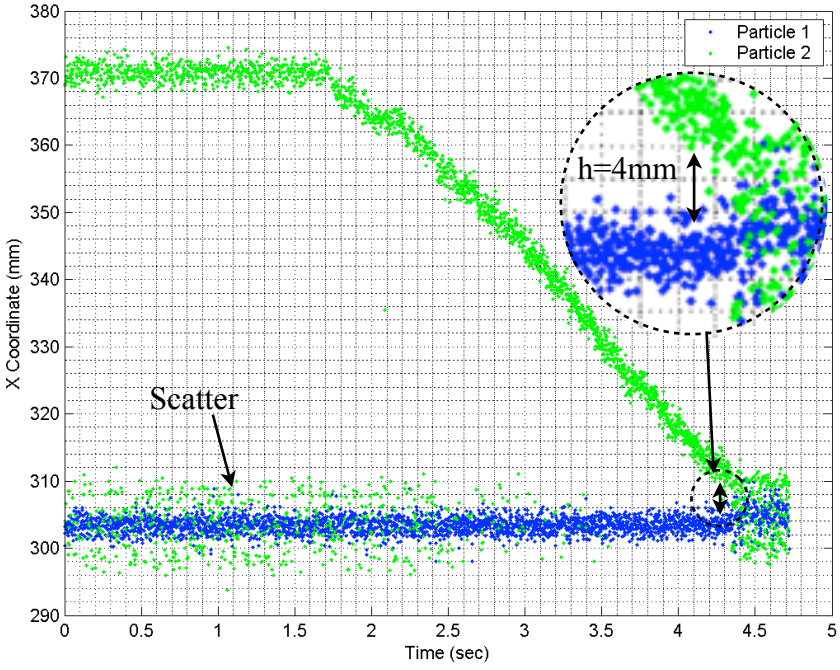

Figure 267. A location vs. time plot, showing the X-coordinates of the moving and stationary particles.

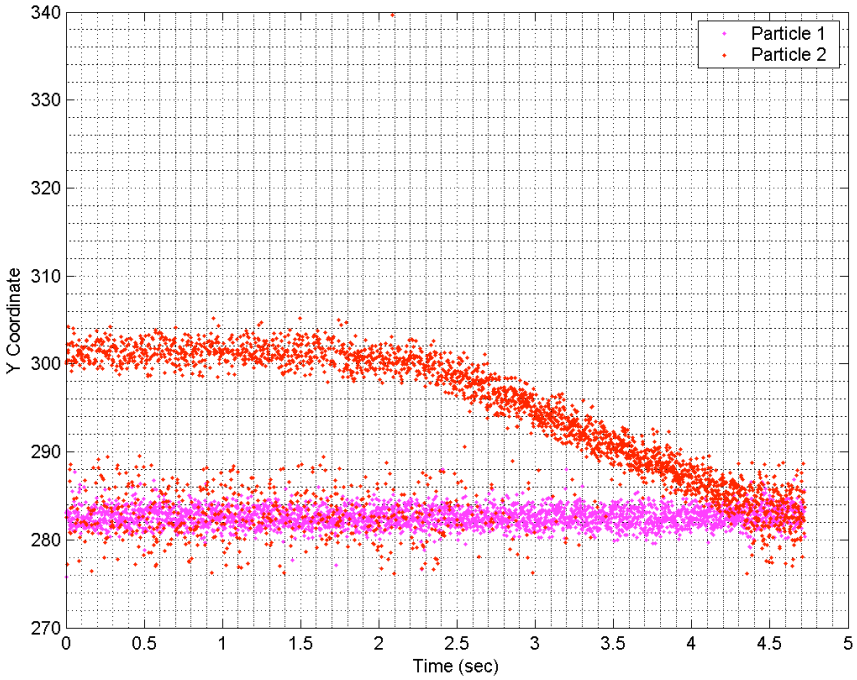

Figure 268. A location vs. time plot, showing the Y-coordinates of the moving and stationary particles.

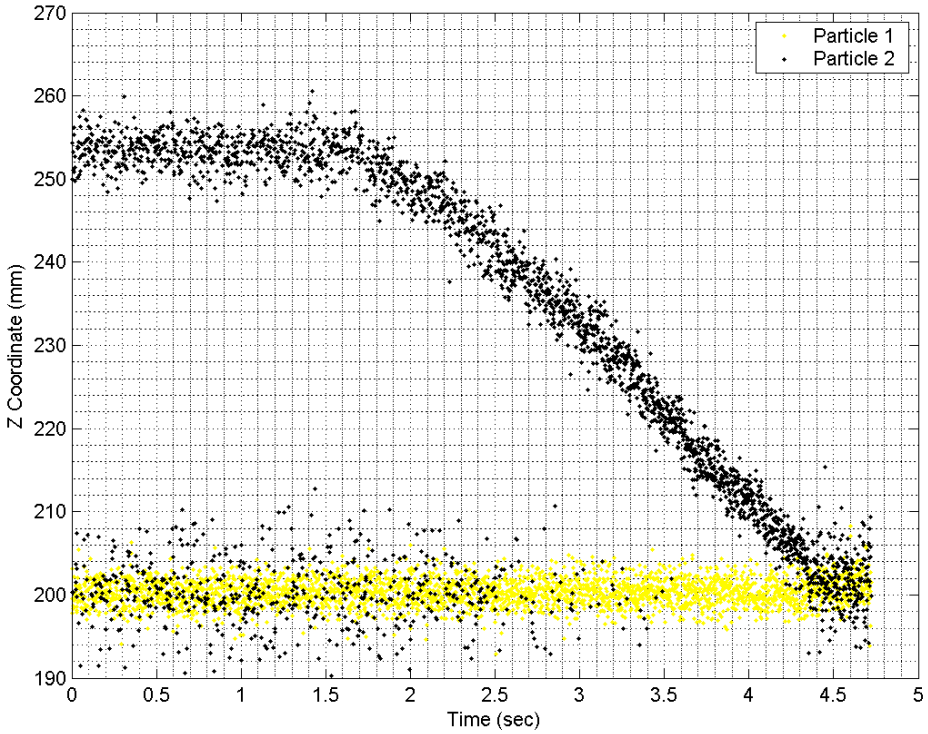

Figure 269. A location vs. time plot to showing the Z-coordinates of the moving and stationary particles.

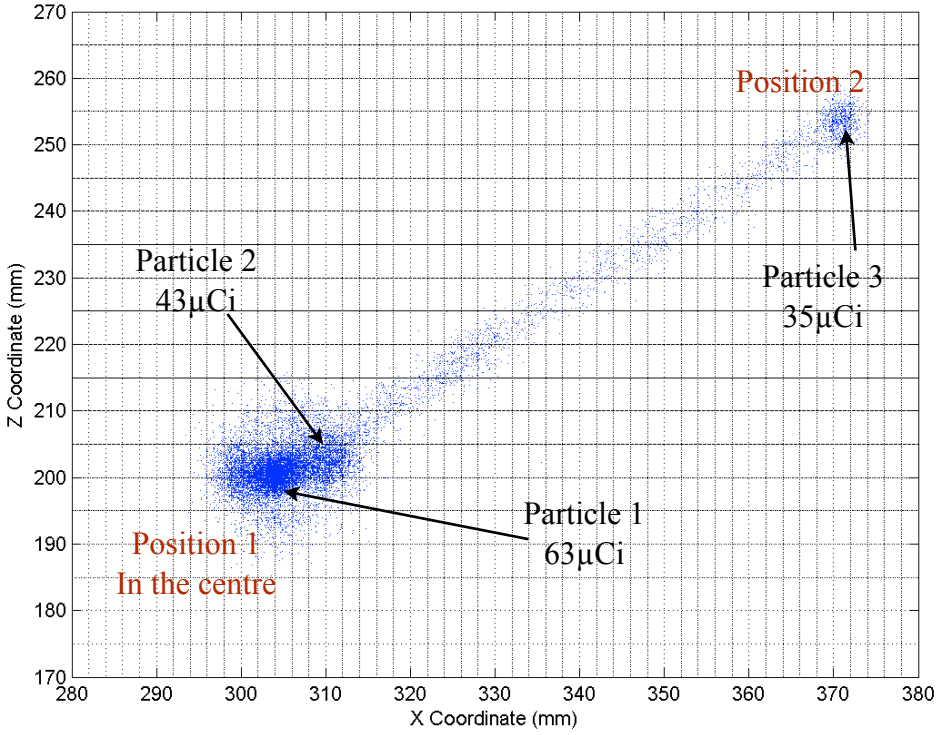

Figure 270. A 2D view of the 3rd particle being moved towards the 2 particles in the centre of the wood board.

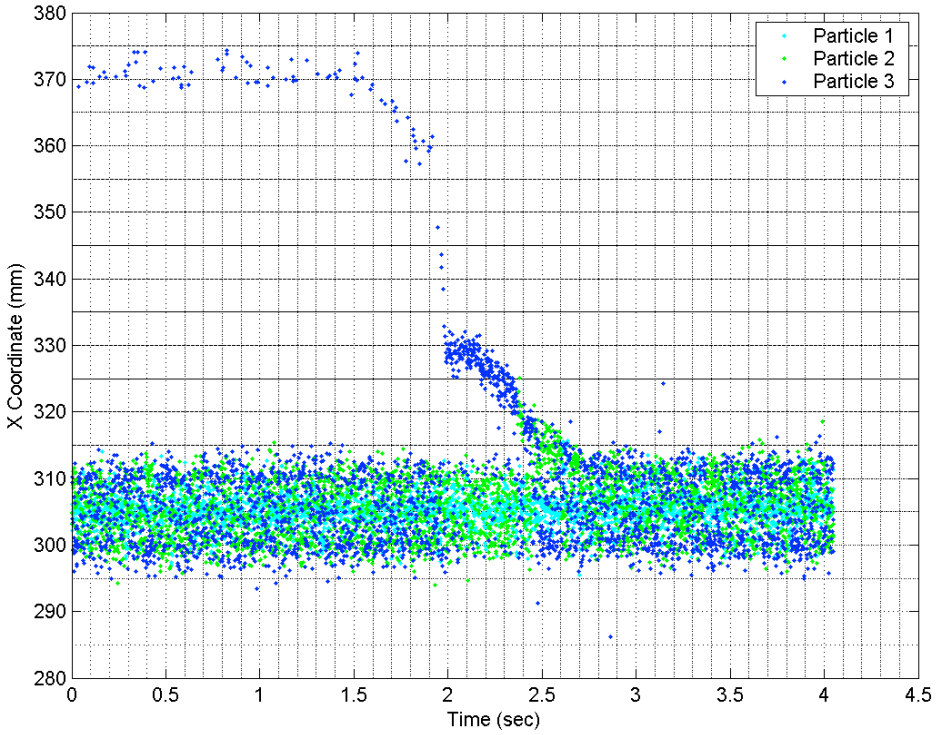

Figure 271. The X-coordinates plotted against time for 3 particles.

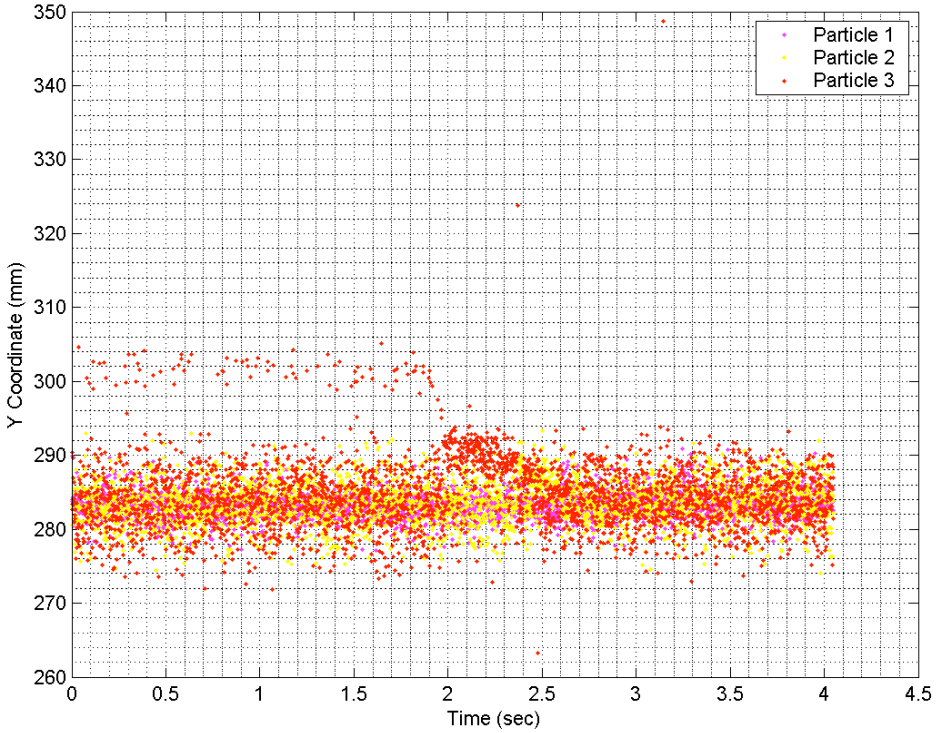

Figure 272. The Y-coordinates plotted against time for 3 particles.

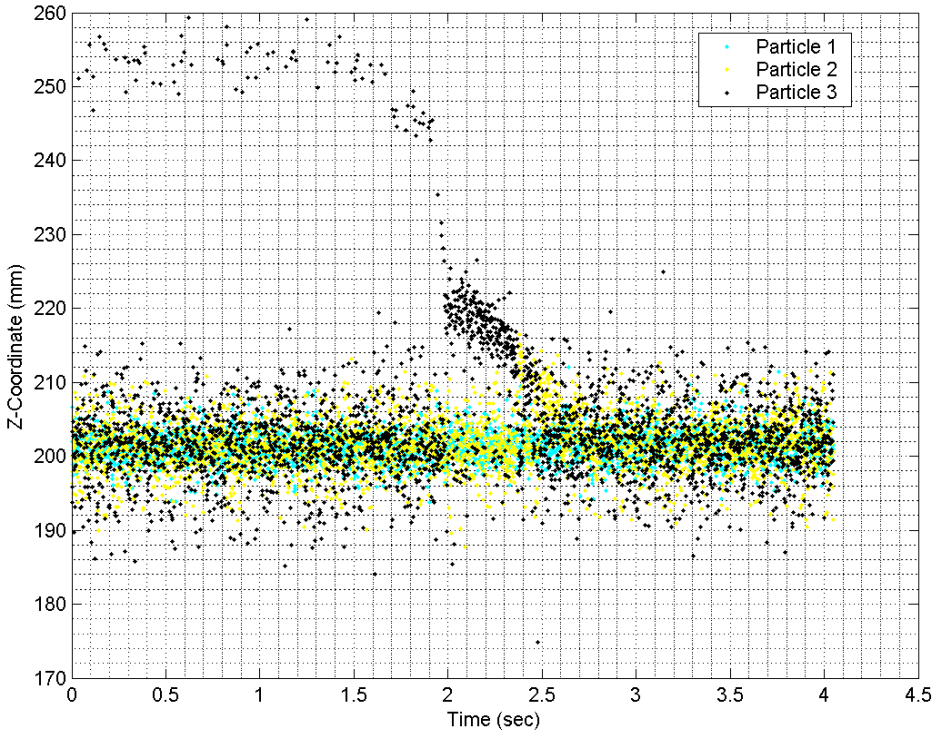

Figure 273. The Z-coordinates plotted against time for 3 particles.

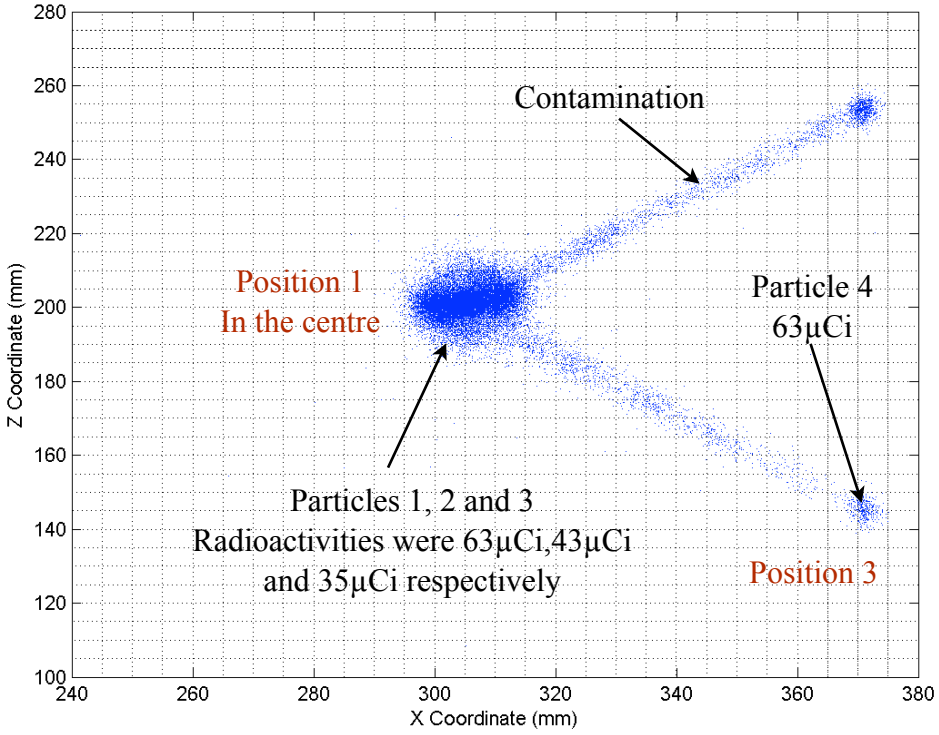

Figure 274. A 2D view of the 4th particle being moved towards the 3 particles in the centre of the wood board.

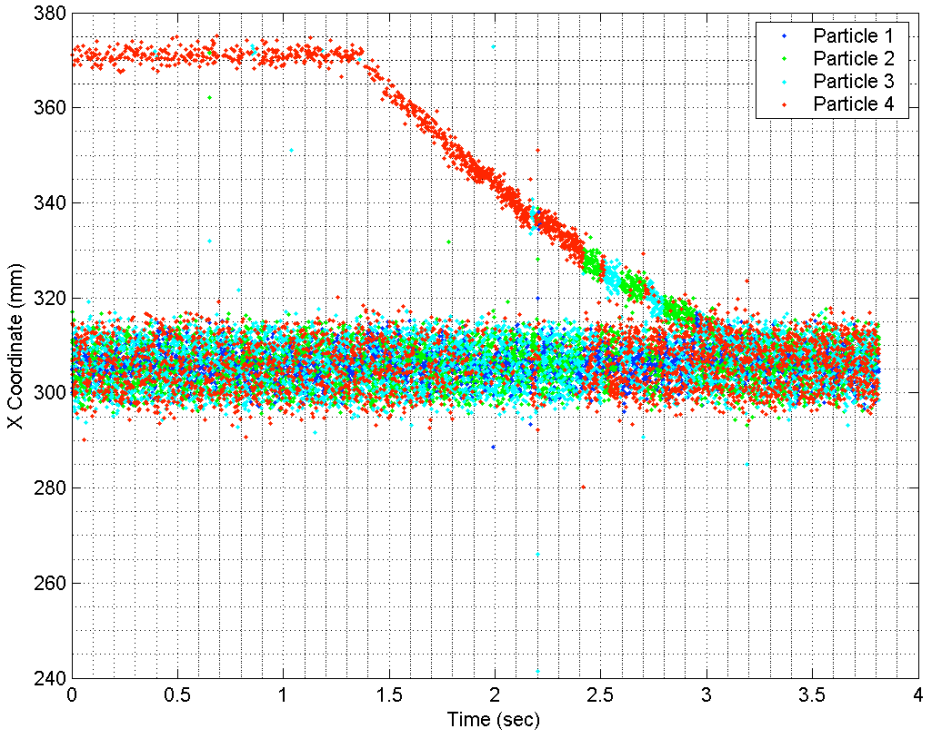

Figure 275. The X-coordinates plotted against time for 4 particles.

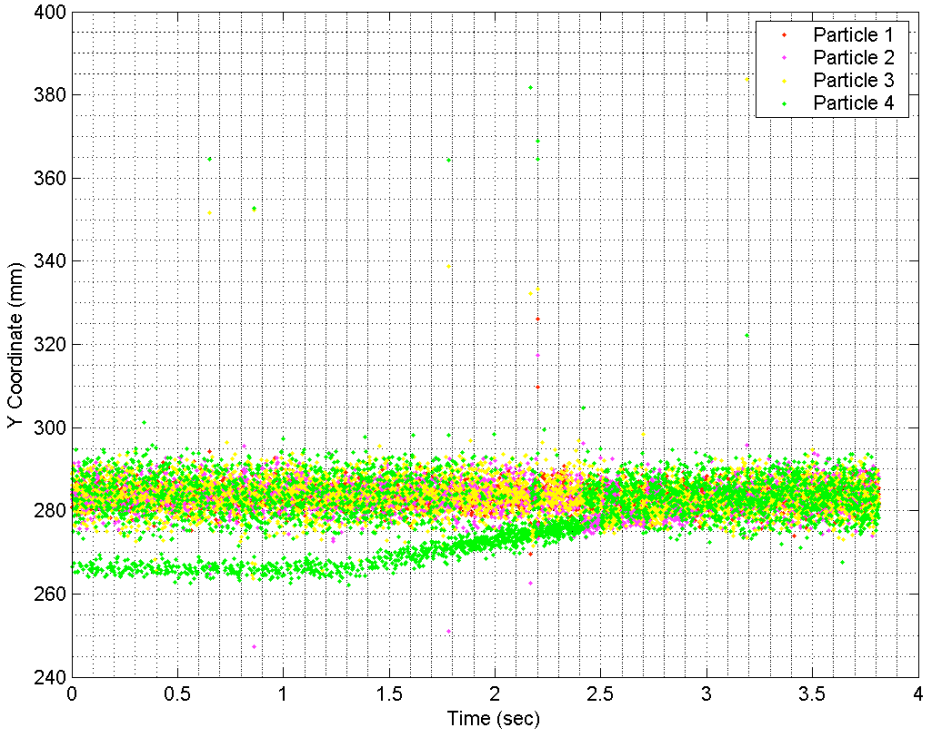

Figure 276. The Y-coordinates plotted against time for 4 particles.

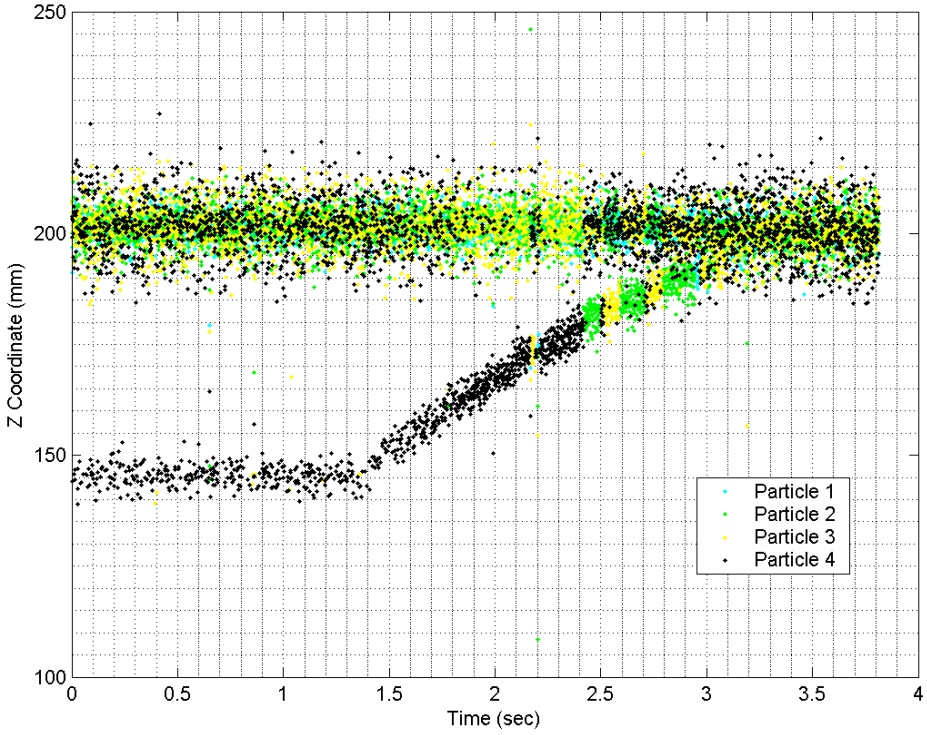

Figure 277. The Z-coordinates plotted against time for 4 particles.

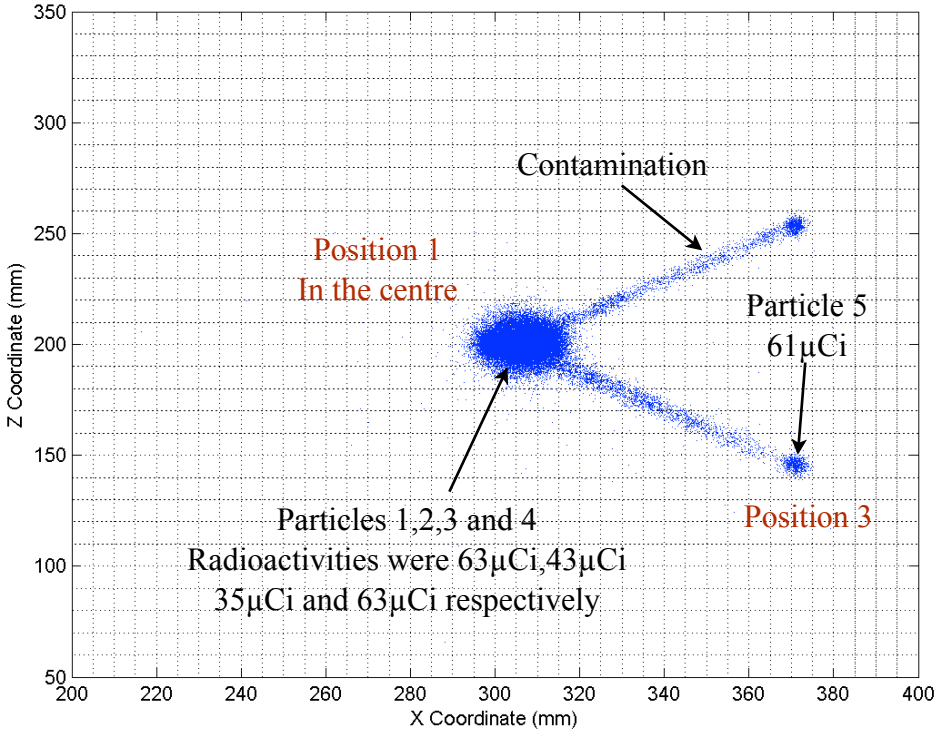

Figure 278. A 2D view of the 5th particle being moved towards the 4 particles in the centre of the wood board.

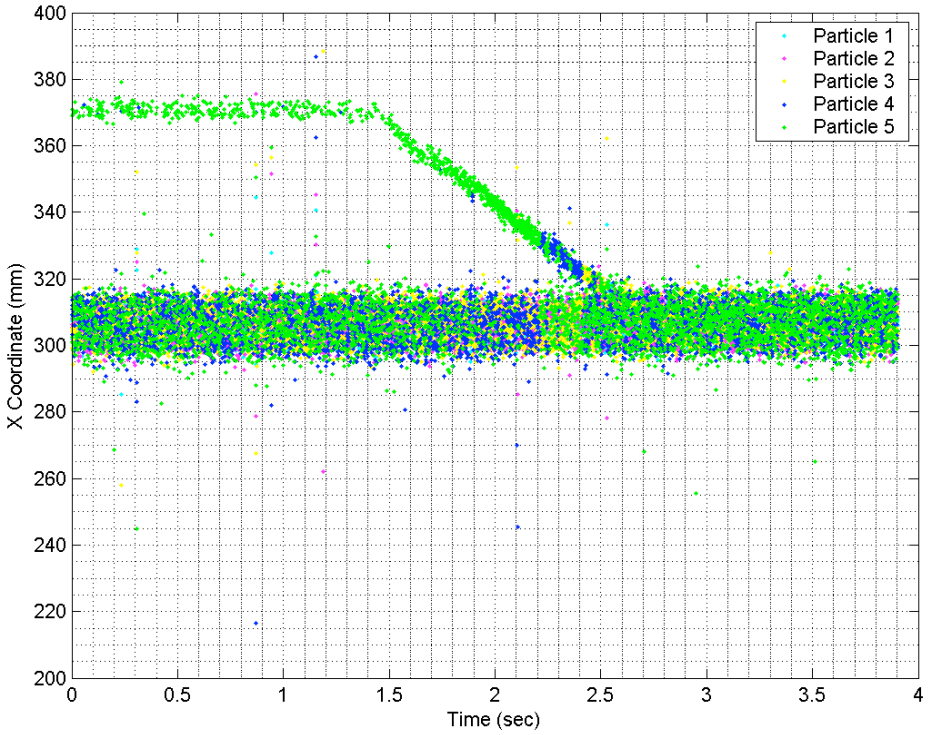

Figure 279. The X-coordinates plotted against time for 5 particles.

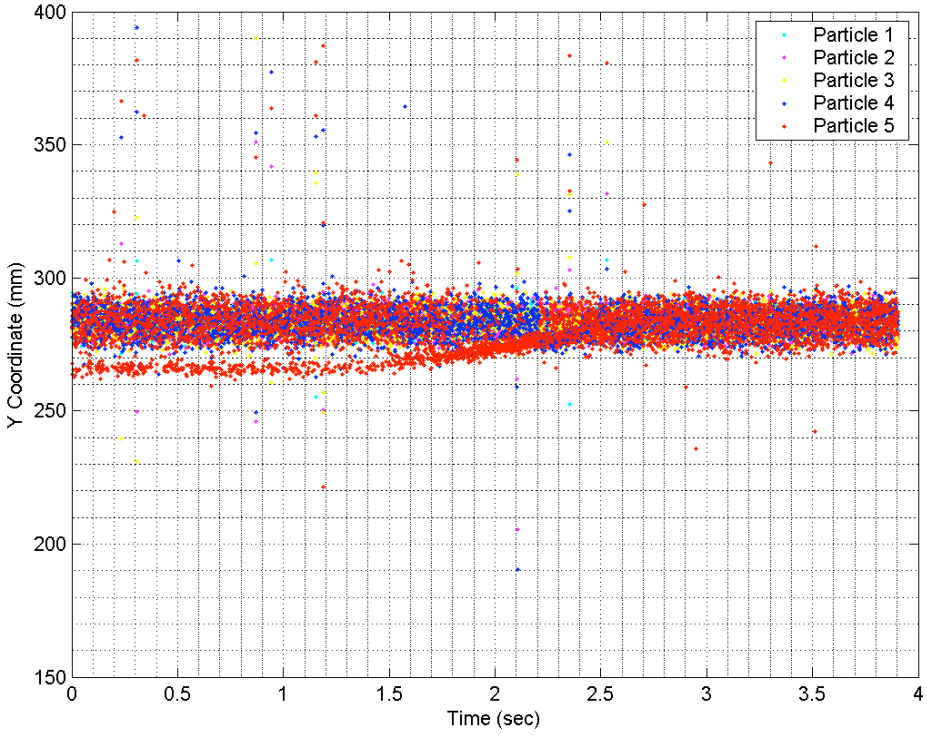

Figure 280. The Y-coordinates plotted against time for 5 particles.

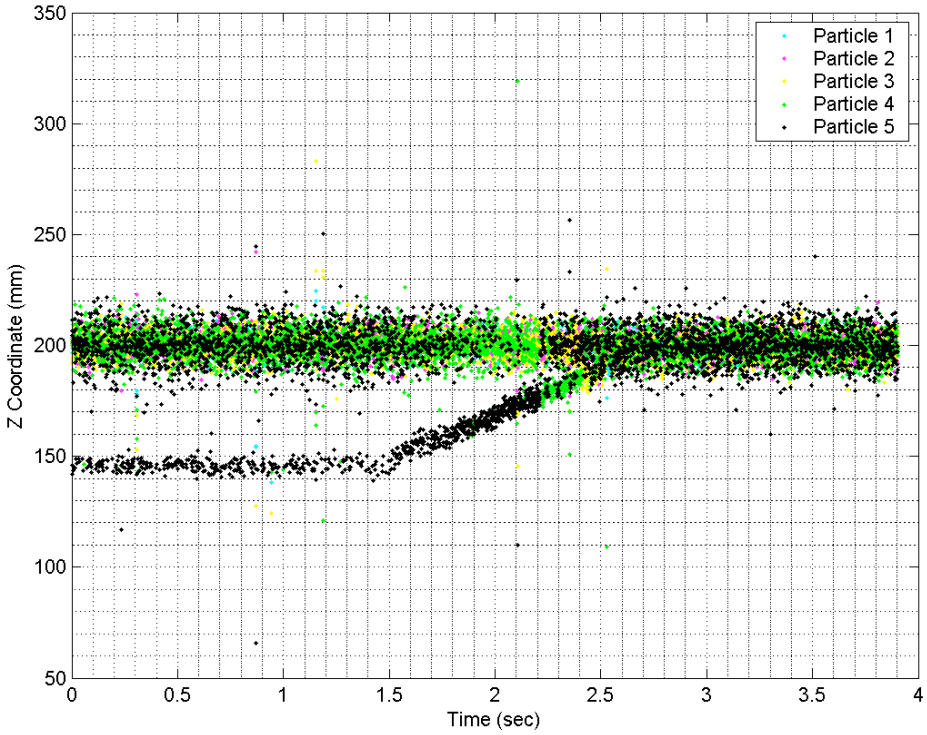

Figure 281. The Z-coordinates plotted against time for 5 particles.

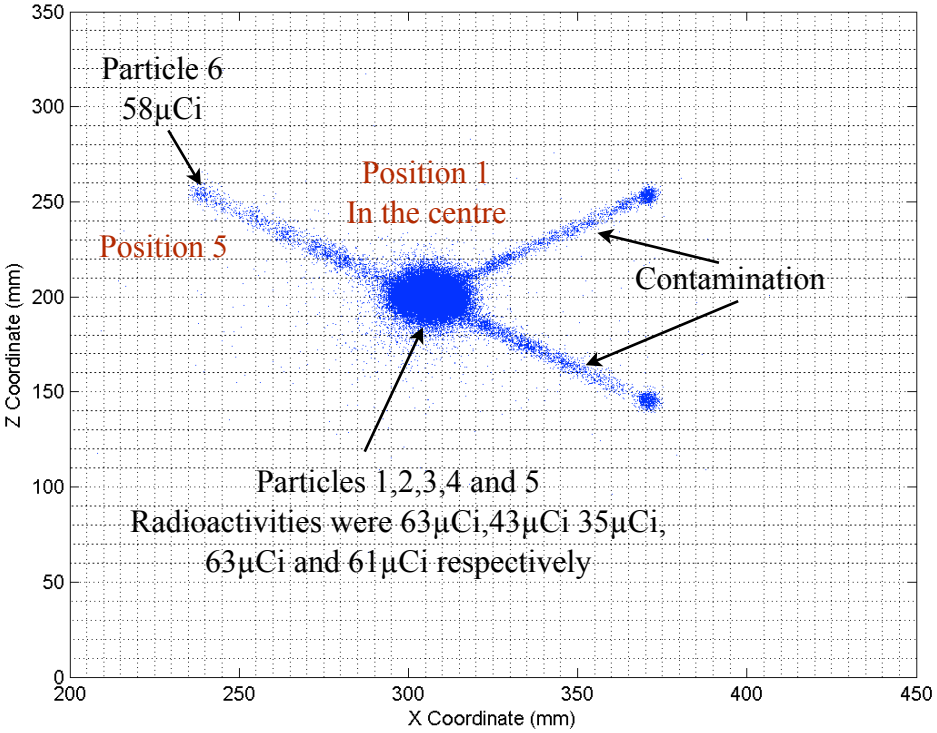

Figure 282. A 2D view of the 6th particle being moved towards the 5 particles in the centre of the wood board.

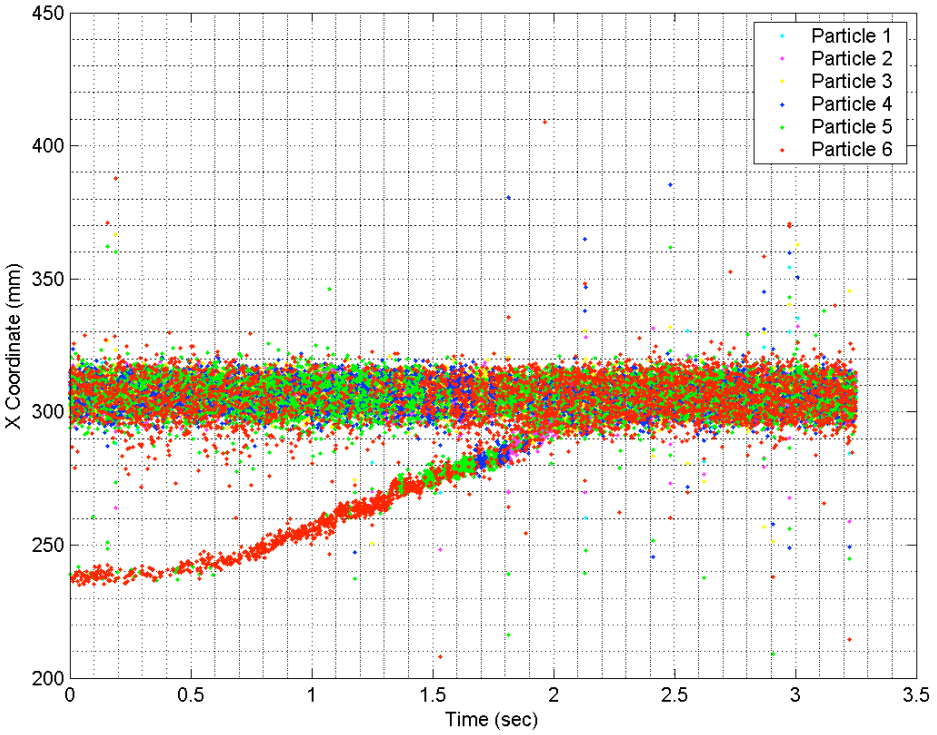

Figure 283. The X-coordinates plotted against time for 6 particles.

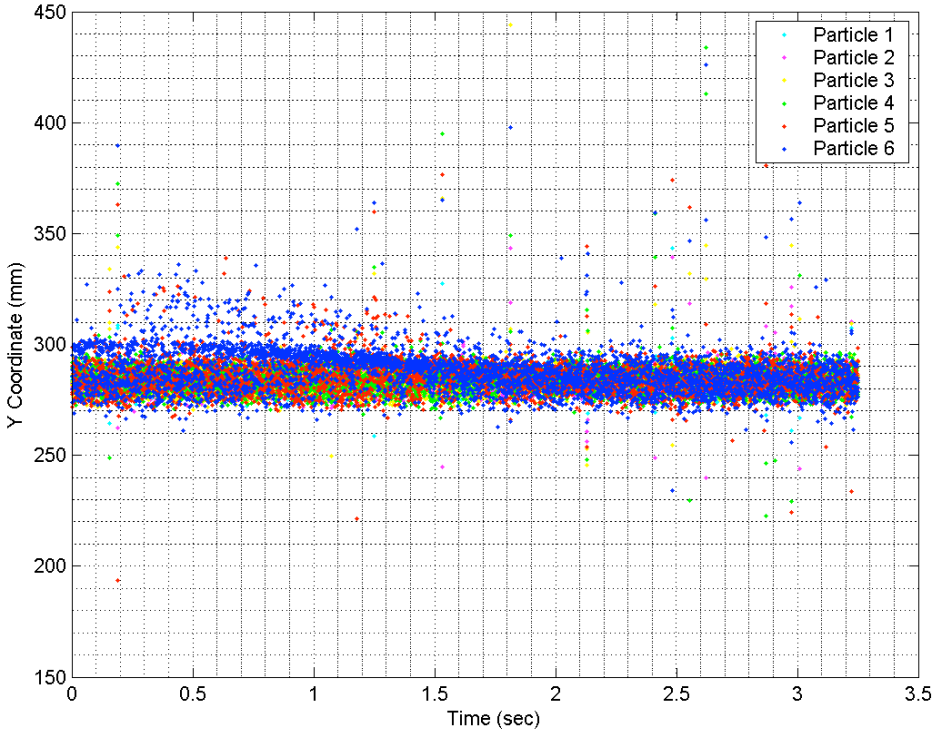

Figure 284. The Y-coordinates plotted against time for 6 particles.

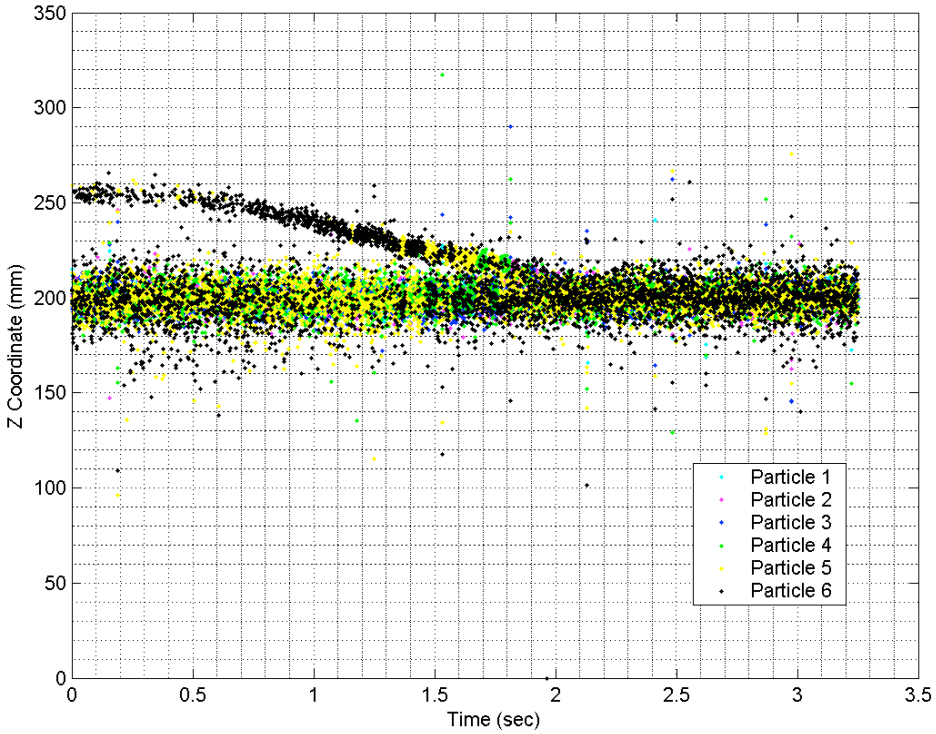

Figure 285. The Z-coordinates plotted against time for 6 particles.

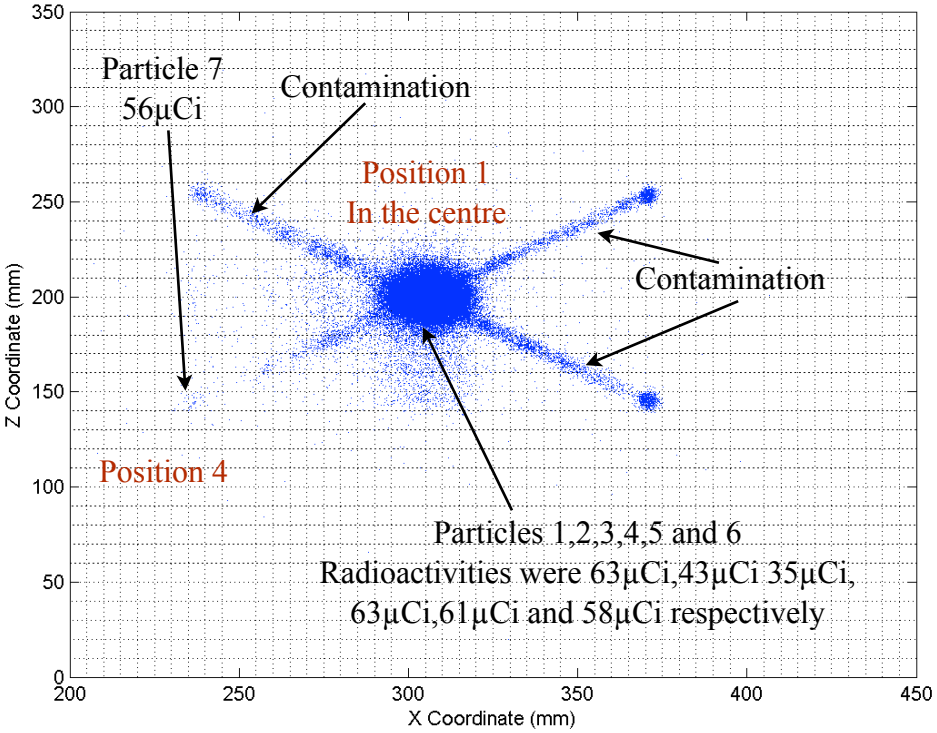

Figure 286. A 2D view of the 7th particle being moved towards the 6 particles in the centre of the wood board.

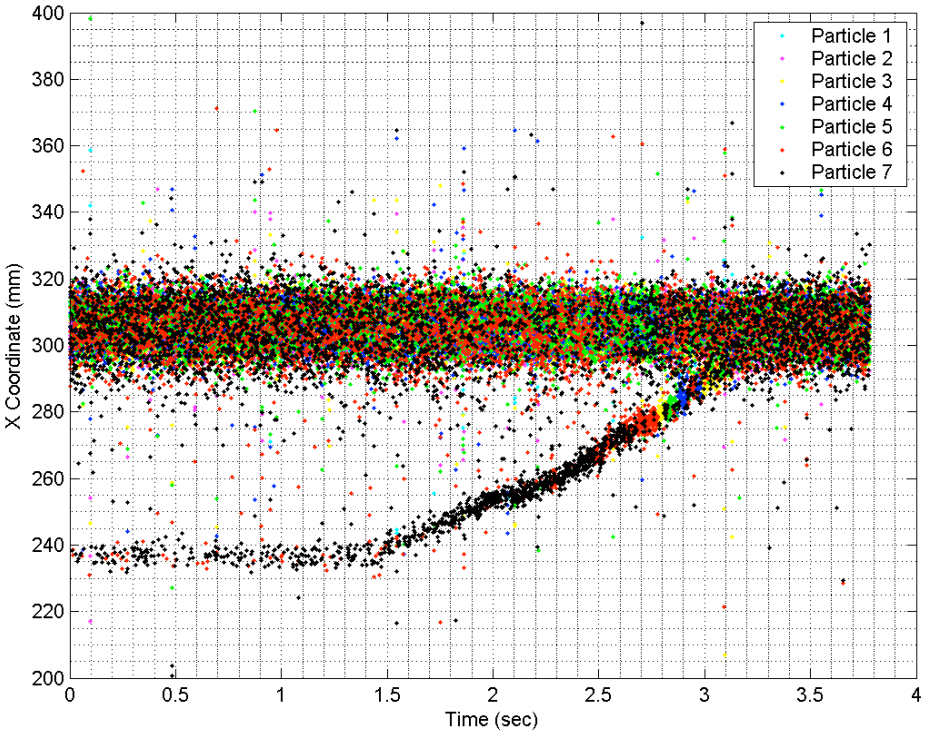

Figure 287. The X-coordinates plotted against time for 7 particles.

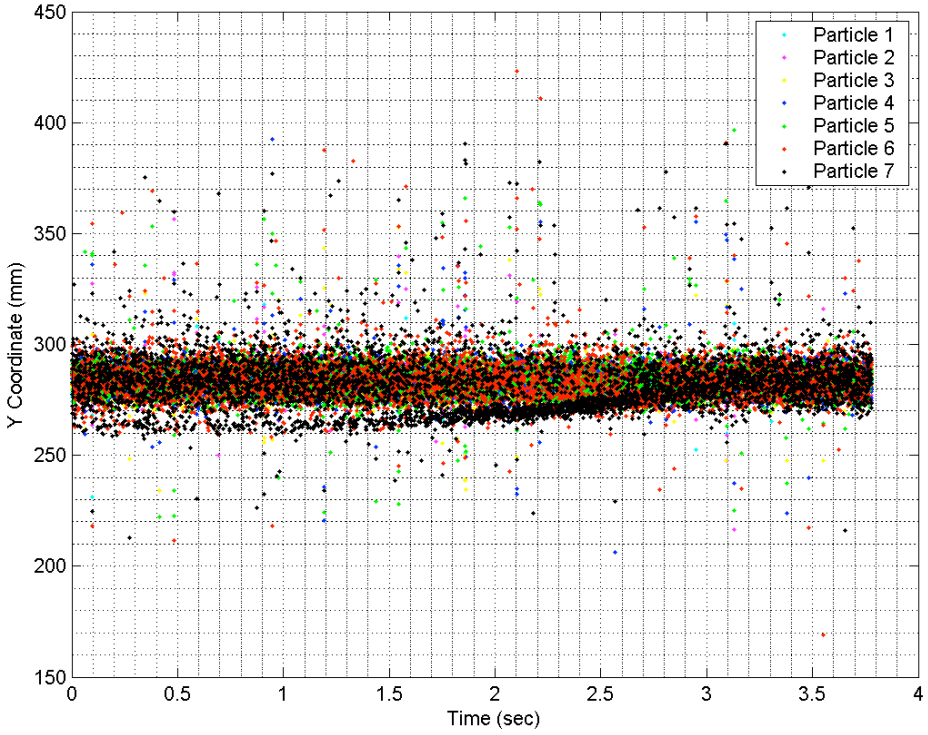

Figure 288. The Y-coordinates plotted against time for 7 particles.

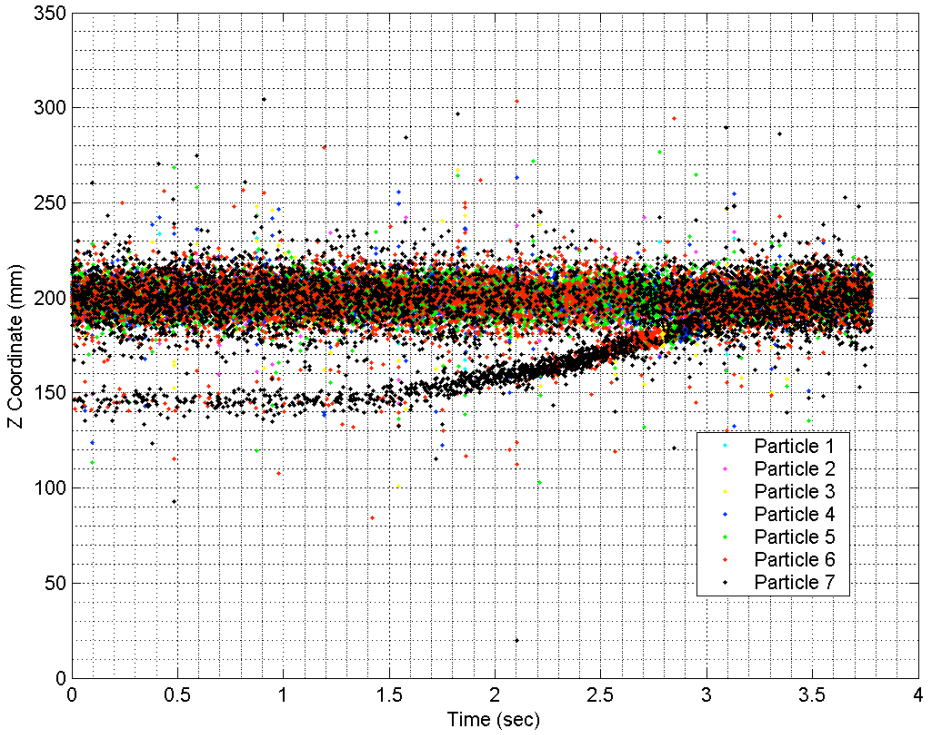

Figure 289. The Z-coordinates plotted against time for 7 particles.

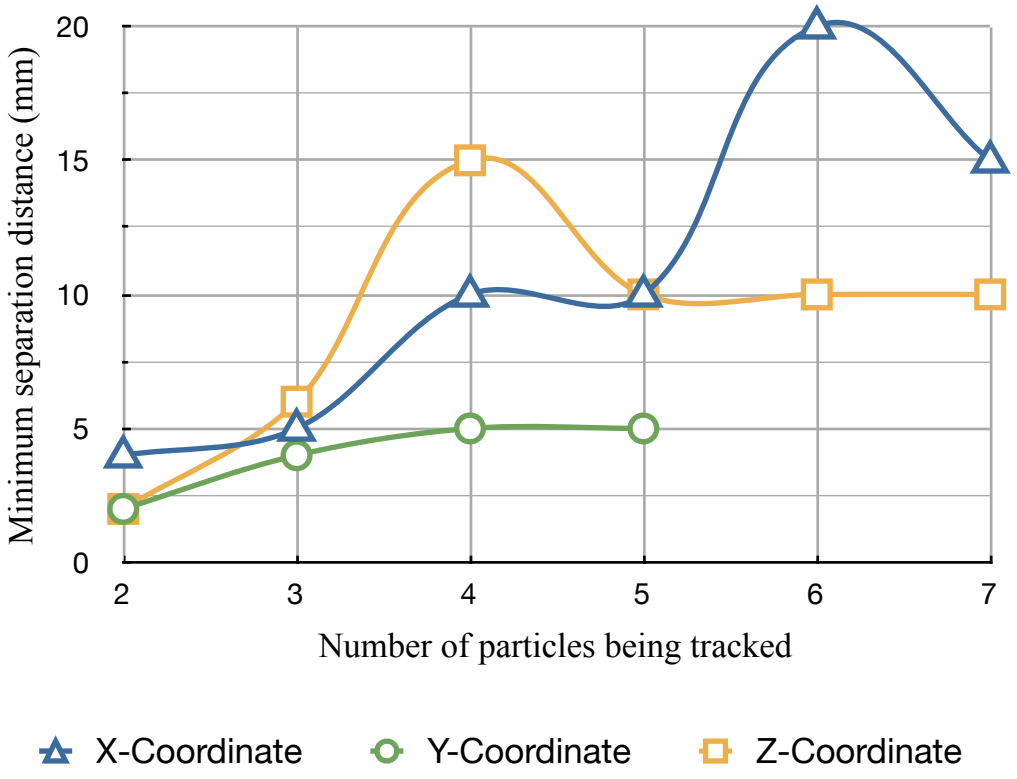

Figure 290. The minimum separation distance required plotted against the number of particles being tracked.

Figure 290 shows the minimum separation distance that was measured for each coordinate plotted versus the number of particles being tracked. It was apparent that the minimum separation distance between 2 particles that is required for the algorithm to distinguish between them in 3-D, is 4 mm. This separation distance would have to be increased to 6 mm if 3 particles are to be tracked,to 15 mm for 4 particles and 20 mm for 6 particles. This is provided that the particles had a sufficient difference in their radioactivities from each other, the larger the range the easier it would be for the algorithm to distinguish them.

4.7.2 Multiple Particle Tracking in a Stirred Liquid Metal Bath

These experiments were carried out to investigate the degree of discrimination with which the NTrack algorithm can differentiate between two alumina particles, of a size typical of inclusions in castings, within a liquid metal bath. Two radioactive alumina particles of size 63-100 μm were introduced into a Lensalloy-136 liquid metal bath, which was continuously stirred using a magnetic stirrer, see section 3.3.2. The obtained tracking results obtained have not been illustrated in 3D because of the limited amount of information that could be derived from such a diagram in this case.

Figure 291 is a graph depicting the behaviour of the two irradiated particles introduced into a stirred bath, by the vertically oriented rod, where they were initially 15 mm apart in the Y-direction, shown schematically in figure 55. The rod entered the liquid metal (the temperature of the stirred bath was 84^{o}C) at approximately 3.5 seconds. The X-coordinates for both particles show that as the rod was being pushed down through the liquid metal, it was moved to one side slightly by roughly 5 mm due to the moving metal bath (see figure 291, point a). When the rod was in position, central and 20 mm above the bottom of the tube, both particles began to move at approximately 5.8 seconds, when the Lensalloy-136 rod holding the particles in place had melted. Both particles rose to the surface at roughly estimated velocities of 3.6 and 2.6 cms^{-1} respectively.

Figure 292 shows the result obtained from repeating this experiment. The rod carrying the particles was placed into the liquid metal at 2.5 seconds and it was also displaced slightly in

the X-direction by roughly 10 mm (see figure 292, points a and b). This meant that the particles did not start from the required initial positions as was indicated by the irregular hump observed in the X-coordinates of both particles between 3 and 6 seconds. At 6 seconds both particles started rising to the surface at roughly 7.4 and 6.8 cms^{-1} respectively.

Figure 293 shows the results obtained from a third attempt, which was carried out to repeat the previous experiments, but in this case each particle was introduced using a separate rod, where the particles were 15 mm apart in the Z-direction, see figure 54, and 35 mm above the bottom of the tube. The rods entered the surface of the liquid metal at 9.5 seconds and reached their intended positions at approximately 12 seconds. Both rods were moved slightly in the X-direction during their descent through the liquid metal, (see figure 293, point a), but the particles were released when the rods were in position at approximately 12 seconds. Both particles rapidly rose to the surface at an estimated velocity of 5.8 cms^{-1}.

These results showed that it was possible to track two moving particles simultaneously in a liquid metal. The level of discrimination between the particles and the accuracy with which their location was determined was a function of the radioactivity of both particles. Because both particles were at the same X-coordinate before they were released in each of the three experiments, the X-coordinate can be used to demonstrate how the discrimination of the particles varied with their radioactivity.

In figure 291, the particles had a ratio of radioactivities of 1.3, and a large scatter was associated with the X-coordinates of particle 2. This meant that the X-coordinate of particle 2

could only be determined within 40 mm, which was poor accuracy. In figure 292, the ratio of the radioactivity was 2, and unlike the first experiment, minimal scatter was observed but in this case the X-coordinates of both particles were often mixed, as shown between 21-22 seconds for example. This meant, although the location of both particles was determined, but the algorithm could assign one particle's coordinate to the other and vice versa. In figure 293, the ratio of radioactivity was 2.5 and the particle paths obtained were clearly defined, without any scatter and only negligible mixing of their coordinates.

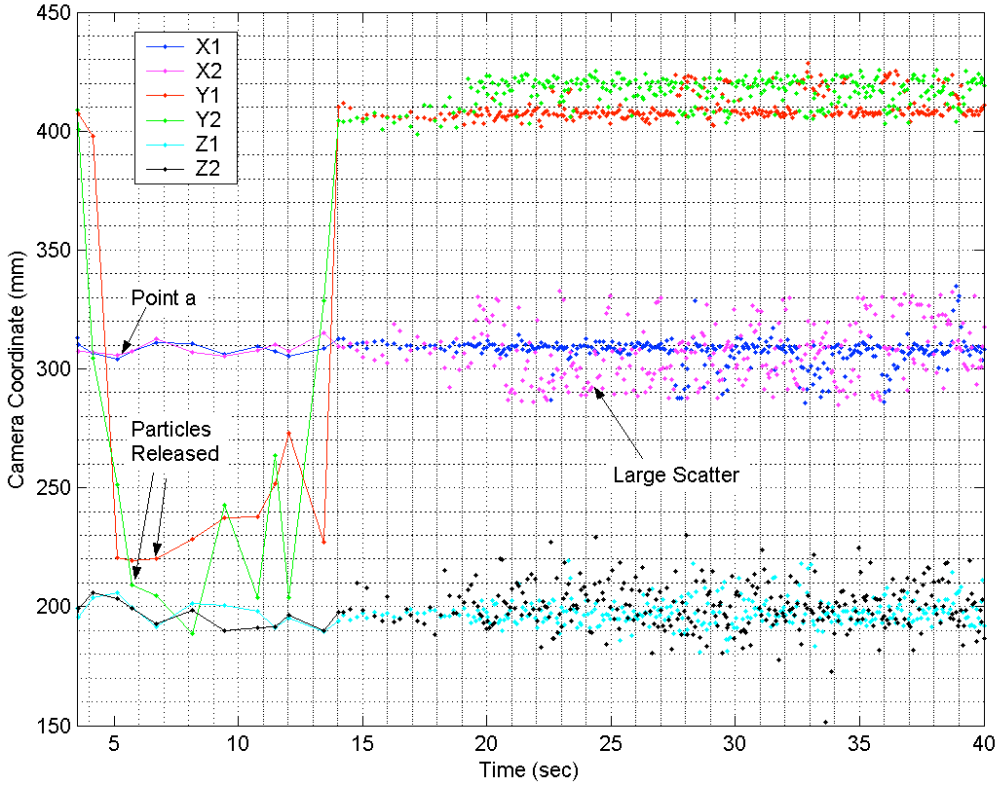

Figure 291. The X,Y and Z coordinates of both particles used in the first tube experiment, plotted versus the tracking time. X1 and X2 are the X-coordinates for particles 1 and 2 respectively.

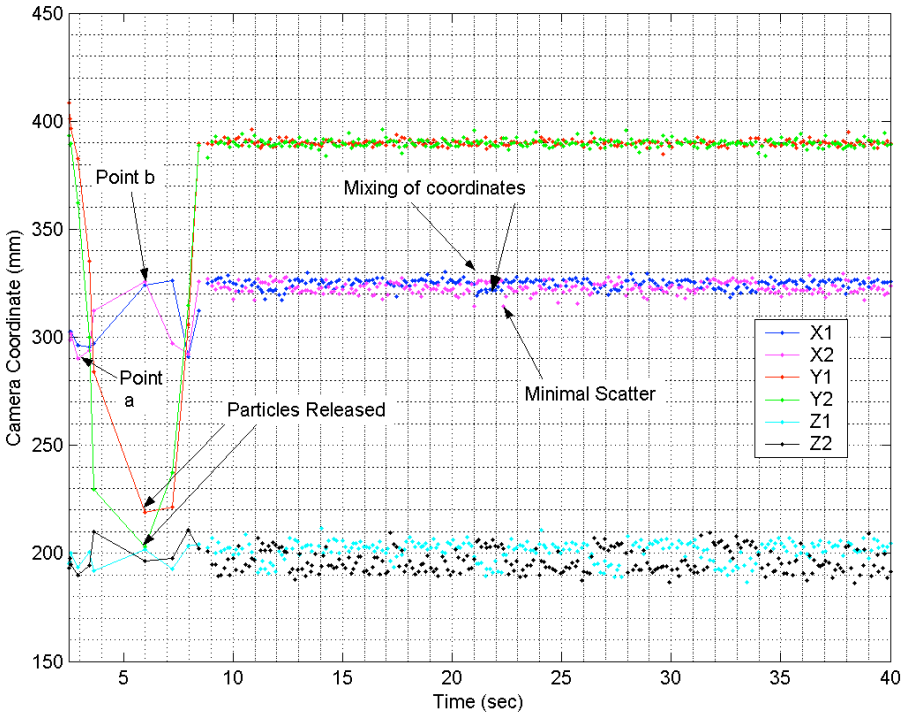

Figure 292. The X,Y and Z coordinates of both particles used in the second tube experiment, plotted versus the tracking time. X1 and X2 are the X-coordinates for particles 1 and 2 respectively.

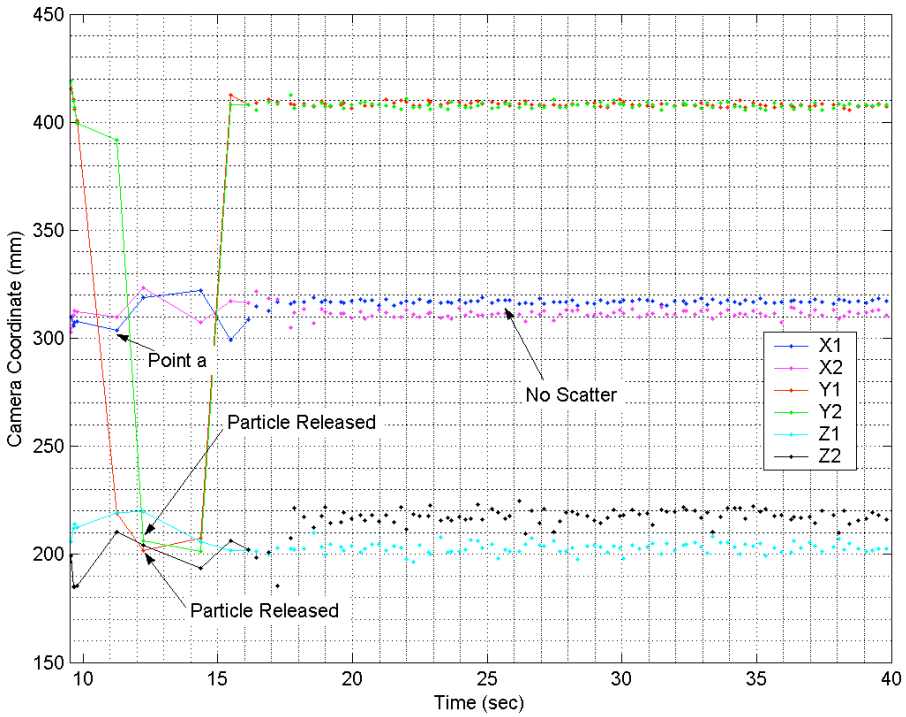

Figure 293. The X,Y and Z coordinates of both particles used in the third tube experiment, plotted versus the tracking time. In this experiment 2 rods were used to introduce 2 particles on the same level. X1 and X2 are the X-coordinates for particles 1 and 2 respectively.

4.7.3 Multiple Particle Tracking in Steel and Lensalloy-136 Castings

Figure 294 shows the tracking results obtained for a steel casting where 5 alumina particles were placed on the circumference of a 5mm radius circle, centred at the centre of the sprue opening. The results obtained represent just 1 particle rather than all 5. A Geiger counter was used to estimate the final location and it was found that all particles were almost in the same place nearer the bottom end of the downsprue. Tracking results for each individual particle were difficult to obtain because of limitations in the technique used to interpret the binary data collected from the positron camera (see section 5.1 for more details). As a result the accuracy achieved in this experiment was poor.

Another attempt to use and track multiple particles in a casting, is shown in figure 295. In this case 2 alumina particles were placed at the centre of the downsprue opening and Lensalloy-136 was cast at 87^{o}C into the acrylic mould. The results obtained were unusable, as shown in figure 295, which could be attributed to the algorithm being unable to distinguish events received from each particle correctly and hence producing unrealistic particle coordinates.

These results meant that the currently available, multiple particle tracking algorithms, need to be developed specifically for casting applications in order to facilitate the tracking of multiple particles simultaneously in castings.

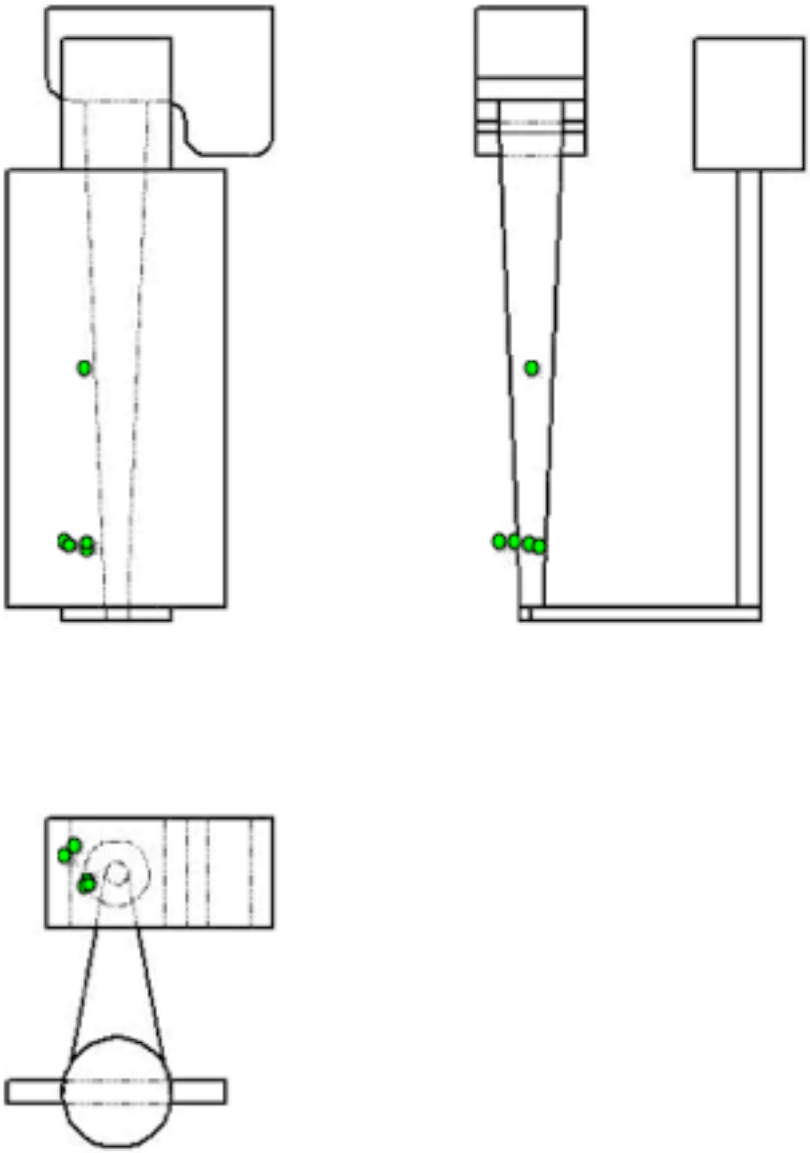

Figure 294. Three engineering views showing the final location of 5 particles that were cast together as a first attempt with multiple particle tracking. Individual particle locations could not be determined.

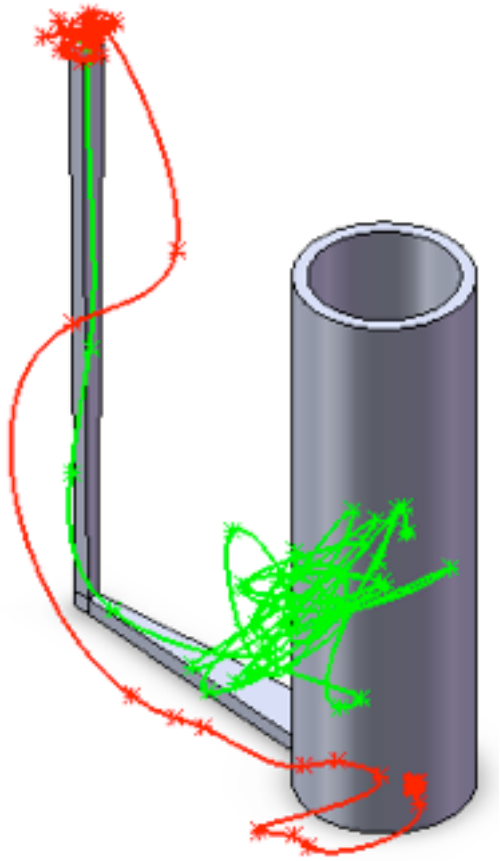

Figure 295. An isometric view of the casting showing the unclear particle paths obtained using PEPT data that was processed using a 2 particle tracking algorithm.

4.7.4 Multiple Particle Tracking in an Industrial Casting Using the Modular Camera

4.7.4.1 Modular Camera PEPT Results

Four experiments were carried out where multiple radioactive alumina particles were tracked in an aluminium plate casting simultaneously, using the portable modular camera. Figures 296-300 show the results obtained from the 2 successful modular camera experiments. The particles remained in their initial positions in the other 2 experiments and were therefore not processed in detail. Figures 296,a) and b) are isometric views, showing the behaviour of 2 particles that were initially placed at the centre of the downsprue opening (particle 1, radioactivity 32μCi) and 120mm below that centre (particle 2, radioactivity 11μCi), respectively. Both particles remained in the right hand side of the cast plate cavity during filling after which they came to rest in the top right hand side corner when the casting had solidified. No tracking data was obtained for the particle paths within the downsprue or the runner bar due to the high speed at which they were moving. The obtained particle tracks appear to be outside the casting due to a slight misalignment of the mould in between the modular camera faces, and a rotation about an unknown axis is required to show the correct location of the results. Figures 297,a) and b) are a 2-D representation of the particle's behaviour within the plate. The reported error in the measured particle location was ± 4.4 mm and 8.3 mm for particle 1 and particle 2 respectively.

Figures 299 and 300 show the results obtained when 4 particles were initially placed, below each other, at 60 mm increments along the downsprue with the first particle at the centre of the downsprue opening. Particle 1 (23μCi) came to rest a few millimetres below its initial position and seems to not have been entrained in the liquid metal as intended. No data was

obtained for particle 2 (14 μCi) which is believed to be due to its radioactivity being close to that of particle 1, which may have led the algorithm to assume they were 1 particle. Particle 3 (30μCi) however, was entrained into the liquid metal and it came to rest half way along the length of the runner bar. Particle 4 (38μCi) was unfortunately not released from the rod and remained at its initial position. The reported error ranged from 5.4-7.6 mm for all 4 particles.

The results obtained showed that multiple particle tracking is possible in an industrial application such as sand casting of aluminium. The algorithm used to process the data was able to process the tracking data with more accuracy when 2 particles were used and both of those particles were successfully relocated and identified using an SEM with an EDX attachment (see section 4.5). However it is difficult to comment on the results obtained using 4 particles due to the experimental errors that led to the unsuccessful entrainment of 3 particles.

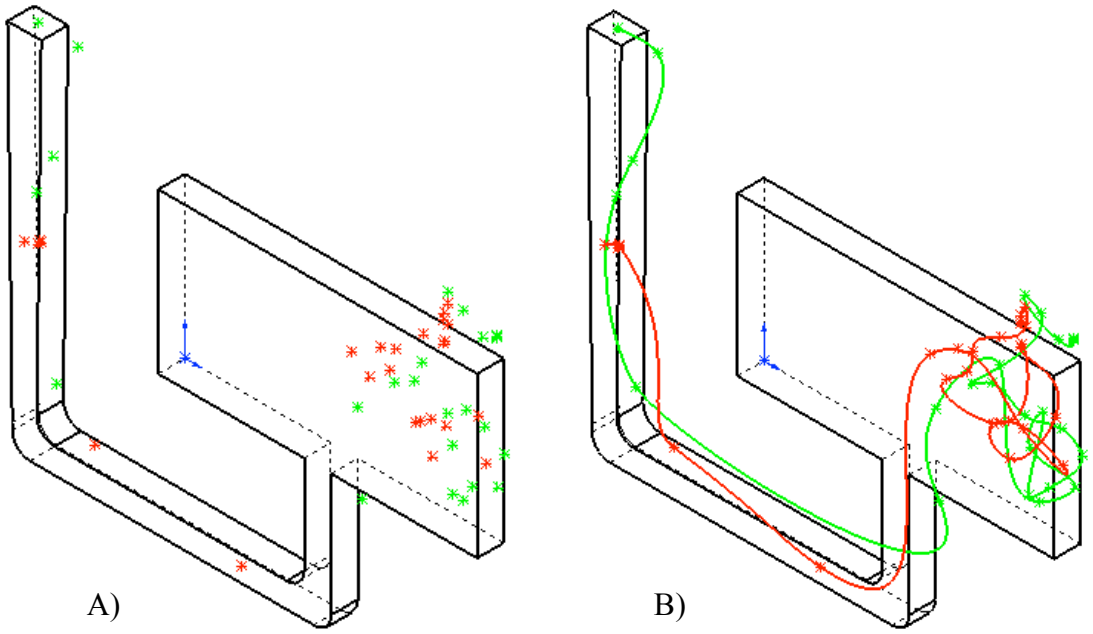

Figure 296. An isometric view showing the tracking results obtained when 2 directly irradiated alumina particles, of size 90-150 µm, were initially placed at the centre of the downsprue opening and 120 mm below the centre of the downsprue opening. Particle radioactivities were 32 µCi and 11 µCi respectively. A) the particle paths presented as points and B) the particle path presented as a spline connecting the points.

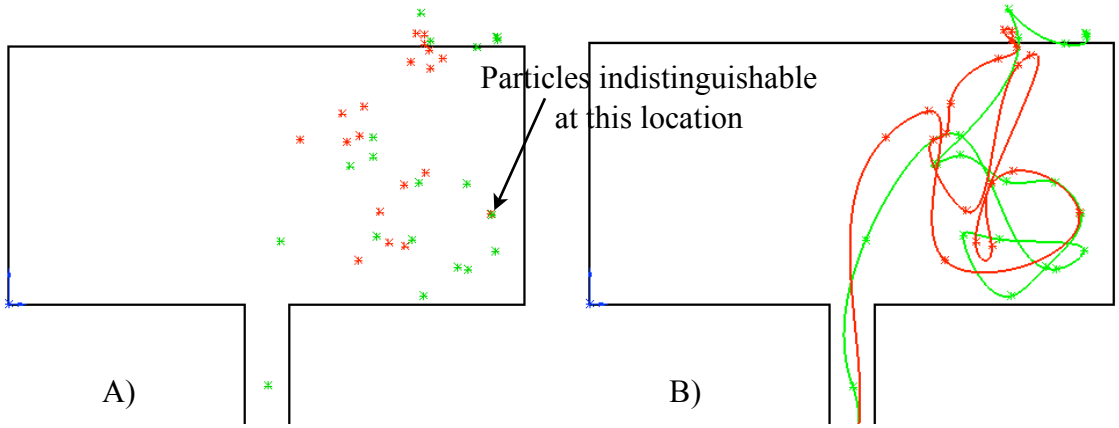

Figure 297. A front view showing the tracking results obtained when 2 directly irradiated alumina particles, of size 90-150 µm, were initially placed at the centre of the downsprue opening and 120 mm below the centre of the downsprue opening. Particle radioactivities were 32 µCi and 11 µCi respectively. A) the particle paths presented as points and B) the particle path presented as a spline connecting the points.

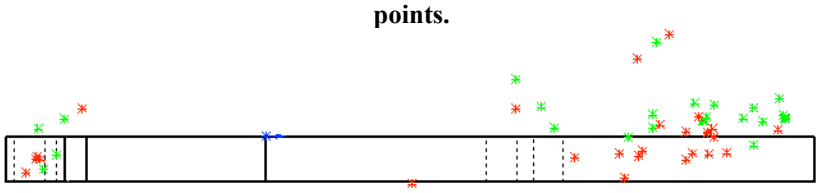

Figure 298. A top view showing the effect of the slight misalignment of the mould between the modular camera faces, were the particle tracks appear to be outside the casting, which is not possible.

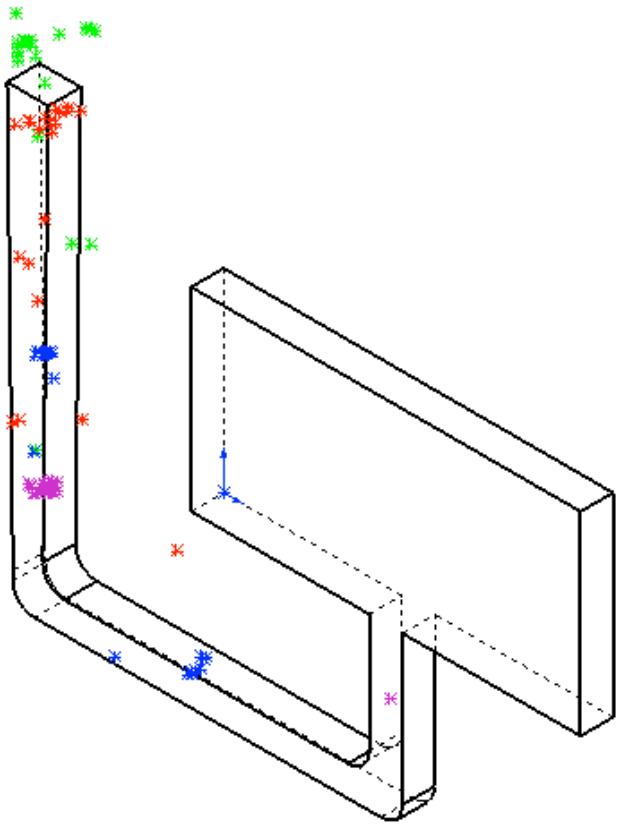

Figure 299. An isometric view showing the tracking results obtained when 4 directly irradiated alumina particles, of size 90-150 µm, were initially placed at the centre of the downsprue opening and 60, 120 and 180 mm below the centre of the downsprue opening, respectively. Particle radioactivities were 23 µCi, 38µCi, 14 µCi and 30 µCi respectively.

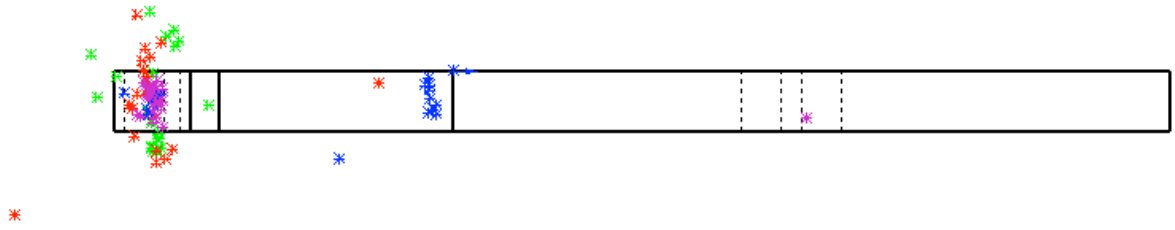

Figure 300. A top view showing the location of the four particles within the mould, where only one particle was entrained in the liquid aluminium as intended. This particle came to rest half way along the runner bar.

4.7.4.2 An X-ray of The Al Casting

Figures 301-313 were extracted from a video recorded by casting an aluminium alloy into a sand mould inside the University of Birmingham, X-Ray casting facility. The casting in this case was carried out without using a stopper rod due to the difficulty of handling the stopper rod, remotely when it is inside the X-ray facility. The cast plate was the same plate used for several of particle tracking experiments. Figure 301 shows that as the liquid aluminium approached the ingate with a 45^{o} left hand side slope. This slope had changed to a right hand side slope as the metal was entering the plate cavity. The metal then rose vertically through the cavity and collapsed to both sides after 0.38 seconds as shown in figures 303-306

Figures 307-310 show that the liquid aluminium continued to fill the plate in the same manner, by rising through the ingate and collapsing to the sides until it started to build up on both sides and sloping towards the ingate, see figure 309. These slopes started decreasing gradually as more metal entered the mould and the level of the liquid inside the plate started to plateau after 0.75 seconds.

This turbulent filling that took place during the first 5 seconds resulted in several overlapping waves, which is a known oxide film defect formation mechanism, see figure 311. The mould filling was complete after 1.68 seconds.

The results obtained from this x-ray video could not be directly compared to the PEPT results shown in figures 296-298 due to the difference in inlet conditions. However figures 311 and 311 showed that the liquid aluminium fills the right hand side of the plate first, which is where the PEPT results showed the particles to be moving within the liquid metal.

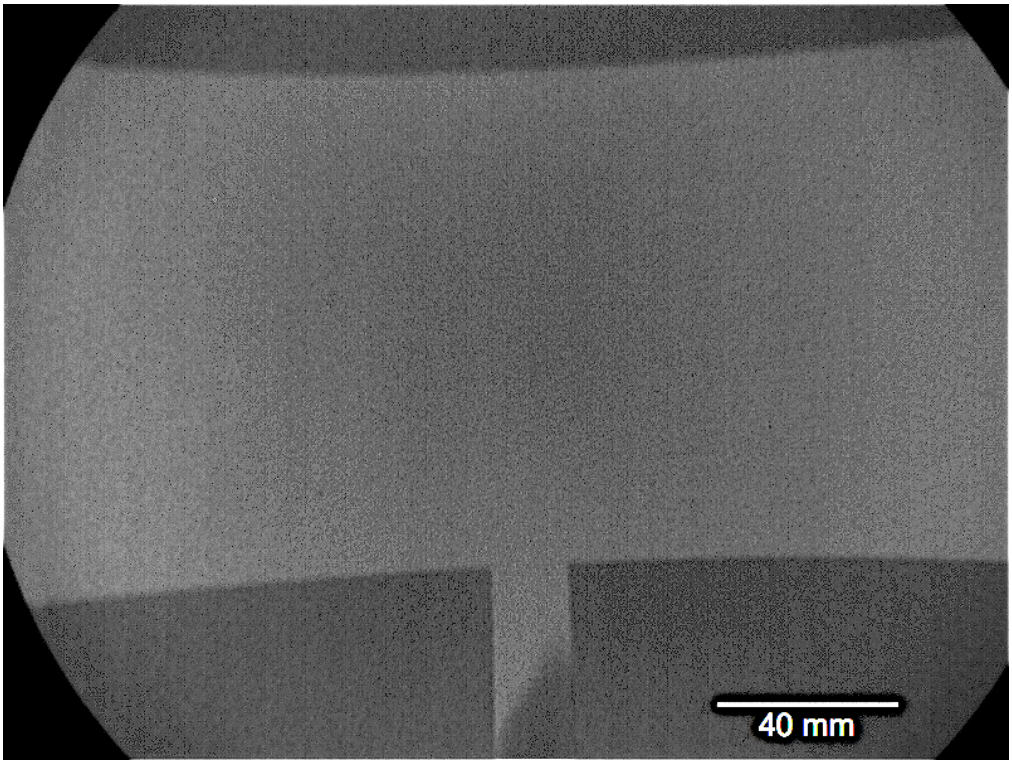

Figure 301. An X-Ray image showing the liquid Al approaching the ingate, at 0.09s filling.

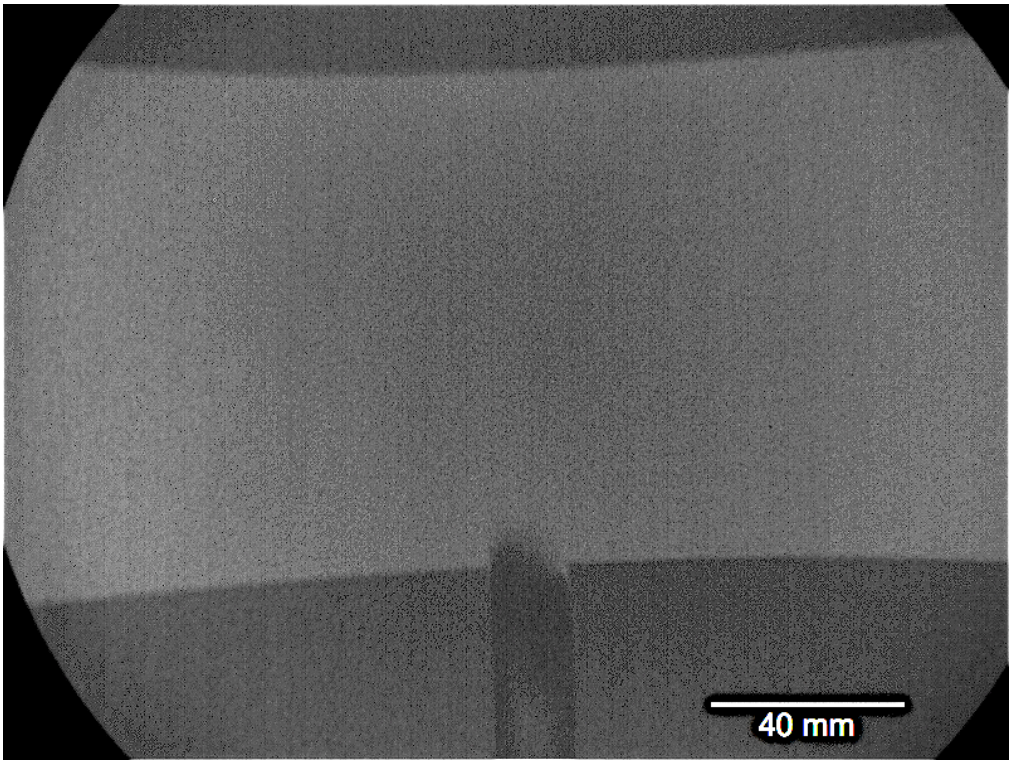

Figure 302. An X-Ray image showing the liquid Al entering the cast plate cavity, while carrying an air bubble, at 0.16s filling.

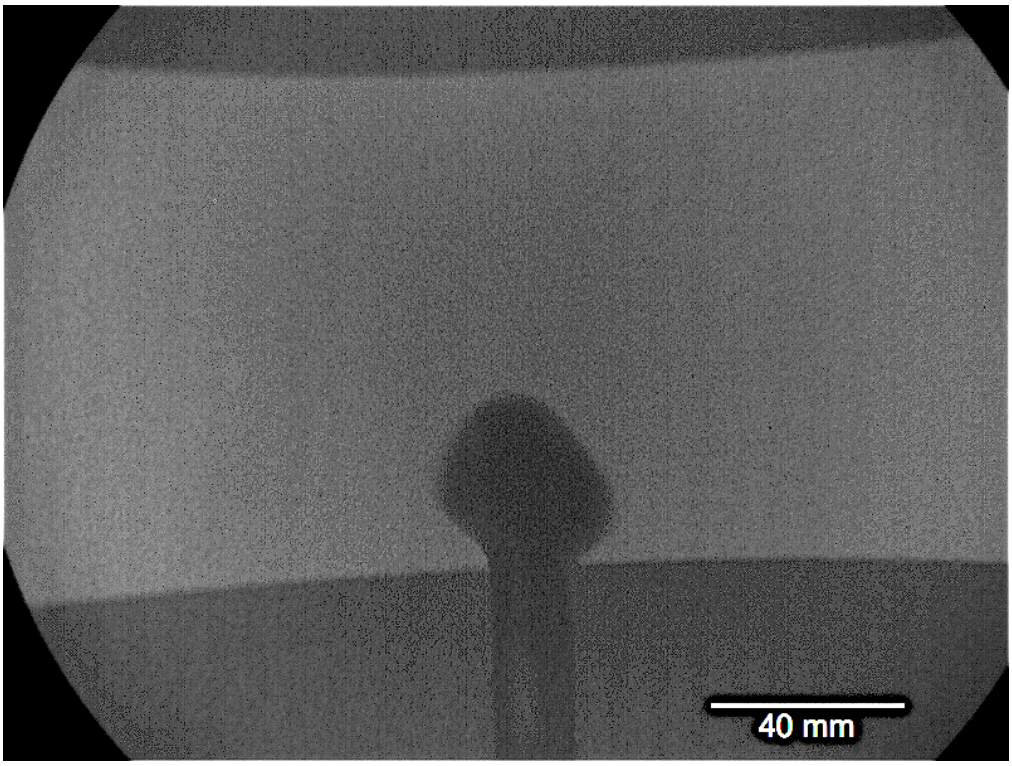

Figure 303. An X-Ray image showing the liquid Al rising inside the cast plate cavity, at 0.24s filling.

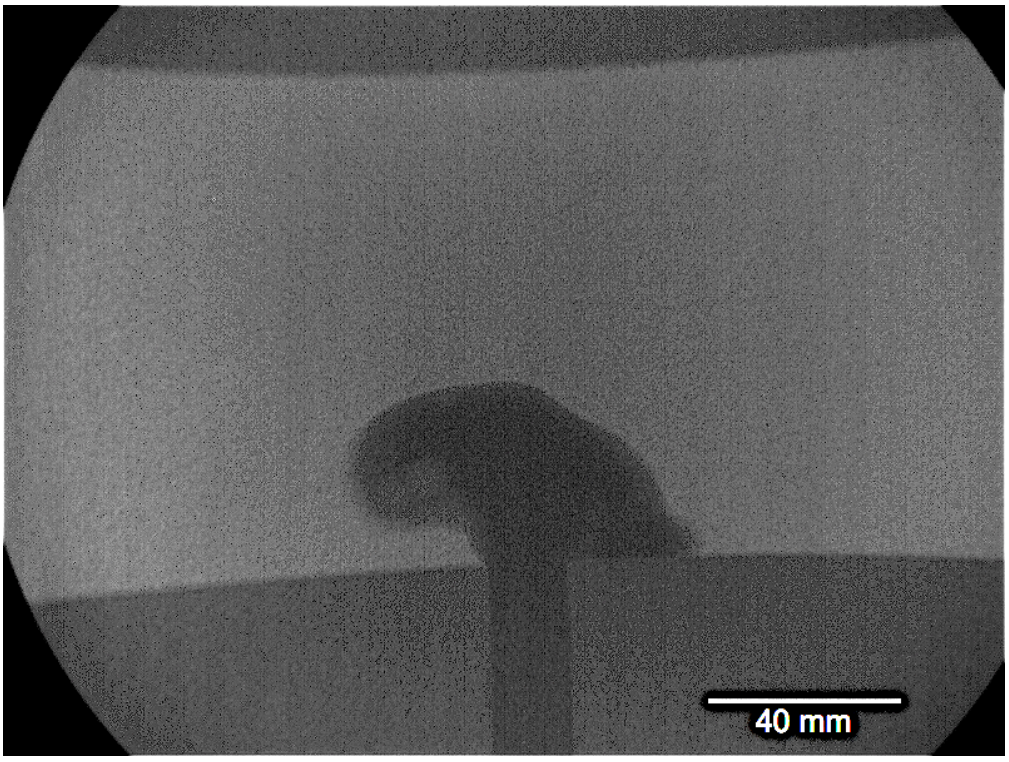

Figure 304. An X-Ray image showing the liquid Al collapsing to the sides after rising through the cast plate cavity, at 0.31s filling.

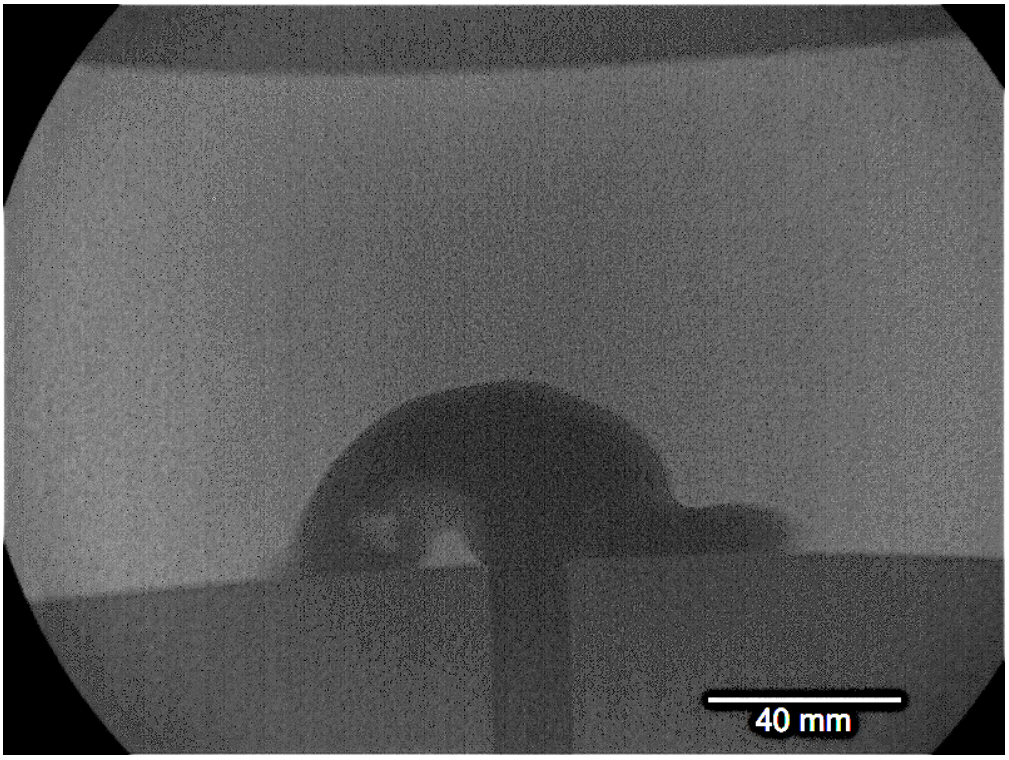

Figure 305. An X-Ray image showing the liquid Al collapsing to the sides after rising through the cast plate cavity, at 0.36s filling. Note the folding metal wave and the entrained bubble on the left hand side.

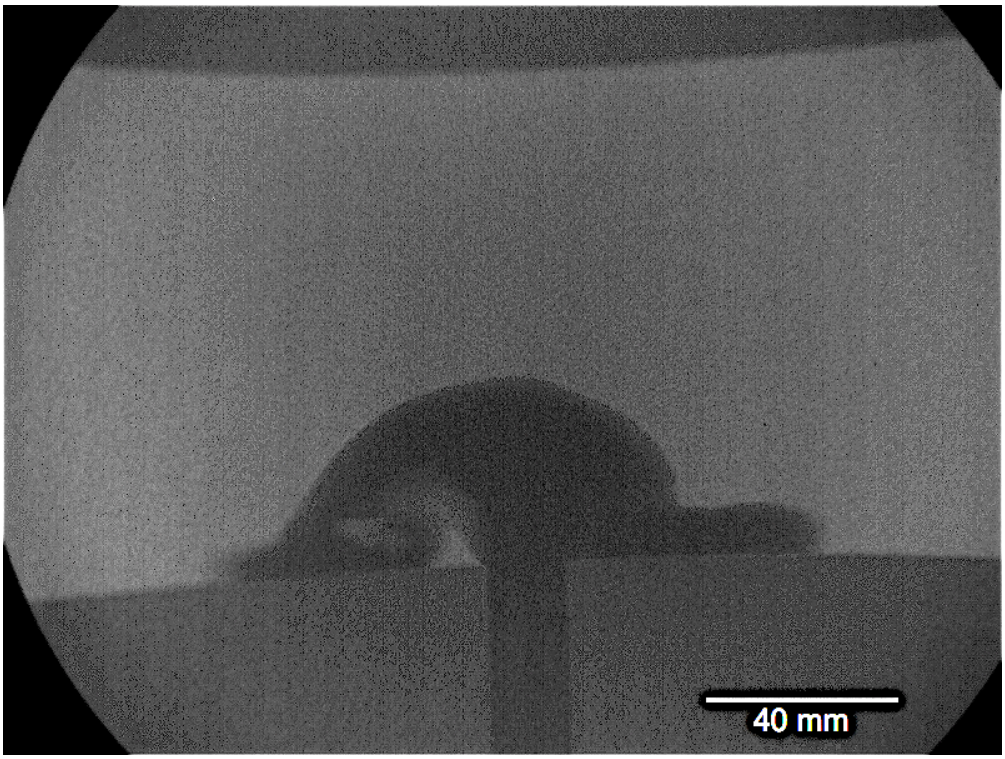

Figure 306. An X-Ray image showing the liquid Al collapsing to the sides after rising through the cast plate cavity, at 0.38s filling. Note the folding metal wave and the entrained bubble on the left hand side.

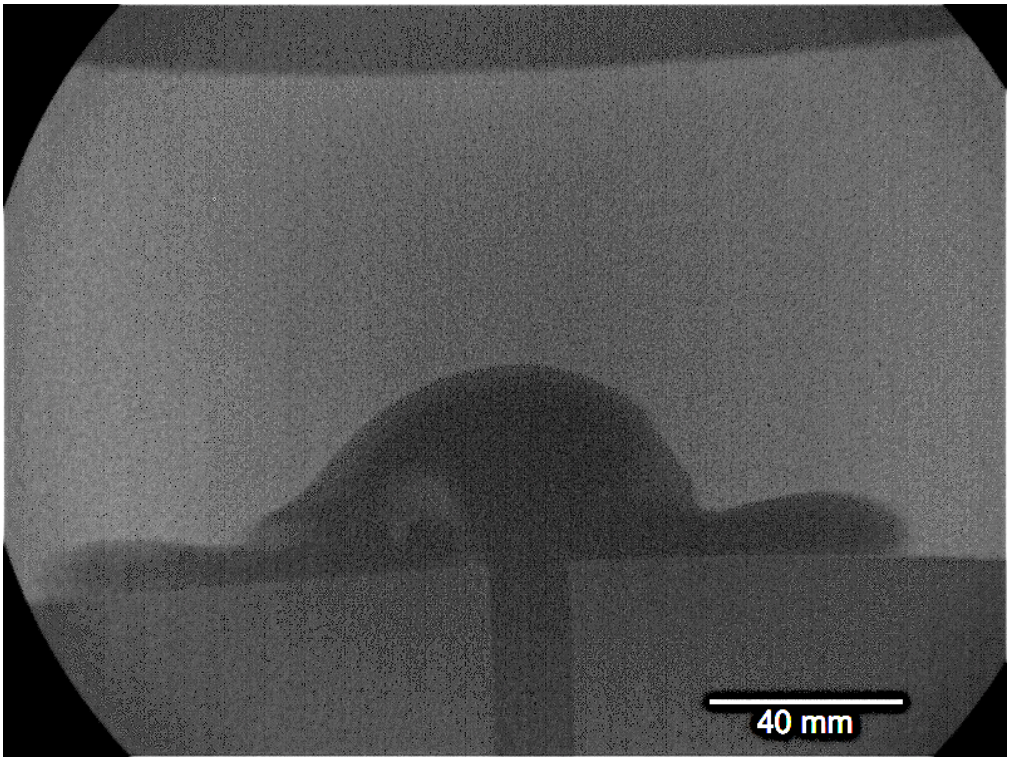

Figure 307. An X-Ray image showing the liquid Al filling the mould at 0.43s filling..

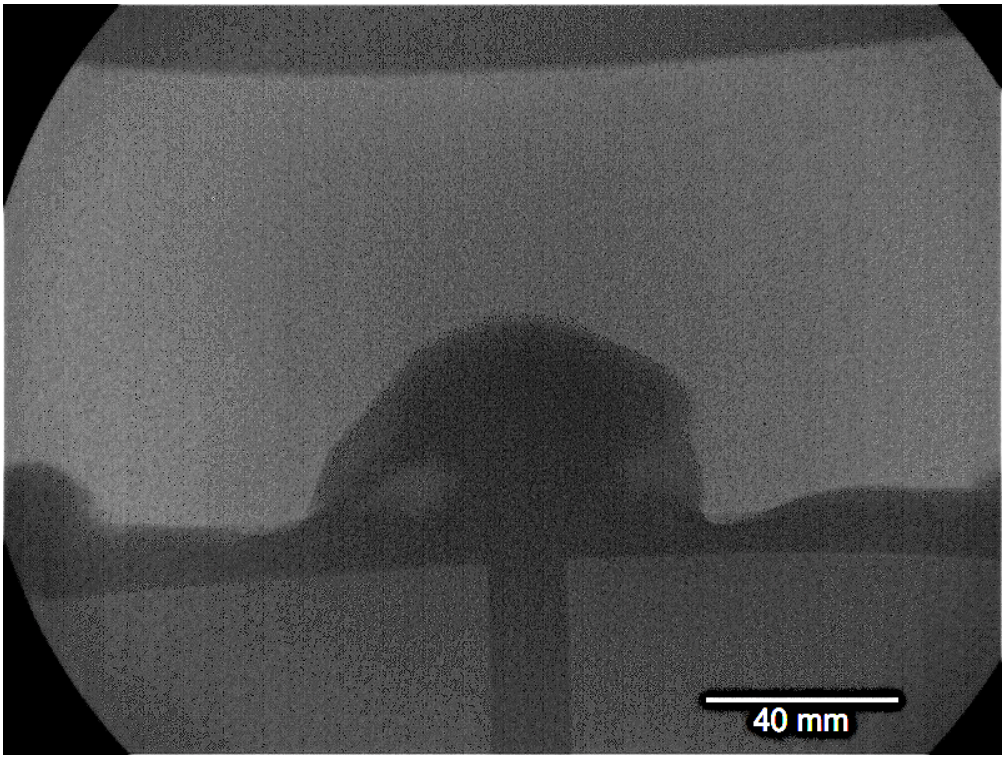

Figure 308. An X-Ray image showing the liquid Al filling the mould at 0.53s filling..

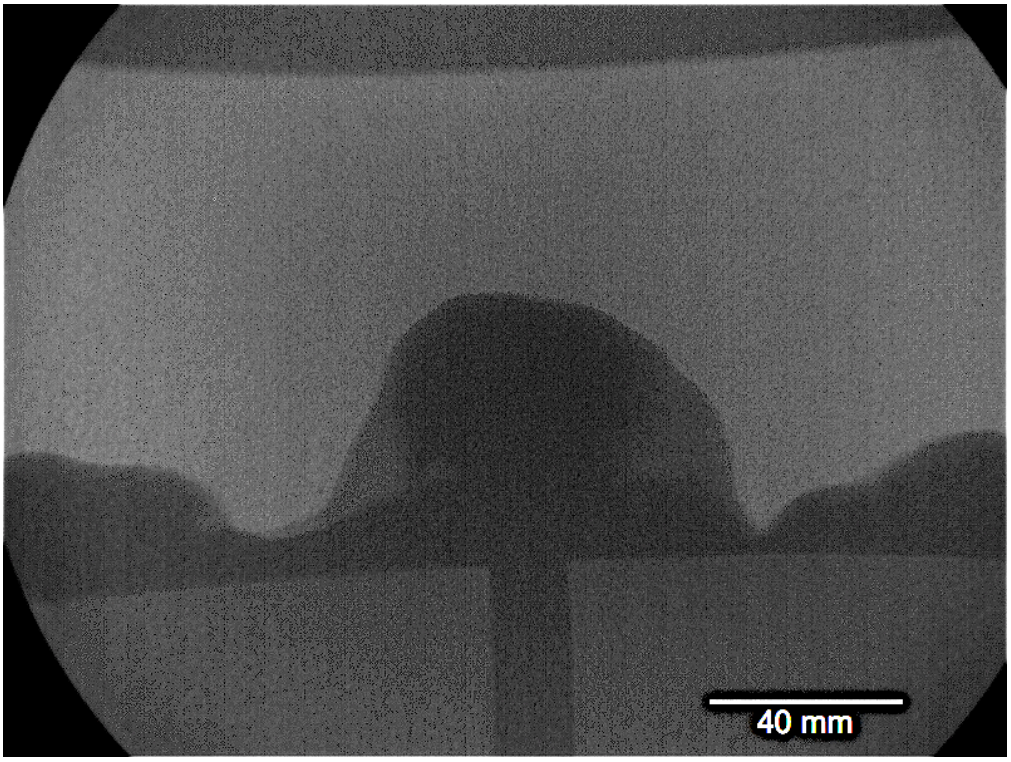

Figure 309. An X-Ray image showing the liquid Al filling the mould and building up on the sides and sloping towards the ingate at 0.59s filling..

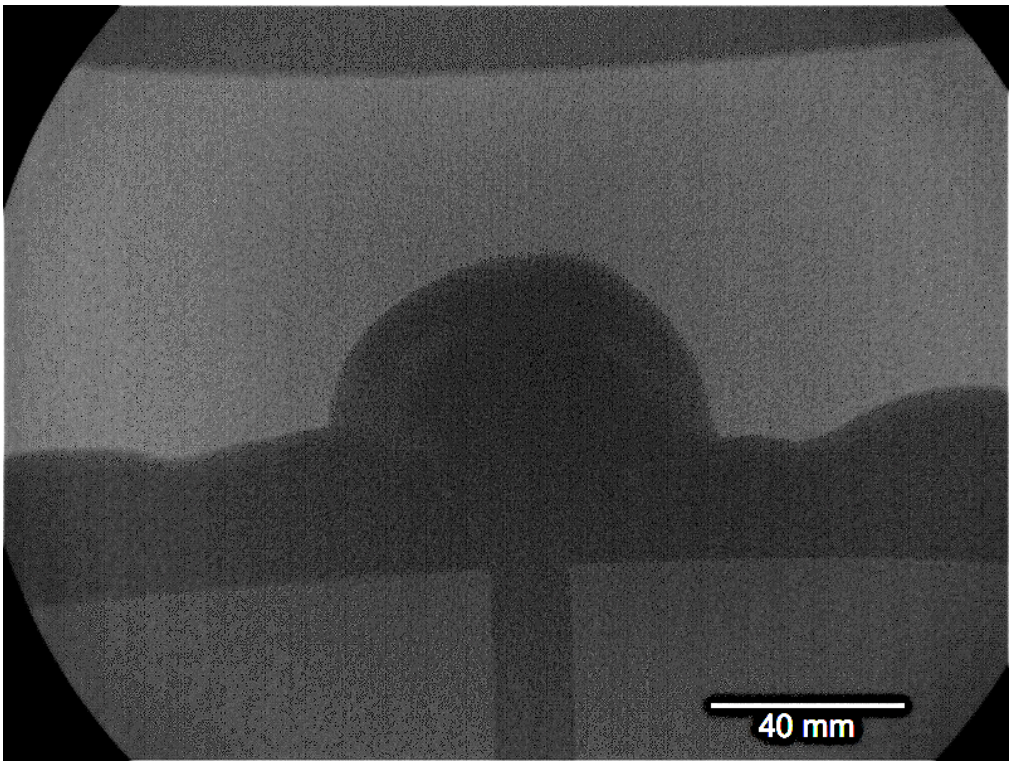

Figure 310. An X-Ray image showing the liquid Al build up on the sides flattening down at 0.75s filling..

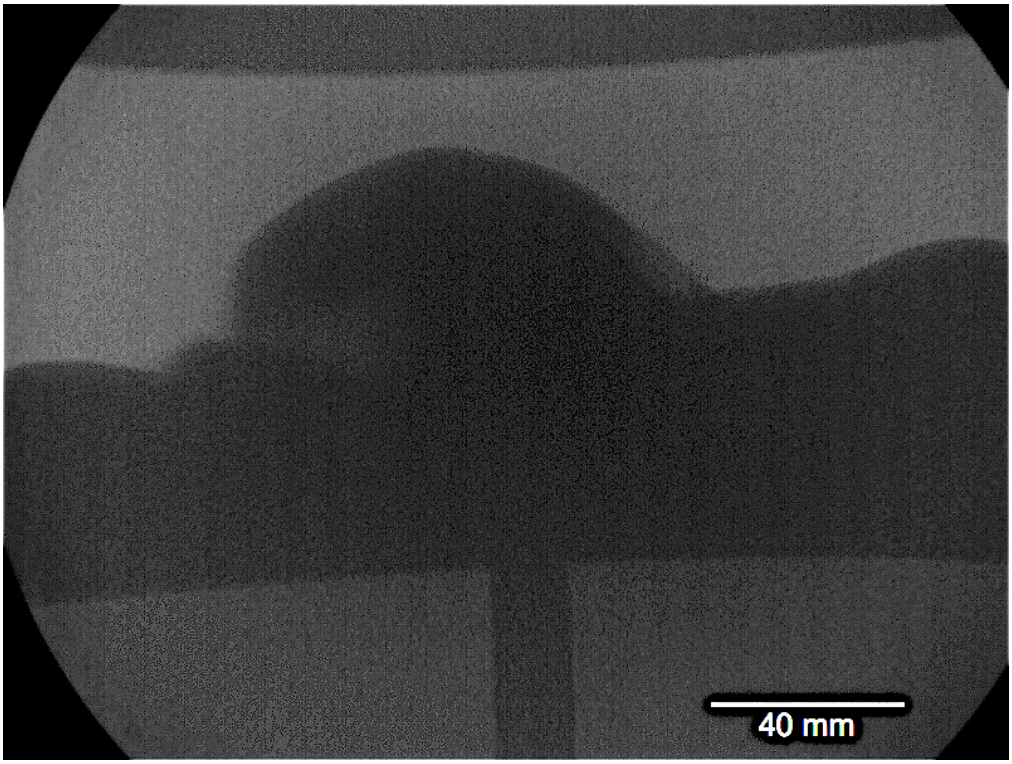

Figure 311. An X-Ray image showing the liquid Al overlapping wave at 1.11s filling. - a known oxide film formation mechanism.

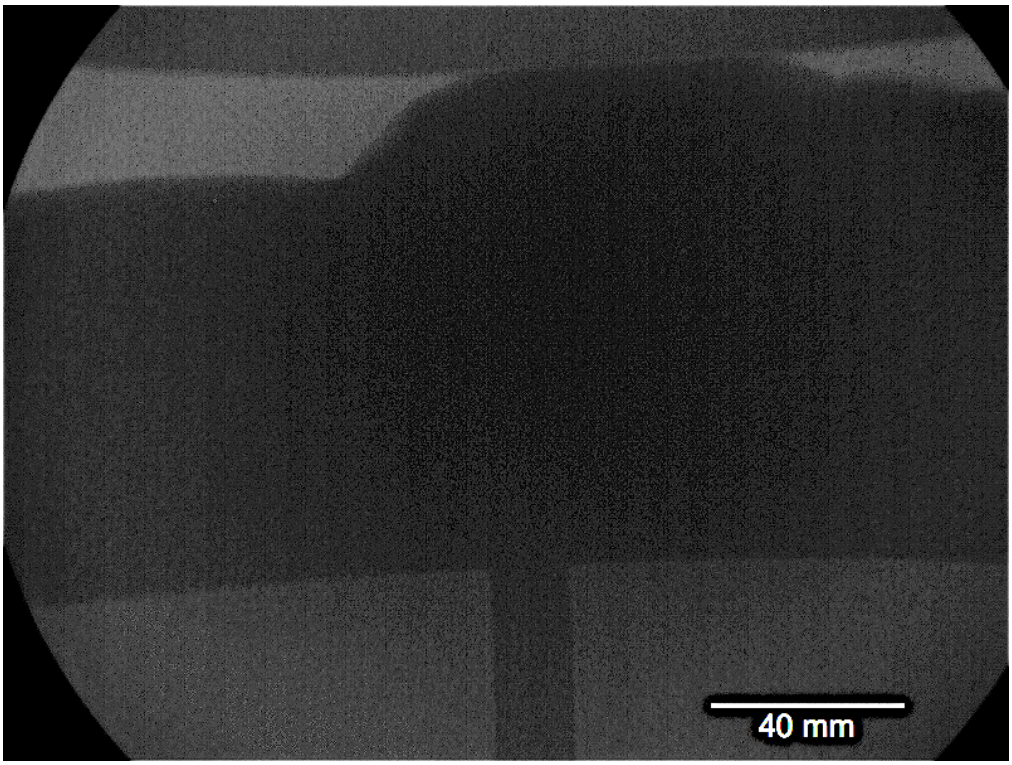

Figure 312. An X-Ray image showing the mould nearing complete filling at 1.53s filling..

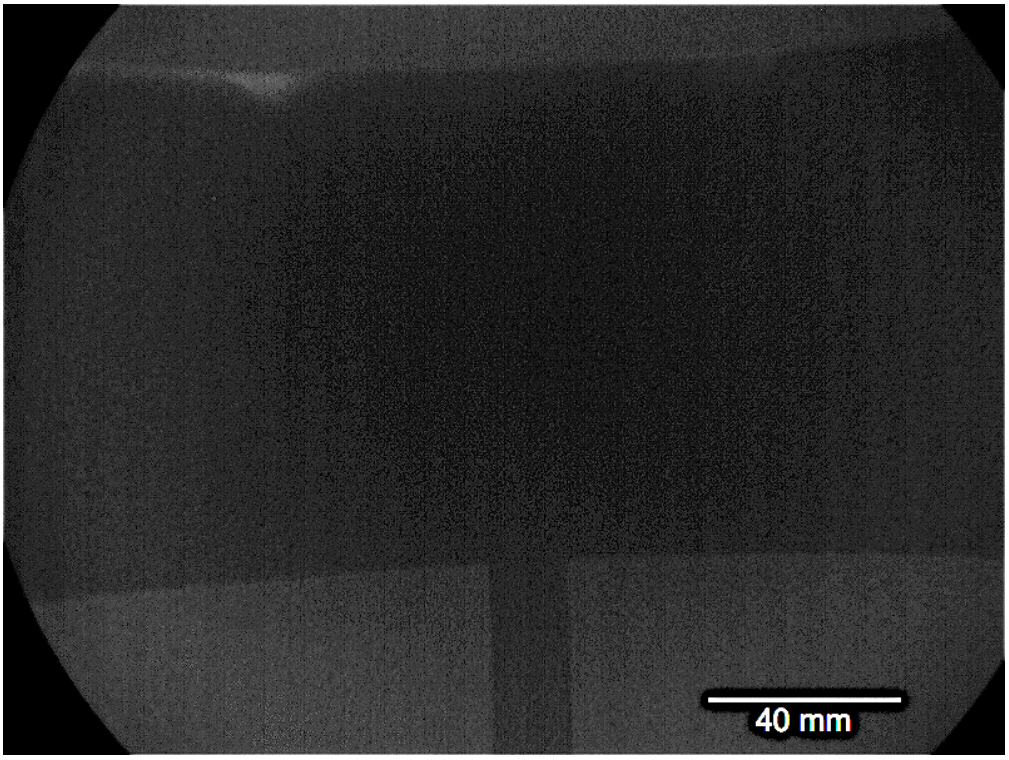

Figure 313. An X-Ray image showing the sand mould full at 2s filling.. Note the symmetrical gas pores at the top of the plate.

4.8 New Industrial Tracers

Table 27 shows the results obtained for the radiation penetration depth, through steel and aluminium using 2 particles of a newly developed Zircon (Zirconium Silicate) tracer, with initial radioactivities of 220μCi and 160μCi. Figure 314 depicts those results, where it is clear that these tracers were detectable through 350mm of steel and 600mm of aluminium. Both particles were used together to determine whether a more radioactive particle (the radioactivity equivalent to both of these particles, was 380μCi) would show better detectability through steel. This however was found to only extend the detectability to 400mm.

Table 27. The penetration depths of the gamma rays through steel and aluminium.

	Steel	Aluminium,	Steel using 2 particles
Distance (mm)	Steel, Events (Counts / Sec)	Events (Counts / Sec)	Events (Counts / Sec)
0 mm	9600	9600	16800
50 mm	3000	8000	9000
100 mm	600	5000	1500
150 mm	120	2500	200
200 mm	50	900	90
250 mm	30	400	50
300 mm	25	200	40
350 mm	20	100	35
400 mm	20	80	25
450 mm	20	70	25
500 mm	20	50	20
550 mm	20	40	20
600 mm	20	30	20

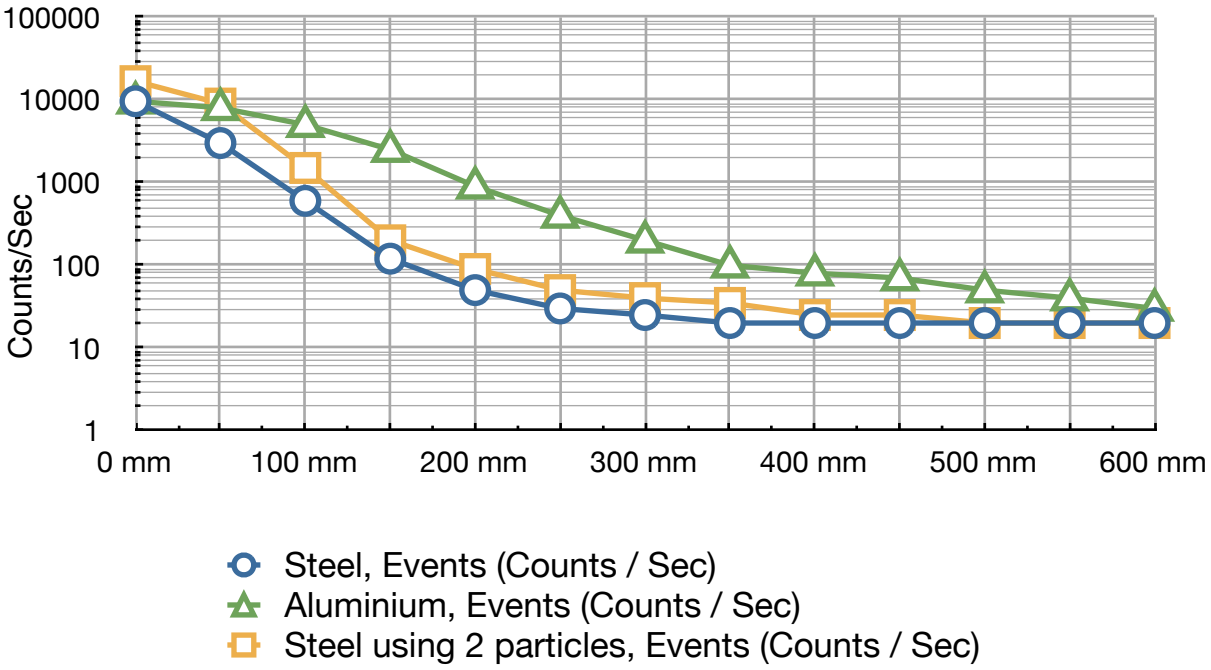

Figure 314. The radioactive counts/sec plotted against the penetration depth for steel, aluminium and a second time through steel when 2 particles were used together.

Table 23. A comparison between the fluid flow behaviour observed from the video of the mould filling and the obtained PEPT results.

Mould Filling Video	Results Obtained Using PEPT
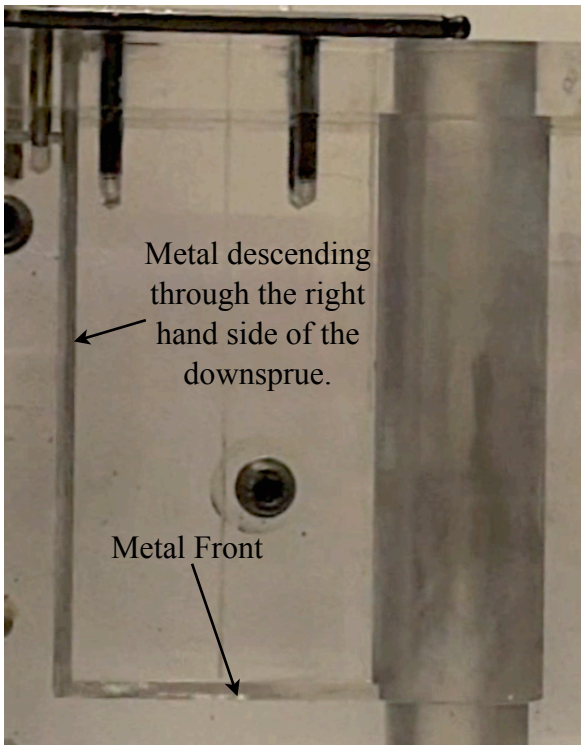	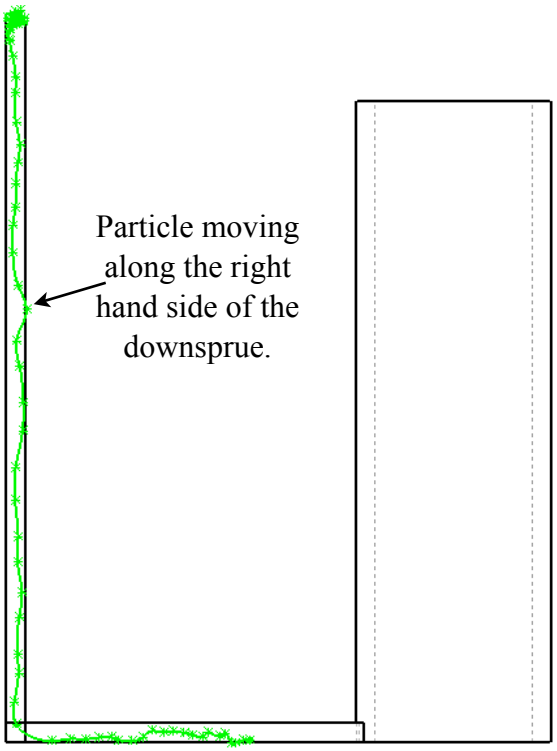
Figure 101. The acrylic mould filling at 1s.	**Figure 102. The PEPT results at 1s.**
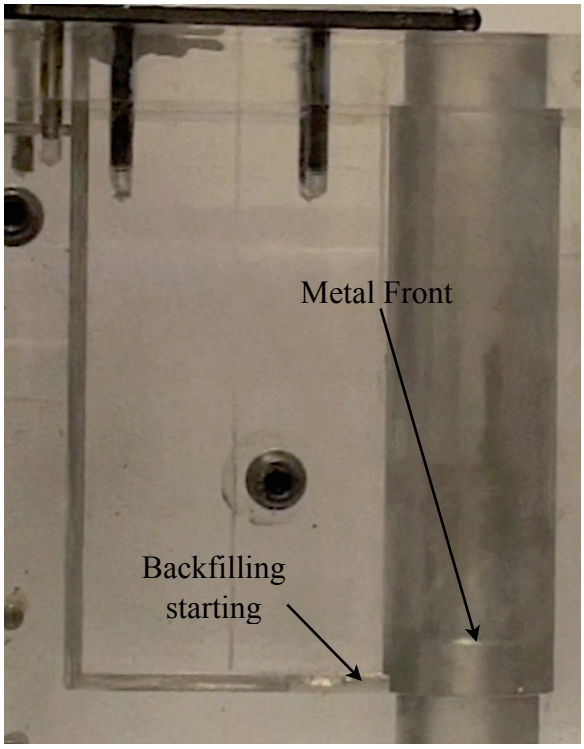	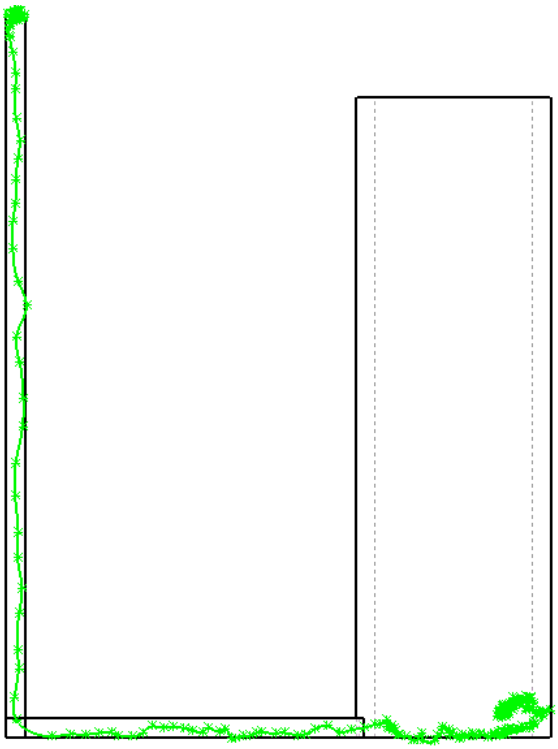
Figure 103. The acrylic mould filling at 2s.	**Figure 104. The PEPT results at at 2s.**

Mould Filling Video	Results Obtained Using PEPT
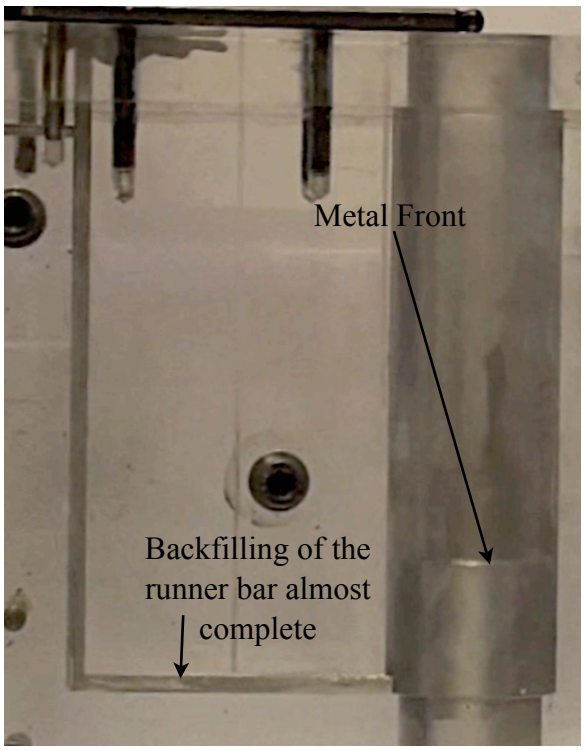	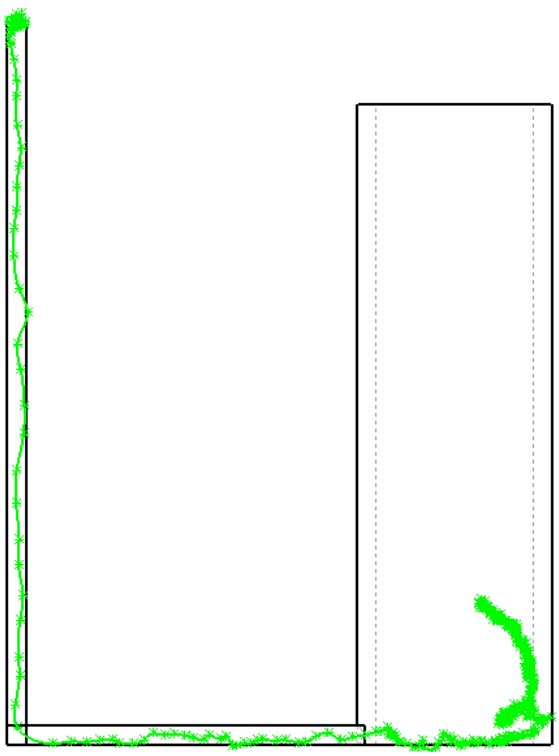
Figure 105. The acrylic mould filling at 3s.	**Figure 106. The PEPT results at 3s**
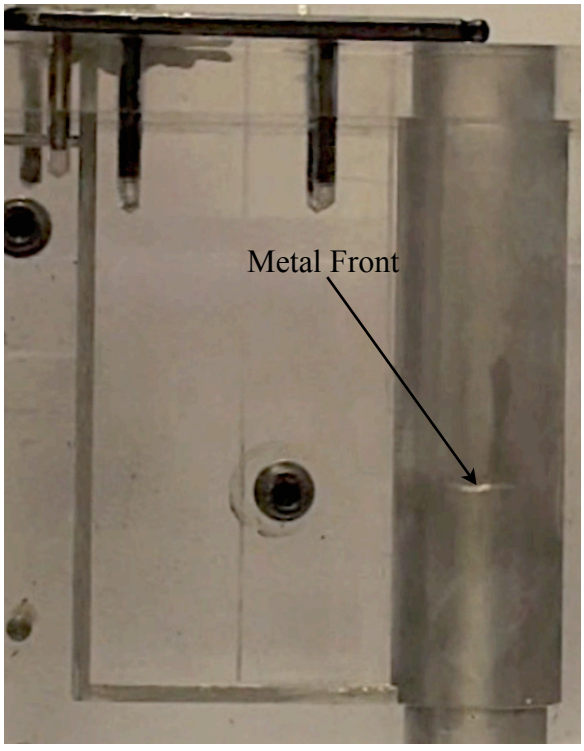	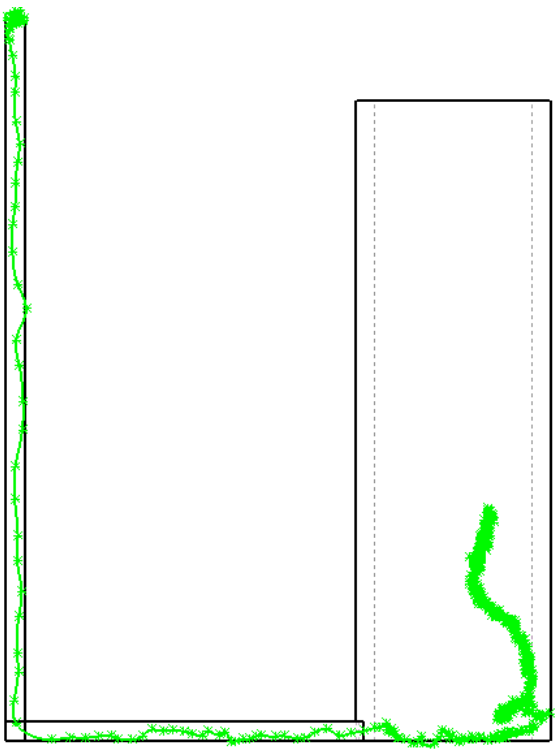
Figure 107. The acrylic mould filling at 4s.	**Figure 108. The PEPT results at 4s.**

Mould Filling Video	Results Obtained Using PEPT
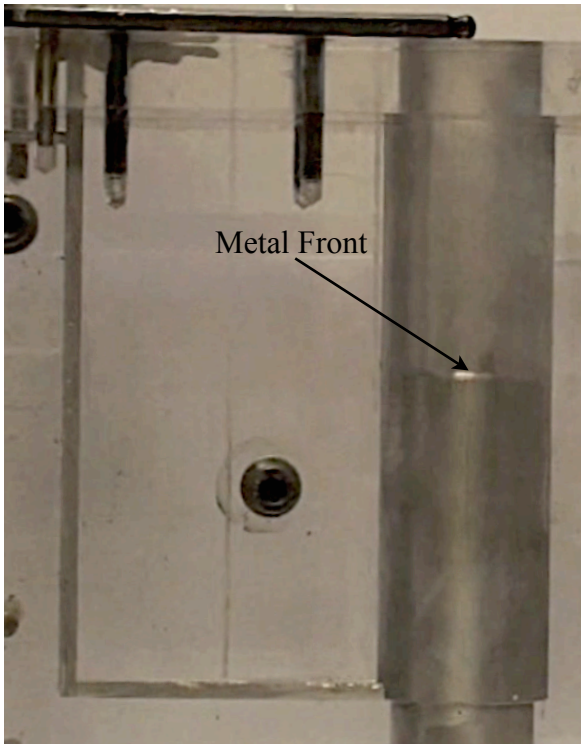	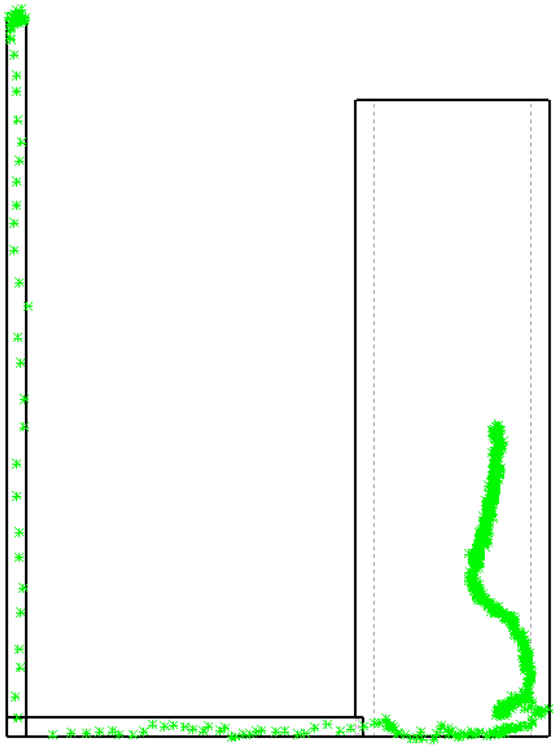
Figure 109. The acrylic mould filling at 5s.	**Figure 110. The PEPT results at 5s.**
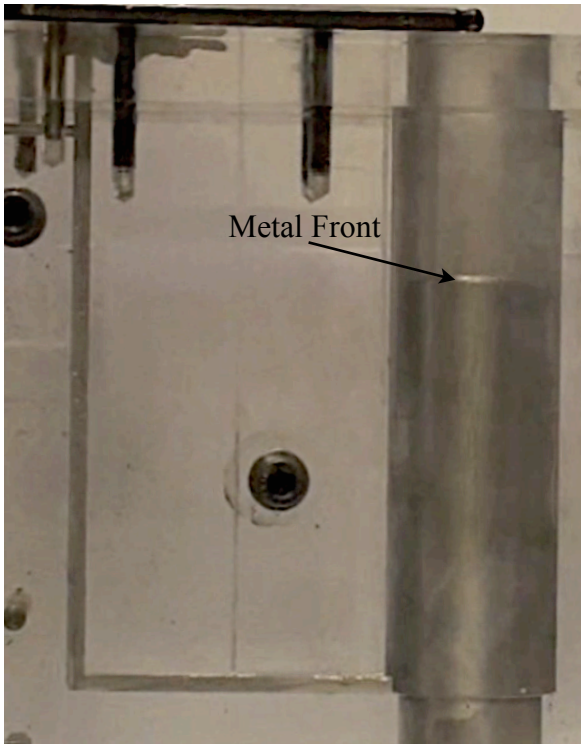	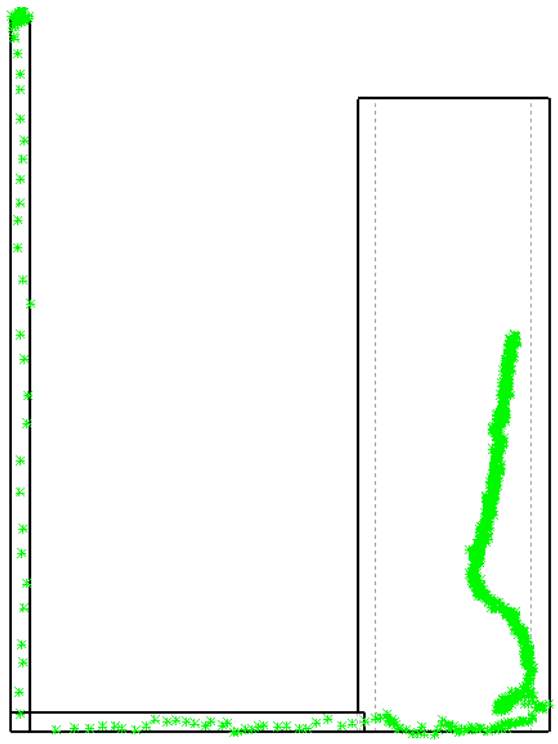
Figure 111. The acrylic mould filling at 6s.	**Figure 112. The PEPT results at 6s**

Mould Filling Video	Results Obtained Using PEPT
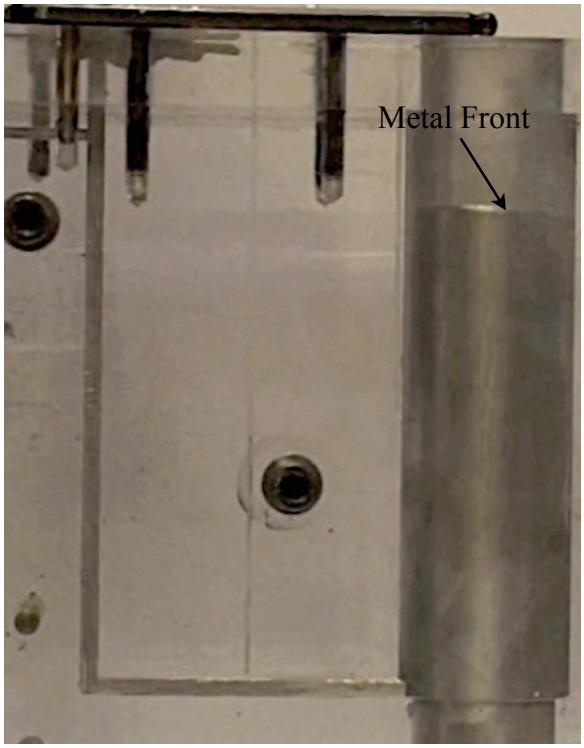	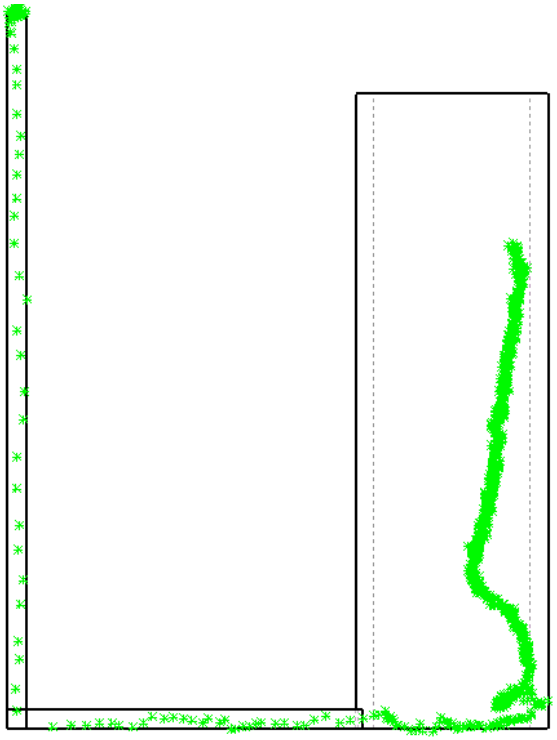
Figure 113. The acrylic mould filling at 7s.	**Figure 114. The PEPT results at 7s.**
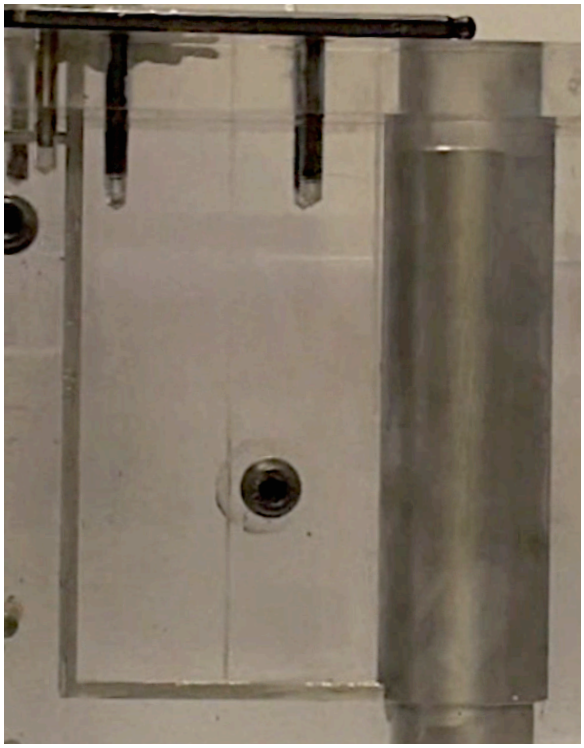	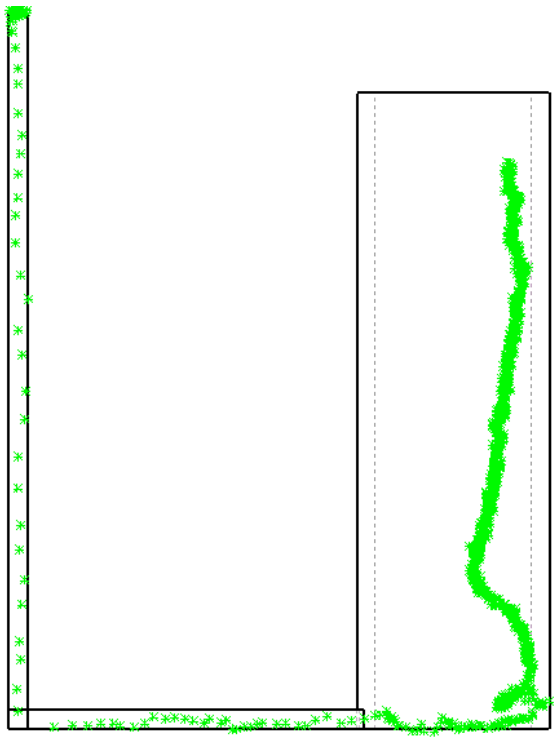
Figure 115. The acrylic mould filling at 8s.	**Figure 116. The PEPT results at 8s.**

Mould Filling Video	Results Obtained Using PEPT
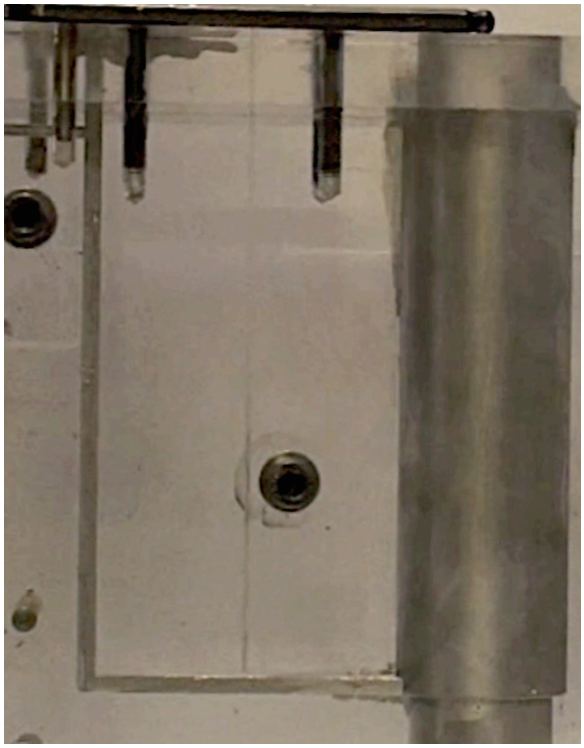	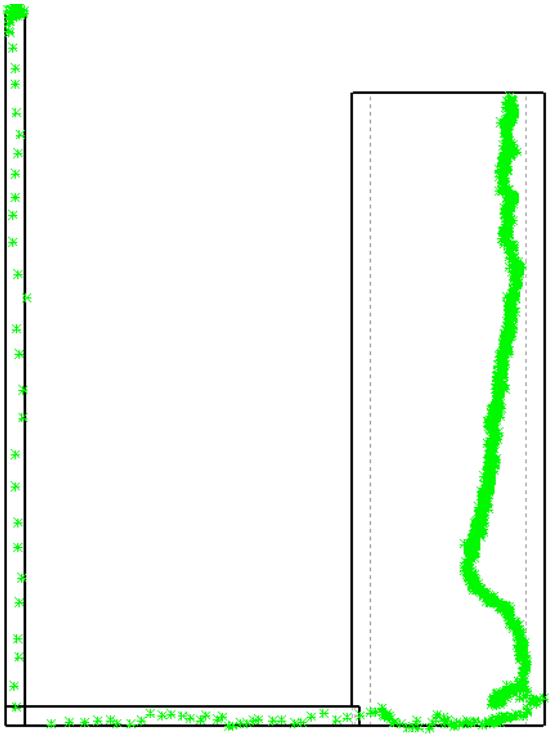
Figure 117. The acrylic mould filling at 9s.	**Figure 118. The PEPT results at 9s.**

4.4.2 The Low melting point alloy baseline experiments

Figures 119-129 show the PEPT results that were obtained when Field's Metal was cast into an acrylic mould with an entrained alumina particle of size 63-100 μm, which was made radioactive by ion exchange and initially placed at the centre of the downsprue opening. Casting was carried out at 85-87^{o}C.

Figure 119 showed that, upon casting, the alumina particle moved down the downsprue together with the liquid metal after which it entered the runner bar. The particle followed the left hand side of the runner bar, after which it entered the cast tube cavity at roughly 20^{o}. The particle then moved clockwise (as viewed from above) around the tube and started rising to the top. The particle came to rest at approximately 150^{o}, at the top surface of the cast tube. The average error in the tracking results was ± 1.8 mm in each of the X,Y and Z coordinates.

This experiment was repeated and cast at 86^{o}C and the results obtained are shown in figure 120. The alumina particle entered the mould with the liquid metal, moved through the downsprue and entered the runner bar at the midpoint of the bottom of the downsprue opening. The particle then moved together with the liquid metal along the right hand side corner of the runner bar up to roughly 50 mm of the length of the runner bar after which it started moving gradually towards the centre line where it entered the cast tube cavity, at 0^{o}. The particle did not rise to the top surface of the cast tube in this case, but came to rest at approximately 6 mm from the bottom. The average error recorded for the X,Y and Z coordinates obtained in this experiment was ±1.76 mm.

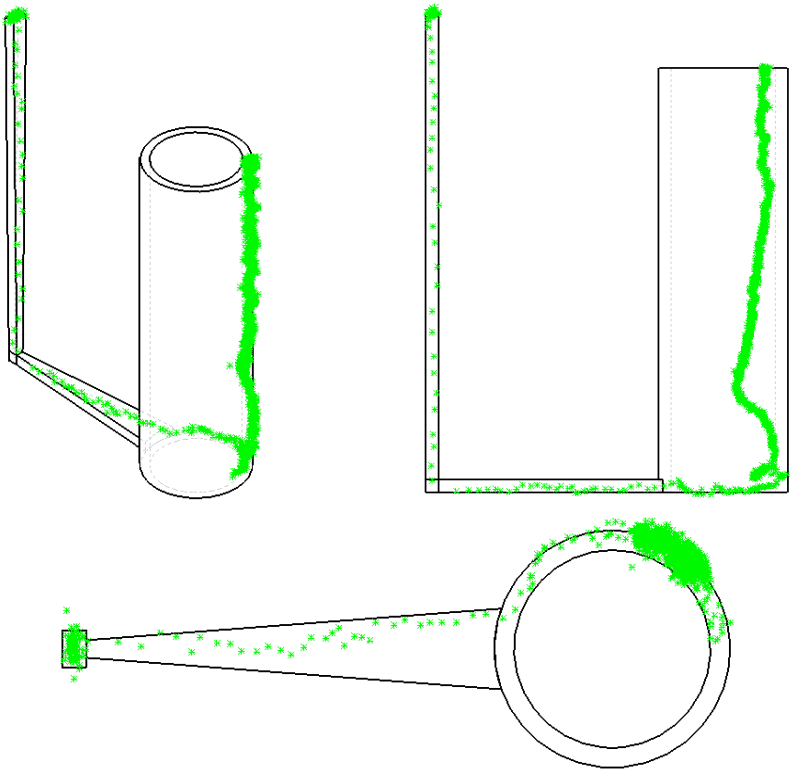

Figure 119. Three engineering views showing the PEPT tracking result obtained when an alumina particle was placed at the centre of the downsprue opening and Field's metal cast at 87°C. Particle size and radioactivity were 63-100µm and 607µCi respectively.

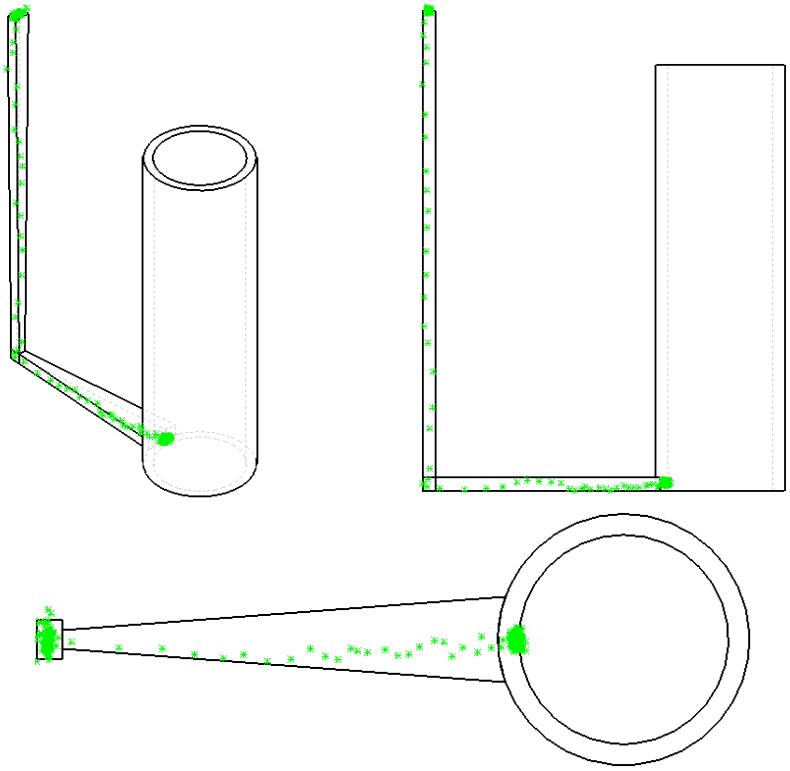

Figure 120. Three engineering views showing the PEPT tracking result obtained when an alumina particle was placed at the centre of the downsprue opening and the Field's metal cast at 86°C. Particle size and radioactivity were 63-100µm and 335µCi respectively.

Figure 121 showed the result obtained for a third experiment where the Field's metal was cast at 85°C. In this case the alumina particle moved within the pouring basin before it entered the downsprue (see figure 122), and the particle entered the runner bar at the left hand side. The particle then moved gradually towards the right hand side of the runner bar and entered the cast tube cavity at roughly 330°. Afterwards the particle moved anti-clockwise and came to rest at roughly 250° and 8 mm above the bottom of the cast tube. These tracking results have an average error of ± 2 mm in all directions.

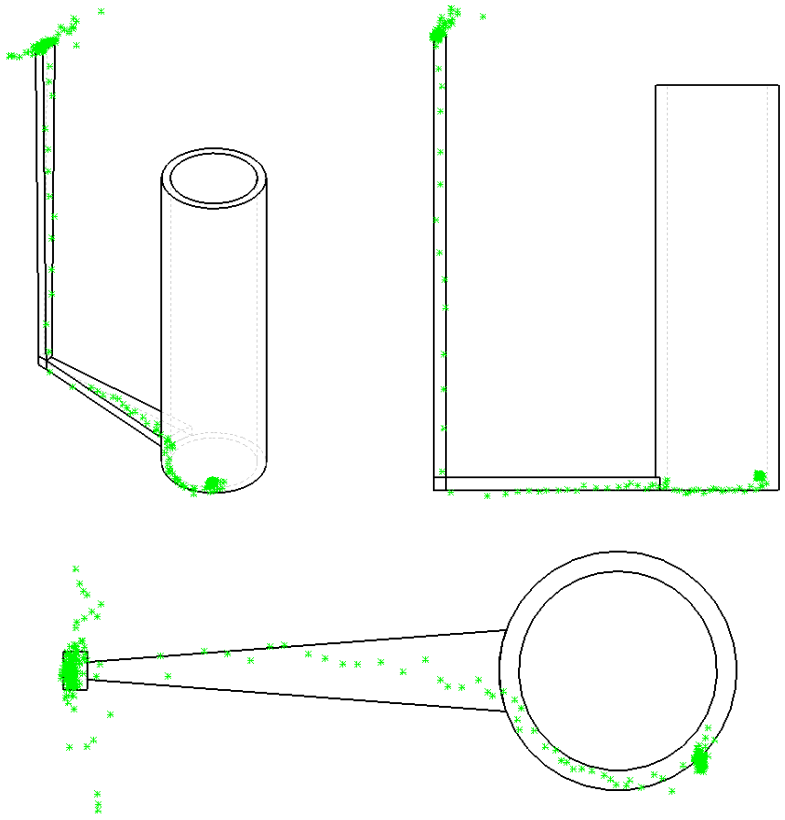

Figure 121. The tracking result obtained when an alumina particle was placed at the centre of the downsprue opening and the Field's metal cast at 85°C. Particle size and radioactivity were 63-100µm and 274µCi respectively.

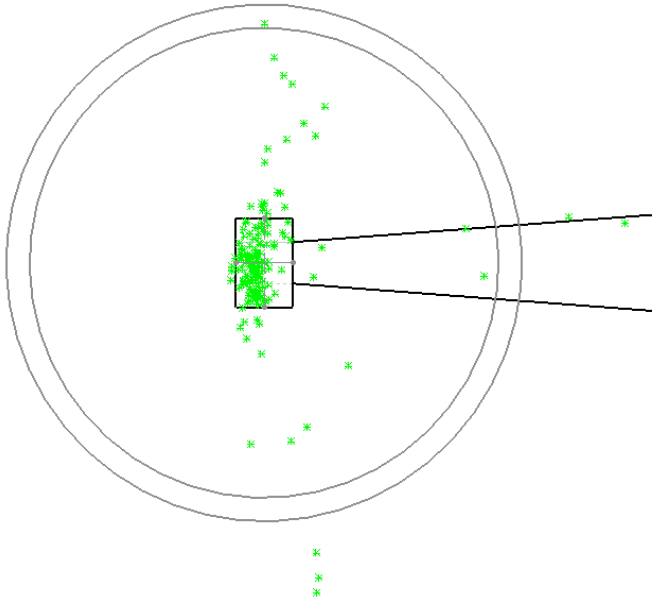

Figure 122. A close up top view showing the pouring basin in place to demonstrate that the particle has moved within the pouring basin.

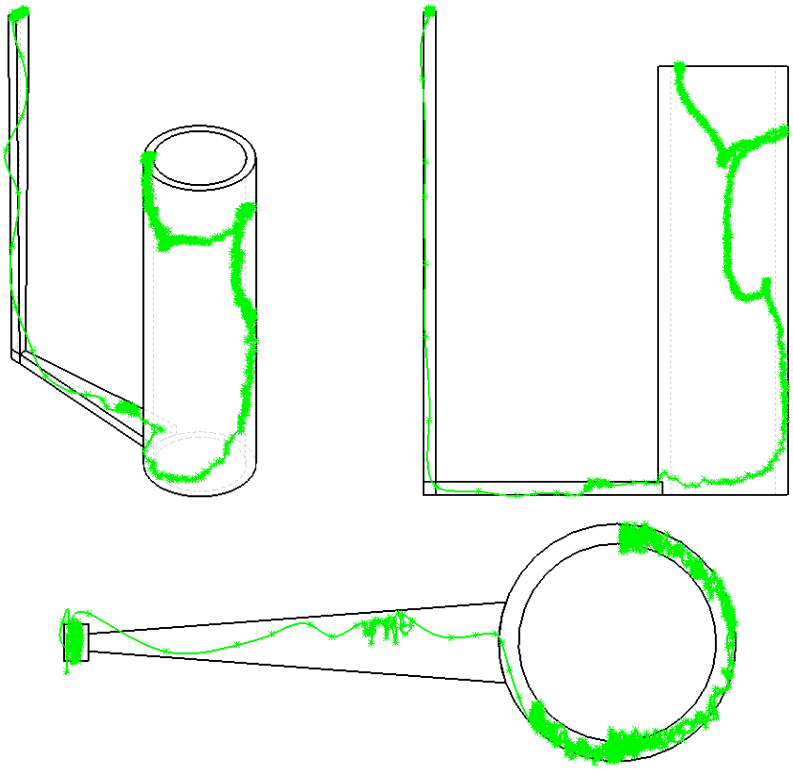

Figure 123. The tracking result obtained when an alumina particle was placed at the centre of the downsprue opening and the Field's metal cast at 87°C. Particle size and radioactivity were 63-100µm and 99µCi respectively.

This experiment was repeated a fourth time, with the metal cast at 86^{o}C. The result obtained is shown in figure 123. The particle moved down the downsprue with the liquid metal without prior movement in the pouring basin. It entered the runner bar and rose to its upper surface, just before it entered the cast tube cavity at 0^{o}. The particle then moved anticlockwise around the tube while rising to the top surface where it came to rest at approximately 90^{o}. The particle, however did not rise smoothly to the top, but followed an unexpected path up the length of the tube.

This baseline experiment was also carried out using Lensalloy-136, with a melting point of 57.8^{o}C, and the result has been shown in figure 124. The particle path was not entirely within the mould cavity, an error that was also observed with later experiments where the Perspex^{TM} mould was twisted (not exactly parallel to camera faces) by an average of 1.2°. The particle in this case seemed to have had a similar path to that obtained in figure 121 (cast with Field's metal), where it entered the cast tube cavity at 0^{o}, and moved anticlockwise and came to rest at roughly 90^{o} at the bottom surface of the tube. The average tracking error was ±2.2 mm, for all coordinates.

Finally this experiment was repeated once again with the aim of maximising reproducibility, where an upper pouring basin as well as a stopper rod, to better control the entry conditions of the liquid metal into the mould, were used. Four castings were carried out with the metal cast at 87^{o}C, and the tracking results obtained from these experiments have been shown in figures 125-129.

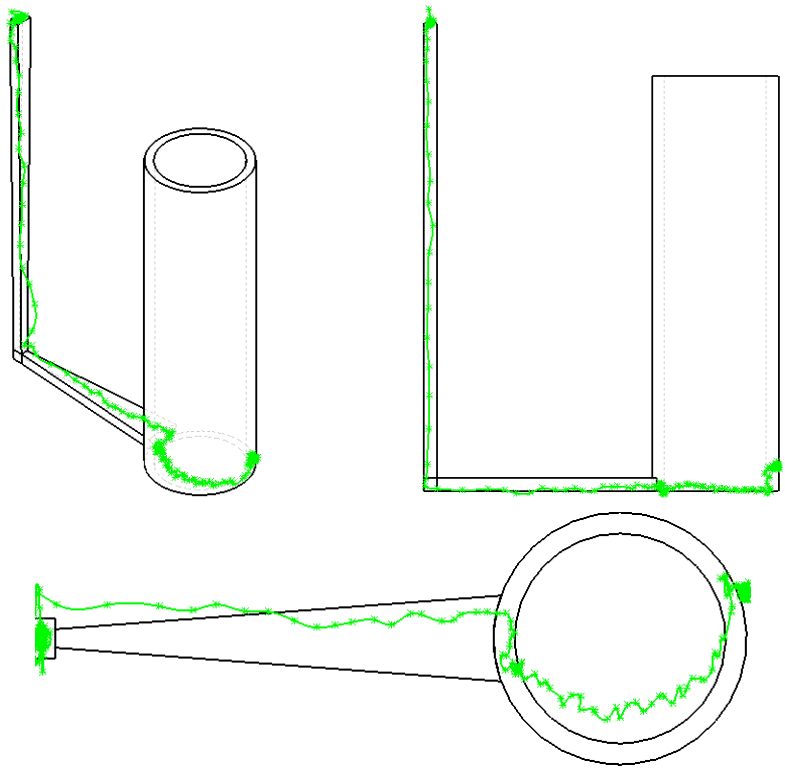

Figure 124. The tracking result obtained when an alumina particle was placed at the centre of the downsprue opening and the Lensalloy-136 cast at 87°C. Particle size and radioactivity were 63-100µm and 390µCi respectively.

In figure 125, the particle track is shown descending the downsprue, making its way along the right hand side of the runner bar, entering the tube casting and rising upwards until it came to rest in the lower third of the tube, at about 140° from the point of entry. The zig-zag path shown in the plan view in figure 129 is due to the error of several mm with which the particle location has been determined; the actual particle path was probably smoother. Figures 126, 127 and 128 showed very similar particle paths up to the runner bar, provided the symmetry of the casting was considered.This means that if the equal chance of the particle moving along the right hand side of the runner bar or the left hand side was considered, the particle paths would be similar or in other words a mirror image of each other (see figure 129). In figure 126, as the particle entered the tube, it was washed around with the rising metal until it started rising vertically upwards and was trapped just above the lower third of the tube. Figure 127 shows that the particle started rising upwards immediately as it entered the tube until it also

came to rest in the lower third of the tube. Figure 128 showed the most similarity to figure 125 where the particle moved around the tube and started rising at roughly 140° from the point of entry until it also came to rest in the lower third of the tube.

Figure 129 shows the particle paths depicted by figures 125-128 in plan view and superimposed on the same casting in order to allow for a clearer comparison. Although the mould filling in all 4 experiments was carried out with some reproducibility, the particle paths were not identical, especially compared to the results shown in figure 126 (which showed the most difference). This could be attributable to minor errors associated with the particles initial position, where it may have been anywhere within a 1 mm diameter hole, which could have led to the particle being released slightly differently and hence behaving differently as it entered the tube. Another explanation could be the changing heat transfer between the metal and the mould as the mould got hotter from one experiment to the next. This may have delayed solidification and hence increased the particle's chance of moving with the liquid metal before being trapped and coming to rest.

No reproducibility was observed prior to controlling the inlet conditions, as was the case for the first 5 experiments. When a stopper rod was used and the mould filling was reproduced carefully, 75% of the results showed a similar particle path and final particle location, which was the bottom third of the tube.

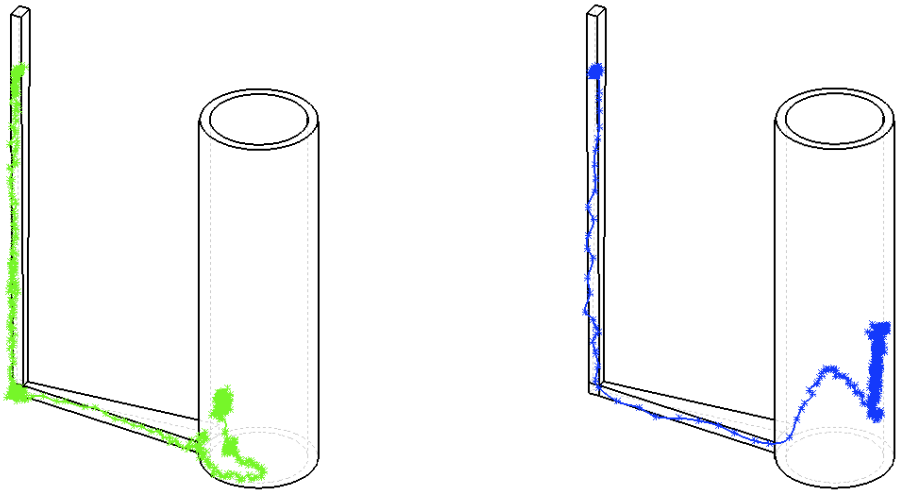

Figures 125 and 126. The tracking result obtained when an alumina particle was placed at the centre of the downsprue opening and the Lensalloy-136 cast at 87°C. In this experiment an upper pouring basin and a stopper rod were used for reproducibility. Particle size was 63-100µm in both cases and particle radioactivities were 822µCi and 235µCi respectively.

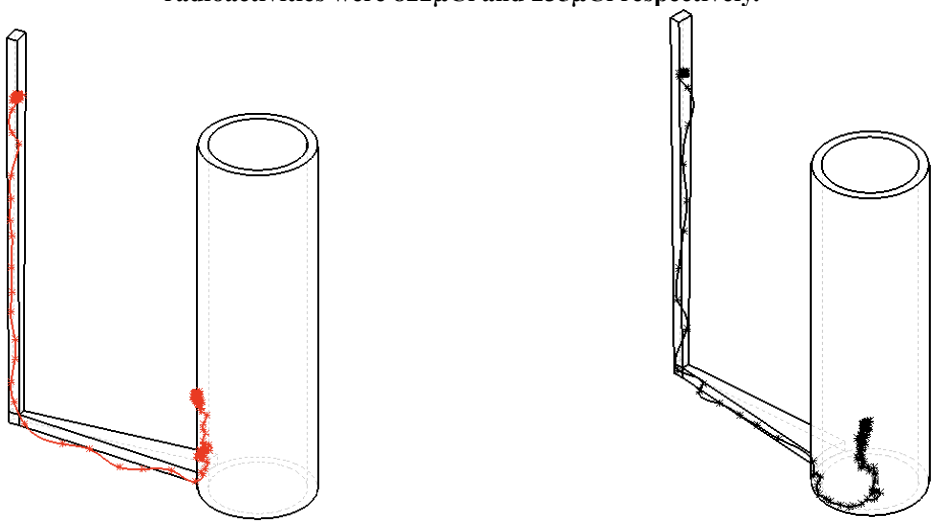

Figure 127 and 128. The tracking result obtained when an alumina particle was placed at the centre of the downsprue opening and the Lensalloy-136 cast at 87°C. In this experiment an upper pouring basin and a stopper rod were used for reproducibility. Particle size was 63-100µm in both cases and particle radioactivities were 240µCi and 178µCi respectively.

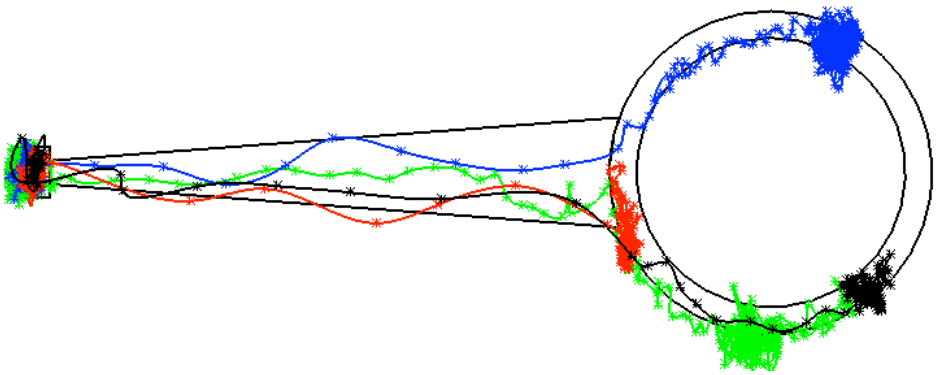

Figure 129. A plan view showing the results in figure 125-128 superimposed on 1 casting for comparison..

4.4.3 The Effects of Using Resin Particles

The results presented in this section were obtained when resin particles of size 63-73µm were used instead of alumina, to investigate the possibility of tracking and irradiating a smaller particle, more representative of inclusions found in metals and that could potentially be used to study inclusion agglomeration in low melting point alloys. Figure 130 showed that the particle moved within the pouring basin before it was swept into the downsprue. The particle then moved with the liquid metal where it entered the runner bar from the right hand side and followed the upper right corner after which it gradually moved towards the centre line of the runner bar where it entered the cast tube cavity. The particle started rising while gradually moving anticlockwise and finally came to rest at approximately 260^{o}. The average error in all coordinates was ± 2 mm.

A resin particle was also used as a tracer particle for the identical casting shown in figure 131. In this experiment, the particle entered the runner bar and moved along the upper left hand side corner until it moved to the right hand side just before it entered the casting tube cavity at 330^{o}. The particle then moved anticlockwise while it continued to rise into the cast tube where it came to rest at 280^{o}, roughly 80 mm from the bottom of the tube. The average error recorded for the tracking data was ± 1.6 mm.

In both experiments the particle entered the tube cavity from the right hand side and came to rest almost halfway along the length of the tube. Results were probably not identical due to the different entry conditions where the particle moved within the pouring basin before it

entered the mould as shown in figure 130. However, these results were somewhat similar to those obtained when an alumina particle was used, figures 125, 127 and 128, where the alumina particle also entered the tube cavity from the right hand side and came to rest in the lower third of the tube.

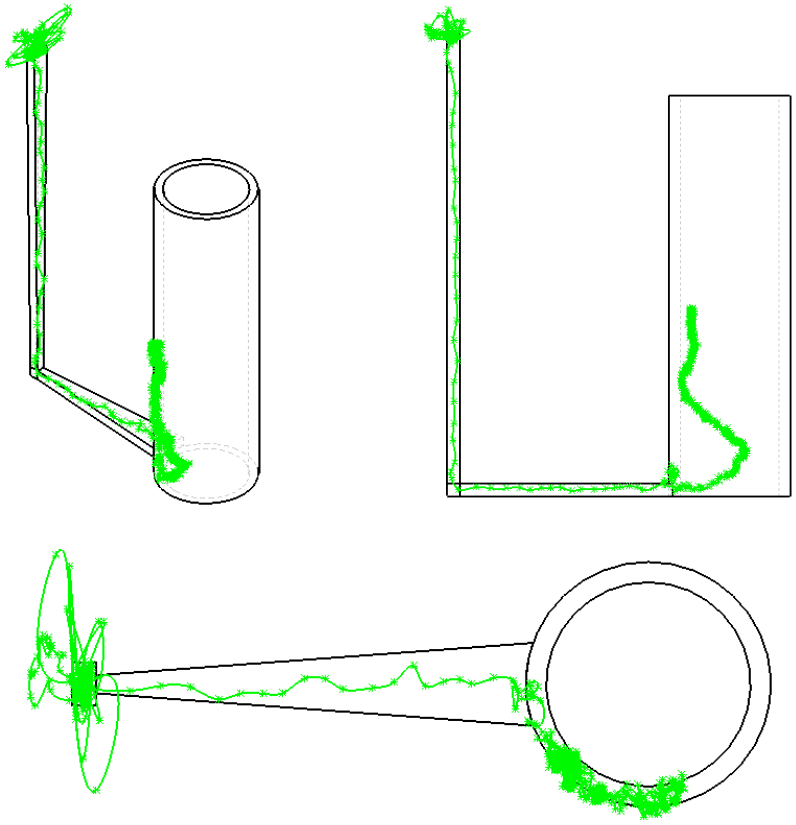

Figure 130. The tracking result obtained when a resin particle of size 63-73µm was initially placed at the centre of the downsprue opening. Particle radioactivity was 418µCi.

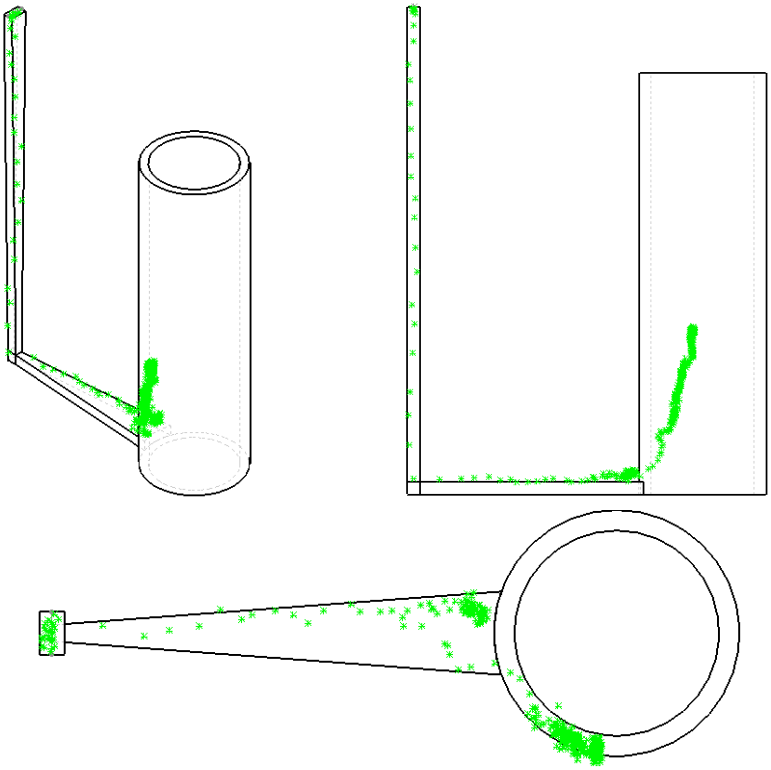

Figure 131. The tracking result obtained when a resin particle of size 63-73µm was initially placed at the centre of the downsprue opening. Particle radioactivity was 250µCi.

4.4.4 The Effect of Increasing The Pouring Temperature

In this experiment the effect of increasing the pouring temperature on the particle's radioactivity / tracking error was investigated, in order to determine a maximum temperature at which a particle irradiated by ion exchange could be tracked accurately. It was also of interest to find out whether delaying solidification by increasing the pouring temperature would show a higher level of reproducibility in the results.

The low melting point alloy casting was carried out with a radioactive alumina particle, initially placed at the centre of the downsprue opening, but the metal in this case was cast at 110^{o}C rather than the previous 87^{o}C. The tracking results obtained are shown in figure 132.

The alumina particle moved in the pouring basin before it entered the downsprue with the liquid metal. However, after the particle entered the runner bar, it moved along the runner bar centre line, close to the runner bar upper surface. As the particle entered the casting tube cavity, it moved clockwise and began to rise. Soon after that, the particle came to rest at 175^{o} and at about 25 mm above the bottom of the cast tube. The average error in the tracking results was recorded to be ± 1.5 mm in all directions.

Therefore, increasing the pouring temperature did not affect the tracking results or the particle movement. However, several regions of the solidified casting were found to be radioactive when a Geiger counter was used to verify the particle's final location within the casting. This contamination was believed to be attributable to the casting temperature being above 100^{o}C,

which may have broken the weak van-der-Waal's forces binding the ^{18}F to the particle surface leading to the release and distribution of the radioactive water molecules around the liquid metal.

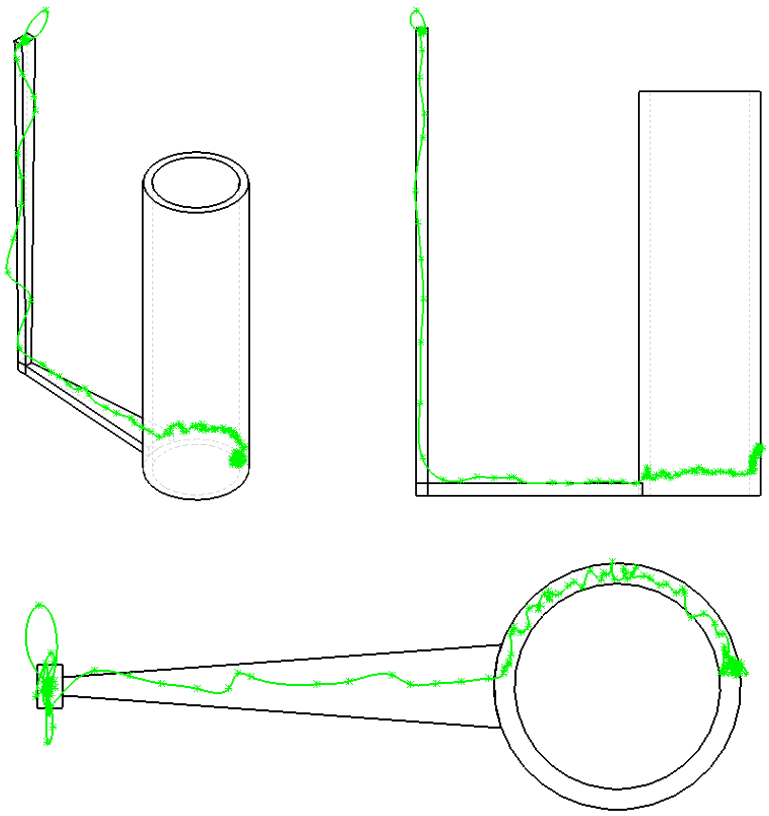

Figure 132. The tracking result obtained when an alumina particle was placed at the centre of the downsprue opening and the Field's metal cast at 110°C. Particle size and radioactivity were 63-100µm and 168µCi respectively.

4.4.5 The effect of using ceramic foam filters

4.4.5.1 30 ppi filters

Three sets of experiments were carried out where the low melting point alloy Lensalloy-136 was cast into an acrylic mould with a ceramic foam filter, to investigate the effects of the presence of such filters on the particle path, as well as the effect of changing the filter pore sizes on filtration efficiency. In the first set of experiments, 4 castings were carried out using 30 ppi (pores per linear inch; ≈ 1.5-1.7 mm in diameter) filters. Another 4 experiments were carried out using 20 ppi filters and, 4 castings were carried out using 10 ppi filters. In all castings an alumina particle of size 63-100μm was made radioactive by ion exchange and introduced at the centre of the downsprue opening. The average error in the tracking data for the experiments where a 30ppi filter was used was ± 2.3, 2.4, 1.9 and 2 mm respectively.

Figures 133-136 show the results obtained when a 30 ppi filter was used. In all cases the particle entered the lower runner bar, rose up to the filter and was trapped there. In figures 133 and 135, the particle came to rest at roughly 9 and 19 mm respectively from the bottom surface of the filter. Figure 134 showed that the particle was also trapped in the filter but at the right hand side. Figure 136 shows that the particle entered the filter but moved back down to the top of the lower runner bar where it came to rest (see green particle path on figure 137). Figures 137 and 138 show the superimposition of the particle paths, for comparison. In all 4 castings the particle had a similar particle path. Three particles came to rest towards the end of the filter except 1 particle which came to rest at the top of the runner bar, which is believed to be due to a small leakage from the bottom of the mould, in this case, which would have drained a small amount of the liquid metal and led to the particle path shown in figure 138.

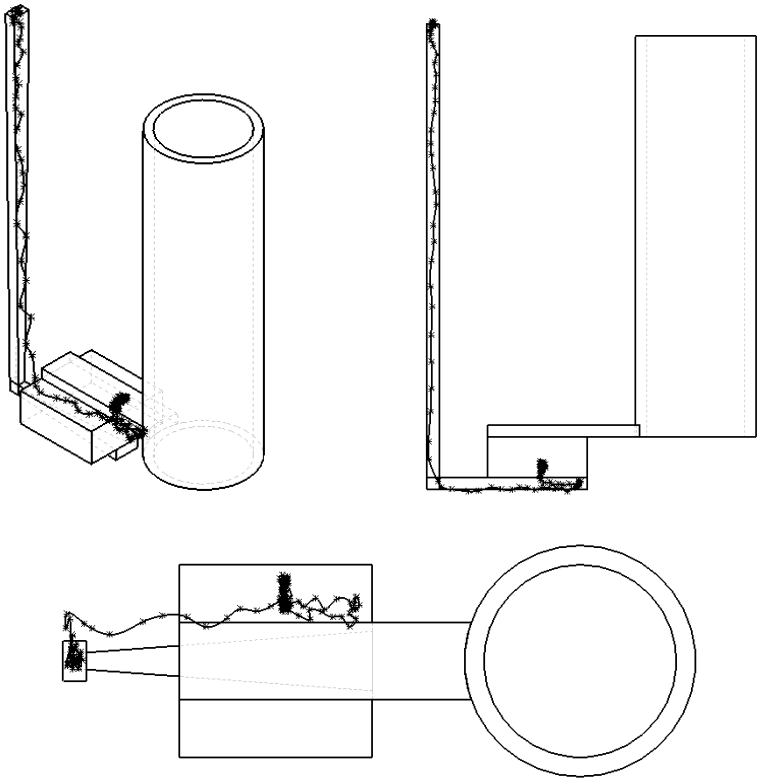

Figure 133. The particle tracking results obtained for a 30ppi filter casting. Particle size and radioactivity were 63-100µm and 532µCi respectively.

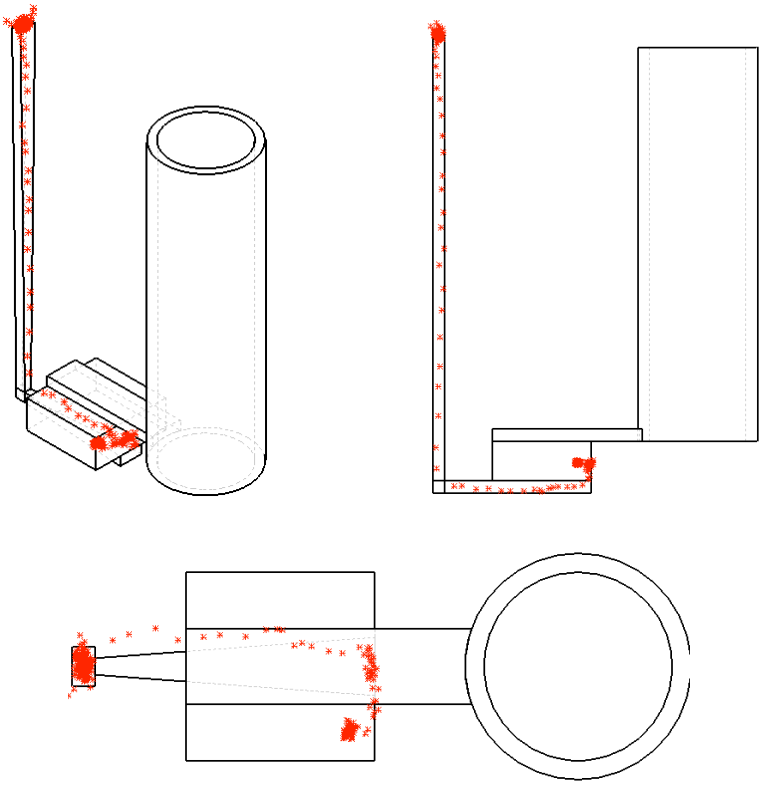

Figure 134. The particle tracking results obtained for a 30ppi filter casting. Particle size and radioactivity were 63-100µm and 351µCi respectively.

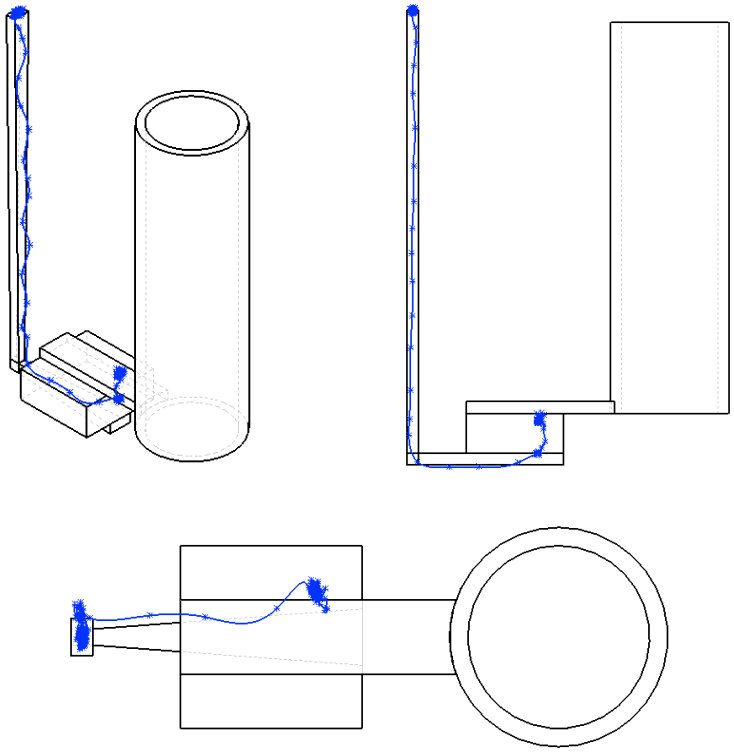

Figure 135. The particle tracking results obtained for a 30ppi filter casting. Particle size and radioactivity were 63-100µm and 190µCi respectively.

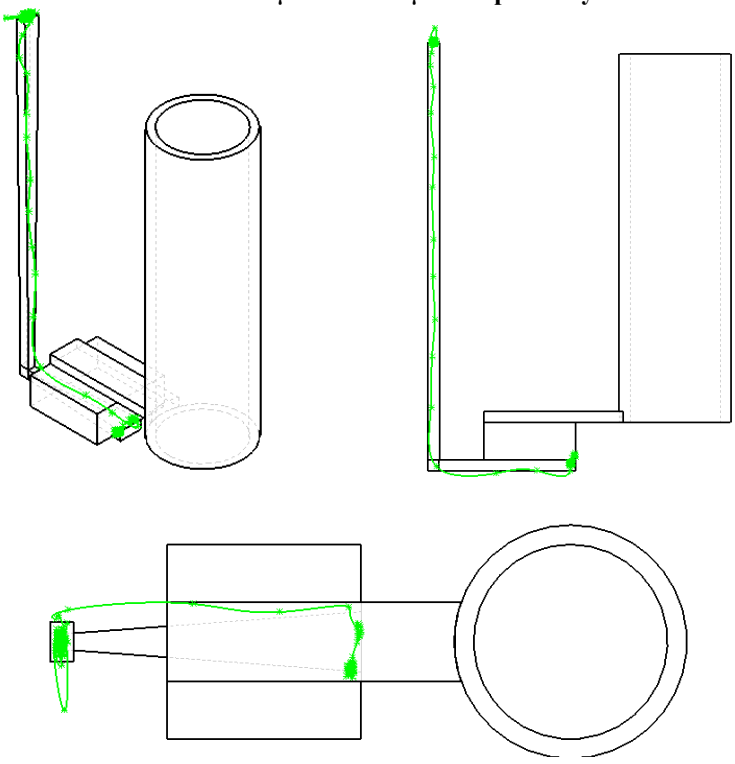

Figure 136. The particle tracking results obtained for a 30ppi filter casting. Particle size and radioactivity were 63-100µm and 145µCi respectively.

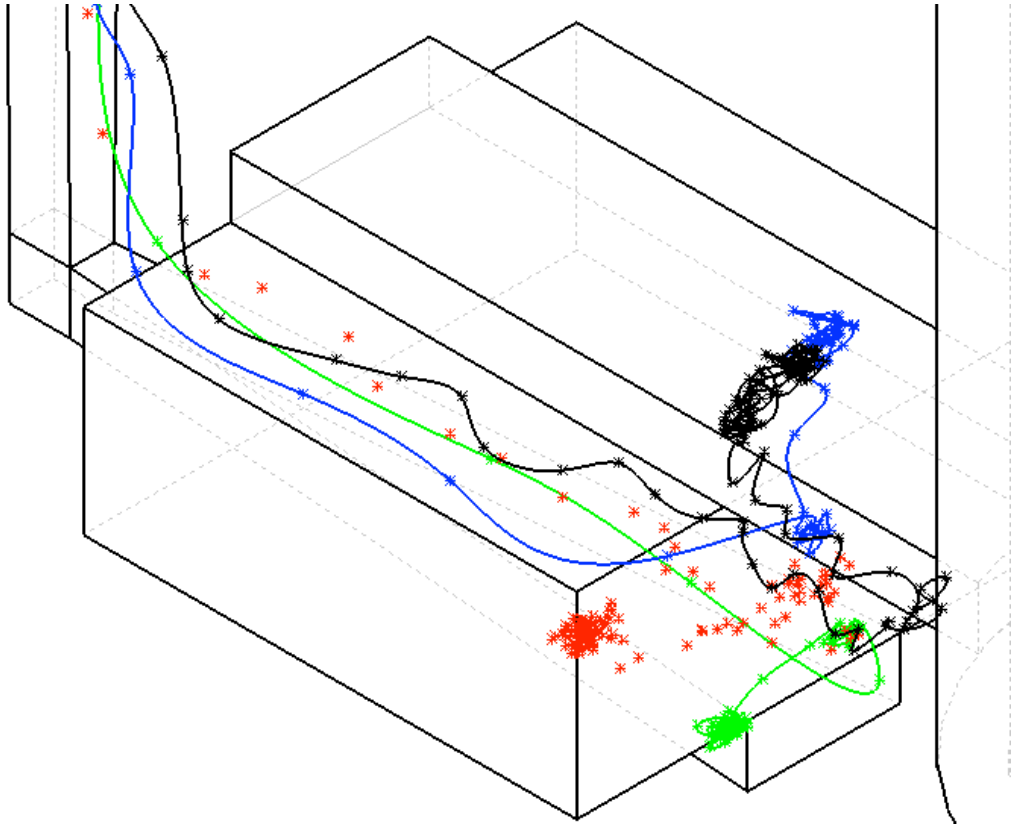

Figure 137. The results obtained for all the castings where a 30ppi filter was used, superimposed onto 1 3D casting for comparison.

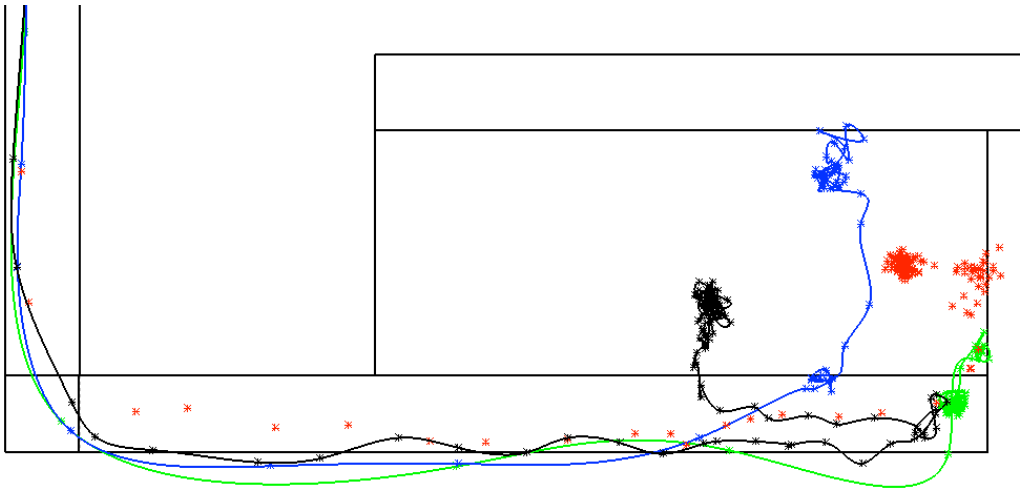

Figure 138. A 2-D side view showing the results obtained for all the castings where a 30ppi filter was used, superimposed onto 1casting for comparison.

4.4.5.2 20 ppi filters

Figures 139-142 show the particle tracking results obtained when a 20 ppi filter was used. In one experiment (figure 139), the particle was not trapped by the filter; it moved down the downsprue, through the left hand half of the filter and made its way into the cast tube where it came to rest at 250^{o}, one third from the top of the tube. The mismatch observed between the particle path and the casting geometry was found to be due to a slight twist, of approximately 2.5^{o}, in the mould positioning between the camera faces. Figure 140 shows the particle path obtained from another experiment where the particle moved down the downsprue and remained within the left hand side of the filter where it came to rest.

The particle paths shown in figure 141 showed that the particle moved down the downsprue and moved centrally through the lower runner bar where it came to rest within the filter. The particle did not go through the filter although this could be attributed to the fact that this casting did not completely fill, 10 mm from of the tube mould cavity was not filled due to insufficient material cast. Figure 142 showed that the particle was trapped by the filter and came to rest a few millimetres above the bottom surface of the filter.

Figures 143 and 144 show the superimposition of the particle paths, within the filter, for comparison. The average error in the tracking data for the experiments where a 20ppi filter was used was ± 1.7, 1.9, 1.6 and 1.8 mm respectively.

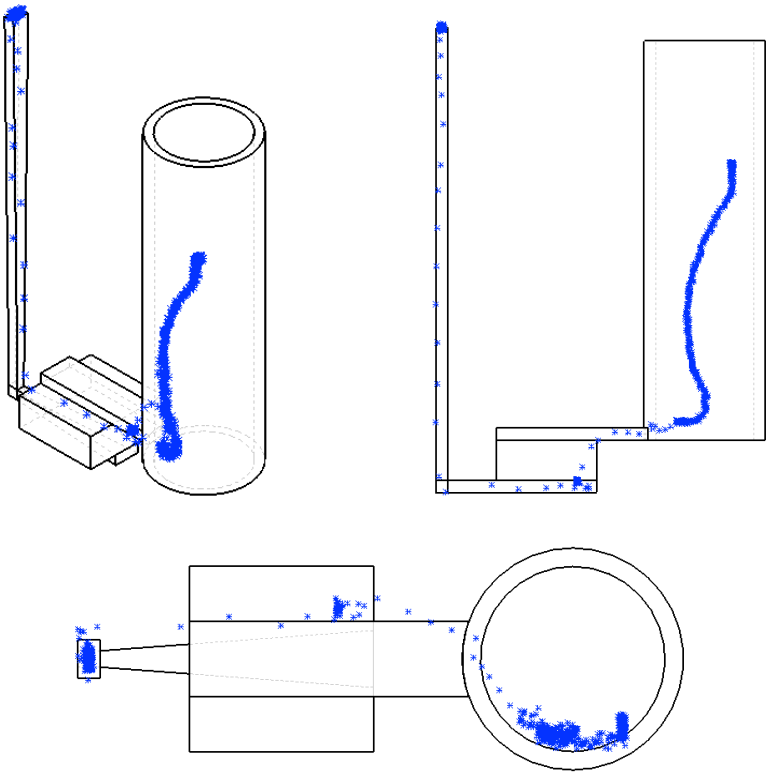

Figure 139. The particle tracking results obtained for a 20ppi filter casting. Particle size and radioactivity were 63-100µm and 130µCi respectively.

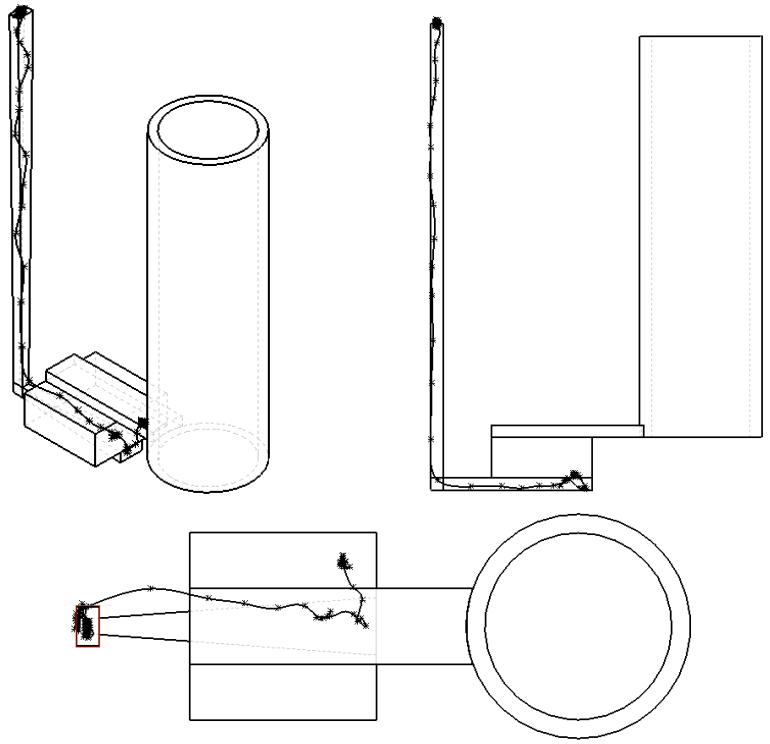

Figure 140. The particle tracking results obtained for a 20ppi filter casting. Particle size and radioactivity were 63-100µm and 150µCi respectively.

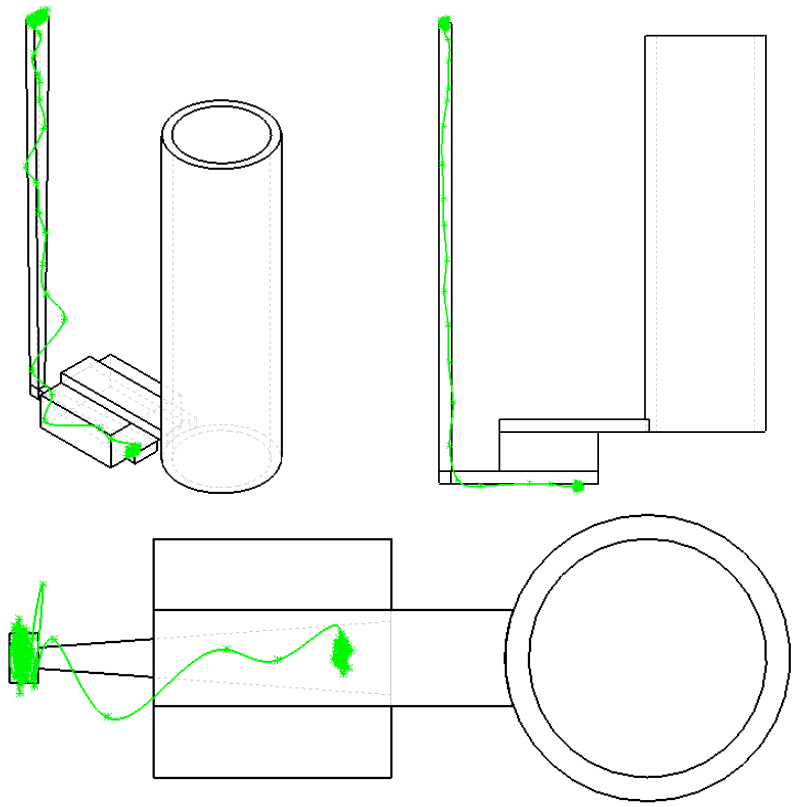

Figure 141. The particle tracking results obtained for a 20ppi filter casting. Particle size and radioactivity were 63-100µm and 211µCi respectively.

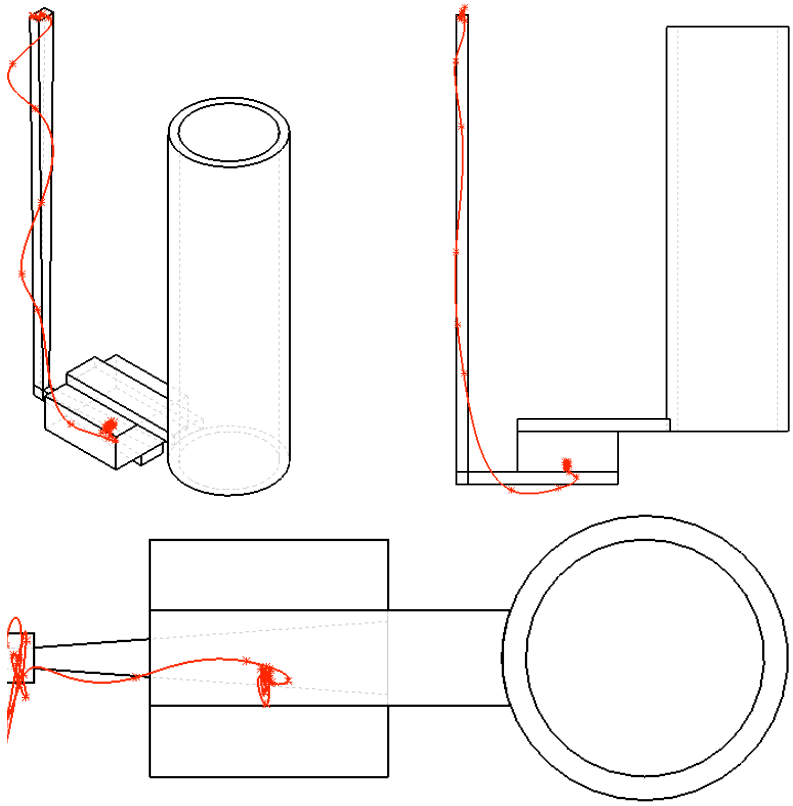

Figure 142. The particle tracking results obtained for a 20ppi filter casting. Particle size and radioactivity were 63-100µm and 64µCi respectively.

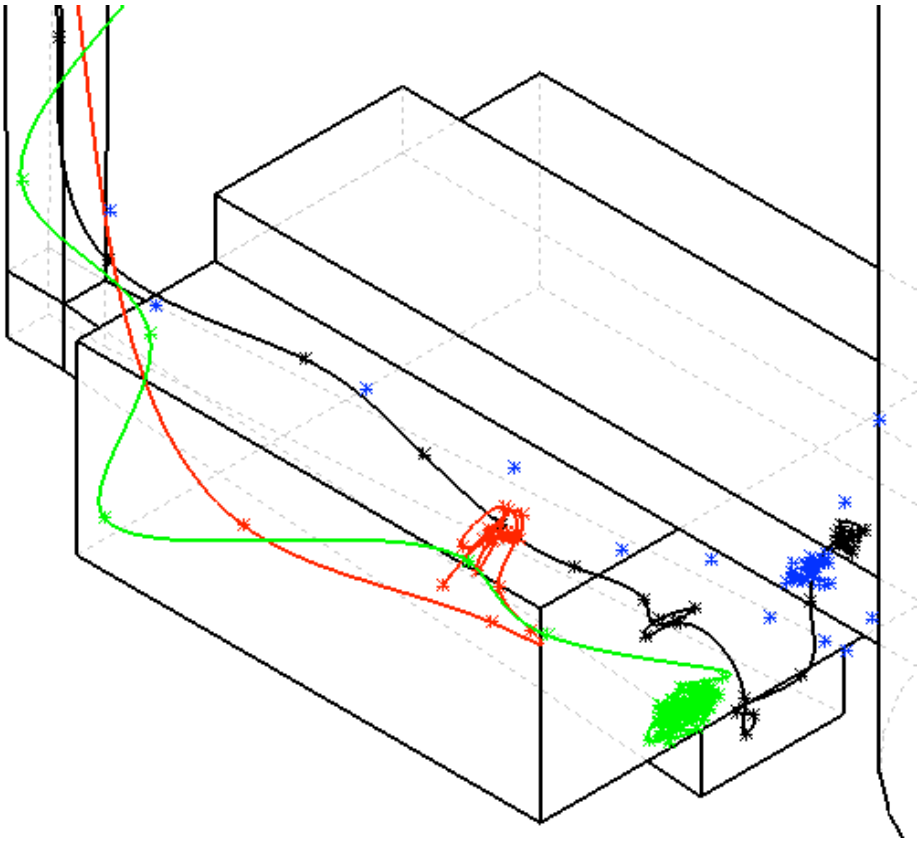

Figure 143. The results obtained for all the castings where a 20ppi filter was used, superimposed onto 1 3D casting for comparison. Note the blue particle path is not completely shown in this case as the particle came to rest in the cast tube.

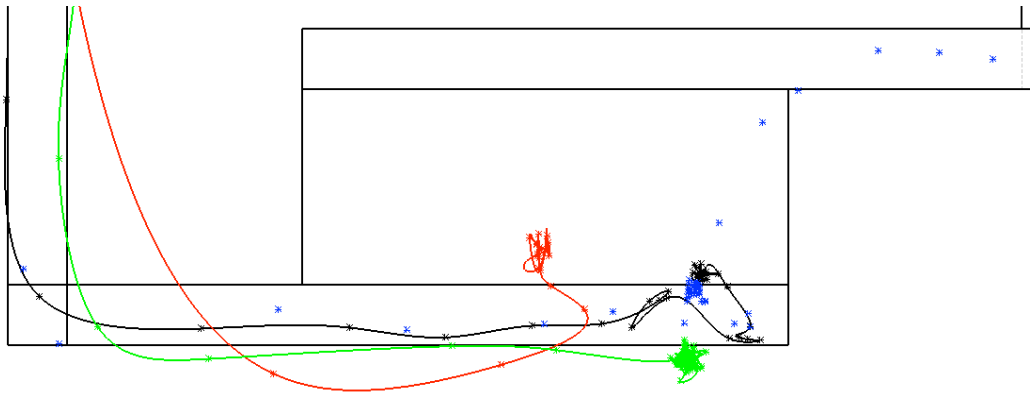

Figure 144. A 2-D side view showing the results obtained for all the castings where a 20ppi filter was used, superimposed onto 1casting for comparison. Note the blue particle path is not completely shown in this case as the particle came to rest in the cast tube.

4.4.5.3 10 ppi filters

Figures 145-148 illustrate the results obtained when a 10 ppi filter was used. Figure 145 shows that the particle came to rest in the filter. The particle entered the lower runner bar and moved close to the bottom surface after which it rose upwards and came to rest, about 12 mm above the bottom of the lower runner bar. In the casting shown in figure 146, the particle remained in the pouring basin. Figures 147 and 148 also show another 2 results where the particle remained in the pouring basin. 75% of the particles remained in the pouring basin. The average error in the tracking data for the experiments where a 10ppi filter was used was ± 1.5, 2.2, 1.5 and 3.3 mm respectively.

Using ceramic foam filters therefore affected the final location of an inclusion. It has been found that when a 30ppi (pore size 1.5-1.7 mm) filter was used, 75% of the particles were trapped and remained in the filter. When a 20ppi (pore size 1.2-2 mm) filter was used, 50% of the particles were trapped in the filter, 25% came to rest in the pouring basin and 25% came to rest in the casting. When a 10ppi (pore size 3.5-5 mm) filter was used 25% of the particles were trapped in the filter and 75% came to rest in the pouring basin.

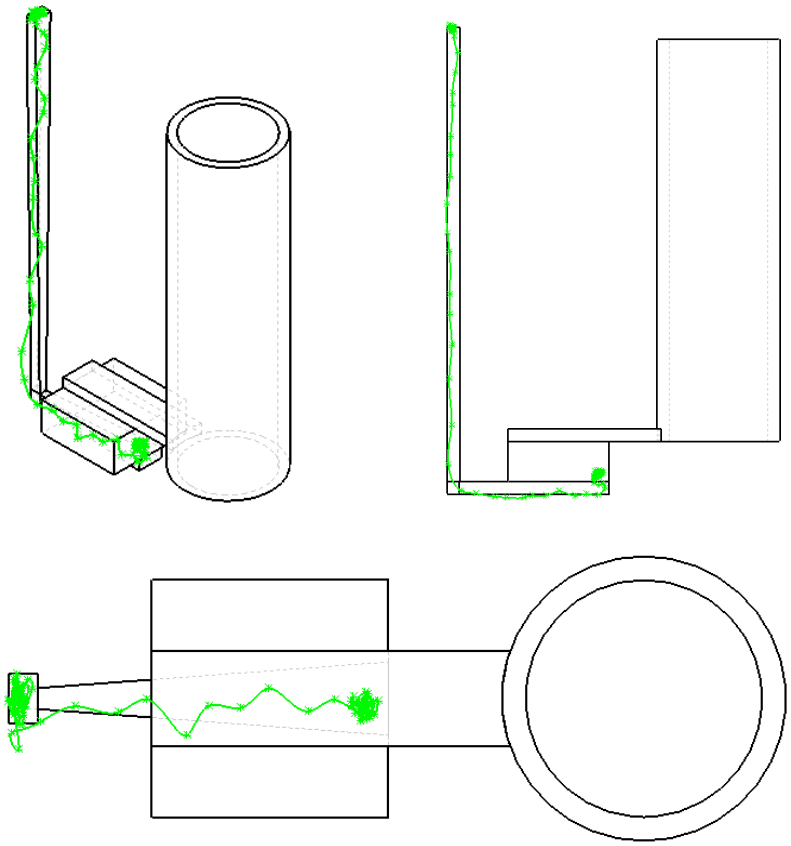

Figure 145. The particle tracking results obtained for a 10ppi filter casting. Particle size and radioactivity were 63-100µm and 240µCi respectively.

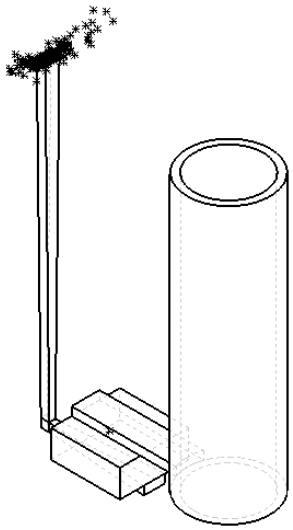

Figure 146. The particle tracking results obtained for a 10ppi filter casting. Particle size and radioactivity were 63-100µm and 141µCi respectively.

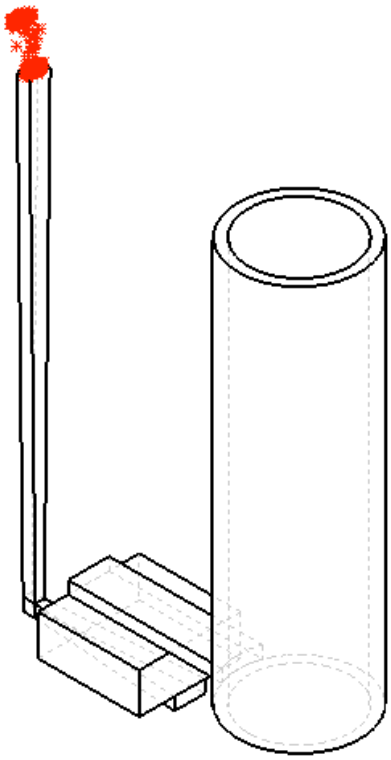

Figure 147. The particle tracking results obtained for a 10ppi filter casting. Particle size and radioactivity were 63-100µm and 240µCi respectively.

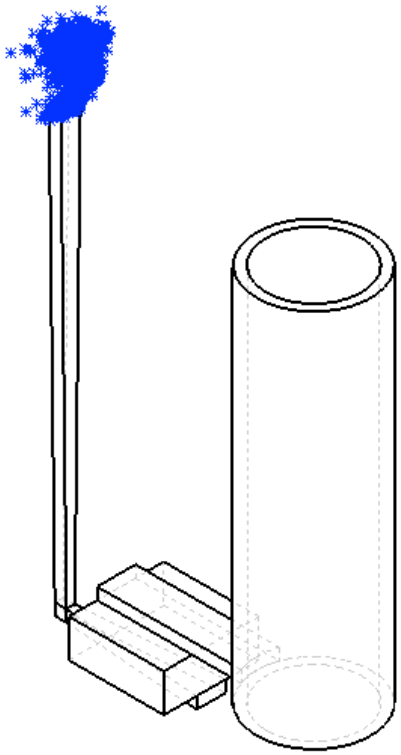

Figure 148. The particle tracking results obtained for a 10ppi filter casting. Particle size and radioactivity were 63-100µm and 497µCi respectively.

4.4.6 The Effects of Preheating The Mould

The castings shown in figures 149-152 were also cast using the same acrylic (Perspex^{TM}) mould, Lensalloy-136 and an irradiated alumina particle of size 63-100μm, placed at the centre of the downsprue opening. However in these experiments the acrylic mould was preheated to temperatures varying between 84 and 90^{o}C prior to casting, in order to investigate the effects of delayed solidification on the particle path. The temperature of the mould was also recorded immediately before casting as was shown in figure 42.

Figure 149 shows the result obtained when the mould was preheated to 90^{o}C which decreased to 56.4^{o}C before casting (the melting point of Lensalloy-136 is 57.8^{o}C). As the metal was cast the alumina particle moved down the downsprue with the liquid metal and entered the runner bar from the right hand side, close to the runner bar lower surface. The particle moved towards the centre line of the runner bar after which it moved back to the left hand side before it entered the casting tube cavity at approximately 10^{o}. The particle then moved clockwise, back and forth between the tube walls while rising gradually until it came to rest at 150^{o}, 14mm above the bottom of the cast tube. The recorded average error was ± 2 mm.

For the next casting, shown in figure 150 the mould was preheated to 86^{o}C which decreased to 48^{o}C immediately before casting. The particle in this case moved towards the right hand side of the runner bar, close to the lower surface and again entered the cast tube cavity at 10^{o}. The particle came to rest at 160^{o}, and 6 mm above the bottom of the tube. Thus in this experiment the tracking results were similar to those obtained for the previous experiment (figure 149), if the symmetry of the casting was considered (in the runner bar). The average

error obtained in the tracking data was ± 1.4 mm in all directions and the mould was found to be twisted by 0.7º between the camera faces. Note, the angle by which the mould was twisted was calculated by measuring the offset between the centre line of the mould and the centre line of the table underneath, after the experiment was carried out. This could not have been avoided due to the time limitation of assembling the mould and casting while trying to prevent the mould temperature from dropping below 87ºC.

The results obtained for the casting shown in figure 151 show the particle path of the alumina particle when the metal was cast into a mould, preheated to 86ºC which decreased to 62ºC before casting. The particle appears to have moved down the downsprue, entered the runner bar from the right hand side and came to rest at the end of the runner bar, at the intersection between the runner bar and the casting tube cavity at roughly 5º. The particle's final position was approximately 112 mm along the runner bar and 4 mm above the bottom of the runner bar / cast tube. The average error of the tracking data was ± 2 mm and the mould was twisted by 2.3º between the camera faces.

Figure 152 shows the results obtained when the mould was preheated to 96ºC, which decreased to 77ºC before casting. It appears that as the particle entered the runner bar from the right hand side, it followed the lower right hand side corner until it entered the cast tube cavity, after which the particle moved anticlockwise while rising gradually to roughly 45 mm above the bottom of the tube and coming to rest at 260º. The average error for the tracking data in the X,Y and Z coordinates was ± 1.4 mm and the mould was found to be twisted by 1.4º between the camera faces.

Due to the practical difficulty in controlling the mould temperature, the results shown in figures 149 and 150 do not represent the effect of delaying solidification and show results that are similar to those obtained from the baseline castings, shown in figures 121 and 124. However, the results shown in figures 151 and 152 were obtained when the mould temperature was above the melting point of Lensalloy-136, immediately before casting, but also did not show a significant difference to previous results obtained from the baseline castings (see figures, 120, 125 and 128). This meant that preheating the mould probably did not have a significant effect on the particle path and its final location.

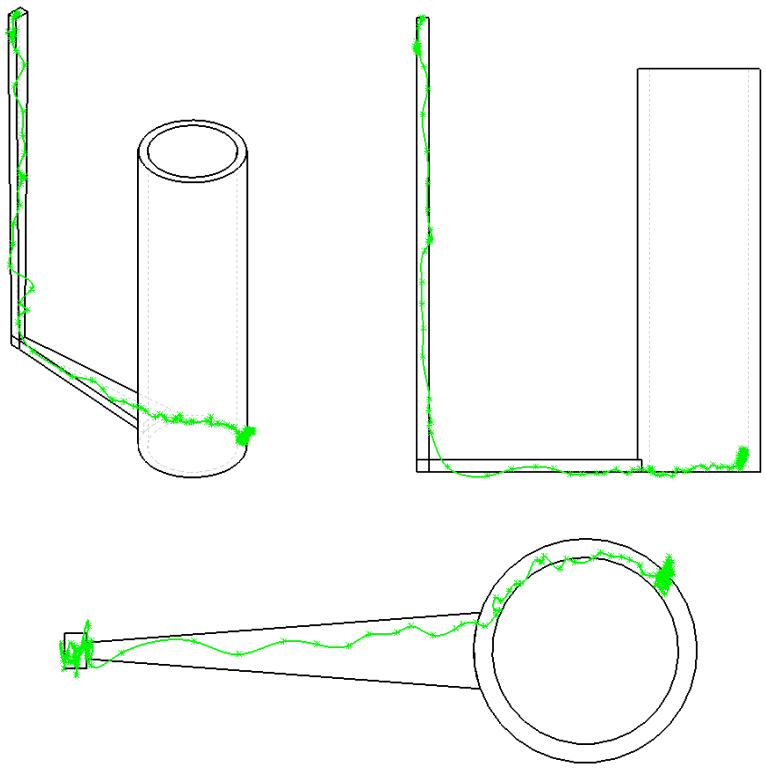

Figure 149. The results obtained from a low melting point alloy casting, where the mould was preheated, showing the particle coming to rest in the lower third of the cast tube. Particle size and radioactivity were 63-100µm and 123µCi respectively.

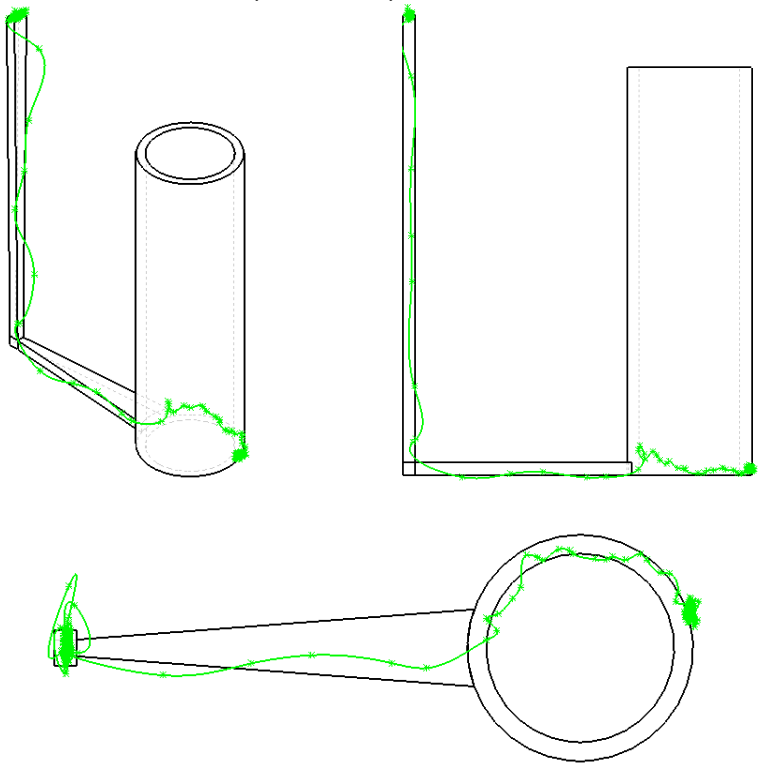

Figure 150. The results obtained from a low melting point alloy casting, where the mould was preheated, showing the particle coming to rest in the lower third of the cast tube. Particle size and radioactivity were 63-100µm and 98µCi respectively.

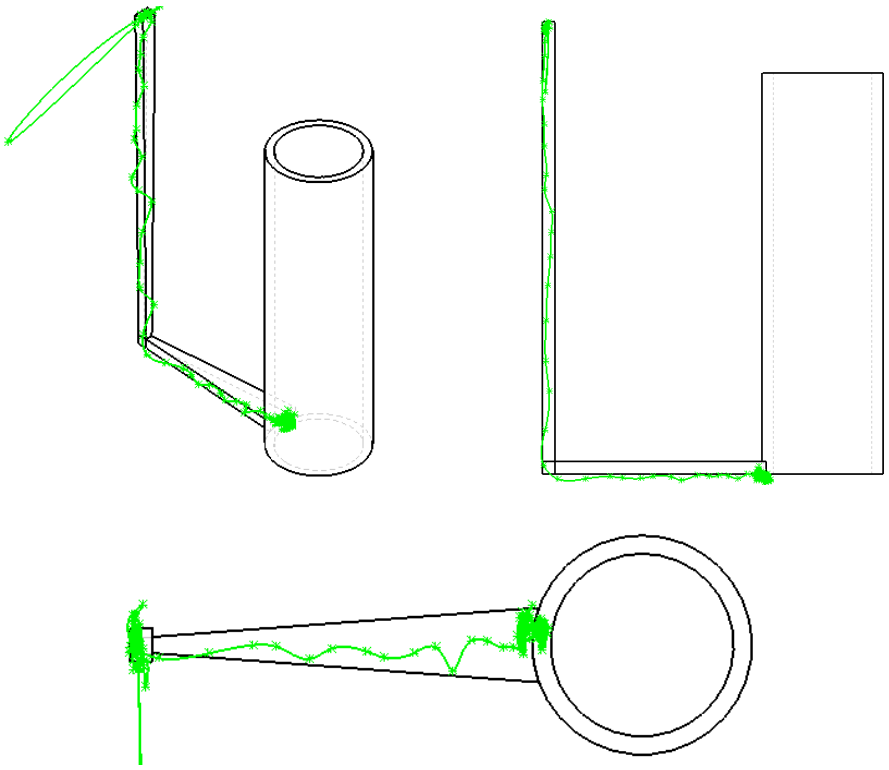

Figure 151. The results obtained from a low melting point alloy casting, where the mould was preheated, showing the particle coming to rest at the end of the runner bar. Particle size and radioactivity were 63-100µm and 406µCi respectively.

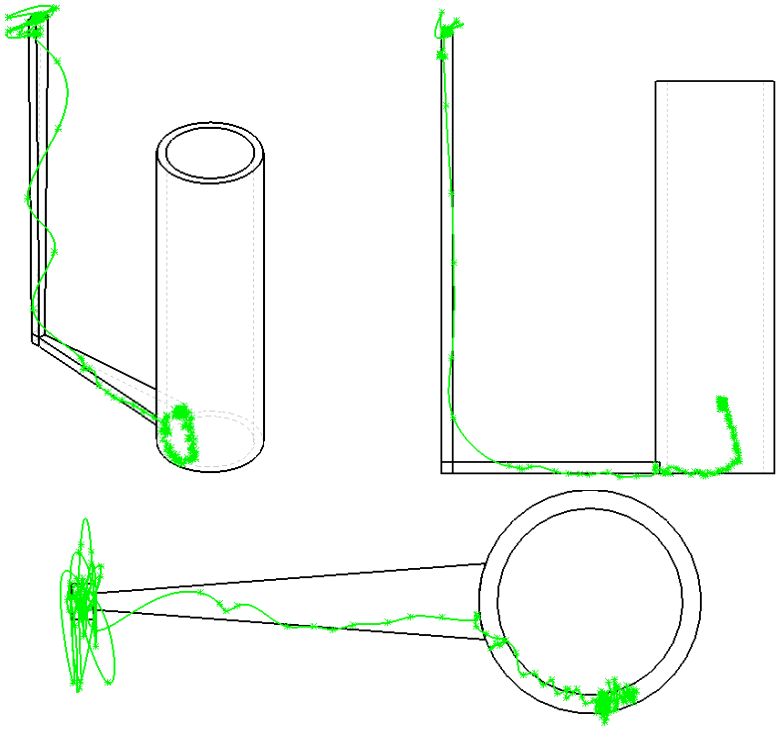

Figure 152. The results obtained from a low melting point alloy casting, where the mould was preheated, showing the particle coming to rest in the lower third of the cast tube. Particle size and radioactivity were 63-100µm and 66µCi respectively.

4.5 Locating a Tracked Particle

An initial attempt to find the particle in one of the investment steel castings was carried out by cutting out the volume of steel containing the particle, grinding at 100μm steps and examining the ground surface using an optical microscope until the particle was found. Unfortunately, the particle was not found, but a hole of the same size as the particle (355-425μm) was found 1mm away from the expected particle location. Thus it was assumed that the particle could have been washed away during grinding leaving a void behind, as shown in figure 153, (the SEM micrograph of the hole).

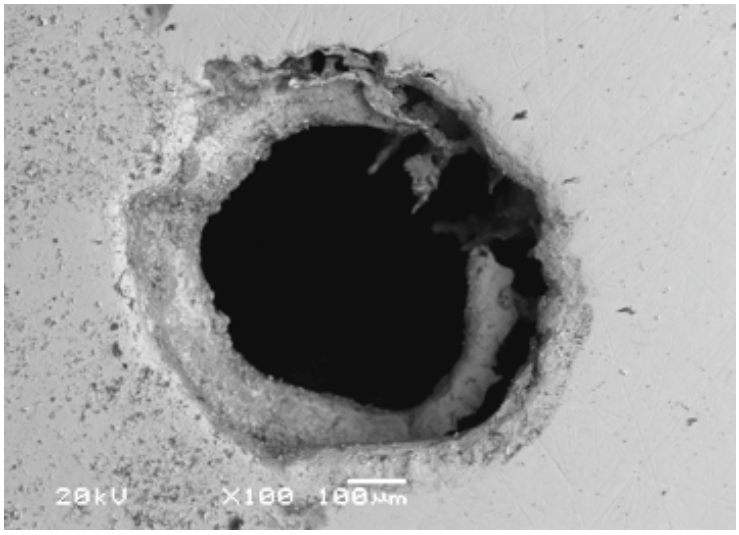

Figure 153. An SEM image showing the void where the particle was believed to be at a x100 magnification.

The result obtained from another attempt to locate a tracked particle is shown in figure 154. In this case an alumina particle, of size 63-100μm, was trapped in a 30 ppi filter in a Lensalloy-136 casting, (as shown in figure 135). A particle was found at this location by grinding through the material at 15μm intervals, and using a 100-200x USB microscope, as shown in figure 155. Figures 156 and 157 show an SEM micrograph of the particle and the

EDX peaks identified it was Al_2O_3. The particle size, location and EDX identification (47 wt % Al, 43 wt% O, the same ratio as Al_2O_3), confirmed that this was the entrained alumina particle.

Although the recorded particle tracking error for this casting was ± 2.4 mm, the particle was found within 1.2 mm from its predicted location. Figure 154 shows the determined average final location of the particle, indicated by a red point.

The particle was found to be almost centrally in the filter pore, surrounded by the solidified metal. This showed that it was not trapped by sticking to the filter's walls, a filtering mechanism that has been proposed.

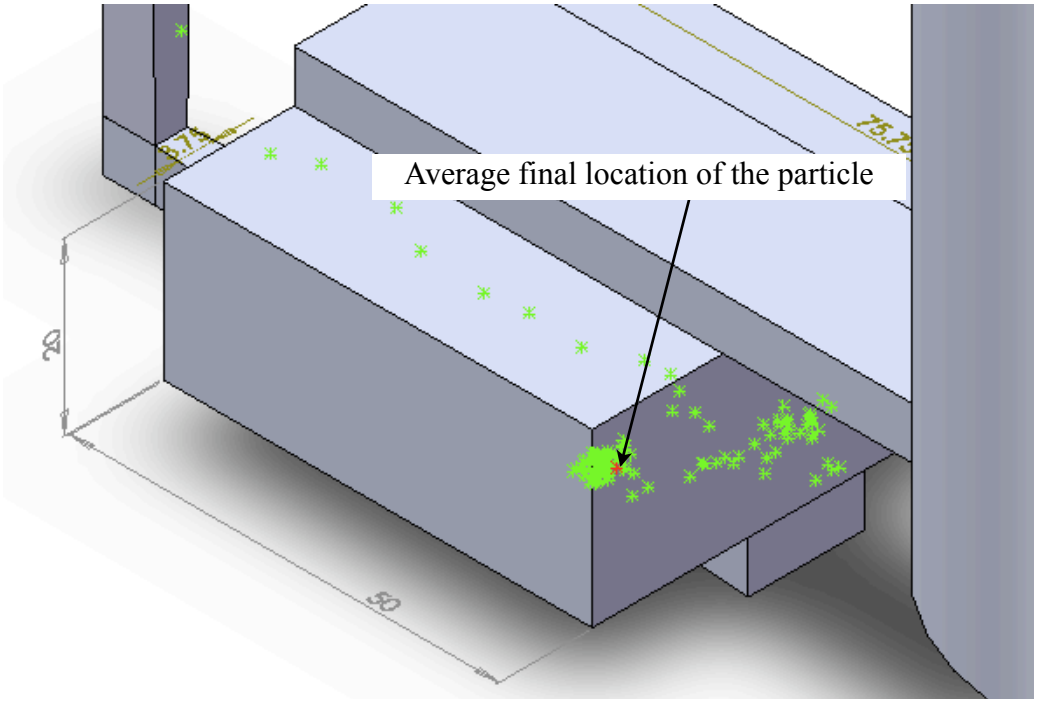

Figure 154. The particle final location illustrated on a 3D isometric view of the casting.

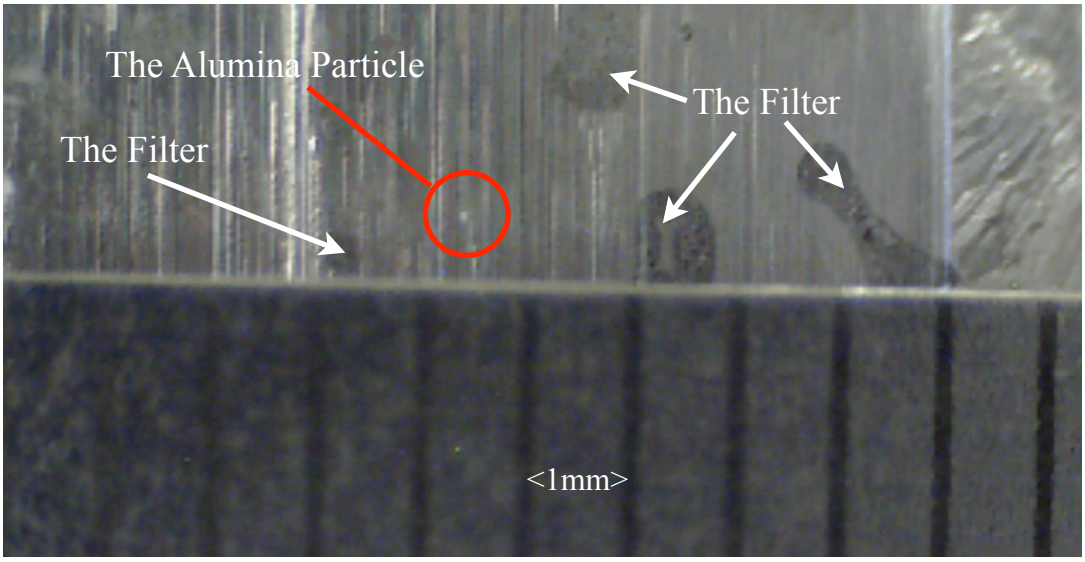

Figure 155. An image captured from the USB microscope showing the particle when it was first observed.

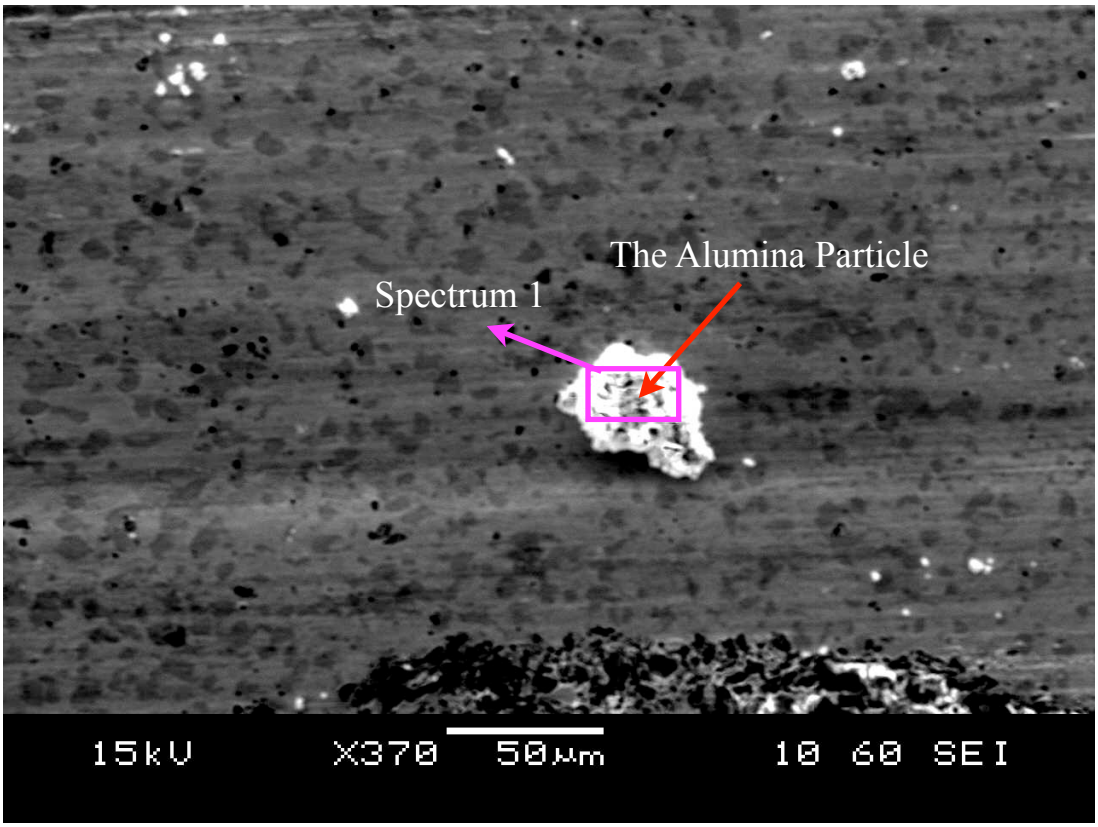

Figure 156. An SEM micrograph showing a 63-100 µm alumina particle, that was successfully found in a 30ppi filter.

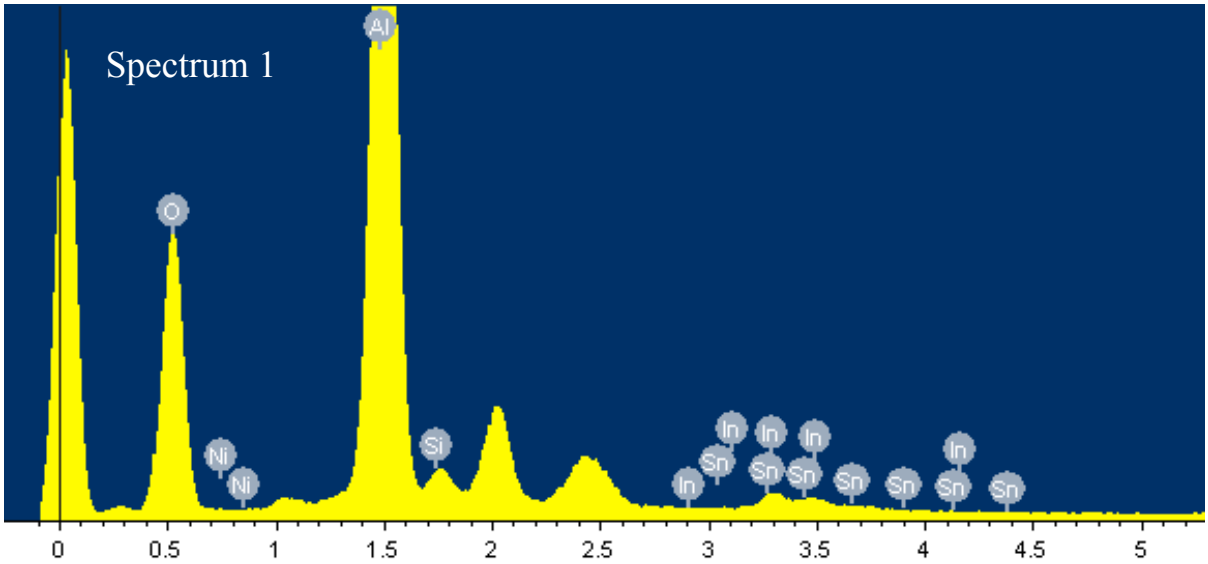

Figure 157. An EDX spectrum showing the Al and Oxygen peaks detected from the particle's surface.

Two other particles were successfully relocated in the Al plate casting where the modular camera was used to track 2 particles entrained at the same time, (see figures 158 and 159). The particles were found by milling the sample surface at 50µm intervals while using a 100-200x USB microscope, to identify the particles. Tables 24 and 25 are the EDX results which confirmed the composition of the particle to be Al_2O_3. Particle 1 was found to be within 3.6 mm from its predicted location, while the reported uncertainty in the predicted position was ±4.4 mm. Particle 2 was found to be within 10 mm from its predicted location, while the reported error was ± 8.3 mm. Note that particle 2 was found to be within gas pore on the top surface of the cast plate which suggests that this particle may have been attached to a gas bubble which broke on contact with the mould surface.

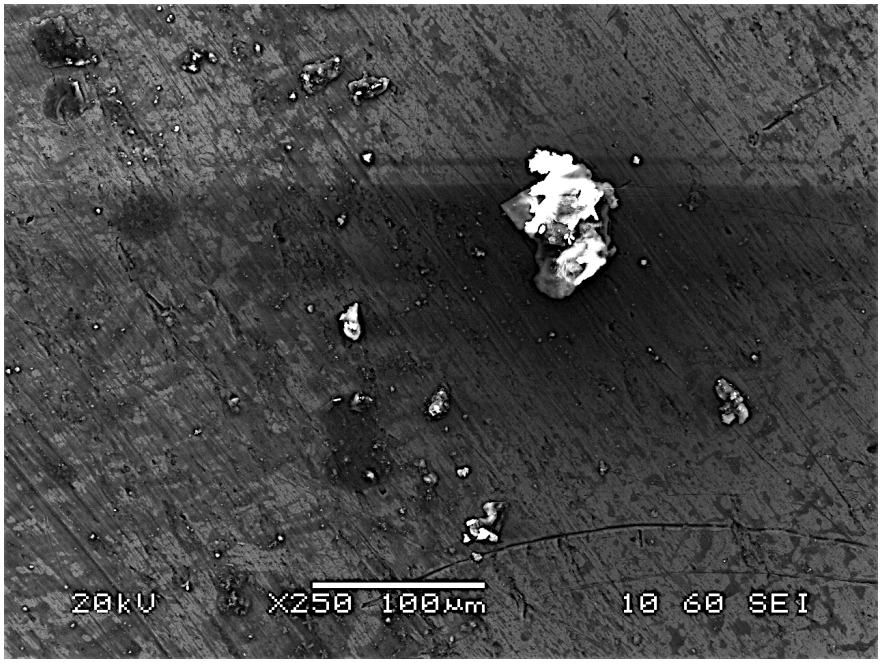

Figure 158. An SEM micrograph showing a 90-150 µm alumina particle entrained in an Al cast plate, that was successfully tracked using the modular camera.

Table 24. The EDX results obtained for the tracked alumina particle.

Element	Weight%	Atomic%
O K	50.06	65.41
Al K	28.32	21.94
Si K	7.52	5.60
S K	6.39	4.16
Fe K	7.71	2.89
Totals	100.00	

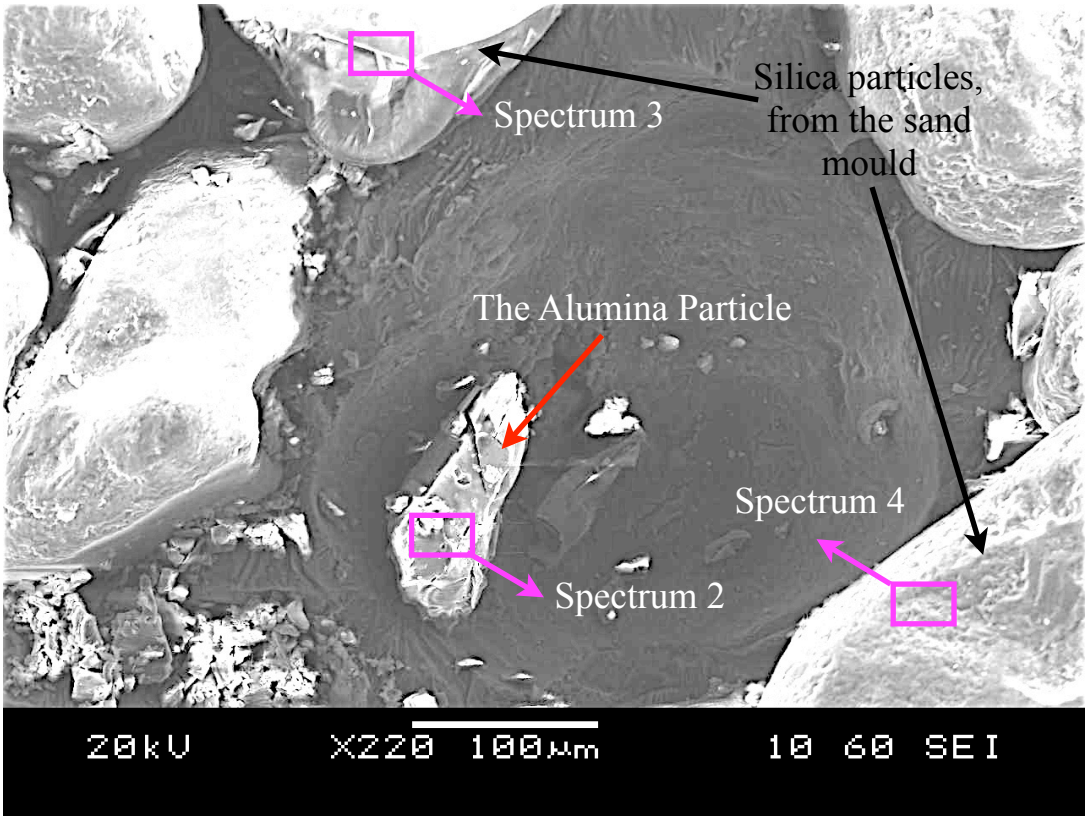

Figure 159. An SEM micrograph showing, a 90-150 µm alumina particle entrained in an Al cast plate, that was successfully tracked using the modular camera.

Table 25. The EDX results obtained for the tracked alumina particle.

Processing option : All elements analysed (Normalised)

Spectrum	In stats.	C	O	Mg	Al	Si	K	Total
Sum Spectrum	Yes	31.35	4.62		51.20	12.82		100.00
Spectrum 2	Yes	9.33	19.57	0.96	36.54	33.10	0.50	100.00
Spectrum 3	Yes	11.62	42.12		0.71	45.55		100.00
Spectrum 4	Yes	18.56	43.36			38.08		100.00
Max.		31.35	43.36	0.96	51.20	45.55	0.50	
Min.		9.33	4.62	0.96	0.71	12.82	0.50	

All results in weight%

Chapter 5
DISCUSSION

5.1 The Applicability of PEPT to Shape Casting Applications

The results shown in figures 155 and 156, showed that a single particle of size 63-100μm was successfully located within an accuracy of 1.2mm from it's location predicted by PEPT. This level of precision shows that PEPT can be a useful tool for the development and verification of particle tracking models in casting modelling software. The results obtained from the different mathematical models carried out in this research showed that the particle tracking capabilities of the currently available software are far from satisfactory, for simulating the behaviour of inclusions in castings. PEPT can be used to develop these models and perhaps create more realistic solutions to the problems of turbulence and interaction of gas bubbles with solid particles.

However, the current multiple particle tracking capabilities of PEPT are limited [70, 72]. Although the available NTrack algorithm is theoretically capable of tracking any number of particles, it was severely restricted by particle radioactivity and the resolution between particles. In other words the accuracy of determining the particle locations varied greatly with

their radioactivity and how close they were to each other. For example, if two particles are being tracked, the radioactivity of 1 particle has to be roughly double the radioactivity of the other particle [70]. This is because the algorithm determines the particle locations incrementally; first it locates the first particle after which it deletes a specified percentage of the acquired data that was associated with finding that first particle, then it starts looking for the second particle within the remainder of the data. Therefore when one of the particles that has a radioactivity of 50μCi for instance, is located and the data associated with that particle has been deleted, the algorithm has a better chance to find a particle of radioactivity of 100μCi within the remaining pool of acquired data.The larger the difference in radioactivity between the particles the easier for the NTrack algorithm to distinguish between them. If a large number of particles are being tracked, it becomes more difficult for the algorithm to determine their location accurately due to the progressively decreasing amount of data available to incrementally determine the location of each subsequent particle.

These effects were clearly observed in the results obtained from the assessment of the Ntrack algorithm, figures 267-289. Figure 267 showed the X-coordinates of 2 particles plotted versus time, where it was clear that until 3.5s there was a scatter of points associated with particle 2, which were falsely determined to be in the same location as particle 1. Particles 1 and 2 had radioactivities of 63μCi and 43μCi respectively, a ratio of 1.4, (ideal ratio of >2). Accordingly the algorithm showed some error in distinguishing between the particles, as shown by the scatter in figure 267. This error appeared to be of a greater extent in the Z-direction, which is the perpendicular direction between the camera detectors as shown in figure 269. Less scatter was observed in the X and Y-directions, see figure 267 and 268. It is also to be noted that the

scatter was usually associated with the particle of lower radioactivity, (particle 2 in the previous example). As the number of particles increased this scatter gradually increased due to the increasing difficulty in distinguishing between particles. Another example was the results shown in figures 291-293, where 2 particles were tracked within a stirred Lensalloy-136, liquid metal bath. The particle tracks were most distinguishable when the particles had a ratio of radioactivity of 2.5, and were less distinguishable at ratios of 2 and 1.3 respectively.

The NTrack algorithm assessment also provided an understanding of the required minimum separation distance between the particles, beyond which the algorithm failed to distinguish between them. It was reported in the literature that two particles must be at least 5-7mm apart, at all times, in order to be distinguished by the algorithm [108]. The minimum separation distance in these experiments was found to be 4 mm, as shown in figure 290. Figure 290 also illustrated that the required minimum separation distance is increased if a larger number of particles is to be tracked. These values were obtained by measuring the distance h as shown in figure 267, in the X,Y and Z coordinates for all the trials. The required minimum separation distance was found to be between 4-20mm for 2-7 particles.

However, despite these restrictions, multiple particle tracking is still promising for casting applications, as was demonstrated by the results obtained using the modular camera to track 2 and 4 alumina particles in real time in two aluminium sand castings, (figures 296-300). In figures 296-298, particles were initially placed 120mm apart and during casting they were detected to have entered the mould cavity and come to rest a few centimetres apart near the

top right hand side corner. The minimum separation distance was obviously not controlled and in fact is believed to be an advantage rather than a hindrance in casting applications. When two particles come close to each other and are less than 4mm apart, the algorithm may detect them as one particle or detect particle 1 as particle 2 and vice versa, at that particular moment in time. This is for example indicated in figure 297, where at the indicated location, there was some uncertainty about which particle is which. However, the points at which the particles come close to each other are important to determine because these could be the points at which agglomeration occurs, which is information that could not have been obtained experimentally before. In fact in this particular casting it is clear that both particles travelled together in the plate and were separated near the top right hand side of the cast plate cavity where they came to rest. On the other hand the technique is still somewhat limited when detecting particles moving at high speeds, which explains why only 2 points were detected in the runner bar where the metal velocity was estimated to be 2.3 ms^{-1}. Fan *et al*. reported that the limiting velocity of a moving particle, for the positron camera, was 1-2 ms^{-1} [70, 108].

A new multiple particle tracking algorithm has to be written specifically for casting applications using the modular camera in order to be able to widely apply the technique to the casting industry. One example could be using flow field models in order to provide the particle location algorithm with information about where the particles are most likely to be, at a given time, and therefore improve the efficiency of the algorithm by minimising the volume within which it looks for the particles. Single particle tracking however can be carried out using the currently developed technique.

As explained earlier, the tracer particle radioactivity and halflife could be limitations to the uses of PEPT in the castings industry. In order to widely apply the technique to study the behaviour of inclusions in various metallurgical processes, stronger positron emitting tracers with longer half lives need to be developed in order to allow for transport to an industrial facility, for example. ^{18}F has a half life of 109 minutes which is clearly not sufficient to transport the tracer to an industrial facility a few hours away. Also the radioactivity levels by direct activation of oxide particles are not sufficient considering the levels of attenuation to be expected from the thick walls of industrial vessels, in which liquid metal is typically processed.

A zirconium silicate tracer particle was directly irradiated for 30 minutes, where the Zr atoms were converted into ^{90}Nb, which has a half life of 14 hours and emits ɣ-rays of 1.5MeV (compared to 511keV for ^{18}F). The radioactivities obtained from 2 particles were measured using an ^{18}F calibrated, dose calibrator, and were found to be 220μCi and 160μCi. This is equivalent to 600μCi if the correct radioactive decay mechanism was considered because unlike ^{18}F, ^{90}Nb is not a positron emitter, but decays by emitting ɣ-rays directly, and in all directions. An investigation of the ɣ-ray penetration depth was carried out for steel and aluminium where it was found that this level of radioactivity was detected through 350mm of steel, and 600 mm of aluminium, respectively.

These tracers were merely an investigation of the required radiation levels that would be required to counter the high attenuation levels in industrial environments, whether by the steel moulds in die casting applications or the thick steel vessels used in liquid aluminium

processing for example. This is, of course, in addition to the large thicknesses of liquid metal in which the radioactive particles would be entrained. Therefore a positron emitter of radioactivity above 600μCi needs to be developed; ɣ-ray emitting particles such as ^{90}Nb would not be located accurately by the positron camera.

5.2 Using Lensalloy-136 to Study Inclusion Behaviour Using PEPT

Water models have been extensively used to study metal castings and fluid flow problems in general. They have been used to develop and verify mathematical models of fluid flow, in industrial applications, such as the work reported by Qiang *et al*. [98] where the difference in inclusion removal efficiency between a conventional flow inhibitor and a swirling chamber in a model tundish were studied. Similar work has been reported by Alizadeh *et al*. where the mixing behaviour of various flow inhibitor designs was investigated [101]. The consensus was that water models can be used to model the fluid flow of liquid metals provided that the Reynolds and Froudes numbers were reproduced in both the model and in reality. When particle behaviour was studied using water models [101], it was assumed that because the kinematic viscosity of water (at room temperature) and steel at 1600^{o}C were nearly the same, (10^{-6} and $0.9x10^{-6}$ m^2s^{-1} for water and steel respectively),water could be used as a good medium to model inclusion behaviour in steel [102]. The effects of solidification on the inclusion path within the liquid metal were not considered.

Table 28 shows the calculations obtained for the Reynold's number for the geometry used in the low melting point alloy castings, at the points designated 1-4 on figure 315, for Lensalloy-136, Fe, Al and water. It was clear that in the case of Fe and Al the fluid flow was only significantly turbulent at the bottom of the downsprue, more turbulent in the case of Al than Fe. In the case of Lensalloy-136 turbulence was estimated to occur in the downsprue (points 1 and 2) and decrease in the runner bar (point 3), after which laminar flow would have taken place in the cast tube cavity (point 4). Water showed a similar behaviour to that of Fe

and Al where it was slightly turbulent at the bottom of the downsprue and moved with laminar flow in other parts of the mould cavity. Although this assessment proves that water is a closer match for the turbulence behaviour of liquid Fe and Al, it does not mean that other factors affecting particle behaviour and PEPT are well represented, such as particle buoyancy and interfacial tension, for example.

Table 28. The calculation of Reynolds number at points 1-4 on the Lensalloy-136 casting, see figure 315.

Pt.	Velocity (ms^{-1})	Area (m^2)	Perimeter (m)	Hydraulic Diameter (m)	Flow Rate (m^3s^{-1})	Reynolds Number (Re) Lensalloy-136	(Re) Fe	(Re) Al	(Re) Water
1	1	6.00E-05	0.032	0.0075	5.90E-06	27,237	9,475	13,628	8,347
2	3	1.90E-05	0.018	0.0044	5.90E-06	49,523	17,227	24,779	15,176
3	0.47	1.24E-04	0.052	0.0095	5.90E-06	16,634	5,786	8,323	5,097
4	0.19	3.10E-04	0.93	0.0016	5.90E-06	937	326	469	287

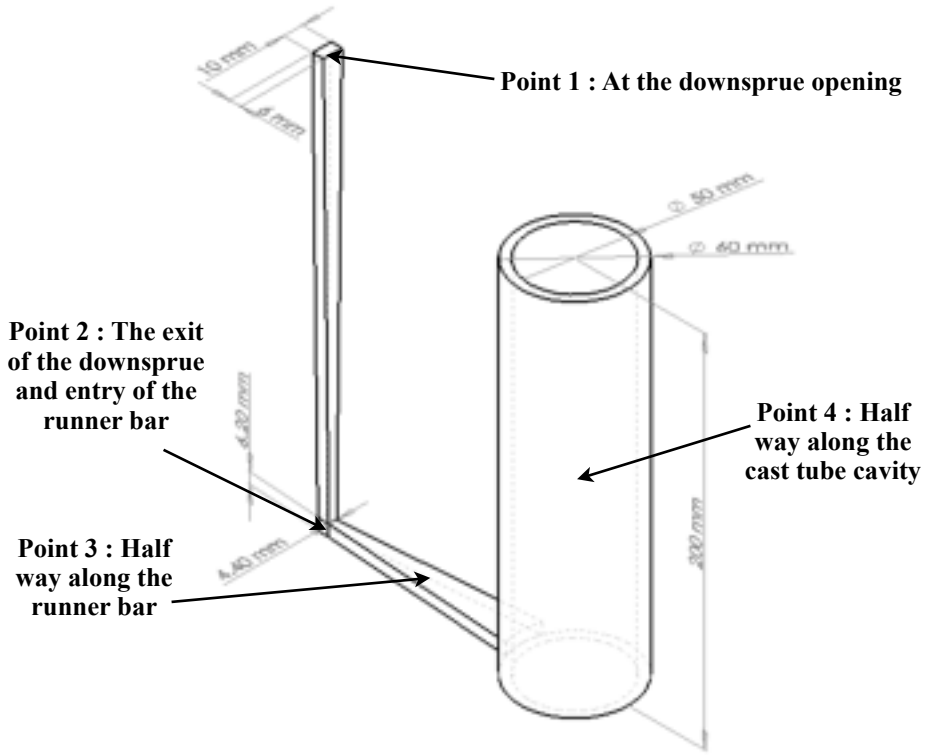

Figure 315. A schematic diagram showing the points at which Reynold's number was calculated for the low melting point alloy casting.

Table 29 shows a calculation of the terminal velocity that would be predicted by Stoke's Law for an alumina particle as an inclusion in the low melting point alloy castings. It is clear that in the case of water, an alumina inclusion of size 80μm, would have had a settling velocity of 0.04 ms^{-1} while in Lensalloy-136 the particle would travel upwards at a terminal velocity of -0.03 ms^{-1} which is much closer to the value obtained for Fe at -0.01 ms^{-1}. Hence due to its similar density, Lensalloy-136 would provide a better medium, than water, to model inclusion flotation.

Table 29. The terminal velocity of an 80μm alumina particle, for Lensalloy-136, Fe, Al and water. These values were calculated using Stoke's Law assuming a density of 3730 $kg.m^{-3}$ for alumina.

	Lensalloy-136	Fe	Al	Water
Density of Fluid ($Kg.m^{-3}$)	8800	7015	2385	1000
Dynamic Viscosity (Pa.s)	0.0024	0.0055	0.0013	0.00089
Terminal Velocity ($m.s^{-1}$)	-0.03	-0.01	0.01	0.04

The effects of specific heat capacity and thermal conductivity were also assessed using a similar analogy where the thermal diffusivity was calculated and compared in the case of Fe, Al, Lensalloy-136 and water, as shown in table 30. Thermal diffusivity (α) is the ratio between the thermal conductivity and specific heat capacity and is given by equation 21, where k is the thermal conductivity, ρ is the density and C_p is the specific heat capacity.

$$\alpha = \frac{k}{\rho C_p} \text{ ----------Equation 21}$$

If the specific heat capacity is large, the thermal diffusivity is low, which means that heat energy is transferred slowly within the material, and hence solidification would take longer to occur, allowing more time for a particle to move with the fluid flow. However, a larger value of thermal diffusivity means that heat energy is transferred quickly within the material and consequently solidification can take place quickly, which allows less time for the particle to move with the fluid flow. Lensalloy-136 had thermal diffusivity of $3x10^{-5}$ m^2s^{-1} which was much closer to the values of α for Al, and also Fe, compared to water, and is therefore a better liquid than water in this regard.

Table 30. The calculation of thermal diffusivity for Lensalloy-136, Fe, Al and water. [109]

	Lensalloy-136	**Fe**	**Al**	**Water**
Density of Fluid ($Kg.m^{-3}$)	8800	7015	2385	1000
Thermal Conductivity ($Wm^{-1}K^{-1}$)	36	80	91	0.58
Specific Heat Capacity ($JKg^{-1}K^{-1}$)	134	824	1180	4180
Thermal Diffusivity (m^2s^{-1})	3.00E-05	1.30E-05	3.20E-05	1.39E-07

Finally the surface tension of Lensalloy-136 (0.4 Nm^{-1}) is a much closer match to that of Fe (1.87Nm^{-1}) and Al (0.871Nm^{-1}), than the very low surface tension of water (0.073Nm^{-1}). Accordingly interactions between an inclusion and liquid Lensalloy-136 would be more representative of what occurs in high melting point metals such as Fe and Al, than in the case of water.

Using Lensalloy-136 also had some disadvantages; firstly due to its high density, the ɣ-rays obtained from the tracked particle suffered from higher attenuation levels than would be expected if steel or aluminium were used. But this was counterbalanced by the fact that the acrylic mould caused less attenuation than sand moulds for example (89% reduction in intensity for the sand mould and 51% for the perspex mould). Another disadvantage was the lead content in Lensalloy-136, and the toxicity associated with that. The alloy was not heated over 150^{o}C in order to minimise the formation of Pb vapour that may cause health risks.

Thirdly, Lensalloy-136 does not solidify by dendritic solidification as steels and Al-Si alloys, but it solidifies by planar solidification. Also particle agglomeration cannot yet be studied due to the fact that the alumina tracer particles used do not have sticky liquid films around them at these low temperatures. New tracers, polymers for example, that can be sufficiently irradiated and can form a sticky film on their surface at 85-100^{o}C need to be developed, which is an important area of work for future development of the technique.

5.3 The Study of Inclusion Filtration With Ceramic Foam Filters Using PEPT

PEPT was used to study the effects of using ceramic foam filters in both steel and low melting point alloy castings. It was found that 100% of the 355-425µm alumina particles introduced into the steel castings, where a 10 ppi filter (pore size 3.5-5mm) was used, came to rest in the pouring basin. This may have occurred due to the restriction of the liquid metal flow due to the presence of the filter. As the liquid metal reached the filter, it's velocity was significantly reduced and this allowed the less dense alumina particles to rise back up the downsprue and come to rest in the pouring basin. This, however, could not be verified using the PEPT results obtained, since only the final particle location was determined. However a rough estimate of the particle's terminal velocity was calculated using Stoke's Law and was found to be -0.99 ms^{-1}, where the densities of the particle and steel were 3730 and 7800 kgm^{-3} respectively, the dynamic viscosity of the steel was $3.7x10^{-4}$ Pa.s and the radius of the particle was 195µm. When this value was compared to the metal's expected velocity at the bottom of the downsprue, which was 2.3 ms^{-1} ($V_{metal} = \sqrt{2gh}$, where h=0.276 m), it was clear that the liquid metal velocity had to be reduced by 57% due to the presence of the filter in order to allow the particle to rise upwards. Similar liquid metal velocity reductions due to the presence of filters were reported by Campbell *et al*. [110] which support the suggestion. (The metal slows due to the tortuous nature of the filter or due to partial solidification [111]).

Another explanation could be that the large thickness of the investment moulds (17mm) may have reduced the mould permeability and hence encouraged air bubbles to escape by rising

through the downsprue towards the pouring basin, rather than escaping through the mould walls. The particles may have been attached to an air bubble and hence came to rest in the pouring basin, as was suggested by Zhang Li Feng *et al*. [21].

A third possibility could be that the particles never entered the mould with the liquid metal, but remained in the pouring basin. This is however unlikely, because the steel mesh carrying the particle (glued to a steel pin) was placed in such a way that the particle was in the centre of the downsprue opening and should have eliminated any chance of it not being carried down the downsprue with the liquid metal.

The results obtained showed 100% reproducibility of the final particle location in all of the steel castings where a filter was used, and it is suggested that a combination of reduced metal velocity and escaping gas bubbles led to the particle coming to rest in the pouring basin.

In the case of the low melting point alloy castings, where 4 castings were made in each case, with alumina particles of size 63-100μm, it was found that for 30 ppi filters (pore size 1.5-1.7mm), 3 of the particles came to rest in the filter and 1 was found a few millimetres after the filter, in the upper runner bar. When 20 ppi filters (pore size 1.7-2mm) were used, 2 of the particles came to rest in the filter, 1 in the pouring basin and 1 in the casting, and when 10 ppi filters (pore size 3.5-5mm) were used, 2 of the particles were found to be in the pouring basin and 2 of the particles were found in the filter.

It was expected that the smaller the filter pore size the more the liquid metal flow would have been decelerated, upon reaching the filter, and hence the more likely it would have been for a particle of lower density to rise up the downsprue and come to rest in the pouring basin. Although this appeared to apply to large particles of size 355-425μm used in the steel castings, it did not apply to the 63-100μm alumina particles used for the low melting point alloy experiments. This could be explained using a similar analogy to that used earlier using Stoke's Law. The particle's terminal velocity would be -0.0059 ms^{-1} (density and viscosity of Lensalloy-136 of 8100 kgm^{-3} and 0.0024 Pas respectively, and the particle radius of 40μm were used in the calculation) compared to the metal velocity of 2.2 ms^{-1} at the bottom of the downsprue opening ($V_{metal} = \sqrt{2gh}$, where h=0.25 m). This means that for the particle to rise to the pouring basin, as it did in case of the steel castings, a reduction in metal velocity of 99% was required which is obviously less feasible.

Further evidence was shown in Figures 147 and 148, which showed the results obtained where the particle came to rest in the pouring basin. There was no indication that the particle moved down the downsprue and started to rise up again, upon the liquid metal reaching the filter. Although it has been suggested that the PEPT technique struggles with determining the location of particles moving at a speed higher than 2 ms^{-1} [4], the particle path in the downsprue was clearly defined in several other low melting point alloy castings, where the particle was moving at speeds of about 2.2ms^{-1}. This means that in this case the particles probably remained in the pouring basin and did not enter the casting.

A particle smaller than the filter pore size can clearly be trapped by the filter. Figure 155 shows that an alumina particle of size 63-100μm, found in a 30ppi filter (pore size 1.5-1.7mm) was roughly in the centre of the filter pore. It was also confirmed that the particle was not in contact with the filter wall as the region of metal within the filter pore fell out of its own accord. This meant that a likely filtration mechanism that took place in this case was filtration by settling, where an inclusion settles in the filter pore due to the slowing of the metal velocity due to the tortuous path of the filter. The particle may not have been allowed sufficient time to settle and come to rest at the filter wall due to the rate of solidification within the ceramic filter. Another possibility could be that the alumina inclusion kept recirculating within the the filter pores, with favourable balances of buoyancy lift forces over drag inertia forces, as was suggested by Maldonado *et al* [112].

5.4 Sources of Error in PEPT

5.4.1 Sources of Error in the Static Steel Casting Experiments

Various types of errors affected the accuracy with which the final location of the entrained particles could be determined. Errors were due to the (low) particle radioactivity and attenuation, as well as experimental errors that occurred during the development of the technique. Both types of errors had varying effects on the accuracy of the results, depending upon particle radioactivity, casting alignment between the (ADAC) positron camera faces, and the method employed to handle the reference particles used to locate the entrained particles.

Attenuation

In figures 65-67 and 70, the particle's final location was the pouring basin. In this case the large scatter in the data points was caused by the attenuation of the ɣ-rays produced from the particle due to the large thickness of the material the ɣ-rays are passing through. The loss of detection of true coincident events was due to absorption in the material, and/or scattering out of the detector's field of view of one or both of the back to back ɣ-rays [113]. The consequences of attenuation on the PEPT results can therefore be understood by understanding the contribution of absorption and scattering to the errors separately.

Figure 316 is a schematic diagram illustrating the effects of the absorption of ɣ-rays on the algorithm's ability to determine the particle location. Figure 316 a) is the case where no

absorption occurred and hence there is a large number of detected events to allow the algorithm to calculate the minimum perpendicular distance between the back-to-back ɣ-rays , which is where the particle is located. However, when the number of detected events decreases, figure 316 b), the algorithm is limited to a small number of events and therefore the calculated minimum perpendicular distance between the ɣ-rays will be larger giving less accurate results. Note that the "error" reported by the detection algorithm in millimetres is the average of the calculated minimum perpendicular distance between the ɣ-rays and was found to be up to ± 6 mm in the results shown in figures 65-67 and 70.

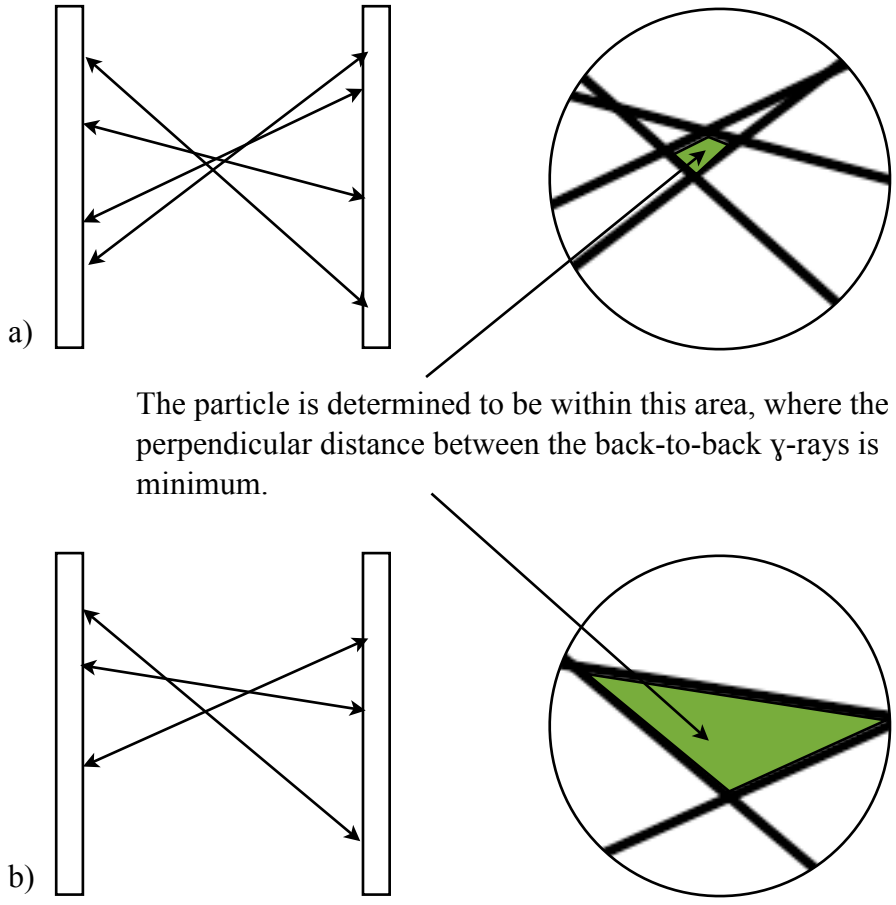

Figure 316. A schematic diagram showing the difference between a) a case where no absorption of the ɣ-rays occurred and hence the particle could be located accurately, within a small area of uncertainty and b) a case where absorption of ɣ-rays occurred and therefore the particle could only be located within a large area of uncertainty due to the insufficient amount of detected events.

Scattering

Figure 317 a) is a schematic diagram showing the case where the ɣ-rays are not scattered and therefore the particle location could be determined reasonably accurately. Note that, for simplicity, it has been assumed that the particle location is the exact intersection point between the ɣ-ray pairs. Figure 317 b) shows the case where one of the back-to-back ɣ-rays was scattered out of the field of view of the camera, leading to the algorithm associating the single ɣ-ray that was detected with one from another pair or even a cosmic ray, as shown by the dotted line. The result is a wrong location, shown by the dotted line, which changes the average of minimum perpendicular distances between all of the detected back-to-back ɣ-rays and hence an incorrect particle location is determined by the algorithm. The third possibility is the case where both back-to-back ɣ-rays are scattered out of the field of view of the camera, which has a similar effect to the absorption described previously (see figure 318), where a smaller number of detected events increases the error (uncertainty) in the particle location.

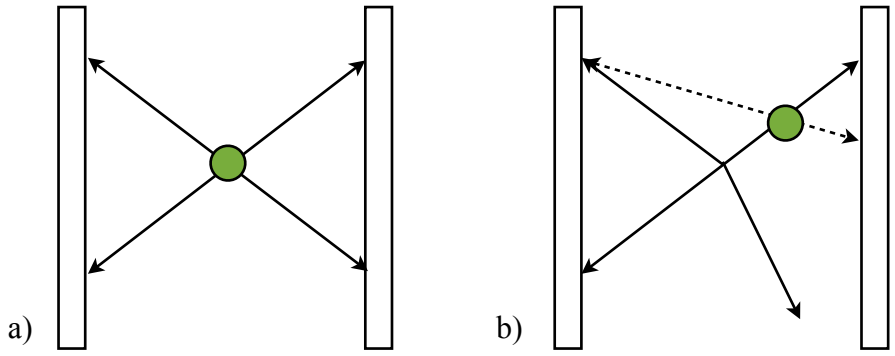

Figure 317. A schematic diagram showing a) the particle location determined as the intersection point of 2 pairs of ɣ-rays and b) the case where one of the ɣ-rays is scattered by the dense material and consequently a false particle location is determined as the intersection point between the corrupt event and the other ɣ-ray pair.

The radioactivity of an entrained particle was found to have a direct impact on the accuracy of the results. If the particle radioactivity was high, its final location could be determined more

accurately with less scatter of data points, because more radioactive decay events per second occurred and hence losses of data due to attenuation would be less significant. The attenuation coefficient of steel is 0.66 cm^{-1} which means that 1cm of steel is sufficient to absorb and/or scatter 52% of the ɣ-ray intensity and therefore a low particle radioactivity would result in less accurate tracking results being obtained, similar to the case described in figure 316. One example is the results shown in figures 60 and 61, where the particles were of radioactivities 11μCi and 30μCi when collected and therefore were probably only about 6μCi and 15μCi respectively, when the particle final location was being determined. This low radioactivity meant that a statistically reliable amount of events could not be obtained to estimate the minimum perpendicular distance between the ɣ-rays (the particle location) accurately, especially when that small number of events was reduced further by 52%, due to the large degree of attenuation caused by steel. However this does not mean that a strongly radioactive particle will always be located accurately by the algorithm (see figure 71, a particle that was 111μCi had an error of over ± 6 mm) due to other factors that could negate the effects of the strong radioactivity and decreased attenuation effects, which are discussed as follows. Note that the scatter observed in figures 60 and 61 was not solely due to attenuation but a mixture of other sources of error, as will be explained later.

Casting Alignment

Figure 318 is a schematic diagram showing the efficiency of the detectors with respect to the camera's geometry [114]. The camera is most efficient at its centre point and this efficiency decreases rapidly the further the particle is from the camera's centre [114, 115]. This is because when the particle is parallel to the centre of the camera, the largest number of ɣ-ray

pairs are detected, but when the particle is further from the centre the probability of losing one of the back-to-back ɣ-ray pairs, past the edge of the camera, increases. This is shown schematically by figure 319. Figure 319,a) shows that the coincident ɣ-rays produced around the particle facing the centre of the camera were detected and the particle location was correctly determined, while figure 319,b) shows that some coincident events are lost when the particle was facing the edge of the camera. These losses would result in corrupt events in the same manner as that shown earlier in figure 317,b) and hence an inaccurate particle location would be determined (see figure 319,b) indicated by the red particle.

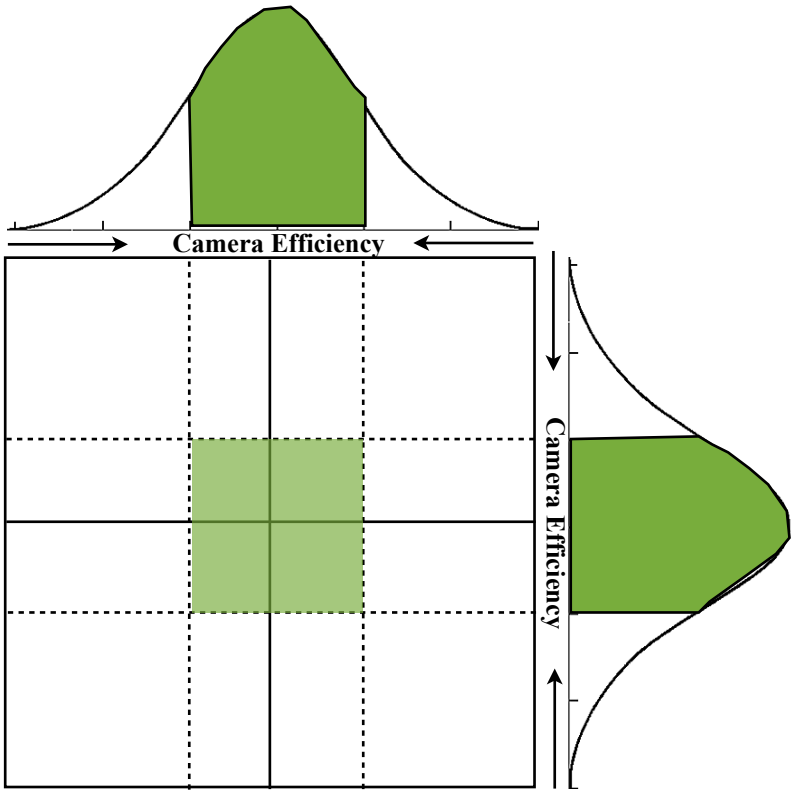

Figure 318. A schematic diagram showing the optimum field of view of the camera being in its centre.

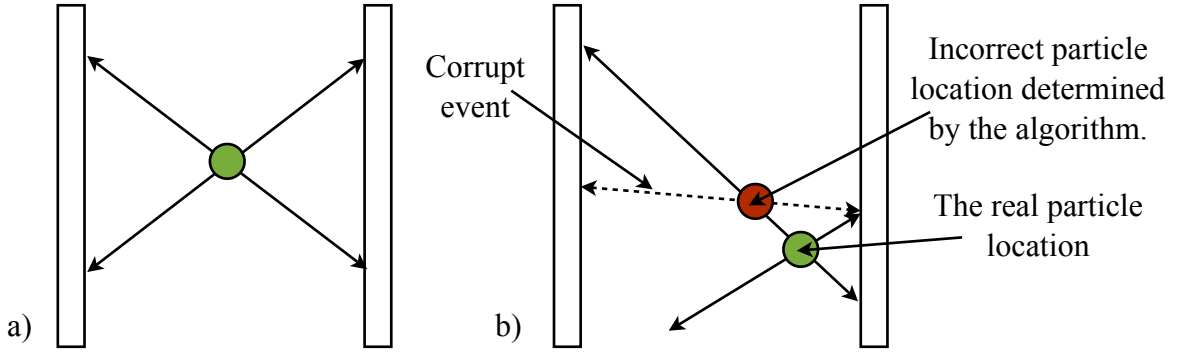

Figure 319. A schematic diagram showing the difference between, a) a particle at the centre of the camera faces that can be accurately located in comparison to b) a particle that is far from the centre of the camera where ɣ-rays can be lost and therefore leading to corrupt events that may lead to an inaccurate determination of the particle's location.

Therefore a casting should be aligned so that the part containing the embedded radioactive particle is parallel to the centre of the camera faces. How well this could be achieved depends on the casting geometry. The effect of misalignment was observed in the results shown in figures 60 and 61, where in both cases the particle was found to be half way along the runner bar, which was far from the camera's centre, as shown in figure 36.

Figures 62 and 63 also show another example of errors due to misalignment. In figure 62 the particle was found to be somewhere around the centre of the cast plate but with poor accuracy and scattered data points despite the particle's initial radioactivity of 38.8μCi (this level of radioactivity is considered low but was similar to that used in other PEPT experiments in steel castings which produced reasonable results). On the other hand figure 63 shows the location of an embedded particle, with lower initial radioactivity of 11μCi, to be the upper right hand side corner of the cast plate with a similar level of scatter to that observed in figure 62. Figure 320 is a schematic diagram showing the alignment of the casting between the camera faces (the same alignment was used in both experiments) where the final particle locations from both experiments have been superimposed on the one casting for comparison. The particle in

red is the alumina particle shown in figure 62, where it is clear that the ɣ-rays produced were attenuated to a much higher degree than in the case of the green particle of figure 63, because of the thick downsprue obstructing the path of the ɣ-rays. On the contrary the particle in green, shown in figure 63, produced ɣ-rays that were only attenuated by a few millimetres of steel and were therefore sufficient for an accurate determination of the particle location, despite the lower particle radioactivity. Unfortunately, at this time this method of alignment was used for many of the steel casting experiments and hence most of the results obtained where the particle was found to be near the edges of the cast plate (see figure 64), were more accurate than others where the particle came to rest in the centre of the plate.

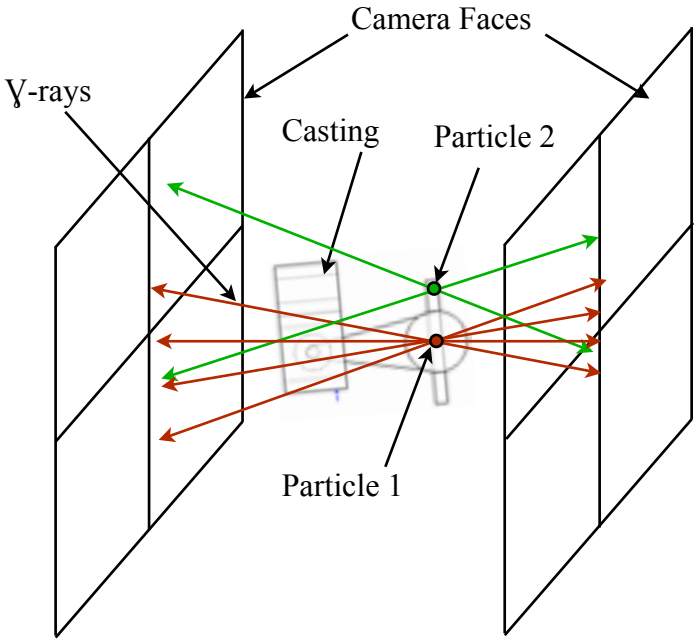

Figure 320. A schematic diagram showing the casting alignment between the (ADAC) positron camera faces. The particles showed in figures 62 and 63 were superimposed on the same casting for comparison and were labelled as particle 1 (in red) and particle 2 (in green) respectively.

A second important factor is the method employed to handle the reference particles that were required to determine the final location of the particle entrained in the casting. Given that the standard reported accuracy of the PEPT camera is ± 2-3 mm [62-64], the reference particles

had to be placed at exactly the chosen reference position, otherwise additional errors would be introduced to the measured particle location. Initially reference particles were glued to pin heads where the pins were used to move them, and these pins were then fixed in position using a commercial tack adhesive, so that the reference particle would be as close as possible to the reference position. But this was in most cases more than several millimetres away due to the thickness of the tack adhesive and therefore additional errors were observed in the results from these experiments. An example of such errors is shown by the points that were reported to be outside the body of the casting, such as those shown in figures 60, 61 and 63. The points reported to be outside the casting were obtained due to large errors in the placement of the reference particle, which were then transferred to the predicted location of the particle, since that was established relative to the intended location of the reference particle.

Another method was adopted to improve the accuracy of the results and in this case the reference particles were stuck to a strip of Sellotape™ which was used to manipulate them and place them in position. Figures 62,66,67 and 70 showed that this method to handle the reference particles was not ideal because it could lead to them shattering when pressure was applied to push the reference particles in place. Fragments were left behind that the algorithm detected as the imbedded particle. These false data points are clearly shown in the corners of the cast plates, which were usually the reference positions of choice. This, however, showed that the algorithm was capable of detecting 2 stationary particles simultaneously. Note that shattered particles could also occur when pressure was applied to glue them to the pin heads.

5.4.2 Sources of Error in The Low Melting Point Alloy Experiments

The sources of error in the low melting point alloy experiments were also of two types; ɣ-ray attenuation and experimental error. Attenuation was caused by both the casting and the acrylic mould. Errors arising from the various experimental procedures required for the PEPT experiments were due to the alignment of the mould between the camera faces, inconsistencies (lack of reproducibility) in preparing the radioactive particles, and inconsistencies in the casting conditions.

As explained earlier, see section 5.4.1, the attenuation of the ɣ-ray photons could have a considerable effect on the accuracy of the tracking results obtained. The attenuation coefficient is a quantitative description of the amount of reduction of the ɣ-ray photons reaching a detector due to absorption and scattering, and is given in cm^{-1}. The mass attenuation coefficient is the attenuation coefficient divided by the density of the material, and is given by cm^2g^{-1}. Figure 321 shows how the mass attenuation coefficient increases exponentially as the atomic number increases. In order to be able to estimate the level of attenuation taking place in Lensalloy-136 and in Field's metal, a mean atomic number was calculated for both alloys, using weighted averages of the constituent elements, as shown in table 31. Figure 321 shows Field's metal and Lensalloy-136 were estimated to have attenuations of 0.96 cm^{-1} and 1.17 cm^{-1} respectively, while steel (or pure Fe) had a much smaller attenuation coefficient of 0.66 cm^{-1}.

Table 31. An estimation of the attenuation coefficient of the low melting point alloys used.

Element	Atomic Number (Z)	Field's Metal	Lensalloy-136
In	49	51 wt%	21 wt%
Bi	83	32.5 wt%	49 wt%
Sn	50	16.5 wt%	12 wt%
Pb	82	-	18 wt%
Mean Atomic Number (Z_{eq})		60.2	71.7
Mass Attenuation Coefficient (cm^2/g)		0.118	0.133
Attenuation Coefficient (cm^{-1})		0.96	1.17

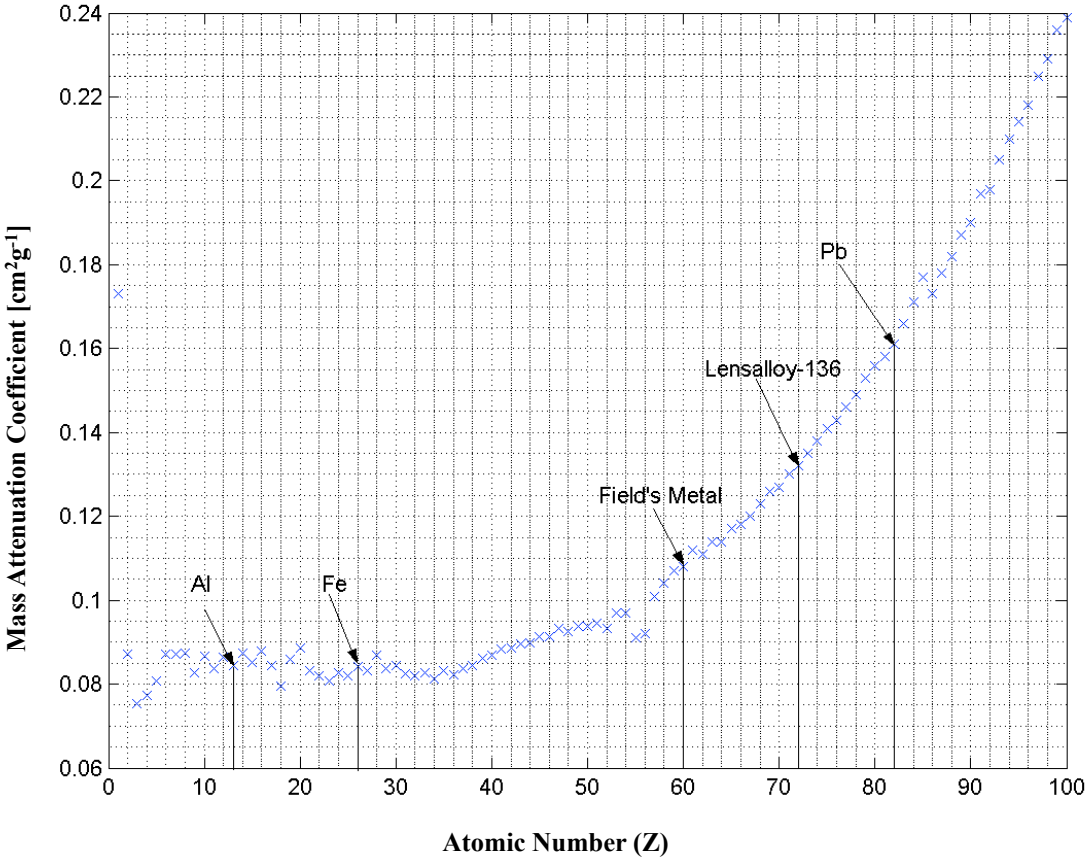

Figure 321. The mass attenuation coefficients plotted versus the atomic number [116].

Equations 22-24 describes the relationship between the intensity of the ɣ-rays penetrating a material with thickness d and attenuation coefficient μ. Equations 23 and 24 show that 5mm of the low melting point alloy resulted in a reduction in the ɣ-ray intensity by 38% and 44%, for Field's Metal and Lensalloy-136 respectively. The level of attenuation varied depending on the particle location within the casting and hence the distance through which the ɣ-radiation was passing. Table 32 is presented to show the magnitude of the ɣ-ray attenuation for different particle locations with respect to a datum, the outer surface of the casting, from which positions 1, 2, 3 and 4 were measured.

$$I_d = I_0 e^{-\mu d} \text{ ----------Equation 22}$$

$$I_d = I_0 e^{-0.96\times0.5} = 0.62 I_0 = 38\% \text{ reduction in intensity ----------Equation 23}$$

$$I_d = I_0 e^{-1.17\times0.5} = 0.56 I_0 = 44\% \text{ reduction in intensity ----------Equation 24}$$

Table 32. Examples of the possible variations in attenuation depending on the particle location in the casting, for both Field's metal and Lensalloy-136.

Position	Distance from datum (mm)	Attenuation in Field's Metal	Attenuation in Lensalloy-136
1	0	$I_d = I_0$	$I_d = I_0$
2	1	9%	11%
3	2.5	21%	25%
4	5	38%	44%

Of course, for a particle located at the casting surface, one ɣ-ray is attenuated the most, while its other back-to-back partner is attenuated the least. The worst case of attenuation, with

respect to the particle position in the low melting point alloy, is considered and added to the attenuation that would have been obtained from the acrylic mould (μ=0.1 cm^{-1}) [117], the intensity of the ɣ-rays reaching the (ADAC) positron camera would be reduced by 68% for Field's Metal and 71% for Lensalloy-136 (see equations 25 and 26). This explains the large scatter observed when the particle moved within the pouring basin (which was 50 mm in diameter) which would have reduced the intensity of the ɣ-rays by 99%, see figures 121 and 130.

$$I_d = (I_0 e^{-0.96\times0.5}) \times (I_0 e^{-0.1\times6.5}) = 0.32 I_0 = 68\% \text{ reduction in intensity} \quad \text{----------Equation 25}$$

$$I_d = (I_0 e^{-1.17\times0.5}) \times (I_0 e^{-0.1\times6.5}) = 0.29 I_0 = 71\% \text{ reduction in intensity} \quad \text{---------- Equation 26}$$

Therefore the maximum thickness of Lensalloy-136 that can be reliably used for PEPT experiments should be around 5mm, which corresponds to an attenuation of 44%. Using different low melting point alloys with lower atomic numbers than Lensalloy-136 and Field's Metal, may be advisable in order to further minimise the level of attenuation incurred. One candidate could be a eutectic composition of an In-Sn binary alloy, which is 48 wt% In and 52 wt% Sn (see figure 322), with a melting point of 140^{o}C. This alloy would have an equivalent atomic number of 49.5 which is 18% and 31% less than Field's Metal and Lensalloy-136 respectively. However, more work needs to be carried out to determine the maximum temperature, at which particles which were made radioactive by the ion exchange technique, could be used.

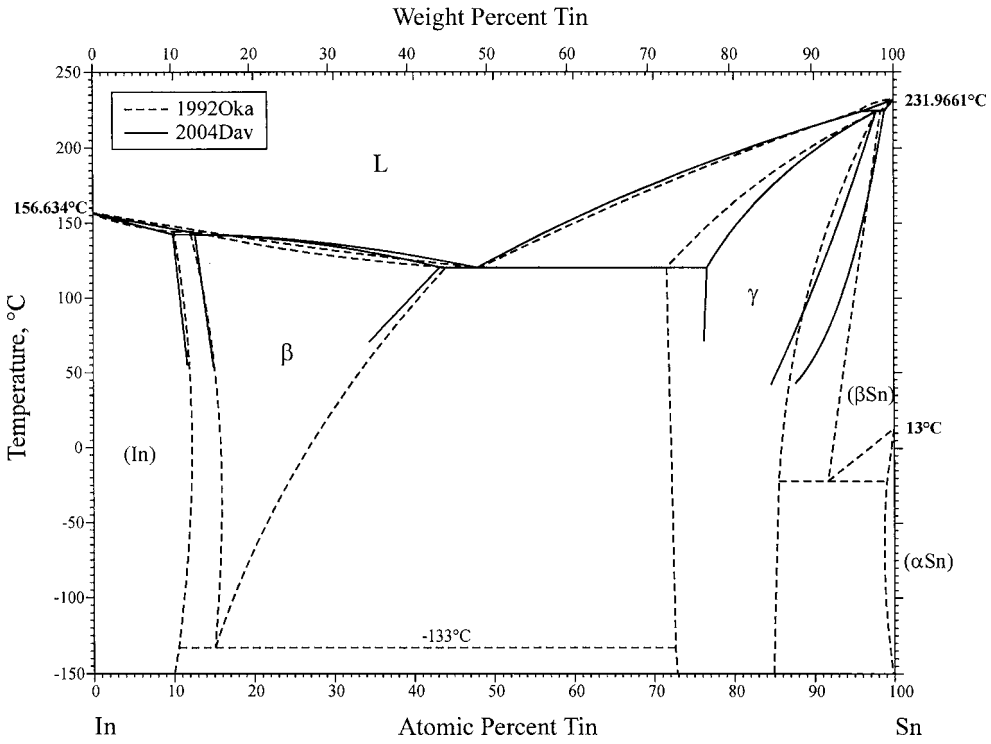

Figure 322. The binary phase diagram of In-Sn. The dotted lines were adopted from the literature and the solid lines represent the simulated phase diagram but for for temperatures above 50°C only [118].

A further source of experimental errors is the mould alignment between the camera faces. If the mould was not perfectly parallel to the camera faces, the measured particle path could not be superimposed accurately on the casting. Figures 124 and 139 clearly show that the particle path needed to be rotated in order to fit within the actual casting. This angle was calculated for some of the experiments by measuring the distance between the centreline of the mould and the centre line between the camera faces (marked on the table carrying the mould). A correction was not applied to the results in order to demonstrate the effect of this type of error, and that it should be avoided in order to increase the accuracy with which the tracking results are interpreted.

A second source of error arose from the experimental procedure carried out to radioactively label the porous alumina particles by ion-exchange. As explained previously in chapter 3, the

particles became radioactive due to the adsorption of irradiated water onto the particle surface, and the binding of ^{18}F ions to the Fe^{3+} ions that were introduced at the particle surface via prior surface modification techniques. After the particles have been labelled they are dried using an infrared lamp and a continuous stream of nitrogen. On several occasions the particles were not dried fully and this led to several contamination sites in the casting, due to radioactive water droplets leaving the particle's surface and moving with the liquid metal. This, however, did not affect the camera's ability to detect the particle path and its final location, with an error of ±1.5 mm.

Reproducibility

The lack of reproducibility in the casting conditions was due to the variable pouring rates of the liquid metal and not using a stopper rod for most experiments. Eliminating or minimising these sources of error was shown to improve reproducibility of the casting procedure and hence the particle paths obtained. In order to quantify the similarity or difference between particle paths from each experiment, a resultant particle path was calculated and compared for all experiments. This value was obtained by plotting the X,Y and Z coordinates of the particle versus time, and determining the distance travelled by the particle in each direction until it reached its final location. Afterwards the resultant particle path length (RPPL) was calculated, as shown in equation 27, where "X" is the distance travelled in the X-direction, "Y" in the Y-Direction and "Z" in the Z-direction.

$$RPPL = \sqrt{X^2 + Y^2 + Z^2} \quad \text{----------Equation 27}$$

Figure 323 shows the particle path lengths that were calculated for the base line experiments where an alumina particle was used (castings 1-9), the experiments where a resin particle was used, (casting 10 and 11), and the resultant particle path length (RPPL) values obtained for the experiments when the acrylic mould was preheated before casting, (casting 12-15). Castings 1-5 were influenced by the variable pouring rates of the liquid metal, which was done by hand. The mean of the RPPL values was 461 mm and the standard deviation for these castings was 248 mm. Castings 6-9 were the castings where an upper pouring basin and a stopper rod were used in order to make the entry conditions of the liquid metal into the mould reproducible, as well as the mould filling rate, and which resulted in a reasonable reproducibility of the particle path. The RPPL values obtained for castings 6-9 had a mean of 313 mm and a standard deviation of 27 mm, which meant that controlling the inlet conditions was critical for achieving good reproducibility.

Castings 10 and 11 used the resin particles and the liquid metal was hand poured, and therefore showed poorer reproducibility than that obtained when the inlet conditions were controlled. The obtained RPPL values had a mean of 374 mm and a standard deviation of 36 mm. Figure 130 (casting 10) also shows that the particle moved within the pouring basin before entering the mould, which is further evidence for the importance of reproducible pouring in order to obtain a reproducible casting.

Furthermore, castings 12-15 showed RPPL values with a mean of 277 mm and a standard deviation of 22mm. This meant that these experiments had the best reproducibility, despite the

practical difficulty in reassembling the acrylic mould after it has been preheated, before the mould temperature dropped below 80^{o}C.

Figure 324 shows the RPPL values obtained for the low melting point alloy experiments where ceramic foam filters were used. In castings 1-4 30ppi filters were used, and showed a mean RPPL value of 263 mm and a standard deviation on 6 mm. This low standard deviation showed good reproducibility despite the liquid metal being hand poured into the mould, but this is due to the particle being retained in the filter and not entering the mould cavity, which meant that there was little chance of variation in the particle path within the downsprue and the pouring basin. The same applies to the RPPL values obtained for the experiments where a 20ppi filter was used, castings 6-8, where the mean RPPL value was 301 mm and the standard deviation was 77 mm. Casting 5 had a much higher RPPL value than the other 20ppi experiments because the particle was not trapped in the filter, and came to rest in the top third of the tube, significantly increasing the particle path length in the Y-coordinate and consequently the RPPL value. The standard deviation of the castings where a 10ppi filter was used could not be determined because the particle entered the mould in only 1 casting (RRPL value shown as casting 9 on figure 324) while it remained in the pouring basin in the other 3 castings.

Table 33 shows a comparison between the ratio of standard deviation and the mean for the each set of experiments, where it was clear that, for the baseline experiments, the most reproducible RPPL were obtained when the inlet conditions were controlled and when the moulds were preheated.

Table 33. A comparison of the ratio of standard deviation and the mean RRPL values obtained from the low melting point alloy castings.

Experiment	Mean μ (mm)	Standard Deviation σ (mm)	σ/μ
Base Line Experiments - Alumina (castings 1-5)	461	248	0.5
Base Line Experiments - Alumina (castings 6-9)	313	27	**0.086**
Base Line Experiments - Resin (castings 10 and 11)	374	36	0.096
Preheated Mould Experiments - Alumina (castings 12-15)	277	22	**0.079**
30 ppi Filters	263	6	0.023
20 ppi Filters	301	77	0.26

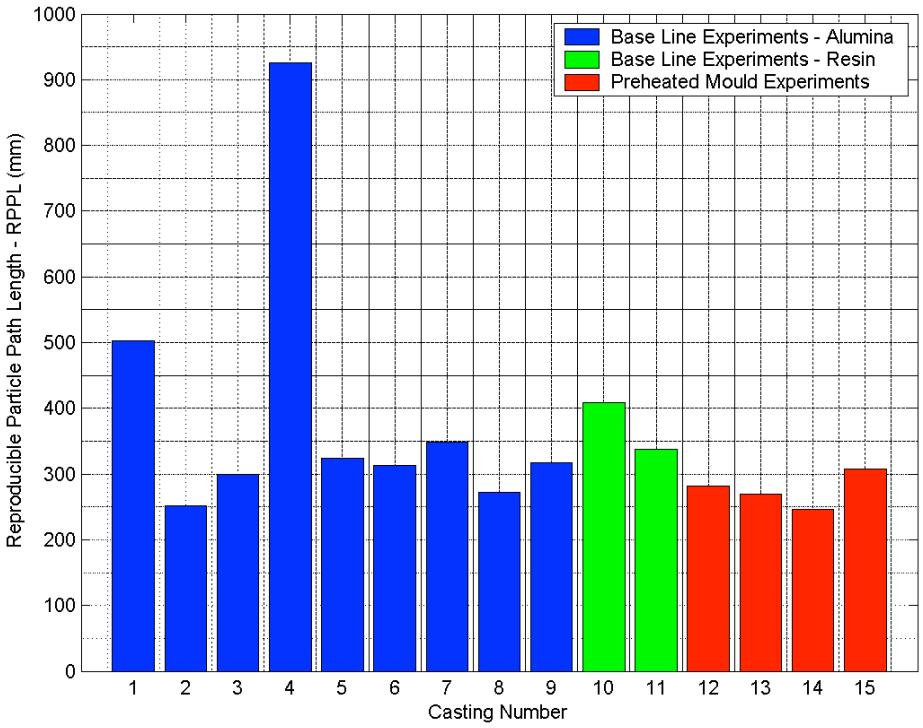

Figure 323. A bar chart showing the calculated Reproducible Particle Path Length (RPPL) values for the base line experiments where alumina and resin particles were used (castings 1-9 and 10-11 respectively). The RPPL values for the experiments where the mould was preheated are shown (castings 12-15).

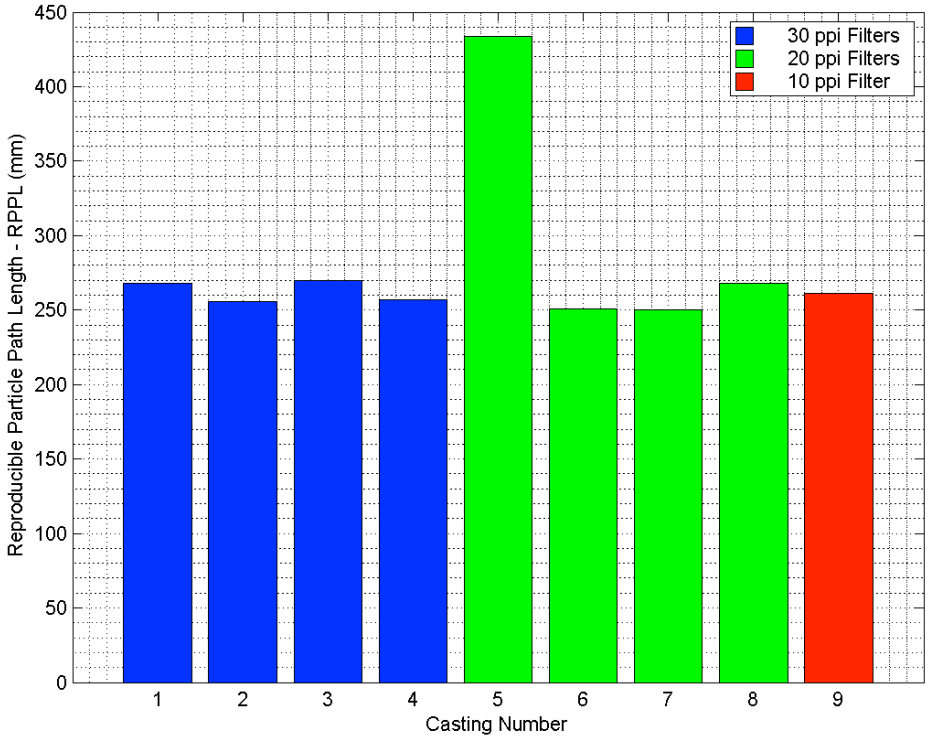

Figure 324. A bar chart showing the calculated Reproducible Particle Path Length (RPPL) values for the experiments where 30 ppi and 20 ppi filters were used (castings 1-4 and 5-8 respectively). The RPPL values for the experiment where a 10ppi filter was used and the particle entered the casting is shown as casting 9

5.5 Mathematical Modelling of Inclusions in Castings

5.5.1 Modelling Steel Castings Using MAGMAsoft™

MAGMAsoft™, as a widely used commercial software for castings, was chosen to model both the sand and investment cast steel plates, (geometries shown in figures 34 and 38), in which the final location of an entrained alumina particle was determined using PEPT. The aim was to determine wether the particle tracking feature in MAGMAsoft™, could produce useful predictions of particle movement within liquid steel. It was found that the predicted final location of the particle was different to that determined experimentally using PEPT. This was believed to be attributable limitations of the MAGMAsoft™ particle tracking model and its sensitivity to uncertainties in the thermophysical properties used.

5.5.1.1 Particle Tracking Limitations of MAGMAsoft™

MAGMAsoft™ is only capable of tracking a dimensionless tracer particle with no mass, which was a feature that was introduced to visualise how a defect present or formed at an initial position within a casting would behave [92]. This dimensionless tracer particle does not represent a solid inclusion within the liquid metal, because all interactions between this solid particle and the liquid metal surrounding it are ignored; owing to the absence of a particle size and density. One example is the drag and buoyancy forces, where the particle's size and density must be specified, which cannot be calculated.

In addition, the complex effects of turbulence on momentum diffusion within the liquid metal as it fills the mould, heat and mass transfer, chemical reactions, and species transport can not yet be modelled using MAGMAsoft™ [90]. Only an estimation of the effects of turbulence on the fluid flow behaviour is carried out in the model, by using an effective turbulent viscosity, which is essentially multiplying the viscosity by a factor of 10 [92]. This is based on the k-ε turbulence model, which is commonly used in commercial modelling packages [90, 119]. Although this may be a reasonable way of estimating the net effect of turbulence on fluid flow, it is not ideal to model the behaviour of a single inclusion within the liquid metal [90].

5.5.1.2 Thermophysical Property Sensitivity Analysis

The uncertainties associated with the thermophysical properties used in these models, (see table 14), were not reported by MAGMAsoft™. However, the experimental techniques used to measure the density and specific heat capacity were reported elsewhere in the literature to have roughly ± 2% uncertainty, depending on the technique used and the melting point of the alloy being investigated [109]. Uncertainties associated with thermal conductivity measurements were reported to range between ± 2-5% for steels [120] while the uncertainties in viscosity measurements for liquid metals could vary between ± 4-60% depending on the experimental method employed [121].

A sand cast plate, (see figure 34), was modelled to carry out an analysis of the sensitivity of the modelling results to changes in the thermophysical properties of steel, which were varied approximately within the range with which each property was thought to be known, and the

results obtained were shown in tables 17-22. It was clear that properties such as density, viscosity and the pouring temperature had a direct effect on the particle behaviour, because they directly affected the way in which the mould was filled. Thermophysical properties that did not affect the fluid flow significantly, such as specific heat capacity and thermal conductivity, did not affect the predicted particle path within the casting.

Figure 76 showed that when the correct thermophysical properties of the liquid steel were used, an inclusion was predicted to come to rest at the top left hand side of the plate. When the density was reduced by 5%, (see figures shown in table 17), the particle was predicted to come to rest in the top right hand side of the plate. The liquid metal was predicted to enter the mould at a velocity of about 0.93 ms^{-1}, hit the upper mould surface, and start spreading on the top surface of the cast plate cavity, for 0.7 seconds filling. Afterwards the liquid metal rapidly moved downwards due to gravity, leaving the particle behind at the top right hand surface, apparently, according to the model within a droplet of liquid metal that remained there. The particle did not move further because the model was stopped at 100% filling, and hence the effects of post filling fluid flow within the full mould on the particle final location could not be predicted. Note that no droplet of metal is clearly shown where the particle came to rest, (table 17 (E-H)), because the model only shows a cell that is 50% full [92]. In other words, the particle could not move independently from the metal, as it was modelled as a dimensionless marker point.

When the density was increased by 5% (see table 18) the particle was predicted to come to rest in the same position as that predicted for the case with the unchanged thermophysical

properties. In this case the liquid metal entered the mould at a higher velocity, of approximately 1.31 ms^{-1}, and also spread along the top surface of the mould cavity upon impact. But here the particle was left behind near the top right hand half of the cast plate cavity, again within a droplet of metal separated from the bulk liquid metal, while the rest of the metal continued to fill the mould, see table 18 (E and F). When the liquid metal came in contact with the particle again at 1.9s, the particle moved towards the left hand side of the cast plate cavity, where it came to rest.

When the viscosity was decreased by 25% (table 19) the particle came to rest at the top right hand side of the cast plate cavity. Again the particle was left behind at the top surface, within a splashed liquid metal droplet (table 19 (G and H)), while the bulk metal moved downwards due to gravity. When the viscosity was increased, (table 20), the particle moved with the bulk metal within the left hand side of the plate as shown in table 20 (C-F). It rose to the top as the metal entered the mould but in this case it moved back down with the liquid metal on the left hand side, after which it was swept horizontally to the left and started rising again vertically upwards with the liquid metal. The particle continued to move locally near the top left corner of the cast plate cavity, before it came to rest. The higher viscosity meant higher resistance to fluid flow and perhaps meant that less splashing occurred and hence the particle kept moving within the bulk metal.

Changing the pouring temperature was essentially an indirect variation of both density and viscosity at the same time. When the pouring temperature was reduced by 100^{o}C (table 21), the particle was left behind, at the top right hand side of the cast plate cavity, within a

detached droplet of liquid metal. The particle stayed there until it came into contact with the liquid metal again at 1.9s, where it moved horizontally towards the left hand side and started descending gradually with the colder metal, before it came to rest. When the pouring temperature was increased by 100^{o}C, the particle was also left behind at the top right hand side of the cast plate cavity, within a detached droplet. The particle remained in this position for 0.5 seconds and moved again when more metal splashes came in contact with it, (see table 22 (E-N)). The splashes seemed to have moved the particle slightly to the left until it came in contact with the bulk metal, as the mould was being filled, which swept the particle to the left hand side of the plate where it came to rest (table 22, K-P). Increasing the temperature seemed to increase the amount of splashing in the mould which significantly changed the predicted particle path.

The results obtained from this thermophysical property sensitivity analysis showed that the predicted particle paths should be used with caution. This is because in MAGMAsoft^{TM} models, the particle size and density are not taken into account, and hence particle-metal interactions are not modelled. Also, ignoring the effects of solidification during mould filling, as well as the effects of convection currents and residual fluid flow from pouring, adds significant uncertainty to the predicted particle paths obtained from the MAGMAsoft^{TM} models.

5.5.2 Modelling Lensalloy-136 Castings Using Flow-3D™

In the case of the low melting point alloy castings, modelled using Flow-3D™, limited information was found in the literature for their thermophysical properties, which were only reported for room temperature. Therefore an estimation of the thermophysical data at casting temperature was carried out using weighted averages of the thermophysical properties of the individual alloying elements. This was not ideal, but gave a similar fluid flow model, as evidenced by the video recording of the mould filling, (shown in figures 190-207), but with a filling time that was 3 seconds shorter than that obtained experimentally; the model predicted 6s for filling, while filling was complete after 9s in practice.

This difference in filling time between the experiments and the model is believed to be due to the difference between the calculated thermophysical properties that were used in the model and the real thermophysical properties of the metal. Another possibility could be the difference between the steady head pressure maintained in the model, which could not be achieved experimentally in this case, as the liquid metal was poured manually.

Flow-3D™ was used to model particle movement within the Lensalloy-136 castings, where in this case particle size and density could be specified as input parameters. The modelled particle path was similar to that obtained experimentally within the runner bar, where the particle moved along one side of the runner bar and entered the casting tube cavity from the side. However the particle behaviour within the tube cavity was different to that obtained from the PEPT experiments, where the particle came to rest at the bottom half of the tube (the predicted final particle location in the mould, see figures 125-128).

One reason could be that the model was carried out under the assumption that no solidification occurred before 100% filling and hence the possibility of the particle getting trapped in the solidifying skin advancing from the mould's surface, before the mould is completely filled, were ignored. In principle the effects of solidification could have been included in the simulation, but it was assumed that ignoring solidification during filling was a reasonable for two reasons. Firstly, owing to the slow solidification rate due to the poor thermal conductivity of the Perspex™ mould, where the castings were observed to take between 30-45 minutes to solidify when the experiments were carried out. Secondly, it was assumed that the particle would be unlikely to get trapped in the solidifying skin, due to the flat nature of the planar solidification front that is formed by eutectic alloys, such as Lensalloy-136.

Another reason could be the method by which Flow-3D™ accounts for turbulence using the Renormalization-Group (RNG) model (used in these simulations), which is based on the k-ε models, but in this case equation constants that are found empirically in the k-ε models are derived explicitly in the RNG model [91]. This method proved to give a reasonable prediction of fluid flow, as shown in table 26, where the predicted fluid flow behaviour by the model were similar to the results obtained from the video of the filling. However, it is believed that such an approximation for turbulence does not apply for predicting the effect of turbulence on an inclusion's path as well as it predicts the effects on fluid flow behaviour. This is because in this turbulence model, the size of the turbulence eddies is estimated to be of a default size which is 7% of the smallest cell size, the turbulent length scale (TLEN) [91]. In this case TLEN was 350 μm, which was much larger than the 80 μm particle, meaning that as the

80μm particle goes through a 350 μm diameter eddy, the particle path should be affected by this localised turbulence, and that is not simulated due to computation limitations. To model the turbulence over the whole range of eddy sizes an extremely fine mesh would be required, as well as more powerful computing hardware, than that is currently available.

Another factor affecting the predicted particle path was the coefficient of restitution, which describes the amount of energy retained by the particle upon its impact with a solid surface. In the model the coefficient of restitution was varied between -1 to 1. A value of -1 means that the particle loses all its energy when it first touches the mould wall and that it stops at the location of first impact, and a value of 1 means that the particle retains all of its energy upon impact with the mould wall. A value of zero means that the particle loses half its kinetic energy etc. [7, 91, 122].

The particle tracking model was sensitive to changes in the coefficient of restitution, as shown in figures 249-264. When the coefficient of restitution was set to -1 the particle came to rest in the downsprue upon its first contact with the mould walls. This was in contrast to the results obtained when the coefficient of restitution was set to 0 and 1, where in both cases the particle came to rest at different positions at the top of the cast tube. It was difficult to estimate a correct value of the coefficient of restitution to use, and it was not possible to measure it accurately due to the microscopic size of the studied alumina particles [122]. However it was clear that the model's sensitivity to the changes in values of the restitution coefficient meant that it can, perhaps, be used to obtain more accurate predictions of the particle path in castings.

5.6 Summary

Before the work presented here was carried out, there was no feasible experimental technique capable of tracking a real inclusion in liquid metals. Most of the work reported in the literature where inclusion movement was studied used water models and particles of similar rheological properties to inclusions found in castings. Consequently these qualitative techniques could not be applied to assess the predicted inclusion movement obtained from the currently available casting modelling packages.

This work has developed a novel experimental technique where single or multiple oxide inclusion particles could be tracked in real time. During the development of the technique various casting processes were investigated, such as sand casting, investment casting and the casting of low melting point alloys into a permanent acrylic mould. The sources of error due to attenuation of the ɣ-rays due to the various metals used, as well as the moulding materials, were identified and the experimental procedure was continuously improved until 4 inclusions were located in their predicted places and identified using an SEM with an EDX attachment. Those particles were found to be within 1.2-8 mm of their predicted final locations which was, in some cases, nearly half of the reported error from PEPT.

The tracking results obtained from these experiments were used to explain the behaviour of inclusions when ceramic foam filters were present in the running system and the filtration mechanism that took place with different pore size filters has been explained. The tracking results were also compared with the modelling results obtained from MAGMAsoft™ and Flow-3D™, and the capabilities and limitations of each package were determined. The

objectives of this project of developing a reliable experimental technique that can be used to track inclusions in castings and to compare the results obtained to those produced by the currently available casting modelling packages have been met.

Chapter 6
CONCLUSIONS

(1) PEPT can be used as an accurate experimental technique of tracking oxide inclusions in metal castings. This can be achieved more accurately for a single particle using the currently available tracking algorithm but the multiple particle tracking approach has also been shown to be workable.

(2) Silica and alumina particles, of size 90-425μm have been shown to be suitable particles for direct irradiation and use in the application of PEPT to study inclusions in shape castings.

(3) Alumina particles of size 63-100μm have been shown to be suitable candidates for being made radioactive using the ion-exchange technique where radioactivities up to 1000μCi could be obtained. However, the maximum temperature at which these radioactive particles could be used has not been exactly determined but has been found to be approximately 100^{o}C.

(4) The required radioactivity to obtain accurate tracking results from a directly activated oxide particle should be between 40-200 μCi. Although radioactivities above 200 μCi are theoretically desirable, particles that have been irradiated to this level were not detected after being entrained in a steel casting. The required radioactivity to obtain accurate results from particles irradiated by ion exchange was ≥ 40 μCi. However, these level of radioactivities are affected by the levels of attenuation observed in these experiments and are directly dependant on the alloy cast and the moulding materials used, as well as the general experimental setup between the camera faces.

(5) The effect of changing the initial particle position by 15 mm has been shown to result in a different final particle location, when an alumina particle of size 355-425μm was cast with steel into an investment mould.

(6) The effect of changing the particle size has also been shown to result in a different final particle location, where an alumina particle of size 530-630μm came to rest in the pouring basin, after being cast with steel into an investment mould. This was not the case when a similar casting was produced using an alumina particle of size, 355-425μm, where the particle came to rest in the cast plate.

(7) The reported errors of the final particle locations within the steel castings varied between 2.65-7.8 mm, in the X, Y and Z coordinates. These errors were found to vary with the level of attenuation caused by the section thickness of the material in which the particle came to rest. The largest standard deviations of up to 1.3mm were associated

with results where the particles were detected within the thick pouring basin, while the lowest standard deviation, 0.05mm was obtained when the particle came to rest in the runner bar (6mm in thickness). When the particles came to rest in the cast plate, the standard deviation varied between 0.1-0.6 mm.

(8) Ceramic foam filters of different pore sizes were shown to be able to remove inclusions from steel castings. Large particles of size 355-425μm were removed by a 10ppi filter, by a mechanism in which the liquid metal velocity was slowed so that the buoyancy of particles allowed them to float.

(9) Alumina particles of size 63-100μm were also successfully removed using ceramic foam filters, in the case of the low melting point alloy castings. But in this case it was demonstrated that the deceleration of the metal and flotation of the inclusions was a filtration mechanism which was dependant on the inclusion size, filter pore size and metal velocity. 10 ppi filters removed the alumina inclusions, of size 63-100μm, from the castings by allowing them to float out to the pouring basin. 30ppi filters were found to be able to trap all of the alumina inclusions, of size 63-100μm, that were used. 20ppi filters were not as efficient as 10 and 30ppi filters as 1 particle came to rest in the casting.

(10) Using a stopper rod has been demonstrated to be critical in controlling the inlet conditions and therefore the reproducibility of the low melting point alloy castings, carried out in the acrylic mould. The Reproducible Particle Path Length (RPPL) was

calculated for all the low melting point alloy castings and it was shown that the particle path was of most reproducibility when a stopper rod was used where a standard deviation / mean (σ/μ) value of 0.086 was obtained, in comparison to a (σ/μ) value of 0.5 when the liquid metal was poured manually, without a stopper rod.

(11) The NTrack algorithm was capable of distinguishing multiple particles that were ≥ 4mm apart, provided the radioactivities of the tracked particles were significantly different. This minimum separation distance was found to be increased if more particles were tracked, e.g reaching 20 mm with 6 particles. It was very difficult to control the ratio of obtained radioactivity in more than 3 particles, but it was demonstrated that more accurate results could be obtained if the radioactivities of the tracked particles, were of ratio > 2:1.

(12) Four particles were located in the castings carried out in this work. A 355-425 μm alumina particle, that was initially directly activated and cast in steel was located in an investment mould within 1.6mm from its predicted position. A 63-100μm alumina particle was located within a ceramic foam filter that was cast with Lensalloy-136 within 1.2 mm from its predicted location. Finally two, 90-150 μm alumina particles were located within 3.6mm and 8mm when both particles were cast at the same time in aluminium and tracked using the modular camera.

(13) Changing the thermophysical properties, mainly density and viscosity, affected the predicted particle paths obtained using MAGMAsoft™. Flow-3D™ has been shown to

be a more promising candidate than MAGMAsoft™, in predicting inclusion movement within a casting. But in both cases the modeled particle path was different to that obtained experimentally. The predicted particle paths obtained from Flow-3D™ were sensitive to changes in the coefficient of restitution as well as the initial particle position.

Chapter 7
FUTURE WORK

- A new type of tracer with a longer half life than ^{18}F, needs to be developed in order to maximise the use of the modular camera in liquid metal processing applications, such as continuous casting of steel and aluminium.

- The multiple particle tracking, NTrack, algorithm could be better optimised for casting applications where the detected events/sec may be significantly reduced due to unavoidable attenuation from the cast metal and the moulding materials.

- More work is required to study the filtration mechanisms of ceramic foam filters using the developed PEPT technique, which could not be carried out using the X-ray techniques available previously. A wider range of particle sizes and filter pore sizes should be used in order to determine the relationship between metal velocity, particle size and filter pore size , and consequently obtain a criteria with which the correct filters can be chosen for an application, rather than relying on trial and error.

- ^{11}C can be used to produce radioactive CO_2 or CO that can be used to study air entrainment in castings and the interaction of inclusions with bubbles in castings. This can be particularly beneficial to validate the various numerical models describing possible interaction processes between a gas bubble and an inclusion.

- More work is required to further improve the available ion-exchange technique to allow for labelling smaller particles of size < 63μm in order to study the behaviour of smaller inclusions in castings.

- More work is required to find a suitable, sticky, resin or polymer particle that could be successfully made radioactive by ion-exchange and could be cast with a low melting point alloy in order to study and validate the currently available theories of agglomeration mechanisms in liquid metals.

REFERENCES

[1] R. Kiessling, Non-Metallic Inclusions in Steel, Part I-IV: The Institute of Materials, 1976.

[2] D.J. Parker, C.J. Broadbent, P.Fowles, M.R. Hakesworth and P.McNeil, Positron Emission Particle Tracking - A Technique for Studying Flow within Engineering Equipment, Nuclear Instruments and Methods in Physics Research (1993); A326, p. 592-607

[3] D.J. Parker, T.W. Leadbeater, X. Fan, M.N.Hausard, A.Ingram and Z. Yang, Positron imaging techniques for process engineering: recent developments at Birmingham, Measurement Science and Technology (2008); 19, p. 094004

[4] J.R. Jones and J. Bridgwater, A case study of particle mixing in a ploughshare mixer using Positron Emission Particle Tracking, International Journal of Mineral Processing (1998); 53, 1-2, p. 29-38

[5] D.J. Parker, A.E. Dijkstra, T.W. Martin and J.P.K. Seville, Positron emission particle tracking studies of spherical particle motion in rotating drums, Chemical Engineering Science (1997); 52, 13, p. 2011-2022

[6] B.P.B. Hoomans, J.A.M. Kuipers, M.A. Mohd Salleh, M. Stien and J.P.K Seville, Experimental validation of granular dynamics simulations of gas-fluidised beds with homogenous in-flow conditions using Positron Emission Particle Tracking, Powder Technology (2001); 116, 2-3, p. 166-177

[7] R.D. Wildman and J.M. Huntley, Experimental measurements and modelling of rapid granular flows, Powder Technology (2008); 182, p. 182-191

[8] P.W. Cox, S. Bakalis, H. Ismail, R. Forster, D.J. Parker and P.J. Fryer, Visualisation of three-dimensional flows in rotating cans using positron emission particle tracking (PEPT), Journal of Food Engineering (2003); 60, 3, p. 229-240

[9] K. Mehauden, P.W. Cox, S. Bakalis, P.J. Fryer, X. Fan, D.J. Parker and M.J.H. Simmons, The flow of liquid foods in an agitated vessel using PEPT: Implications for the use of TTI to assess thermal treatment, Innovative Food Science and Emerging Technologies (2009); 10, p. 643-654

[10] Y. Payandeh and M. Soltanieh, Oxide Inclusions at Different Steps of Steel Production, Journal of Iron and Steel Research - International (2007); 14, 5, p. 39-46

[11] Y. Wang and S. Sridhar, The effect of gas flow rate on the evolution of the surface oxide on a molten low carbon Al killed steel, JOM (2005); 40, p. 2179-2184

[12] J.M. Zhang, J.F. Zhang, Z.G. Yang, G.Y. Li, G. Yao, S.X. Li, W.J. Hui and Y.Q. Weng, Estimation of maximum inclusion size and fatigue strength in high-strength ADF1 steel, Material Science and Engineering (2005); A394, p. 126-131

[13] P.K. Trojan, Inclusion Forming Reactions, vol.9, ASM Handbook: ASM International, 1999

[14] J. Campbell, Castings: Butterworth-Heinmann, 2003

[15] E. Evrasti and U. Stahlberg, Void initiation close to a macro-inclusion during single pass reductions in the hot rolling of steel slabs: A numerical study, Journal of Materials Processing Technology (2005); 170, p. 142-150

[16] E.T. Turkdogan, Fundamentals of Steel Making: The institute of Materials, 1996

[17] H.S. Kim, H.G. Lee and K.S. Oh, Precipitation Behavior of MnS on Oxide Inclusions in Si/Mn Deoxidized Steel, Metals and Materials (2000);6, 4, p. 305-310

[18] Steel Making Notes, Unpublished Work, Prof. C. Davis, University of Birmingham, UK

[19] S. Beretta, C. Anderson and Y. Murakami, Extreme value models for the assessment of steels containing multiple types of inclusion, Acta Materialia (2006); 54, p. 2277-2289

[20] Z.K. Wen, Z.L Hu and W.X. Hu, Nonmetallic Inclusion Control of 350 km/h High Speed Rail Steel, Journal of Iron and Steel Research - International (2009); 16, 3, p. 20-25

[21] Z.L. Feng, Inclusion and Bubble in Steel - A Review, Journal of Iron and Steel Research - International (2006); 13, 3, p. 1-8

[22] K.C. Mills, A Literature Review of Inclusion Removal by Filtration and Flotation: National Physical Laboratory, 1991

[23] M. Zhou, D. Shu, K. Li, W.Y. Zhang, H.J. Ni, B.D. Sun, and J. Wang, Deep Filtration of Molten Aluminum using Ceramic Foam Filters and Ceramic Particles with Active Coatings, Metallurgical and Materials Transactions A (2003); 34, 5, p. 1183-1191

[24] K.C.Taylor and I.N. Delaney, The determination of ductile iron reaction product retention in ceramic filter media, 60th World Foundry Congress, 1993

[25] J. Wikstrom, K. Nakajima, H. Shibata, A. Tilliander, P. Jonsson, *In situ* studies of the agglomeration phenomena for calcium–alumina inclusions at liquid steel–liquid slag interface and in the slag, Material Science and Engineering (2008); A495, p. 316-319

[26] R.V. Väinölä, L.E.K. Holappa, P.H.J. Karvonen, Modern Steelmaking Technology for Special Steels, Journal of Materials Processing Technology (1995); 53, p. 453-465

[27] D.T.Llewellyn and R.C.Hudd, Steels : Metallurgy and Applications : Butterworth-Heinmann, 2000

[28] Y.B. Kang, H.S. Kim, J. Zhang and H.G. Lee, Practical application of thermodynamics to inclusions engineering in steel, Journal of Physics and Chemistry of Solids (2005); 66, p. 219-225

[29] Y. Ying, L. Chaobin, W. Fuming, Y. Zhanbing and S. Bo, Effect of inclusions on the formation of acicular ferrite in Ti-bearing non quenched-and-tempered steel, Journal of University of Science and Technology Beijing, Mineral, Metallurgy, Material (2007); 14, 6, p. 501-506

[30] T. Pan, Z.G. Yang, C. Zhang, B.Z. Bai and H.S. Fang, Kinetics and mechanisms of intragranular ferrite nucleation on non-metallic inclusions in low carbon steels, Material Science and Engineering (2006); A438, 440, p. 1182-1132

[31] J.H. Shim, Y.J. Oh, J.Y. Suh, Y.W. Cho, J.D. Shim, J.S. Byun and D.N. Lee, Ferrite Nucleation Potency of Non-Metallic Inclusions in Medium Carbon Steels, Acta Materialia (2001); 49, p. 2115-2122

[32] C.H. Lee, H.K.D.H Bhadeshia and H.C. Lee, Effect of plastic deformation on the formation of acicular ferrite, Material Science and Engineering (2003); A360, p. 249-257

[33] M. Trokar, B. Breskvar, M. Tandler, D. Mandrino and M. Dobersek, EPMA and HRAES determination of complex inclusions in primary aluminium, Vacuum (2001); 62, p. 379-385

[34] Z.B. Wen, R.Z. Ming and W.J. Xiong, Continuous electromagnetic separation of inclusion from aluminum melt using alternating current, Transactions of Nonferrous Metals Society of China (2006); 16, p. 33-38

[35] D.M. Stefanescu and R. Ruxanda, Solidification Structures of Aluminium Alloys, vol.9, ASM Handbook: ASM International, 2004

[36] S. Fox and J. Campbell, Visualisation of Oxide Film Defects During Solidification of Aluminium Alloys, Scripta Materialia (2000); 43, p. 881-886

[37] R. Raiszadeh and W.D. Griffiths, The behaviour of double oxide film defects in liquid Al alloys under atmospheric and reduced pressures, Journal of Alloys and Compounds (2010); 491, p. 575-580

[38] J.E. Eklund, On The Effects of Impurities on The Solidification and Mechanical Behaviour of Primary and Secondary Commercial Purity Aluminium Alloys : PhD, Helsinki University of Technology, 1991

[39] V. P. Sylovanyuk, O. A. Mityaev, A. E. Ostrovs'ka, N. A. Ivantyshyn, and I. P. Volchok, Influence of Intermetallic Inclusions on The Endurance of Aluminium Alloys, Materials Science (2009); 45, 2, p. 299-308

[40] R. Ambat, A.J. Davenport, G.M. Scamans and A. Afseth, Effect of iron-containing intermetallic particles on the corrosion behaviour of aluminium, Corrosion Science (2006); 48, p. 3455-3471

[41] O. Majidi, S.G. Shabestari and M.R. Aboutalebi, Study of fluxing temperature in molten aluminum refining process, Journal of Materials Processing Technology (2007); 182, p. 450-455

[42] N.S. Cyrill and A. Fatemi, Experimental evaluation and modeling of sulfur content and anisotropy of sulfide inclusions on fatigue behavior of steels, International Journal of Fatigue (2009); 31, p. 526-537

[43] A. Ghosh, Secondary Steelmaking - Principles and Applications : CRC Press, 2000

[44] L.E.K Holappa and A.S. Helle, Inclusion Control in High-Performance Steels, Journal of Materials Processing Technology (1995); 53, p. 177-186

[45] H.V. Atkinson and G.Shi, Characterization of inclusions in clean steels: a review including the statistics of extremes methods, Progress in Materials Science (2003); 48, p. 457-520

[46] L. Zhang and B.G. Thomas, State of the Art in Evaluation and Control of Steel Cleanliness, ISIJ International (2003); 43, 3, p. 271-291

[47] M. Fernandes, N. Cheung and A. Garcia, Investigation of nonmetallic inclusions in continuously cast carbon steel by dissolution of the ferritic matrix, Materials Characterization (2002); 48, p. 255-261

[48] C.J. Simensen and G. Strand, Analysis of inclusions in aluminium by dissolution of the samples in hydrochloric/nitric acid, Fresenius' Journal of Analytical Chemistry (1981); 308, p. 11-16

[49] G. Canella, F. Monti, L. Pedicelli and A. L'Erede, Some results on the resolution of small inclusions in ultrasonic immersion testing of steel with focussed probes, NDT International (1983); 16, 3, p. 151-153

[50] J. Wannasin, D. Schwam, J.F. Wallace, Evaluation of methods for metal cleanliness assessment in die casting, Journal of Materials Processing Technology (2007); 191, p. 242-246

[51] D. C. Chesonis, D. H. DeYoung, D. E. Lake and N. R. Ridler, LiMCA Comparison of a Bed Filter and a Two Stage Ceramic Foam Filter, Light Metals : TMS, 2002

[52] Y. Ono, J.F. Moisan, Y. Zhang, C.K. Jen and C.Y. Su, An On-Line Ultrasonic Cleanliness Analyzer for Molten Light Metals, JOM (2004); 2, p. 59-64

[53] Department of Energy Fundamentals Handbook, Nuclear Physics and Reactor Theory, vol. Atomic and Nuclear Physics

[54] W.R. Hendee, G.S. Ibbott and E.G. Hendee, Radiation Therapy Physics : John Wiley & Sons, Inc., 2005

[55] T.F. Budinger and H.F. VanBrocklin, Positron-Emission Tomography (PET), The Biomedical Engineering Handbook : CRC Press LLC, 2000

[56] G.C.L. Ho, The evolution of positron emission tomography, Singapore Medical Journal (2005); 46, 6, p.257-258

[57] Greitz, Torgny, Ingvar, David H and Widén, Lennart, The metabolism of the human brain studied with positron emission tomography, Positron Emission Tomography : New York - Raven Press, 1983.

[58] C.S. Stellema, J. Vlek, R.F. Muddle, J.J.M. Goeij and C.M. Bleek, Development of an improved positron emission particle tracking system, Nuclear Instruments and Methods in Physics Research (1998); A404, p. 334-348

[59] A. Sadrmomtaz, D.J. Parker and L.G. Byars, Modification of a medical PET scanner for PEPT studies, Nuclear Instruments and Methods in Physics Research Section A (2007); 573, 1-2, p. 91-94

[60] Ö. Gündoğdu and E. Tarcan, Location-allocation algorithm for multiple particle tracking using Birmingham MWPC positron camera, Nuclear Instruments and Methods in Physics Research Section A (2004); 523, 1-2, p. 223-233

[61] X. Fan, 2006, A discussion about the maximum temperature an oxide particle could reach during direct irradiation. (Personal Communication, 2006)

[62] X. Fan, D.J. Parker and M.D. Smith, Labelling a single particle for positron emission particle tracking using direct activation and ion-exchange techniques, Nuclear Instruments and Methods in Physics Research Section A (2006); 562, 1, p. 345-350

[63] D.J. Parker and X. Fan, Positron emission particle tracking-Application and labelling techniques, Particuology (2008); 6, 1, p. 16-23

[64] X. Fan, D.J. Parker and M.D. Smith, Enhancing ^{18}F uptake in a single particle for positron emission particle tracking through modification of solid surface chemistry, Nuclear Instruments and Methods in Physics Research Section A (2006); 558, 2, p. 542-546

[65] P.G. Fairhurst, M. Barigou, P.J. Fryer, J.P. Pain and D.J. Parker, Using positron emission particle tracking (PEPT) to study nearly neutrally buoyant particles in high solid fraction pipe flow, International Journal of Multiphase Flow (2001); 27, 11, p. 1881-1901

[66] Ö. Gündoğdu, Positron Emission Tomography Particle Tracking Using Cluster Analysis, Nuclear Instruments and Methods in Physics Research Section A (2004); 534, 3, p. 562-576

[67] A. Guida, X. Fan, D.J. Parker, A.W. Nienow and M. Barigou, Positron emission particle tracking in a mechanically agitated solid-liquid suspension of coarse particles, Chemical Engineering Research and Design (2009); 87, 4, p. 421-429

[68] D.J. Parker, R.N. Forster, P. Fowles and P.S. Takhar, Positron emission particle tracking using the new Birmingham positron camera, Nuclear Instruments and Methods in Physics Research Section A (2002); 477, 1-3, p. 540-545

[69] S. Bakalis, P.W. Cox, W.W. Nolan, D.J. Parker and P.J. Fryer, Use of Positron-Emission Particle Tracking (PEPT) Technique for Velocity Measurements in Model Food Fluids, Journal of Food Science (2003); 68, 9, p. 2684-2692

[70] Z. Yang, D.J. Parker, P.J. Fryer, S. Bakalis and X. Fan, Multiple-particle tracking-an improvement for positron particle tracking, Nuclear Instruments and Methods in Physics Research Section A (2006); 564, 1, p. 332-338

[71] Ö. Gündoğdu, Multiple particle tracking using the Birmingham positron camera: PhD, University of Birmingham, 1999

[72] Z. Yang, P.J. Fryer, S. Bakalis, X. Fan, D.J. Parker and J.P.K. Seville, An improved algorithm for tracking multiple, freely moving particles in a Positron Emission Particle Tracking system, Nuclear Instruments and Methods in Physics Research Section A (2007); 577, 3, p. 585-594

[73] A. Guida, A.W. Nienow, M. Barigou, PEPT measurements of solid–liquid flow field and spatial phase distribution in concentrated monodisperse stirred suspensions, Chemical Engineering Science (2010); 65, p. 1905-1914

[74] M. Barigou, Particle Tracking in Opaque Mixing Systems: An Overview of the Capabilities of PET and PEPT, Chemical Engineering Research and Design (2004); 82, 9, p. 1258-1257

[75] S. Bakalis, P.W. Cox, A.B. Russel, D.J. Parker and P.J. Fryer, Development and use of positron emitting particle tracking (PEPT) for velocity measurements in viscous fluids in pilot scale equipment, Chemical Engineering Science (2006); 61, 6, p. 1864-1877

[76] K.E. Cole, K.E. Waters, D.J. Parker, S.J. Neethling and J.J. Cilliers, PEPT combined with high speed digital imaging for particle tracking in dynamic foams, Chemical Engineering Science (2010); 65, p. 1887-1890

[77] M. Velden, J. Baeyens, J.P.K. Seville and X. Fan, The solids flow in the riser of a Circulating Fluidised Bed (CFB) viewed by Positron Emission Particle Tracking (PEPT), Powder Technology (2008); 183, 2, p. 290-296

[78] R.D. Wildman, S. Blackburn, D.M. Benton, P.A. McNeil and D.J. Parker, Investigation of paste flow using positron emission particle tracking, Powder Technology (1999); 103, 3, p. 220-229

[79] B.G. Anderson, R.A. Santen and L.J. Ijzendoorn, Positron emission imaging in catalysis, Applied Catalysis (1997); A160, p. 125-138

[80] K.E. Waters, N.A. Rowson, X. Fan, D.J. Parker and J.J. Cilliers, Positron emission particle tracking as a method to map the movement of particles in the pulp and froth phases, Minerals Engineering (2008); 21, 12-14, p. 877-882

[81] Z. Yang, X. Fan, S. Bakalis, D.J. Parker and P.J. Fryer, A method for characterising solids translational and rotational motions using Multiple-Positron Emission Particle Tracking (Multiple-PEPT), International Journal of Multiphase Flow (2008); 34, 12, p. 1152-1160

[82] P.P. Oprych, A.W. Nienow and M. Barigou, Positron emission particle tracking (PEPT) compared to particle image velocimetry (PIV) for studying the flow generated by a pitched-blade turbine in single phase and multi-phase systems, Chemical Engineering Science (2009); 64, p. 4955-4968

[83] P.E. Valk, D.L. Bailey, D.W. Townsend and M.N. Maisey, Positron Emission Tomography : Springer, 2003

[84] R.A. Stoehr and W.S.H, Modeling of Fluid Flow, vol. 15, ASM Handbook : ASM International, 1988

[85] C.W. Hirt and B.D. Nichols, Volume of fluid (VOF) method for the dynamics of free boundaries, Journal of Computational Physics (1981); 39, p. 201-255

[86] P. Cleary, J. Ha, V. Alguine and T. Nguyen, Flow modelling in casting processes, Applied Mathematical Modelling (2002); 26, p. 171-190

[87] P.K. Kundu and I.M. Cohen, Fluid Mechanics : Academic Press, 2001

[88] H. Chanson and C. Gualtieri, Similitude and Scale Effects of air Entrainment in Hydraulic Jumps, Journal of Hydraulic Research (2008); 46, p. 35-44

[89] D. Mazumdar and J.W. Evans, Modeling of Steelmaking Processes : Taylor and Francis Group, 2010

[90] P. Forlag, Fundamentals of Numerical Modelling of Casting Processes : Natayana Press, Gylling, 2005

[91] Flow-3D™ User Manual V.9.3

[92] MAGMAsoft™ User Manual V.4.1

[93] J.C.S. Lai and C.Y. Yang, Numerical simulation of turbulence suppression: Comparisons of the performance of four k-e turbulence models, International Journal of Heat and Fluid Flow (1997); 18, p. 575-584

[94] P. Ferrey and B. Aupoix, Behaviour of turbulence models near a turbulent/non-turbulent interface revisited, International Journal of Heat and Fluid Flow (2006); 27, p. 831-837

[95] P.W. Cleary, J. Ha, M. Prakash and T. Nguyen, Short shots and industrial case studies: Understanding fluid flow and solidification in high pressure die casting, Applied Mathematical Modelling (2010); 34, p. 2018-2033

[96] C. Ertbruggen, P. Corieri, R. Theunissen, M.L. Riethmuller and C. Darquenne, Validation of CFD predictions of flow in a 3D alveolated bend with experimental data, Journal of Biomechanics (2008); 41, p. 399-405

[97] C. Pfeiler, M. Wu and A. Ludwig, Influence of argon gas bubbles and non-metallic inclusions on the flow behavior in steel continuous casting, Material Science and Engineering (2005); A413, 414, p. 115-120

[98] Y. Qiang, Z.Z. Sho, H.Q. Fu and C. Zhou, Water Modeling of Swirling Flow Tundish for Steel Continuous Casting, Journal of Iron and Steel Research- International (2009); 16, 5, p. 17-22

[99] Y. Qiang, Z.Z. Shu and H.Q. Fu, Aggregation Kinetics of Inclusions in Swirling Flow Tundish for Continuous Casting, Journal of Iron and Steel Research- International (2010); 17, 5, p. 6-10

[100] L. Zhang and B.G. Thomas, Numerical Simulation on Inclusion Transport in Continuous Casting Mold, Journal of University of Science and Technology Beijing (2006); 13, 4, p. 293-300

[101] M. Alizageh, H. Edris and A. Shafyei, Fluid Flow and Mixing in Non-Isothermal Water Model of Continuous Casting Tundish, Journal of Iron and Steel Research - International (2008); 15, 2, p. 7-13

[102] O. Smirnov, P. Väyrynen, A. Kravchenko and S. Louhenkilpi, Modern Methods of Modeling Fluid Flow and Inclusions Motion in Tundish Bath: General View, 3rd International Conference on Simulation and Modelling of Metallurgical Processes in Steelmaking, Leoben, Austria, 2009

[103] J.W. Han and U. Yoon, A Numerical Simulation for Mini-mill Tundish Design -Effects of FC Pad on Tundish Flow Characteristics, Metals and Materials (1998); 4, 3, p. 173-182

[104] Acton Bright Steel, Unpublished Work, Technical Guide EN3B, p. 1-3, 2007

[105] International BS. Specification for Aluminium and Aluminium Alloy Ingots and Castings for General Engineering Purposes. BSI, 1988.

[106] MAGMAsoft™ GmbH, Thermophysical Property Database, V.4.4

[107] ASM International, Cerrolow-136 Alloy, New Jersey : Engineering Alloys Digest, Inc., 1979

[108] J. Bridgwater, S. Forrest and D.J. Parker, PEPT for agglomeration?, Powder Technology (2004); 140, 3, p. 187-193

[109] K.C. Mills, Recommended Thermophysical Properties for Selected Commercial Alloys : Woodhead Publishing, 2002

[110] A.H. Zadeh and J. Campbell, Metal Flow through a Filter System, AFS Transactions (2002); 2, 20, p. 1-17

[111] J.C. Gebelin and M.R. Jolly, Modeling Filters in Light Alloy Casting Processes, AFS Transactions (2002); 110, p. 109-120

[112] O. Maldonado, A. Adams, L. Oliveira, B. Alquist and R.D. Morales, Simulation of Fluid and Inclusions Dynamics during Filtration Operations of Ductile Iron Melts Using Foam Filters, Metallurgical and Materials Transactions B (2008); B39, p. 818-839

[113] University of Virginia, 2010, Attenuation Correction, Online, Updated 2006, Available at:http:// www.med-ed.virginia.edu/courses/rad/PETCT/Attenuation.html, Accessed March 2010

[114] A. Ingram, M. Hausard, X. Fan, D.J. Parker, J.P.K. Seville, N. Finn and M. Evans, Portable Positron Emission Particle Tracking (PEPT) for Industrial Use, ECI Conference on The 12th International Conference on Fluidization - New Horizons in Fluidization Engineering, Vancouver, Canada, 2007

[115] D.J. Parker, 2010, The Efficiency of the ADAC (positron) Camera. (Personal Communication, 2010)

[116] M.J. Berger and J.H. Hubbel, Photon Attenuation Coefficients, vol.10, Handbook of Chemistry and Physics, p. 235-238 : CRC Press, 2009-2010

[117] S. Brown, D.L. Bailey, K. Willowson and C. Baldock, Investigation of the relationship between linear attenuation coefficients and CT Hounsfield units using radionuclides for SPECT, Applied Radiation and Isotopes (2008); 66, 9, p. 1206-1212

[118] H. Okamoto, In-Sn (Indium-Tin), Journal of Phase Equilibria and Diffusion (2006); 27, 3, p. 313

[119] P.G.Q. Netto, R.I.L. Guthrie, The importance of turbulence modelling in the design of a novel delivery system for a single-belt steel casting process, International Journal of Heat and Mass Transfer (2000); 43, p. 21-37

[120] Standard Test Method for Thermal Conductivity of Solids by Means of the Guarded- Comparative-Longitudinal Heat Flow Technique : ASTM International, 2009

[121] S.I. Bakhtiyarov and R.A. Overfelt, Measurement of liquid metal viscosity by rotational technique, Acta Materialia (1999); 47, 17, p. 4311-4319

[122] N. Farkas and R.D. Ramsier, Measurement of coefficient of restitution made easy, Physics Education (2006); 41, 1, p. 73-75

Appendix I
LIST OF PUBLICATIONS

The following is a list of publications produced from the work presented in this thesis, including an article published in the Foundry Trade Journal that was awarded the British Foundry Medal in 2009:

(1) W.D.Griffiths, Y.Beshay, D.J.Parker and X.Fan, Positron Emission Particle Tracking (PEPT) of Inclusions in Metals, The Conference of Mineral Industries, Research Centre for Mineral Industries, Shahid Bahonar University of Kerman, Kerman, Iran, 2010

(2) W.D.Griffiths, Y.Beshay, D.J.Parker, X.Fan and M.Hausard, The Application of Positron Emission Particle Tracking (PEPT) to Study The Movement of Inclusions in Shape Castings, 3rd International Symposium on Shape Casting, San Francisco, CA, 2008

(3) W.D.Griffiths, Y.Beshay, D.J.Parker and X.Fan, The Determination of Inclusion Movement in Steel Castings by Positron Emission Particle Tracking (PEPT), Journal of Materials Science (2008); 43, 21, p.6853-6856

(4) W.D.Griffiths, Y.Beshay, A.Caden, D.J.Parker, X.Fan and M.Hausard, The Application of Positron Emission Particle Tracking (PEPT) to the study of inclusions in metal castings, The Foundry Trade Journal, 2008

(5) Y.Beshay, W.D.Griffiths, D.Parker and X.Fan, Radioactively Labelled Particle Tracking in Steel Castings, 2nd International Symposium on Shape Casting, Orlando, FL, 2007

Appendix II
ATTACHMENTS

A CD has been attached at the back of this thesis, which contains some of the videos described in the previous sections. The following is a list of these videos:

1. **FLOW-3D MODEL OF THE BASELINE CASTING**

   This is a 3-D isometric view, showing the filling of the Perspex mould with Lensalloy-136. The video shows a particle of diameter 80 microns that was visually enlarged for clarity.The predicted total filling time was 6.09 seconds.

2. **INVESTMENT CASTING**

   A video showing one of the investment castings carried out in this research, where steel was poured directly from the furnace into the mould.

3. **THE FILLING OF THE PERSPEX MOULD WITH LENSALLOY-136**

   The filling of the Perspex mould with Lensalloy-136 was video recorded, when Lensalloy-136 was manually poured into the mould. The total filling time was 8.7 seconds.

4. **THE FILLING OF THE PERSPEX MOULD WITH LENSALLOY-136, IN SLOW MOTION**

   This is the same video as in (3) but in this case it was slowed by 50% in order to allow for a clearer demonstration of the filling pattern of the mould.

5. **X-RAY OF THE ALUMINIUM SAND CASTING**

   This is a video recorded when the Al sand cast plate was reproduced in the X-ray casting facility of the University of Birmingham. The mould was completely filled in 1.86 seconds. In this case a stopper rod was not used due to the practical difficulties involved.